

DELFT UNIVERSITY OF TECHNOLOGY

GRADUATION PROJECT
SET3901

Modelling of Spar Cap Shear Web Assembly to Identify and Localize Damage

by
Sharnish K Shanmugasundaram

to obtain the degree of Master of Science
in Sustainable Energy Technology
at the Delft University of Technology,
to be defended publicly on Thursday, November 26, 2020 at 2:00 PM.

Student Number: 4836960

Project Duration: December 19 2019 - October 31 2020

Thesis Committee: Prof. Dr. Simon Watson TU Delft, Internal supervisor
Dr. Dimitrios Zarouchas TU Delft, Committee
Dr. Julie Teuwen TU Delft, Committee
Sharif Khoshmanesh TU Delft, Internal supervisor

An electronic version of this thesis is available at <http://repository.tudelft.nl/>



Abstract

Wind energy is one of the cleanest methods of producing electricity. It plays a major role in the transition towards green energy. It is estimated that the installed capacity of wind energy will cover more than 6% of total global electricity demand by the end of 2019. As the demand grows the requirement for bigger wind turbine also grows. Each year larger wind turbine blades are being manufactured to satisfy the growing demand, resulting in high manufacturing cost and operation and maintenance cost. So, an effective and proactive monitoring system for the wind turbine blades becomes necessary due to the large downtime associated with failure and high replacement cost.

The main objective of this thesis is to use smeared crack modelling and integrating it with FEM tools (ANSYS 18.2) to identify the damage in the wind turbine blade. First, spar cap - shear web assembly is modelled as simple "I" beam in ANSYS. The dimension of the blade is measured from the "NedWind 40 turbine" provided by LM Wind Power. The structure has been modelled using composite materials. The spar cap fibres are laid at 0° and the fibres of face sheet are laid at $\pm 45^\circ$. One end of the structure is fixed to simulate the actual working conditions. Similarly, the material property of all parts was chosen to represent the actual wind turbine blade. To incorporate damping into the structure, the loss factor obtained from experiment is used. Damage is introduced into the structure in the form of microscopic damping into the material property. The damage modelling is done for different severity at different locations of the blade.

The concept that the damping of the structure will increase when it is damaged is used to identify the damage. There will be a lag in the phase angle of the damaged elements compared to the phase angle of the undamaged elements. Change in phase angle of each element is used to localize the damaged elements.

From the results shown in chapter 6, it is evident that this method is more suitable for identifying defects in the fixed end and in the midsection. Since, the kinetic energy transferred by the elements near the tail end is very low, that the change in phase angle is very less to identify the defected elements in these areas. Also, 1st flapwise and edgewise bending frequencies are suitable for identifying the defects near the fixed end and 2nd flapwise bending frequency is suitable for identifying the defect near the mid area.

Acknowledgement

Last two years have been an important journey of my life. Completion of this thesis means the completion of my masters degree. This would not have been possible without the help and assistance of several people.

First, I would like to thank my supervisor, *Prof.Simon Watson* for his support and guidance throughout this thesis. Your unique insights on wind turbine blade bending frequencies provided me a new scopes for plotting the results and understanding it in a better way. Also, thank you for you valuable comments on the report, it help me to deliver the report in more scientific way. I would also like to thank *Sharif Khoshmanesh* for his valuable opinion and leading me in the right direction. I am grateful for all the support and data provided by Sharif. Without him, this work would not have been possible. your positive attitude towards the research gave me more strength to continue the project with high quality. I would also like to convey my gratitude to *prof.Dimitrios Zarouchas* for his valuable insights and comments on my model. Thank you for your swift responses and helpful suggestions even during your busiest time, I was able make improvements to my model.

I would like to all thank my friends from my class, student room whose contributions by discussions were invaluable. I would also like to take this opportunity to thank my dearest friends *Priya Ramakrishnan* for her caring and love through my darkest times. She made my stay in the Netherlands a truly enjoyable. I would also like to extend my thanks to my friend *Sai* for his long calls, advises and motivations.

Finally but more importantly, I am forever indebted to my parents and my brother for supporting my dreams and their constant encouragement.

Contents

Abstract	i
Acknowledgement	iii
List of Figures	vii
List of Tables	xiii
Abbreviations	xv
Nomenclature	xvii
1 Introduction	1
1.1 Wind energy background	1
1.2 Failure in wind turbine	1
1.3 Maintenance of wind turbine blade	3
1.3.1 Vibration analysis methodology	3
1.3.2 Categories of vibration measurement	4
1.4 Research Scope	4
1.5 Report Layout	4
2 Background	7
2.1 Crack identification using vibration analysis	7
2.1.1 Vibration analysis techniques	7
2.1.2 Crack analysis in a cantilever beam using modal parameters	7
2.1.3 Multiple crack identification in cantilever beam	8
2.1.4 Crack detection in beam using fuzzy logic	8
2.1.5 Crack detection in beam structures using wavelet transform	8
2.2 Vibration analysis in wind turbine blade with composite materials	9
2.2.1 Detection of crack in wind turbine blade	9
2.3 Viscoelastic material basics	11
2.4 Viscoelastic damping basics	15
2.5 Material damping properties	18
2.6 Inverse Finite Element Analysis	20
2.7 Research Problem	20
2.8 Methodology	21
3 Vibration Modelling	23
3.1 Constitutive equation of a linear viscoelastic material	23
3.2 Finite element vibration equation of a linear viscoelastic material	23
3.2.1 Time domain equation of motion	24
3.2.2 Laplace form of equation of motion	25
3.3 Eigenvalue and eigenvector of vibration equation	26
3.3.1 Eigenvalue and eigenvector of non proportional damping	27
4 Damage Modeling	31
4.1 Damage modelling concept	31
4.2 Spar cap - shear web assembly	31
4.2.1 ANSYS model	32
4.3 Damage modelling of spar cap - shear web assembly	35
4.3.1 Scenario 1: Damage only in top surfaces near fixed end with 2 %, 4 %, 6 % defected area	39
4.3.2 Scenario 2: Damage only in top surfaces near mid section with 2 %, 4 %, 6 % defected area	41
4.3.3 Scenario 3: Damage in top and core surfaces near fixed end with 2 %, 4 %, 6 % defected area	43
4.3.4 Scenario 4: Damage in top and core surfaces near mid section with 2 %, 4 %, 6 % defected area	44

5	Damage Identification and Localization	47
5.1	Damage identification and localization concept	47
5.1.1	Damage identification	47
5.1.2	Damage localization	47
5.2	Damage identification and localization of spar cap - shear web assembly	48
5.2.1	Scenario 1: Damage only in top surfaces near fixed end with 2 %, 4 %, 6 % defected area	48
5.2.2	Scenario 2: Damage only in top surfaces near mid section with 2 %, 4 %, 6 % defected area	52
5.2.3	Scenario 3: Damage in top and core surfaces near fixed end with 2 %, 4 %, 6 % defected area	56
5.2.4	Scenario 4: Damage in top and core surfaces near mid section with 2 %, 4 %, 6 % defected area	60
6	Results and Discussions	65
6.1	Scenario 1: Damage only in top surfaces near fixed end with 2 %, 4 %, 6 % defected area	65
6.1.1	Case 1: Top surface damage near fixed end with 2 % defected area	65
6.1.2	Case 2: Top surface damage near fixed end with 4 % defected area	66
6.1.3	Case 3: Top surface damage near fixed end with 6 % defected area	68
6.2	Scenario 2: Damage only in top surfaces near mid section with 2 %, 4 %, 6 % defected area	70
6.2.1	Case 1: Top surface damage near mid section with 2 % defected area	70
6.2.2	Case 2: Top surface damage near mid section with 4 % defected area	71
6.2.3	Case 3: Top surface damage near mid section with 6 % defected area	73
6.3	Scenario 3: Damage in top and core surfaces near fixed end with 2 %, 4 %, 6 % defected area	75
6.3.1	Case 1: Top and core surface damage near fixed end with 2 % defected area	75
6.3.2	Case 2: Top and core surface damage near fixed end with 4 % defected area	77
6.3.3	Case 3: Top and core surface damage near fixed end with 6 % defected area	78
6.4	Scenario 4: Damage in top and core surfaces near mid section with 2 %, 4 %, 6 % defected area	80
6.4.1	Case 1: Top and core surface damage near mid section with 2 % defected area	80
6.4.2	Case 2: Top and core surface damage near mid section with 4 % defected area	82
6.4.3	Case 3: Top and core surface damage near mid section with 6 % defected area	83
7	Sensitivity Analysis	87
8	Conclusion and Recommendation	91
8.1	Using increase in modal damping percent to identify damage location and size	91
8.2	Modelling the vibration analysis based on the viscoelastic damping	92
8.3	Future work	92
	Bibliography	93
	Appendix A:Damage identification and localization support plots	99
	Appendix B:APDL Code	99

List of Figures

1.1	Main causes for wind turbine blade failure	1
1.2	Defect percent of components in a wind turbine	2
1.3	Types of damage in a wind turbine blade	3
2.1	Stress strain plots at constant strain rate	12
2.2	Strain vs time for different load	13
2.3	Creep relaxation and recovery response curve	14
4.1	Spar cap - shear web assembly	32
4.2	Design of spar cap - shear web assembly front view	33
4.3	Design of spar cap - shear web assembly isometric view	33
4.4	Design of spar cap - shear web assembly side view	34
4.5	Front view spar cap - shear web assembly	34
4.6	Isometric view spar cap - shear web assembly	35
4.7	Side view spar cap - shear web assembly	35
4.8	Top surface fixed end damage with 2 % defected area	40
4.9	Top surface fixed end damage with 4 % defected area	40
4.10	Top surface fixed end damage with 6 % defected area	41
4.11	Top surface mid section damage with 2 % defected area	41
4.12	Top surface mid section damage with 4 % defected area	42
4.13	Top surface mid section damage with 6 % defected area	42
4.14	Top and core surfaces fixed end damage with 2 % defected area	43
4.15	Top and core surface fixed end damage with 4 % defected area	43
4.16	Top and core surface fixed end damage with 6 % defected area	44
4.17	Top and core surface mid section damage with 2 % defected area	44
4.18	Top and core surface mid section damage with 4 % defected area	45
4.19	Top and core surface mid section damage with 6 % defected area	45
5.1	Scenario 1 case 1 650 % damage 1 st flapwise bending frequency	49
5.2	Scenario 1 case 1 650 % damage 2 nd flapwise bending frequency	49
5.3	Scenario 1 case 1 650 % damage 1 st edgewise bending frequency	49
5.4	Scenario 1 case 1 650 % damage 2 nd edgewise bending frequency	50
5.5	Scenario 1 case 2 650 % damage 1 st flapwise bending frequency	50
5.6	Scenario 1 case 2 650 % damage 2 nd flapwise bending frequency	50
5.7	Scenario 1 case 2 650 % damage 1 st edgewise bending frequency	51
5.8	Scenario 1 case 2 650 % damage 2 nd edgewise bending frequency	51
5.9	Scenario 1 case 3 650 % damage 1 st flapwise bending frequency	51
5.10	Scenario 1 case 3 650 % damage 2 nd flapwise bending frequency	52
5.11	Scenario 1 case 3 650 % damage 1 st edgewise bending frequency	52
5.12	Scenario 1 case 3 650 % damage 2 nd edgewise bending frequency	52
5.13	Scenario 2 case 1 650 % damage 1 st flapwise bending frequency	53
5.14	Scenario 2 case 1 650 % damage 2 nd flapwise bending frequency	53
5.15	Scenario 2 case 1 650 % damage 1 st edgewise bending frequency	53
5.16	Scenario 2 case 1 650 % damage 2 nd edgewise bending frequency	53
5.17	Scenario 2 case 2 650 % damage 1 st flapwise bending frequency	54
5.18	Scenario 2 case 2 650 % damage 2 nd flapwise bending frequency	54
5.19	Scenario 2 case 2 650 % damage 1 st edgewise bending frequency	54
5.20	Scenario 2 case 2 650 % damage 2 nd edgewise bending frequency	55
5.21	Scenario 2 case 3 650 % damage 1 st flapwise bending frequency	55
5.22	Scenario 2 case 3 650 % damage 2 nd flapwise bending frequency	55
5.23	Scenario 2 case 3 650 % damage 1 st edgewise bending frequency	56
5.24	Scenario 2 case 3 650 % damage 2 nd edgewise bending frequency	56
5.25	Scenario 3 case 1 650 % damage 1 st flapwise bending frequency	56
5.26	Scenario 3 case 1 650 % damage 2 nd flapwise bending frequency	57
5.27	Scenario 3 case 1 650 % damage 1 st edgewise bending frequency	57
5.28	Scenario 3 case 1 650 % damage 2 nd edgewise bending frequency	57
5.29	Scenario 3 case 2 650 % damage 1 st flapwise bending frequency	58
5.30	Scenario 3 case 2 650 % damage 2 nd flapwise bending frequency	58
5.31	Scenario 3 case 2 650 % damage 1 st edgewise bending frequency	58

5.32	Scenario 3 case 2 650 % damage 2 nd edgewise bending frequency	58
5.33	Scenario 3 case 3 650 % damage 1 st flapwise bending frequency	59
5.34	Scenario 3 case 3 650 % damage 2 nd flapwise bending frequency	59
5.35	Scenario 3 case 3 650 % damage 1 st edgewise bending frequency	59
5.36	Scenario 3 case 3 650 % damage 2 nd edgewise bending frequency	60
5.37	Scenario 4 case 1 650 % damage 1 st flapwise bending frequency	60
5.38	Scenario 4 case 1 650 % damage 2 nd flapwise bending frequency	60
5.39	Scenario 4 case 1 650 % damage 1 st edgewise bending frequency	61
5.40	Scenario 4 case 1 650 % damage 2 nd edgewise bending frequency	61
5.41	Scenario 4 case 2 650 % damage 1 st flapwise bending frequency	61
5.42	Scenario 4 case 2 650 % damage 2 nd flapwise bending frequency	62
5.43	Scenario 4 case 2 650 % damage 1 st edgewise bending frequency	62
5.44	Scenario 4 case 2 650 % damage 2 nd edgewise bending frequency	62
5.45	Scenario 4 case 3 650 % damage 1 st flapwise bending frequency	63
5.46	Scenario 4 case 3 650 % damage 2 nd flapwise bending frequency	63
5.47	Scenario 4 case 3 650 % damage 1 st edgewise bending frequency	63
5.48	Scenario 4 case 3 650 % damage 2 nd edgewise bending frequency	63
6.1	Layout of top surface damage near fixed end with 2 % defected area	65
6.2	Defect identification for scenario 1 case 1 for 1 st flapwise bending frequency	65
6.3	Defect identification for scenario 1 case 1 for 2 nd flapwise bending frequency	66
6.4	Defect identification for scenario 1 case 1 for 1 st edgewise bending frequency	66
6.5	Defect identification for scenario 1 case 1 for 2 nd edgewise bending frequency	66
6.6	Layout of top surface damage near fixed end with 4 % defected area	67
6.7	Defect identification for scenario 1 case 2 for 1 st flapwise bending frequency	67
6.8	Defect identification for scenario 1 case 2 for 2 nd flapwise bending frequency	67
6.9	Defect identification for scenario 1 case 2 for 1 st edgewise bending frequency	68
6.10	Defect identification for scenario 1 case 2 for 2 nd edgewise bending frequency	68
6.11	Layout of top surface damage near fixed end with 6 % defected area	68
6.12	Defect identification for scenario 1 case 3 for 1 st flapwise bending frequency	69
6.13	Defect identification for scenario 1 case 3 for 2 nd flapwise bending frequency	69
6.14	Defect identification for scenario 1 case 3 for 1 st edgewise bending frequency	69
6.15	Defect identification for scenario 1 case 3 for 2 nd edgewise bending frequency	70
6.16	Layout of top surface damage near mid section with 2 % defected area	70
6.17	Defect identification for scenario 2 case 1 for 1 st flapwise bending frequency	70
6.18	Defect identification for scenario 2 case 1 for 2 nd flapwise bending frequency	71
6.19	Defect identification for scenario 2 case 1 for 1 st edgewise bending frequency	71
6.20	Defect identification for scenario 2 case 1 for 2 nd edgewise bending frequency	71
6.21	Layout of top surface damage near mid section with 4 % defected area	72
6.22	Defect identification for scenario 2 case 2 for 1 st flapwise bending frequency	72
6.23	Defect identification for scenario 2 case 2 for 2 nd flapwise bending frequency	72
6.24	Defect identification for scenario 2 case 2 for 1 st edgewise bending frequency	73
6.25	Defect identification for scenario 2 case 2 for 2 nd edgewise bending frequency	73
6.26	Layout of top surface damage near mid section with 6 % defected area	73
6.27	Defect identification for scenario 2 case 3 for 1 st flapwise bending frequency	74
6.28	Defect identification for scenario 2 case 3 for 2 nd flapwise bending frequency	74
6.29	Defect identification for scenario 2 case 3 for 1 st edgewise bending frequency	74
6.30	Defect identification for scenario 2 case 3 for 2 nd edgewise bending frequency	75
6.31	Layout of top and core surface damage near fixed end with 2 % defected area	75
6.32	Defect identification for scenario 3 case 1 for 1 st flapwise bending frequency	76
6.33	Defect identification for scenario 3 case 1 for 2 nd flapwise bending frequency	76
6.34	Defect identification for scenario 3 case 1 for 1 st edgewise bending frequency	76
6.35	Defect identification for scenario 3 case 1 for 2 nd edgewise bending frequency	77
6.36	Layout of top and core surface damage near fixed end with 4 % defected area	77
6.37	Defect identification for scenario 3 case 2 for 1 st flapwise bending frequency	77
6.38	Defect identification for scenario 3 case 2 for 2 nd flapwise bending frequency	78
6.39	Defect identification for scenario 3 case 2 for 1 st edgewise bending frequency	78
6.40	Defect identification for scenario 3 case 2 for 2 nd edgewise bending frequency	78
6.41	Layout of top and core surface damage near fixed end with 6 % defected area	79

6.42	Defect identification for scenario 3 case 3 for 1 st flapwise bending frequency	79
6.43	Defect identification for scenario 3 case 3 for 2 nd flapwise bending frequency	79
6.44	Defect identification for scenario 3 case 3 for 1 st edgewise bending frequency	80
6.45	Defect identification for scenario 3 case 3 for 2 nd edgewise bending frequency	80
6.46	Layout of top and core surface damage near mid section with 2 % defected area	80
6.47	Defect identification for scenario 4 case 1 for 1 st flapwise bending frequency	81
6.48	Defect identification for scenario 4 case 1 for 2 nd flapwise bending frequency	81
6.49	Defect identification for scenario 4 case 1 for 1 st edgewise bending frequency	81
6.50	Defect identification for scenario 4 case 1 for 2 nd edgewise bending frequency	82
6.51	Layout of top and core surface damage near mid section with 4 % defected area	82
6.52	Defect identification for scenario 4 case 2 for 1 st flapwise bending frequency	82
6.53	Defect identification for scenario 4 case 2 for 2 nd flapwise bending frequency	83
6.54	Defect identification for scenario 4 case 2 for 1 st edgewise bending frequency	83
6.55	Defect identification for scenario 4 case 2 for 2 nd edgewise bending frequency	83
6.56	Layout of top and core surface damage near mid section with 6 % defected area	84
6.57	Defect identification for scenario 4 case 3 for 1 st flapwise bending frequency	84
6.58	Defect identification for scenario 4 case 3 for 2 nd flapwise bending frequency	84
6.59	Defect identification for scenario 4 case 3 for 1 st edgewise bending frequency	85
6.60	Defect identification for scenario 4 case 3 for 2 nd edgewise bending frequency	85
7.1	Fixed end defect: 1 st flapwise bending frequency	87
7.2	Fixed end defect: 2 nd flapwise bending frequency	88
7.3	Fixed end defect: 1 st edgewise bending frequency	88
7.4	Fixed end defect: 2 nd edgewise bending frequency	88
7.5	Midsection defect: 1 st flapwise bending frequency	88
7.6	Midsection defect: 2 nd flapwise bending frequency	89
7.7	Midsection defect: 1 st edgewise bending frequency	89
7.8	Midsection defect: 2 nd edgewise bending frequency	89
7.9	Comparison of results for 1 st and 2 nd flapwise bending frequency	89
8.1	Scenario 1 case 1 100 % damage 1 st flap wise bending	99
8.2	Scenario 1 case 1 100 % damage 2 nd flap wise bending	99
8.3	Scenario 1 case 1 100 % damage 1 st edge wise bending	99
8.4	Scenario 1 case 1 100 % damage 2 nd edge wise bending	99
8.5	Scenario 1 case 1 350 % damage 1 st flap wise bending	100
8.6	Scenario 1 case 1 350 % damage 2 nd flap wise bending	100
8.7	Scenario 1 case 1 350 % damage 1 st edge wise bending	100
8.8	Scenario 1 case 1 350 % damage 2 nd edge wise bending	100
8.9	Scenario 1 case 2 100 % damage 1 st flap wise bending	101
8.10	Scenario 1 case 2 100 % damage 2 nd flap wise bending	101
8.11	Scenario 1 case 2 100 % damage 1 st edge wise bending	101
8.12	Scenario 1 case 2 100 % damage 2 nd edge wise bending	101
8.13	Scenario 1 case 2 350 % damage 1 st flap wise bending	102
8.14	Scenario 1 case 2 350 % damage 2 nd flap wise bending	102
8.15	Scenario 1 case 2 350 % damage 1 st edge wise bending	102
8.16	Scenario 1 case 2 350 % damage 2 nd edge wise bending	102
8.17	Scenario 1 case 3 100 % damage 1 st flap wise bending	103
8.18	Scenario 1 case 3 100 % damage 2 nd flap wise bending	103
8.19	Scenario 1 case 3 100 % damage 1 st edge wise bending	103
8.20	Scenario 1 case 3 100 % damage 2 nd edge wise bending	103
8.21	Scenario 1 case 3 350 % damage 1 st flap wise bending	104
8.22	Scenario 1 case 3 350 % damage 2 nd flap wise bending	104
8.23	Scenario 1 case 3 350 % damage 1 st edge wise bending	104
8.24	Scenario 1 case 3 350 % damage 2 nd edge wise bending	104
8.25	Scenario 2 case 1 100 % damage 1 st flap wise bending	105
8.26	Scenario 2 case 1 100 % damage 2 nd flap wise bending	105
8.27	Scenario 2 case 1 100 % damage 1 st edge wise bending	105
8.28	Scenario 2 case 1 100 % damage 2 nd edge wise bending	105
8.29	Scenario 2 case 1 350 % damage 1 st flap wise bending	106
8.30	Scenario 2 case 1 350 % damage 2 nd flap wise bending	106

8.31	Scenario 2 case 1 350 % damage 1 st edge wise bending	106
8.32	Scenario 2 case 1 350 % damage 2 nd edge wise bending	106
8.33	Scenario 2 case 2 100 % damage 1 st flap wise bending	107
8.34	Scenario 2 case 2 100 % damage 2 nd flap wise bending	107
8.35	Scenario 2 case 2 100 % damage 1 st edge wise bending	107
8.36	Scenario 2 case 2 100 % damage 2 nd edge wise bending	107
8.37	Scenario 2 case 2 350 % damage 1 st flap wise bending	108
8.38	Scenario 2 case 2 350 % damage 2 nd flap wise bending	108
8.39	Scenario 2 case 2 350 % damage 1 st edge wise bending	108
8.40	Scenario 2 case 2 350 % damage 2 nd edge wise bending	108
8.41	Scenario 2 case 3 100 % damage 1 st flap wise bending	109
8.42	Scenario 2 case 3 100 % damage 2 nd flap wise bending	109
8.43	Scenario 2 case 3 100 % damage 1 st edge wise bending	109
8.44	Scenario 2 case 3 100 % damage 2 nd edge wise bending	109
8.45	Scenario 2 case 3 350 % damage 1 st flap wise bending	110
8.46	Scenario 2 case 3 350 % damage 2 nd flap wise bending	110
8.47	Scenario 2 case 3 350 % damage 1 st edge wise bending	110
8.48	Scenario 2 case 3 350 % damage 2 nd edge wise bending	110
8.49	Scenario 3 case 1 100 % damage 1 st flap wise bending	111
8.50	Scenario 3 case 1 100 % damage 2 nd flap wise bending	111
8.51	Scenario 3 case 1 100 % damage 1 st edge wise bending	111
8.52	Scenario 3 case 1 100 % damage 2 nd edge wise bending	111
8.53	Scenario 3 case 1 350 % damage 1 st flap wise bending	112
8.54	Scenario 3 case 1 350 % damage 2 nd flap wise bending	112
8.55	Scenario 3 case 1 350 % damage 1 st edge wise bending	112
8.56	Scenario 3 case 1 350 % damage 2 nd edge wise bending	112
8.57	Scenario 3 case 2 100 % damage 1 st flap wise bending	113
8.58	Scenario 3 case 2 100 % damage 2 nd flap wise bending	113
8.59	Scenario 3 case 2 100 % damage 1 st edge wise bending	113
8.60	Scenario 3 case 2 100 % damage 2 nd edge wise bending	113
8.61	Scenario 3 case 2 350 % damage 1 st flap wise bending	114
8.62	Scenario 3 case 2 350 % damage 2 nd flap wise bending	114
8.63	Scenario 3 case 2 350 % damage 1 st edge wise bending	114
8.64	Scenario 3 case 2 350 % damage 2 nd edge wise bending	114
8.65	Scenario 3 case 3 100 % damage 1 st flap wise bending	115
8.66	Scenario 3 case 3 100 % damage 2 nd flap wise bending	115
8.67	Scenario 3 case 3 100 % damage 1 st edge wise bending	115
8.68	Scenario 3 case 3 100 % damage 2 nd edge wise bending	115
8.69	Scenario 3 case 3 350 % damage 1 st flap wise bending	116
8.70	Scenario 3 case 3 350 % damage 2 nd flap wise bending	116
8.71	Scenario 3 case 3 350 % damage 1 st edge wise bending	116
8.72	Scenario 3 case 3 350 % damage 2 nd edge wise bending	116
8.73	Scenario 4 case 1 100 % damage 1 st flap wise bending	117
8.74	Scenario 4 case 1 100 % damage 2 nd flap wise bending	117
8.75	Scenario 4 case 1 100 % damage 1 st edge wise bending	117
8.76	Scenario 4 case 1 100 % damage 2 nd edge wise bending	117
8.77	Scenario 4 case 1 350 % damage 1 st flap wise bending	118
8.78	Scenario 4 case 1 350 % damage 2 nd flap wise bending	118
8.79	Scenario 4 case 1 350 % damage 1 st edge wise bending	118
8.80	Scenario 4 case 1 350 % damage 2 nd edge wise bending	118
8.81	Scenario 4 case 2 100 % damage 1 st flap wise bending	119
8.82	Scenario 4 case 2 100 % damage 2 nd flap wise bending	119
8.83	Scenario 4 case 2 100 % damage 1 st edge wise bending	119
8.84	Scenario 4 case 2 100 % damage 2 nd edge wise bending	119
8.85	Scenario 4 case 2 350 % damage 1 st flap wise bending	120
8.86	Scenario 4 case 2 350 % damage 2 nd flap wise bending	120
8.87	Scenario 4 case 2 350 % damage 1 st edge wise bending	120
8.88	Scenario 4 case 2 350 % damage 2 nd edge wise bending	120

8.89	Scenario 4 case 3 100 % damage 1 st flap wise bending	121
8.90	Scenario 4 case 3 100 % damage 2 nd flap wise bending	121
8.91	Scenario 4 case 3 100 % damage 1 st edge wise bending	121
8.92	Scenario 4 case 3 100 % damage 2 nd edge wise bending	121
8.93	Scenario 4 case 3 350 % damage 1 st flap wise bending	122
8.94	Scenario 4 case 3 350 % damage 2 nd flap wise bending	122
8.95	Scenario 4 case 3 350 % damage 1 st edge wise bending	122
8.96	Scenario 4 case 3 350 % damage 2 nd edge wise bending	122

List of Tables

1.1	Types of damage in a wind turbine blade	2
4.1	Material properties of adhesive (Epoxy Resin)	35
4.2	Material properties of PVC foam	36
4.3	Material properties of Epoxy- E glass (face sheet material)	36
4.4	Material properties of Epoxy- S glass (spar cap material)	36
4.5	Loss factor and damping coefficient to represent different damaged condition	37
4.6	Material property for loss factor 0.0114	37
4.7	Material property for loss factor 0.0152	38
4.8	Material property for loss factor 0.0227	38
4.9	Material property for loss factor 0.0332	38
4.10	Material property for loss factor 0.0450	39
4.11	Material property for loss factor 0.0632	39
4.12	Material property for loss factor 0.0776	39
4.13	Number of defected elements for each scenario	46
5.1	Modal damping and percentage increase of damping for scenario 1 case 1	49
5.2	Modal damping and percentage increase of damping for Scenario 1 case 2	50
5.3	Modal damping and percentage increase of damping for scenario 1 case 3	51
5.4	Modal damping and percentage increase of damping for Scenario 2 case 1	52
5.5	Modal damping and percentage increase of damping for scenario 2 case 2	54
5.6	Modal damping and percentage increase of damping for scenario 2 case 3	55
5.7	Modal damping and percentage increase of damping for scenario 3 case 1	56
5.8	Modal damping and percentage increase of damping for scenario 3 case 2	57
5.9	Modal damping and percentage increase of damping for scenario 3 case 3	59
5.10	Modal damping and percentage increase of damping for scenario 4 case 1	60
5.11	Modal damping and percentage increase of damping for scenario 4 case 2	61
5.12	Modal damping and percentage increase of damping for scenario 4 case 3	62
5.13	Increase in overall damping of the structure for different loss factor (microscopic damping coefficients)	64
6.1	Change in phase angle of the structure for different loss factor (microscopic damping coefficients)	86
7.1	Sensitivity analysis results: Modal damping calculation	87
7.2	Sensitivity analysis results: Change in phase angle	87

Abbreviation

GWWT	Gabor-Wigner-Wavelet Technique
STFT	Short Time Fourier Transform
FFT	Fast Fourier Transform
PSD	Power Spectral Density
FEM	Finite Element Modelling
EMA	Experimental Modal Analysis
OMA	Operational Modal Analysis
FEA	Finite Element Analysis
CFD	Computational Fluid Dynamics
FD	Fractal Dimension
EMS	Experimental Modal Analysis
FRF	Frequency Response Function
GHM	Golla Hughes McTavish
WPS	Wavelet power spectrum
SPT	Small Punch Test
PVC	polyvinyl chloride
GFRM	Glass Fibre Reinforced Materials
NPPC	Non-Penetrating Parabolic Crack
PTC	Penetrating Trapezoid Crack
UPC	Uniform-Penetrating Crack
EVA	Experimental Vibration Analysis
MSDC	Mode Shape Difference Curvature
NDT	Non Destructive Testing

Nomenclature

σ	Stress
ε	Strain
τ	Relaxation time
G	Relaxation modulus
δ_L	Phase angle
$\eta; \delta(\omega)$	Loss factor
$E'(\omega)$	Storage term of loss factor
$E''(\omega)$	Loss term of loss factor
M^e	Mass matrix of an element
K^e	Stiffness matrix of an element
$[K^D]^e$	Damping matrix of an element
$y(t)$	Displacement vector of an element
$f(t)$	Force vector
$\bar{F}(\omega)$	Amplitude of harmonic load
$\bar{Y}(\omega)$	Harmonic displacement
M	Mass matrix of the structure
K	Stiffness matrix of the structure
Y	Displacement
E_x, E_y	Young's modulus in x and y direction
G_{xy}	Shear modulus in x-y plane
ν_{xy}, ν_{yz}	Poisson's ratios in x-y and y-z planes
$S[C(S)]$	Dynamic modulus
C_0	Elastic property of viscoelastic material
$S[\bar{C}(s)]$	Viscous property of a viscoelastic material
q_e	Nodal displacement vector
$[N]$	Matrix shape function of an element
S_i	Eigenvalue
ϕ_i	Eigenvector
n	Degree of freedom
ω_i	Natural frequency
U	Undamped matrix
S	Laplace domain
$c; \xi_k$	Damping coefficient
C_d	Viscous damper
$H(t)$	Heaviside step function
$J(t)$	Creep compliance
$E(t)$	Relaxation modulus
η	Viscosity of the fluid
D	Deborah number
ν	Frequency in Hertz
(E_s)	Elastic stiffness
m	Mass of the system
k	Stiffness coefficient
ζ	Damping ratio
μ	Friction coefficient
h	Hysteretic damping coefficient
c_{eq}	Equivalent Damping Coefficient
ΔW	Energy dissipated by the hysteretic damping in one cycle
γ	Structural damping factor

1 Introduction

In this chapter, the background of the thesis is presented along with the introduction of wind energy. A brief note on failure in wind turbines and the causes for failure of different components of a wind turbine are discussed. Also, the methods and techniques used for monitoring the wind turbine blades and research objective is explained.

1.1 Wind energy background

Wind energy is one of the cleanest methods of producing electricity. It plays a major role in the transition towards green energy. By the end of 2019, total wind energy capacity of around 650.8 GW has been installed, which covers more than 6% of total global electricity demand [10]. Each year larger wind turbine blades are being manufactured to satisfy the growing demand, resulting in high manufacturing cost and operation and maintenance cost. On average around \$2.6 to \$4 million USD is spent for manufacturing a wind turbine [25] and around 45 million Euro to 47 million Euro is spent on O&M of onshore and offshore wind turbines respectively [52]. The largest wind turbine built has a hub height of 260 m and the blade length of about 110 m in Rotterdam[50]. Energy from wind is extracted using wind turbines, but the blades tend to break because of the forces that are applied to it. With these long blade, failure in wind turbine blade will result in huge revenue loss and high maintenance cost. So, an effective and proactive monitoring system for the wind turbine blades becomes necessary due to the large downtime associated with failure and high replacement cost.

1.2 Failure in wind turbine

Yearly around 48 million Euro is being spent by Siemens for inspection and replacing the defected parts in the onshore wind turbine. Based on the inspections done by Siemens the most common cause for wind turbine failures are blade design issues, bearing and gearbox issue, mechanical breakdown, axial stress, foundation damage, extreme weather, icing, lightning strike and accumulation of dirt, bugs and other debris [25]. The damage to the blade tip and yaw bearing is the most frequent cause of damage for a typical wind turbine system [16]. The main reasons for wind turbine blade failures are lightning strikes, foreign object damage, poor design, material failure, power regulator failure, extreme load buckling and human errors. Figure 1.1 shows the major causes for wind turbine blade failure

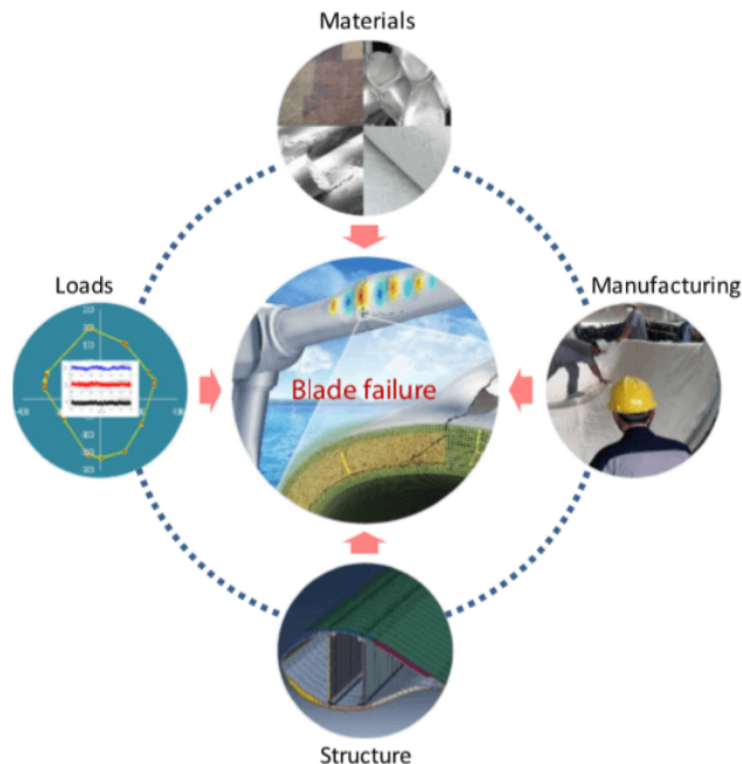


Figure 1.1: Main causes for wind turbine blade failure

The possible defects that can occur in wind turbine blades are surface damage such as erosion, delamination, cracks and structural discontinuities. Figure 1.3 shows the defect percent of different components in a wind turbine. The failure rate of the wind turbine blade is around 7%.

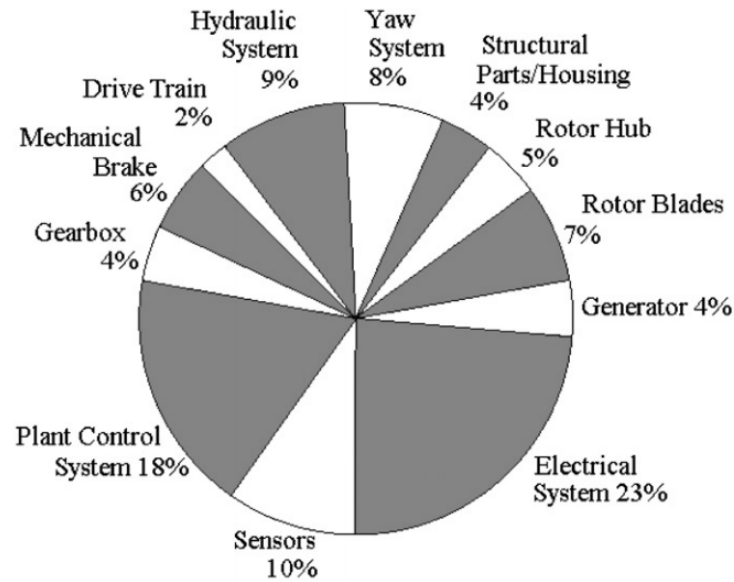


Figure 1.2: Defect percent of components in a wind turbine

Defects that can occur in a wind turbine blade is classified into 7 types and are shown in table 1.1 [16].

Table 1.1: Types of damage in a wind turbine blade

Type 1	Damage formation and growth in the adhesive layer joining skin and main spar flanges (skin/adhesive debonding and/or main spar/adhesive layer debonding)
Type 2	Damage formation and growth in the adhesive layer joining the up- and downwind skins along leading and/or trailing edges (adhesive joint failure between skins)
Type 3	Damage formation and growth at the interface between face and core in sandwich panels in skins and main spar web (sandwich panel face/core debonding)
Type 4	Internal damage formation and growth in laminates in skin and/or main spar flanges, under a tensile or compression load (delamination driven by a tensional or a buckling load)
Type 5	Splitting and fracture of separate fibres in laminates of the skin and main spar (fibre failure in tension; laminate failure in compression)
Type 6	Buckling of the skin due to damage formation and growth in the bond between skin main spar under compressive load (skin/adhesive debonding induced by buckling, a specific type 1 case)
Type 7	Formation and growth of cracks in the gel-coat; debonding of the gel-coat from the skin (gel-coat cracking and gel-coat/skin debonding)

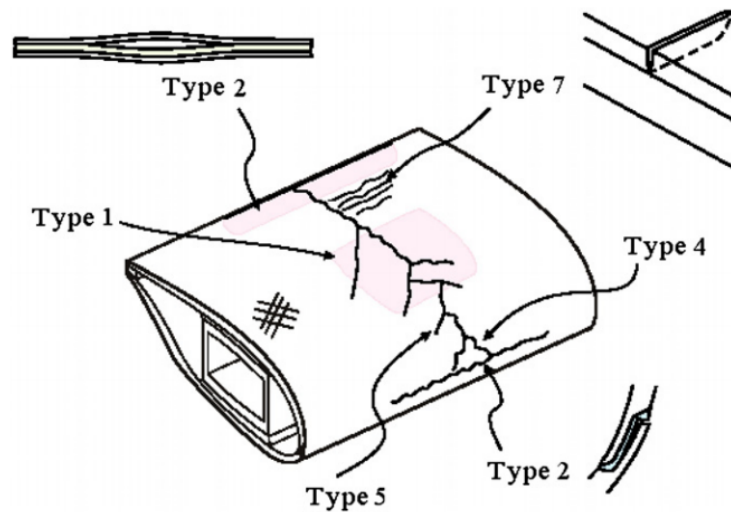


Figure 1.3: Types of damage in a wind turbine blade

The locations at 30–35% and 70% along the length of the blade from the root section and upper spar cap (or) flange of the spar are identified to be the more common section where damage occurs in a typical wind turbine blade. One of the root cause for damages in these sections is crack initiation and propagation [16].

1.3 Maintenance of wind turbine blade

The wind turbine blades are made of glass-fibre, plastic foam and polymer adhesive. These materials are non-homogeneous and isotropic in both mechanical and electrical parameters. Regular inspection is necessary for detection of defects at early stages to prevent critical damages or even complete failure of a wind turbine. Traditionally, industrial climbers have been used to visually inspect the rotor blades on turbines. But the workers face many challenges and safety issues. So many industries follow Non-Destructive Testing (NDT) for inspecting the onshore and offshore wind turbines. The commonly used NDT techniques are infra-red thermography, ultrasonic testing, digital radiography, acoustic emission, tap testing, vibration analysis, microwave and terahertz techniques [13].

Vibration analysis is one of the most commonly used non-destructive technology for condition monitoring of wind turbine blades. Many vibration analysis techniques and methods have been developed by researchers for identifying defects in a wind turbine blades effectively and efficiently. Most of the techniques are suitable only for offline condition monitoring [46]. The main concept behind the vibration analysis is that presence of a crack in a structure modifies the modal parameters such as natural frequencies, damping and mode shape of that structure. The change in the modal parameter can be used inversely to predict the crack parameters like crack depth and crack location.

1.3.1 Vibration analysis methodology

Vibration analysis has four principles. Each principle gives specific information on the working conditions and features of the vibrating parts[29]

1. Time Domain : Vibration signal is considered as a waveform. Useful for identifying the vibration issues in machines [29].
2. Frequency Domain : The waveform is subjected to spectrum analysis and the end result is viewed as frequency vs amplitude. Useful for in-depth analysis of vibration issues in machines [29].
3. Joint Domain : Gabor-Wigner-Wavelet technique (GWWT) is used to calculate more than one spectrum from a single vibrating signal. This technique is useful in calculating variations of the Fast Fourier Transform and Short-Time Fourier Transform (STFT) [29].
4. Modal Analysis : measured frequency response functions are incorporated into a computer model. The computer model can be used to display all the different vibration modes. Mass or stiffness is adjusted to see the effects [29].

In addition to these four principles, there are many algorithms used to determine the different aspect of vibration analysis.

1. Fast Fourier Transform (FFT): Fast Fourier Transform is the most commonly used algorithm. FFT converts the signal from the time domain into the frequency domain and is used to calculate a spectrum from a time waveform [29].
2. Power spectral density (PSD): Power spectral density is calculated by multiplying the amplitude from FFT by its different forms to normalize it with the frequency bin width [29].

Using these algorithms many analysis such as phase measurement, order analysis, envelope analysis, resonance analysis are carried out. Defect detection in a wind turbine blade is based on the concept of resonance analysis. Resonance analysis identifies all the natural vibrations and frequencies of a structure. The presence of resonance means that the structure has high vibration[?].

1.3.2 Categories of vibration measurement

Several categories of vibration measurement is listed below

- Spectral analysis of vibration
- Discrete frequency monitoring
- Shock pulse monitoring
- Kurtosis measurement
- Signal averaging
- Cepstrum analysis

1.4 Research Scope

Currently, discrete crack modelling concepts are being used in Finite Element Modelling (FEM) tools to identify defects in a wind turbine blade. However, discrete crack modelling changes the topology of the material in the place of the defect and vicinity of the defect while modelling the crack growth. Discrete modelling has two disadvantages

1. Growth of small cracks is not captured in the early stages.
2. It required fine and dynamic mesh, which consumes a lot of time to run the model.

The main objective of this thesis is to use smeared crack modelling and integrating it with FEM tools to identify the damage in the wind turbine blade. Different scenarios are created by changing the severity and location of the damage in the FEM model. For each scenario, the mode shapes and natural frequencies are calculated. These characteristics are used as a damage index to identify and localize the defect in a wind turbine blade.

1.5 Report Layout

This report follows the following layout.

Chapter 2 gives brief background information regarding causes for defects of a wind turbine blade. Also, different crack identification techniques and methods that are being used currently to detect the crack in a wind turbine blade.

Chapter 3 has details about constitutive equation of linear viscoelastic material, finite element vibration equation of linear viscoelastic material, time-domain equation of motion, laplace form of the equation of motion, eigenvalue and eigenvector of vibration equation, eigenvalue and eigenvector of non-proportional damping and damping matrix approximation.

Chapter 4 explains the modelling of spar cap- shear web assembly and different defect modelling scenarios.

Chapter 5 explains the guideline followed to identify and localize the damage for different damage scenarios.

Chapter 6 explains the important results obtained from the thesis. Also, few important observations that were observed during the project is discussed.

Chapter 7 contains results of sensitivity analysis

Chapter 8 concludes the thesis and few recommendations for future work are discussed.

2 Background

In this chapter, the background information required to understand this thesis is discussed. Also, literature about the previous work regarding the damage identification in wind turbine based on the change in damping properties is explained. Finally, the research methodology is briefly explained.

2.1 Crack identification using vibration analysis

Vibration analysis is used for identifying defects in a mechanical structures. Lot of techniques and methods are being used in crack size and location detection in structures.

2.1.1 Vibration analysis techniques

There are several techniques available in vibration analysis. They are classified depending on the level of analysis and type of risks. A brief explanation of different techniques is given below.

- **Vibration Surveying and Monitoring:** A vibration sensor is installed on multiple locations on the test specimen by the inspectors to acquire vibration data. The acquired data is examined to get information about the severity of the problem.
- **Experimental Modal Analysis (EMA):** In experimental modal analysis, various load which represents the actual operating condition is applied to the structure, and the resulting signal is acquired. This technique provides a theoretical solution that can be used to calibrate simulated models and is mostly applied when the structure is not operating [26].
- **Operational Modal Analysis (OMA):** In operational modal analysis, the vibration sensors are installed on the machines or structures to acquire the vibration nodes and natural frequencies. Compared to EMA, OMA is performed on structures which are still in service and when background noise is difficult to distinguish from the vibration signal [26].
- **Computer Simulations (CS):** is used to simulate real-world situations and various operating conditions. Two types of computer simulation are
 - Finite Element Analysis (FEA)
 - Computational Fluid Dynamics (CFD)

2.1.2 Crack analysis in a cantilever beam using modal parameters

Initially, vibration analysis methods were used for detection of crack size and location in small structures like a cantilever beam to check its accuracy and effectiveness. Later, these techniques were scaled up for big and complicated structures like wind turbine blades.

Dinesth et al., 2017 [18] uses finite element analysis of cantilever beam using ANSYS 14.5. First three natural frequencies of transverse mode are extracted from the ANSYS FEA model which used to detect a crack in a cantilever shaft beam.

Agarwalla et al., 2013 [2] analysed the effect of an open crack on the modal parameters of the cantilever beam subjected to free vibration and compared the simulated ie., finite element method (FEM) results with the experimental results. The results show that the two results agree with each other.

Barad et al., 2013 [30] He explains the effect of the crack location and the crack depth on the natural frequency. First two frequencies of the cracked beam were obtained experimentally, and the crack location and size was calculated using those frequencies. Jitendra et al., 2014 [28] observed the change in modal performance such as natural frequency, damping and mode shape of cracked cantilever beam and compared these properties with the properties of the defect-free beam to predict the crack size and depth. The vibration signals from the defect-free and cracked beam were studied in the frequency domain with the help of Fast Fourier Transform. First three natural frequencies were taken to identify the crack depth size and the crack location of the beam.

Batabyal et al., 2008 [3] developed a methodology to predict the crack parameters such as crack depth and crack location in a thin cantilever beam using vibration response. A cantilever beam with line crack was

used for this experiment. ANSYS was used to evaluate modal parameters like natural frequencies and mode shapes for different crack parameters. It is observed that both crack location and depth have some effects on the modal parameters of the cracked beam. Also, a certain frequency may correspond to different crack depths and its locations. Contour lines of the cracked beam frequencies have been plotted based on the observed results.

Ranjan et al., 2014 [48] also analysed the influence of cracks on modal parameters such as natural frequencies, mode shapes, stiffness and modal damping of a cantilever beam. Compared to Batabyal et al., 2008 [3], Ranjan et al., 2014 [48] analysed inclined open edge crack on the cantilever beam was analysed in this research. A Finite element model was developed to analyse the variation of modal parameters corresponding to the location, size and inclination of a crack in the cantilever beam.

Nandwana et al., 1996[42] developed a method for detecting the crack location and size based on the natural frequency in a stepped cantilever beam. In this method, a characteristic equation was used to obtain stiffness vs crack locating plot for any three natural modes. The point of intersection of the three curves gives the crack location. The crack size is then computed using the standard relation between stiffness and crack size.

2.1.3 Multiple crack identification in cantilever beam

Khiem et al., 2004 [32] formulated a non-linear optimization problem to identify multi-cracks in a beam using MATLAB functions. The frequency equation of the multi cracked beam is established based on the dynamic stiffness of the beam. The crack parameters such as crack position, crack location and the number of cracks is detected using the frequency equation. Numerical results up to 3 cracks show good efficiency and acceptability. While Ravi et al., 2015 [49] developed a method to identify multiple cracks in a wind turbine blade by considering the blade as a cantilever beam and the shaft as simply support beam and formulated the relation between the modal parameters and crack parameters. Finite element analysis has been done on a cantilever beam and simply supported beams including two transverse open U-notches. Using ANSYS, modal analysis has been done on the cantilever and simply supported beams with two U-notches and the influence of one U-notch on the other has been observed for natural frequencies and mode shapes. Curvature mode shapes were calculated from the displacement mode shapes using central difference approximation. The peak of the curve represents the crack location and depth on the cantilever beam (wind turbine blade).

Wensheng et al., 2017 [27] simulates the complicated dynamic phenomena of a cracked cantilever beam structures with three different crack types. They are non-penetrating parabolic crack (NPPC), penetrating trapezoid crack (PTC) and uniform-penetrating crack (UPC). Both beam element and solid element are considered for FEM in ANSYS. The cracks are evaluated by using the area damage factor, i.e., the ratio of the damaged area to the cross-sectional area. spectrum cascades, acceleration-velocity & velocity-displacement phase portraits, and contact pressure nephograms are used to identify the vibration responses and crack level in the cantilever beam.

2.1.4 Crack detection in beam using fuzzy logic

Harshal et al., 2014 [47] explains the drawback of modern NDT techniques like dye penetrant testing, ultrasonic testing, acoustic emission techniques. The author also explains how improved fuzzy logic techniques and curve fitting in MATLAB are used as an alternative for NDT techniques. As this technique uses simple fuzzy logic, Dayal et al., 2011 [45] uses hybrid fuzzy logic technique to identify the presence of a crack in a cantilever beam. Hybrid fuzzy logic system and finite element analysis were used to find the transverse surface crack. The hybrid membership functions such as combination of triangular, trapezoidal and Gaussian functions are given as input to the fuzzy controller. The output from the fuzzy controller is the trapezoidal function. FEA is done on a cracked cantilever beam, and first three natural frequencies are given as the input parameters to the fuzzy controller. The crack depth and relative crack location are the output parameter from the fuzzy controller. Results obtained from FEA and MATLAB (using several fuzzy rules) are compared and found to be in agreement with each other.

2.1.5 Crack detection in beam structures using wavelet transform

Jiang et al., 2015 [61] presented a hybrid method to detect crack locations using wavelet transform and fractal dimension (FD) estimation in beam structures. Wavelet transform is employed to decompose the mode shape of the cracked beam. And FD estimation method is applied to detect the crack location accurately. The effectiveness of the proposed method is validated by numerical simulations and experimental investigations of a

cantilever beam. The results indicate that the proposed method is feasible in identifying defects in simple beam structures and can be extended for identifying the defects of more complex structures.

Zhang et al., 2009 [58] developed a method combining wavelet analysis with transform matrix to identify cracks in a stepped cantilever beam. First, the crack location is identified by giving the measured natural frequency as input for wavelet analysis. Then the crack depth is identified by using the first two natural frequency in a simple transform matrix method.

2.2 Vibration analysis in wind turbine blade with composite materials

Ganesh et al., 2016 [57] manufactured two small wind turbine blades using the Glass Fiber Reinforced Plastic (GFRP) and GFRP with steel wire mesh reinforcement. Finite Element Analysis (FEA) was carried out using finite element software ANSYS 16.0. From FEA, natural frequencies and mode shapes of two blades manufactured are obtained and compared.

Nigam et al., 2019 [43] performed modal analysis on horizontal axis wind turbine blade using ANSYS. The wind turbine blades are made of E-glass fibre reinforced plastic and carbon fibre reinforced plastic. For this analysis, 14 m long wind turbine blade, with and without the shear web was modelled. Modal analysis was conducted for edgewise, flap wise and tensional deflection. Deformation characteristics of the blade for two above mentioned models at different frequencies are analyzed and compared.

Munteanu et al., 2018 [41] designed a 3D virtual model of a wind turbine blade in Catia V5 and Abaqus software. The structure was built as GFRP laminated composite with 5 layers. First, the modes and natural frequencies of the defect-free wind turbine blade is obtained. Second, the modal response of the delaminated blade was analyzed and compared with the modal parameters of the defect-free blade. The results emphasize that the values of the natural frequencies changes when the blade is delaminated.

Nilesh et al., 2019 [14] performed a finite element analysis on three small wind turbine blades made of different materials using ANSYS 14.5. Experimental Vibration Analysis (EVA) was carried out using fast fourier transform analyzer to find the first two flap-wise natural frequencies of three blades. Similarly, using finite element analysis (FEA), two flap-wise natural frequencies and mode shapes of three blades are obtained. The results obtained from FEA and EVA are compared. The results show that the increase in natural frequency means that the stiffness of the blade is increased.

Yanbin et al., 2010 [59] compares the characteristics of hierarchical structure based on finite element analysis software ANSYS. Laminated shell element is used to create a finite element model. Modal analysis is performed to obtain modal parameters and the natural frequency spectrum of the blade.

Ashwani et al., 2014 [9] done a detailed study on Al 2024 wind turbine blade using structural and modal analysis. The length of the designed blade was 25m. Carbon fibre reinforced polymer (CFRP) and glass fibre-reinforced polymer (GFRP) woven composites were considered for model design. The 3D solid model was prepared using SOLIDEDGE software, and model analysis was done using ANSYS 14.0. In this research, deformations, stresses and natural frequencies for the first six modes shape of the wind turbine blade was analysed and verified with the experimental result from (Andrew 1998) [4]. Andrew has studied the onshore and offshore wind turbines. According to his experimental investigation, the maximum deformation occurs at tip, and the stresses are less for lightweight materials.

2.2.1 Detection of crack in wind turbine blade

A wind turbine blade is a complex structure generally built using composite materials. They rotate and flutter in extreme weather and fatigue loading conditions because of random wind speeds. Condition monitoring of wind turbine blades becomes necessary to identify the defects such as crack in the early stages. Using the modal parameters defects in a structure can be identified. As mentioned earlier, vibration analysis proved to provide reliable results for small structures. This gave researches aspiration to use vibration analysis to identify defects in wind turbine blades.

Chang et al., 2012 [15] explains the relationship between stress and crack growth. ANSYS was used to find the stress intensity factor of a composite crack and compared with the analytical results and loading on the stress intensity factor. This method is suitable only for small size cracks, as the dense of meshing becomes inadequate

for large crack sizes.

Kim et al., 2013 [33] explains how Vibro-Acoustic modulation technique can be used to detect crack in wind turbine blades of WHISPER 100 in its operating environment. The experiment is based on the principle that the non-linear portion of the dynamic response is more sensitive to the presence of a crack than the environmental conditions or operating loads.

Khalid et al., 2017 [1] uses Experimental Modal Analysis (EMA) to investigate the dynamic variations of a structure such as cracks based on the behaviour of the modal parameters. A stepped beam was used instead of a wind turbine blade to assess the structural health using EMA technique. Frequency Response Function (FRF) is obtained at different locations experimentally as a ratio of the structure output to the input excitation force, and 3D plots are generated to define the mode shape of the structure. The results prove that the modal parameters can be used for the detection and estimation of crack size in the stepped beam. Khalid et al., 2018 [31] uses Wavelet Power Spectrum (WPS) in addition to Experimental Modal Analysis to detect defects in wind turbine blades. WPS is calculated at different conditions instead of the traditional FFT spectrum to identify the crack in the wind turbine blade. Experimental modal analysis is used to validate the mathematical model, which correlates the variation of the blade natural frequencies with the crack severity and location. The results prove that the WPS method is effective than FFT method.

Dolinski et al., 2020 [36] presented a numerical and experimental investigation related diagnostic method for determining the location and size of damage in the laminated shell of wind turbine blades. The detection technique is based on the analysis of low-frequency bending vibrations and mode shapes of rotor blades. The research was conducted on a blade of a three-bladed horizontal-axis wind turbine with 36 m diameter rotor. The natural vibrations for defect-free and damaged blade were determined using Laser Doppler Scanning Vibrometry. The results of the research confirm the effectiveness of the modal analysis combined with statistic calculation in damage detection. The method points out the location of relatively small damage.

Yanfeng et al., 2014 [60] proposed a method for blade damage detection and diagnosis by incorporating a finite element method (FEM) for dynamics analysis and the mode shape difference curvature (MSDC) information for damage detection and diagnosis. The finite element model of a wind turbine blade was built and modified via frequency comparison with experimental data and the formula for the model updating technique. The numerical simulation results from the report show that the proposed method can detect the spatial locations of damages in a wind turbine blade. Change in natural frequencies and mode shape for smaller blades occurs at lower frequencies and lower modes. Since the relation between modal parameters and damage information are complicated for larger sized blades, dynamic response analysis with multilayer composite material based on aerodynamic loads calculation has been carried out. The efficiency and precision of damage detection are improved by combining (MSDC) information.

Surendra et al., 2011 [24] uses the concept that change in the physical properties of a structure should cause a change in modal parameters, to identify defects in a wind turbine blade. The author presents the test results from a wind turbine blade with different induced cracks. The results show that some of the modes of the blade are significantly affected by a crack and that the modal parameters change more significantly with a more severe crack. Similarly, Alessandro et al., 2014 [23] investigates the effect of local failure on the modal parameters of a wind turbine blade. The investigated wind turbine blade is made of glass fibres combined with epoxy resin and is 6.4 m long. The blade is assumed to be clamped at the root. The experiment was carried out in three steps. First, modal analysis is done on a blade without any defects, and its modal parameters are obtained. Second, a static test is done to introduce cracks in the blade. Finally, another operational modal analysis is done on the damaged structure, and the modal parameters are noted. By comparing the modal parameters, it was observed that the natural frequencies were decreased, and the modal damping of the structure was increased due to the induced crack.

Emilio et al., 2016 [17] describes a vibration-based approach to identify a crack in a wind turbine blade. Operational modal analysis has been performed and was used to monitor the integrity of the structure. A numerical prediction has been done both with a full-scale model and with a one-dimensional model. Both the results were compared, and it shows that this approach can estimate the presence of damage successfully, and good numerical and experimental correlation has been found.

Cheng et al., 2015 [56] presents vibration and damping analysis of fibre reinforced composite wind turbine

blade with viscoelastic damping. Layerwise displacement theory was employed to analyze the damping, natural frequency, and modal loss factor of the composite shell structure. The curved geometry, transverse shear, and normal strains were considered to depict the in-plane and out-of-plane displacements. The frequency response functions (FRF) of the curved composite structure were calculated. The natural frequency, modal loss factor, and mode shapes of composite fibre reinforced wind blade with viscoelastic damping control were calculated. The results show that the sandwiched viscoelastic damping layer can effectively suppress vibration of the composite wind turbine blade.

Larsen et al., 2002 [35] performed an experimental modal analysis to identify natural frequencies, damping characteristics and mode shapes of 19 m wind turbine blade. Also, FE modelling of the same blade is done to compare the results. For some of the higher modes, substantial discrepancies between the natural frequencies obtained from the FE-modeling and the experimental modal analysis are observed. From comparing the mode shapes, the author demonstrated a good agreement for the dominating deflection direction. Also, for non-dominating deflection directions, the qualitative features of measured and computed modes shapes are in good agreement.

Van der merwe et al., 2015 [34] identified the flap-wise, edge-wise and torsional natural frequencies and used it to detect the defect in a variable length blade. Hollow and solid beams are used to form the fixed portion and movable portion of the variable length blade. Uni graphics NX5 was used to develop the FEA model and MATLAB program was developed to predict natural frequencies.

2.3 Viscoelastic material basics

Luke, 2009 [51] explains the properties, analysis, and uses of viscoelastic materials. The cause of viscoelastic behaviour and the applications of viscoelastic materials was also explained. Viscoelastic phenomena are defined for various materials. Theories regarding viscoelastic composite materials are explained. Few important information about viscoelastic material from this book is explained below.

Viscoelastic material exhibits both viscous and elastic characteristics when undergoing deformation. The relationship between stress and strain for a viscoelastic material depends on time. The following formula gives the Hooke's law for a linearly elastic material.

$$\sigma = E\varepsilon \quad (2.1)$$

where E and ε is strain and strain of a linearly elastic material respectively. All materials exhibit viscoelastic response. Synthetic polymers, wood, and human tissue, as well as metals at the high temperature display viscoelastic effects. The properties of elastic solids are independent of time or frequency, and they support both shear stress and hydrostatic stress. On the other hand, viscous liquids support static hydrostatic stress. Viscous liquids generate shear stress only if the strain is changing with time. Isotropic elastic solids are described by two elastic constants, the shear and bulk modulus. Similarly, liquids and gases are described by two constants, the viscosity and the compressibility (inverse bulk modulus). By contrast, viscoelastic materials require a function of time or frequency to describe the behaviour[51].

The stress-strain curve provides the stiffness and strength of materials. The elastic material is not sensitive to time. For a linearly elastic material, the stress-strain curve is a straight line with a slope proportional to the elastic modulus. It has threshold stress called yield stress. If the applied load exceeds the yield stress, there will be residual strain after load removal. By contrast, the viscoelastic material is sensitive to time. A linearly viscoelastic material has a curved stress-strain plot. This kind of rise is because of the reason that both time and strain increase during constant strain rate deformation. The residual strain recovers to zero in a viscoelastic solid. But viscoelastic fluid undergoes a permanent residual strain. Figure 2.1 shows the stress-strain plots for deformation at constant strain rate followed by unloading. The plot on the left shows the behaviour of a linearly viscoelastic material. The plot on the right shows the behaviour of ideal elastic-plastic material. The response to step strain is known as stress relaxation, and the response to step stress is known as creep [51].

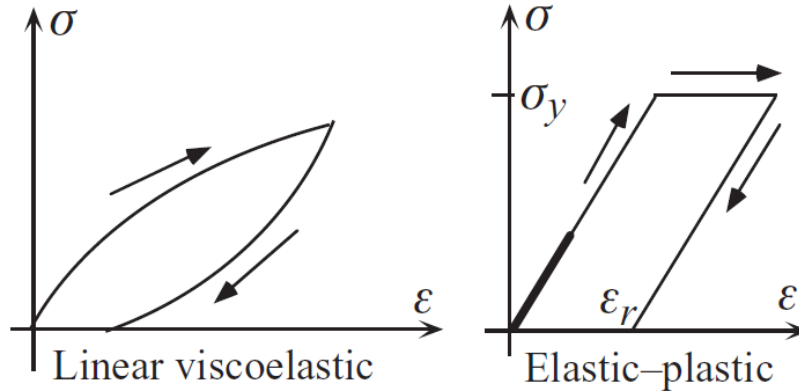


Figure 2.1: Stress strain plots at constant strain rate

Some phenomena in viscoelastic materials are [51]

1. If the stress is held constant, the strain increases with time (creep).
2. If the strain is held constant, the stress decreases with time (relaxation).
3. The effective stiffness depends on the rate of application of the load.
4. If cyclic loading is applied, hysteresis (a phase lag) occurs, leading to a dissipation of mechanical energy.
5. Acoustic waves experience attenuation and frictional resistance occurs during rolling.
6. The rebound of an object following an impact is less than 100 per cent.

Transient properties of viscoelastic material

Creep

Creep is a progressive deformation of a material under constant stress. For one dimension element, the stress history depends on time (t) and is given by the formula 2.2 [51].

$$\sigma(t) = \sigma_o H(t) \quad (2.2)$$

where, σ_o = magnitude of stress at $t = 0$; $H(t)$ = Heaviside step function. The value of Heaviside step function is defined as [51]

- $H(t) = 0$ for $t < 0$;
- $H(t) = 1/2$ for $t = 0$;
- $H(t) = 1$ for $t > 0$

The strain $\varepsilon(t)$ increases with time. The ratio between the strain $\varepsilon(t)$ and σ_o is called creep compliance $J(t)$.

$$J(t) = \frac{\varepsilon(t)}{\sigma_o} \quad (2.3)$$

Creep compliance is independent of stress level for a linearly viscoelastic material. If the loading is considered a mathematical step function, the region around $t = 0$ has an infinite domain on a logarithmic scale. If the load is released at a later time, the strain will exhibit recovery or a progressive decrease of deformation. Strain in recovery may or may not approach zero, depending on the material. The following figure 2.2 shows the creep curves for different loads [51].

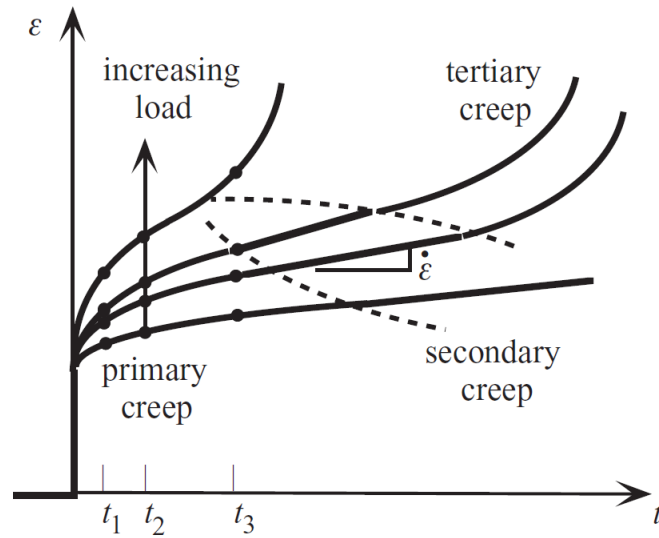


Figure 2.2: Strain vs time for different load

Creep curves have three regions, primary creep, secondary creep and tertiary creep. In primary creep, the curve is concave down. In secondary creep, the deformation is proportional to time. The curve continues as a linear line in the tertiary creep region. The linear response represents the linear relationship between stress and strain at a given time. Secondary creep is usually a demonstration of nonlinear viscoelasticity, not linear viscoelasticity. In tertiary creep, deformation accelerates until creep rupture occurs. In tertiary creep, the curve proceeds as concave up. Tertiary creep is always a manifestation of nonlinear viscoelasticity [51].

Relaxation

Relaxation is a gradual decrease of stress under constant strain. For one dimension element, the stress history depends on time (t) and is given by the formula 2.4 [51]

$$\varepsilon(t) = \varepsilon_0 H(t) \quad (2.4)$$

where, ε_0 = magnitude of strain at $t = 0$; $H(t)$ = Heaviside step function. The ratio between the stress history $\sigma(t)$ and ε_0 is called relaxation modulus $E(t)$ [51].

$$E(t) = \frac{\sigma(t)}{\varepsilon_0} \quad (2.5)$$

The relaxation modulus is a function of time and is independent of strain level for linear materials. The creep curve is increasing with time, whereas the relaxation curve is decreasing with time. The creep and relaxation occur in both shear or volumetric deformation. Figure 2.3 shows the creep, relaxation and recovery response curve of a viscoelastic material [51].

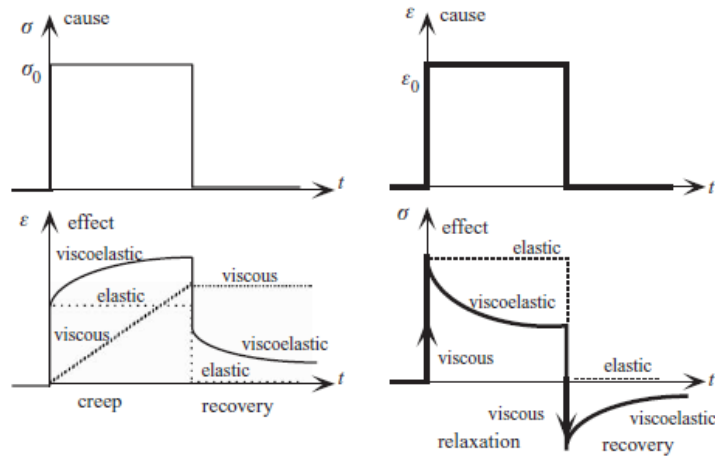


Figure 2.3: Creep relaxation and recovery response curve

Upon releasing the load, the elastic material immediately recovers to zero strain. Creep deformation in a viscous fluid is unbounded. Creep compliance of an elastic material and viscous fluid is given by the formula 2.6 and 2.7 respectively [51].

$$J(t) = J_o H(t) \quad (2.6)$$

$$J(t) = \frac{1}{\eta_V} t H(t) \quad (2.7)$$

where J_o is a constant; η_V is the viscosity of the fluid. Viscoelastic materials exhibit complete recovery after sufficient time following creep or relaxation. Creep, relaxation and recovery response of a viscoelastic material are shown in the figure 2.3 [51].

In the modulus formulation, in a viscoelastic solid, the relaxation modulus $E(t)$ tends to a finite, nonzero limit as to time t increases to infinity. In a viscoelastic liquid, the relaxation modulus $E(t)$ tends to zero. In the compliance formulation, in a viscoelastic solid, the creep compliance $J(t)$ tends to a finite limit as time (t) increases to infinity. In a viscoelastic fluid, the creep compliance $J(t)$ increases without bound as time (t) increases. The time scale can extend from zero to infinity. In practice as the load can be applied so suddenly the creep or relaxation procedures are difficult to accomplish in certain regions of the time scale. The time scale can extend from zero to infinity. In practice as the load is applied so suddenly the creep or relaxation procedures are difficult to accomplish in certain regions of the time scale. The dimensionless Deborah number (D) is defined to overcome the observation of the behaviour of materials for longer times. The Deborah number (D) is given by the formula [51]

$$D = \frac{\text{time of creep or relaxation}}{\text{time of observation}} \quad (2.8)$$

Response to sinusoidal load

While loading of a linearly viscoelastic material dynamically, if the stress $\sigma(t)$ is varying sinusoidally in time (t), then the strain response $\varepsilon(t)$ is also sinusoidal in time. But the response will lag the stress by a phase angle δ_L . The stress and strain response are given by the formula 2.9 and 2.10 respectively [51].

$$\sigma(t) = \sigma_o \sin(2\pi vt) \quad (2.9)$$

$$\varepsilon(t) = \varepsilon_o \sin(2\pi vt - \delta_L) \quad (2.10)$$

where, v is the frequency in Hertz (H_Z). The time required for one cycle known as period $T = \frac{1}{v}$. The phase angle is related to the time lag Δt between sinusoidals. It is derived as follows. The arguments in equation 2.10 can be written as

$$2\pi vt - \delta_L = 2\pi vt - \left(\frac{2\pi v \delta_L}{2\pi v} \right) = 2\pi v \left(t - \frac{\delta_L}{2\pi v} \right) = 2\pi v (t - \Delta t) \quad (2.11)$$

so,

$$\Delta t = \frac{\delta_L}{2\pi v} \quad (2.12)$$

since the frequency is inverse of period $\nu = \frac{1}{T}$, equation 2.12 becomes

$$\delta_L = \frac{2\pi\Delta t}{T} \quad (2.13)$$

As a result of the phase lag between stress and strain, the dynamic stiffness of a viscoelastic material is treated as a complex number E^* . The dynamic stiffness is given by the formula

$$\frac{\sigma}{\varepsilon_o} = E^* = E' + iE'' \quad (2.14)$$

The phase angle (or) loss angle δ_L is a dimensionless measure of the viscoelastic damping of the material. The dynamic functions E' , E'' , and δ depend on frequency. The tangent of the loss angle is called the loss tangent ($\tan\delta_L$). In an elastic solid, $\tan\delta_L = 0$ [51].

2.4 Viscoelastic damping basics

Various damping model are developed to describe the damping properties of viscoelastic material. Most commonly used classical model is explained below.

The viscoelastic materials can be modelled using classical models. Classic models include [39]

- Maxwell model
- Kalvin-Voight model
- Zener model

Maxwell model

The Maxwell model describes the material as a viscous damper (C_d) in series with an elastic stiffness (E_s). The applied stress is uniform in both the elements and is given as [39]

$$\sigma = E_s\varepsilon_s = C_d\dot{\varepsilon}_d \quad (2.15)$$

The total strain of the viscoelastic material can be written as

$$\varepsilon = \varepsilon_s + \varepsilon_d \quad (2.16)$$

by substituting equation 2.16 in equation 2.15 the stress can be written as

$$\varepsilon_s = \frac{\sigma}{E_s}, \varepsilon_d = \int \frac{\sigma}{C_d} dt \quad (2.17)$$

The stress-strain relation the viscoelastic material in Maxwell model can be written as

$$\varepsilon = \frac{\sigma}{E_s} + \int \frac{\sigma}{C_d} dt \Rightarrow \dot{\varepsilon} = \frac{\dot{\sigma}}{E_s} + \frac{\sigma}{C_d} \quad (2.18)$$

Maxwell model characteristics

- **Creep:**

For constant stress, ($\dot{\sigma}$) in equation 2.18 becomes zero, so the stress-strain relation equation becomes

$$\varepsilon = \frac{\sigma}{C_d} t \quad (2.19)$$

This means that the strain will grow to an unbound value as time increases [38].

- **Relaxation:**

For constant strain, ($\dot{\varepsilon}$) in equation 2.18 becomes zero, so the stress-strain relation equation becomes

$$\sigma = \sigma_o e^{-\frac{tE_s}{C_d}} \quad (2.20)$$

This means that the stress will decrease as time grows for the same strain [38].

- **Storage and Loss factors:**

For a harmonic stress, the strain will also vary harmonically. The harmonic stress and the respective strain response is given by the following equation

$$\sigma = \sigma_o e^{j\omega t}; \varepsilon = \varepsilon_o e^{j\omega t} \quad (2.21)$$

from these two equations, the stress-strain relation of the viscoelastic material in the Maxwell model can be written as given in the equation 2.22.

$$\sigma_o = E'(1 + j\eta_M)\varepsilon_o \quad (2.22)$$

It has a complex modulus of elasticity. The real part is called the storage modulus. The imaginary part is called the loss modulus. The ratio of storage modulus and loss modulus is called the loss factor [38].

In the Maxwell model under static loading, the stiffness and storage modulus will become zero. Hence the loss factor will be infinity. However, for very high-frequency loading, the loss factor becomes zero [39].

Kalvin-Voight model

In Kalvin-Voight model describes the viscoelastic material as a viscous damper (C_d) in parallel with an elastic stiffness (E_s). The applied stress is distributed through the elements and is given by the formula 2.23 [39].

$$\sigma = \sigma_s + \sigma_d \quad (2.23)$$

The stress-strain relation of the viscoelastic material in Kalvin-Voight model can be written as

$$\sigma = E_s \varepsilon_s + C_d \dot{\varepsilon}_d \quad (2.24)$$

Kalvin-Voight model characteristics

- **Creep:**

For constant stress, the stress-strain relation equation becomes

$$\varepsilon = \frac{\sigma}{E_s} \left(1 - e^{-\frac{E_s t}{C_d}} \right) \quad (2.25)$$

This means that the strain will grow to a constant value as time increases [38].

- **Relaxation:**

For constant strain, ($\dot{\varepsilon}$) in equation 2.24 becomes zero, so the stress-strain relation equation becomes

$$\sigma = E_s \varepsilon_o \quad (2.26)$$

This means that the stress will remain constant as time grows for the same strain [38].

- **Storage and Loss factors:**

For a harmonic stress, the strain will also vary harmonically. The harmonic stress and the respective strain response is given by the following equations

$$\sigma = \sigma_o e^{j\omega t}; \varepsilon = \varepsilon_o e^{j\omega t} \quad (2.27)$$

from these two equations, the stress-strain relation of the viscoelastic material in Kalvin-Voigt model can be written as given in the equation 2.28.

$$\sigma = (E_s + j\omega C_d)\varepsilon_o \quad (2.28)$$

The real part is called the storage modulus. The imaginary part is called the loss modulus. The ratio of storage modulus and loss modulus is called the loss factor [38].

In the Kalvin-Voight model under all loading, storage modulus is equal to the stiffness. Hence the loss factor is zero. However, for very high-frequency loading, the loss factor increases to infinity [39].

Zener model

The Zener model describes the material as a viscous damper (C_d) in parallel with an elastic stiffness (E_p) and both the damper and spring are in series with another stiffness (E_s).

The strain of the viscoelastic material in Zener model can be written as [39]

$$\varepsilon = \varepsilon_s + \varepsilon_p \quad (2.29)$$

The stress-strain relation of the viscoelastic material in Zener model can be written as

$$\sigma = E_s \varepsilon_s = E_p \varepsilon_p + C_d \dot{\varepsilon}_p \quad (2.30)$$

The stress-strain equation in Zener model can be solved either using Laplace transform (Laplace domain) or time domain.

Using the Laplace domain, the stress-strain relation equation can be written as

$$\varepsilon_s = \frac{\sigma}{E_s}, \varepsilon_p = \frac{\sigma}{E_p + sC_d} \quad (2.31)$$

$$\varepsilon = \frac{\sigma}{E_s} + \frac{\sigma}{E_p + sC_d} = \sigma \left(\frac{E_p + sC_d + E_s}{E_s(E_p + sC_d)} \right) \quad (2.32)$$

Likewise using the time domain, the stress-strain relation equation can be written as

$$E_s(E_p + sC_d)\varepsilon = (E_p + sC_d + E_s)\sigma \Rightarrow E_s E_p \varepsilon + E_s C_d \dot{\varepsilon} = (E_p + E_s)\sigma + C_d \dot{\sigma} \quad (2.33)$$

$$E\varepsilon + E\beta\dot{\varepsilon} = \sigma + \alpha\dot{\sigma} \quad (2.34)$$

The stress-strain relation equation formulated using time domain will be used to determine the characteristics of Zener model [39].

Zener model characteristics

- **Creep:**

For constant stress, ($\dot{\sigma}$) in equation 2.34 becomes zero, so the stress-strain relation equation becomes [40]

$$E\varepsilon + E\beta\dot{\varepsilon} = \sigma_o \Rightarrow \varepsilon = \frac{\sigma_o}{E} - \frac{E^{-t/\beta}}{E_s} \quad (2.35)$$

- **Relaxation:**

For constant strain ($\dot{\varepsilon}$) in equation 2.34 becomes zero, so the stress-strain relation equation becomes [40]

$$E\varepsilon = \sigma + \alpha\dot{\sigma} \Rightarrow \sigma = \sigma_o + E\varepsilon_o(1 - e^{-t/\alpha}) \quad (2.36)$$

- **Storage and Loss factors:**

For a harmonic stress, the strain will also vary harmonically. The harmonic stress and the respective strain response is given by the following equations

$$\sigma = \sigma_o e^{j\omega t}; \varepsilon = \varepsilon_o e^{j\omega t} \quad (2.37)$$

from these two equations, the stress-strain relation of the viscoelastic material in the Zener model can be written as 2.39.

$$E\varepsilon_o + j\omega E\beta\varepsilon_o = \sigma_o + j\omega\alpha\sigma_o \quad (2.38)$$

Rearranging the above equation and solving it gives the simple stress-strain equation.

$$\sigma_o = E'(1 + j\eta_Z)\varepsilon_o \quad (2.39)$$

It has a complex modulus of elasticity. The real part is called the storage modulus. The imaginary part is called the loss modulus. The ratio of storage modulus and loss modulus is called the loss factor. However, equation 2.39 is not suitable for analysis of complex structures. For solving the complex structure, the harmonic stress and strain are solved differently by substituting equation 2.37 in the differential equation that was derived in equation 2.34 [39]

$$\sigma_o e^{j\omega t} + \alpha\sigma_o i\omega e^{j\omega t} = E\varepsilon_o e^{j\omega t} + E\beta\varepsilon_o j\omega e^{j\omega t} \quad (2.40)$$

expanding the real and imaginary parts,

$$\sigma_o(\cos \omega t + j \sin \omega t) + \alpha \sigma_o i \omega (\cos \omega t + j \sin \omega t) = E \varepsilon_o (\cos \omega t + j \sin \omega t) + E \beta \varepsilon_o j \omega (\cos \omega t + j \sin \omega t) \quad (2.41)$$

The stress-strain equation is obtained by equating the real and imaginary parts separately and solving it.

$$\left(\frac{\sigma_d}{\eta_Z E' \varepsilon_o} \right)^2 + \left(\frac{\sigma_e}{E' \varepsilon_o} \right)^2 = 1 \quad (2.42)$$

This equation represents ellipse with major radius = $E' \varepsilon_o$ and minor radius = $\eta_Z E' \varepsilon_o$ [40]

Apart from the classic model, there are other models available to represent the behaviour of viscoelastic material. These models were developed based on the time domain. Golla-Hughes-McTavish model, Augmented Temperature Field model and Fractional Derivative model are few most commonly used models [39].

2.5 Material damping properties

The whole nature of vibration such as its source, frequency and direction is understood first for solving any vibration and acoustics problem. A vibration and acoustics problem can be solved either by passive or active control methods. In the passive control method, the stiffness, mass and damping of the vibration system are modified to reduce the system response. Increasing the damping of a system controls the undesirable vibration and acoustics caused by the resonance of the structure. Adding highly damped polymer material at the vital local of a structure is the most commonly used method for increasing the damping of a structure. For the damping to be effective, the added polymer must dissipate as much energy as possible [12].

There are two types of damping control method available for vibration and acoustics control. They are extensional damping method and shear damping method. The structure is covered by damping material on both sides in the extensional damping method. The damping material will be subjected to tension-compression deformation whenever the structure is subjected to any vibration. In shear damping treatment, the viscoelastic material is constrained as a damping layer. The viscoelastic material will deform in shear whenever the structure is subjected to any vibration [12].

Categories of damping materials

There are several Categories of damping [12]. They are

1. Viscous damping
2. Coulomb or Frictional damping
3. Structural or Hysteretic damping

Viscous damping

Viscous damping is the resistance offered by a viscous medium to the vibrating mechanical system. Because of this resistance, energy from the mechanical system will be dissipated. In viscous damping, the velocity of the vibrating body is proportional to the damping force, and the amount of dissipated energy depends on many factors. An example of viscous damping is a vehicle's shock absorbers [12].

In a simple spring-mass system with viscous damping, the force in viscous damper can be expressed as below.

$$F = -c\dot{x} \quad (2.43)$$

where c is proportionality constant and \dot{x} is velocity of the mass. The equation of motion for this system is given by the equation

$$m\ddot{x} + c\dot{x} + kx = F \quad (2.44)$$

where m = mass of the system, c = damping coefficient, k = stiffness coefficient. The natural frequency of such system is given by the formula

$$\omega_n = \sqrt{k/m} \quad (2.45)$$

The damping ratio for a system with viscous damping is given by the formula

$$\zeta = \frac{c}{c_c} = \frac{c}{2m\omega_n} \quad (2.46)$$

Based on the value of the damping ratio the motion of the mass in the system can be classified into three type

- When $\zeta < 1.0 \Rightarrow$ Oscillatory motion
- When $\zeta > 1.0 \Rightarrow$ Non-oscillatory motion
- When $\zeta = 1.0 \Rightarrow$ Critical damped motion

Rayleigh damping is the most common form of viscous damping and is given by the equation [12]

$$c = \alpha m + \beta k \quad (2.47)$$

Frictional damping

Frictional damping is the results from sliding of two dry surfaces. It is also known as coulomb damping. In frictional damping, the damping force is a product of normal force and friction coefficient (μ) [12].

$$F = -N\mu \quad (2.48)$$

The damping force is independent of velocity and is always opposite to the direction of velocity. The equation of motion of a system under frictional damping is given by the equation [12]

$$m\ddot{x} + kx = F \quad (2.49)$$

Structural or Hysteretic damping

In hysteretic damping, a damping material generally polymer (synthetic rubbers) is used to absorb the vibration from the structure. Polymers are used as damping materials because these materials provide high damping capacities under a broad range of frequency and temperature. When a structure with structural damping is subjected to vibration, the stress-strain diagram looks like a hysteresis loop. Hence, structural damping is also called hysteretic damping. When the polymeric material is deformed, because of friction between the internal planes, the energy is absorbed and dissipated by the polymeric material itself. The area of the loop denotes the energy lost per unit volume of the body per cycle. The energy lost is independent of frequency, but it is proportional to the square of the amplitude [12].

For a harmonic motion, the response x is given by equation

$$x = X e^{i\omega t} \quad (2.50)$$

The hysteretic damping coefficient (h) of hysteretic damping is given by the following equation

$$h = c_{eq}\omega \quad (2.51)$$

where c_{eq} is equivalent damping coefficient. This coefficient is used to calculate the energy dissipated by the hysteretic damping in one cycle.

$$\Delta W = \pi h x^2 \quad (2.52)$$

The equation of motion of a simple spring-mass equation with hysteretic damping is given by equation.

$$m\ddot{x} + c_{eq}\dot{x} + kx = f(t) \quad (2.53)$$

for a harmonic problem, the equation of equation becomes

$$-\omega^2 mx + k \left(1 - i2 \frac{\omega}{\omega_n} \zeta_{eq} \right) x = f(t) \quad (2.54)$$

where $\zeta_{eq} = \frac{c_{eq}}{c_c} = \frac{h}{2m\omega_n\omega}$ is the damping ratio of the hysteretic damping. For model damping, $\omega = \omega_n$, so the motion equation becomes

$$m\ddot{x} + k(1 - i\gamma)x = f(t) \quad (2.55)$$

where $\gamma = 2\zeta_{eq} = h/k$ is called the structural damping factor. $k(1 - ih/k)$ is the complex stiffness, Similarly viscous damping factor of viscous damping, the is given by $\gamma = 2\zeta$ [12].

Complex stiffness

The effectiveness of polymer material in hysteretic damping depends on material stiffness and its damping. These two properties are expressed by the complex Young's modulus $E(1 - i\eta_E)$ and the complex shear modulus $G(1 - i\eta_G)$. Both η_G and η_E are assumed to be equal for a given material. When a cyclic load is applied on the structure the maximum energy stored per cycle is $E\varepsilon_o^2/2$ and maximum energy dissipated per cycle is $\pi E\eta_L\varepsilon_o^2$. Where η_L is the loss factor. loss factor is equivalent to Structural damping factor (γ). Loss factor is used to express the damping performance. The relation between maximum energy dissipated per cycle and maximum strain energy stored (U_m) for a structural damped system is given by [12]

$$\Delta W = 2\pi\eta_L U_m \quad (2.56)$$

The loss factor is also expressed as

$$\eta_L = \frac{1}{2\pi} \frac{\text{maximum energy dissipated per cycle}}{\text{maximum strain energy stored}} \quad (2.57)$$

Higher the loss factor, higher the damping of the material [12].

The journal also explains about vibration damping in ANSYS software. The damping matrix can be modelled using harmonic, damped modal and transient analysis in ANSYS. The journal also explains different command used in ANSYS to input the different damping ratio and coefficient. Several case studies were carried out by the author to explain various models of material damping effects and some key points are explained for the correct application of damping effects for harmonic and modal analysis in ANSYS.

2.6 Inverse Finite Element Analysis

Zhenzhen, 2011 [63] explains how the small punch test (SPT) has been used to evaluate in-service materials in nuclear fusion facilities and advantages of using finite element methods in SPT tests. Also, an improved inverse finite element analysis procedure was proposed to obtain constitutive relations from load-displacement curves recorded in SPT [63].

Small punch test (SPT) provides several mechanical properties like strength, ductility, ductile-brittle transition temperature, and fracture toughness with a small volume of material compared to conventional mechanical test. The experimental data from SPT are in the form of load-displacement curves. Empirical relations or finite element analysis are used to determine the material properties. Inverse finite element method is used to determine unknown material parameters from experiment results. [63].

In a conventional finite element method, elastic modulus, yield stress, and stress-strain curve from a uniaxial test are given as input parameters. Whereas in inverse finite element method, these parameters are evaluated as output. The procedure of an inverse finite element method is described as follows [63]

1. The load-displacement curve is divided into several segments, and an inverse FE analysis is used to obtain the corresponding constitutive relation that matches each segment, in the experimental load-displacement curve .
2. For the first (linear) segment P1, the elastic modulus is obtained in the inverse FEM analysis. It starts with an assumed value of elastic modulus, which is then increased or decreased to match the experiment curve. The yield stress equals the von-Mises stress at the end of the first segment.
3. For the second segment, the load is given as input into the FE model. The plastic strain is adjusted to match the experimental load-displacement curve. The final value of the von-Mises stress and the equivalent plastic strain will be those of the second data point.
4. Similarly, the nth segment of the experimental load-displacement curve should be analyzed.

The mechanical behaviour of the specimen is determined with the elastic modulus, yield stress, and uni axial true stress-strain curve obtained from the above steps.

2.7 Research Problem

In vibration analysis, using modal parameters such as natural frequency, mode shapes, damping, stiffness to identify cracks in structures like wind turbine blade has provided reliable results. Condition monitoring of the wind turbine blades is done by gathering the modal parameters to identify any defects in its early stages.

Based on the literature study, it is evident that current vibration analysis techniques use natural frequency, mode shapes and also stiffness variations to identify the crack location, size and numbers in a wind turbine blade. The limitations in those techniques are

1. The results are reliable only for small and medium-size cracks.
 2. Only limited number of cracks can be identified using current techniques i.e., most of the techniques provide good results up to 3 cracks. If the number of cracks increases the resonance also increases making it difficult to identify the crack location and size correctly.
 3. Crack initiation in adhesive bonds between spar cap and shear web assembly is not explained.
- . So two research questions are formulated to overcome these limitations.
1. Can increase in material damping due to defect be used effectively to identify the defect location and size effectively?
 - Can the modal damping be used to identify defect in spar cap and shear web assembly?
 2. Is it possible to model the vibration analysis based on the viscoelastic damping?

2.8 Methodology

The research methodology to be followed is explained in this sub-chapter. To reduce the computational time, only the spar cap-shear web assembly of a wind turbine blade has been modelled for damage identification and localization. A 3D model of the spar cap-shear web assembly is created using ANSYS 18.2 software. Through modal analysis, the natural frequency of the undamped structure is found, and the stiffness and mass matrices are extracted from ANSYS. The proposed method is based on the change in the damping properties of blade material and its effects on the dynamic response of the blade. Damping is introduced into the dynamic motion of the blade by the viscoelastic damping model and using a loss factor. Two dynamic properties of the blade (the modal damping and the phase of complex mode shapes) are considered to identify and localize the damage [54]. Following is the guideline that was followed to identify the damage index briefed in simple steps.

- Step 1: Extracting mass and stiffness matrix of undamped structure using ANSYS.
- Step 2: Deriving eigenvalues and eigenvectors of undamped structure.
- Step 3: Derive damping matrix using
 1. First order perturbation method
 2. Viscous analogy method
- Step 4: Deriving eigenvalues and eigenvectors of damped system.
- Step 5: Finding the damage index.

3 Vibration Modelling

In this chapter, methods used for vibration modelling of viscoelastic materials is explained. Also damping modelling procedures are explained. The background calculation for this project is derived from the [51].

3.1 Constitutive equation of a linear viscoelastic material

For structures under constant load, creep and relaxation is adequate to understand the responses. But for structures under cyclic (or) arbitrary load, the constitutive equation is necessary to incorporate all possible responses. Various mathematical methods are used to develop the constitutive equation for a viscoelastic material. Boltzmann superposition principle is used to develop the constitutive equation for linear materials [51]. Due to the symmetry, the strain and stress can be expressed in the vector form (or) the Voigt notation and is given by

$$\sigma = \{\sigma_x \sigma_y \sigma_z \sigma_{xy} \sigma_{yz} \sigma_{xz}\} \quad (3.1)$$

$$\varepsilon = \{\varepsilon_x \varepsilon_y \varepsilon_z \varepsilon_{xy} \varepsilon_{yz} \varepsilon_{xz}\} \quad (3.2)$$

Using these Voigt notation, the the general Hooke's law of a linear elastic material can be written as [51]

$$\{\sigma\} = [C]\{\varepsilon\} \quad (3.3)$$

where $\{\}$, $[]$ are symbols for vector and matrix respectively. $[C]$ is the elasticity matrix with 6×6 elements. For a transverse orthotropic material associated with spar-cap shear web assembly, independent variables of the matrix is reduces to 5×5 elements [11]. The independent variables in the Cartesian coordinate system(x, y, z) are

1. Young's modulus in x and y direction, denoted as (E_x, E_y)
2. Shear modulus in x-y plane, denoted as (G_{xy}) and
3. Poisson's ratios in x-y and y-z planes, denoted as (ν_{xy}, ν_{yz})

These variables are constant for an elastic material but these properties are time variant for a viscoelastic material. Using the theory of linear viscoelasticity of material. the constitutive equation for a viscoelastic material can be written as [51],[37]

$$\{\sigma(t)\} = [C(t)]\{\varepsilon(0)\} + \int_0^t [C(t-\tau)]\dot{\varepsilon}(\tau)d\tau \quad (3.4)$$

where $(\dot{\quad})$ is defined as time derivative operator of a variable and is defined as,

$$(\dot{\quad}) = \frac{\partial(\quad)}{\partial t} \quad (3.5)$$

taking the Laplace of equation 3.4 then,

$$\{\sigma(S)\} = S[C(S)]\{\varepsilon(S)\} \quad (3.6)$$

where $S[C(S)]$ is the dynamic modulus. It is decomposed in two parts

$$S[C(S)] = [C_0] + S[\bar{C}(s)] \quad (3.7)$$

where, C_0 is the relaxed elastic property of viscoelastic material. And $S[\bar{C}(s)]$ is the viscous property of a viscoelastic material i.e., for a elastic material $S[\bar{C}(s)] = 0$.

3.2 Finite element vibration equation of a linear viscoelastic material

There are many methods available to derive the finite element vibration equation of linear viscoelastic material.

3.2.1 Time domain equation of motion

Similar to the elastic material, the finite element model of linear viscoelastic material is developed based on the principle of the weak form of the equation of motion is used. The displacement field within an element is approximated by shape functions and nodal displacements of that element. This approximated displacement field is replaced in the weak form of the equation of motion. This leads to the construction of the matrix form of the equation of motion in term of mass, stiffness and damping matrix. The displacement field in the cartesian coordinate system can be written in the vector form as shown below [51]

$$U = \{uvw\} \quad (3.8)$$

where u,v and w are displacement component in i,j and k directions respectively. The structure is divided into n elements. Each element has m nodes, and each node has three degrees of freedom. The displacement field of an element is written in the nodal displacement vector form as shown below. [44],[11]

$$q_e = \{u_1v_1w_1u_2v_2w_2\dots u_mv_mw_m\} \quad (3.9)$$

$$\begin{aligned} u^e &= \sum_{i=1}^m N_i u_i \\ v^e &= \sum_{i=1}^m N_i v_i \\ w^e &= \sum_{i=1}^m N_i w_i \end{aligned} \quad (3.10)$$

q_e is the nodal displacement vector of an element and N_i is shape function [37]. Equation 3.10 can also be written in the matrix notation as

$$\{U^e\} = [N]q_e \quad (3.11)$$

$[N]$ is matrix shape function of an element with the size of 3×3 .

$$N = \begin{bmatrix} N_1(x, y, z) & 0 & 0 & N_2(x, y, z) & 0 & 0 & N_3(x, y, z) & 0 & 0 & \dots \\ 0 & N_1 & 0 & 0 & N_1 & 0 & 0 & N_1 & 0 & \dots \\ 0 & 0 & N_1 & 0 & 0 & N_1 & 0 & 0 & N_1 & \dots \end{bmatrix} \quad (3.12)$$

The weak form of the equation of motion for an element of a structure is written as [37]

$$\int_{v_e} \{\ddot{U}\}^{eT} \delta\{U\}^e \rho dv + \int_{v_e} \{\sigma\}^T \{\varepsilon\} \delta\{\varepsilon\} dv - \int_{S_e} \{t\}^{eT} \delta\{U\}^e dS - \int_{v_e} \{f\}^{eT} \delta\{U\}^e dv = 0 \quad (3.13)$$

Index e is used to identify that a vector or matrix belongs to an element of a structure.

Index T is used to identify the transpose operator of a vector or matrix.

$\{t\}^e$ is boundary forces per unit area for an element.

$\{f\}^e$ is gravitational force per unit volume of an element.

From equation 3.11,

$$\delta\{U\}^e = [N]\delta\{q\}^e \quad (3.14)$$

$$\{\ddot{U}\}^e = [N]\{\ddot{q}\}^e \quad (3.15)$$

Strain in a continuum structure is related to displacement field as

$$\{\varepsilon\} = [D]\{U\} \quad (3.16)$$

where $[D]$ is the operator matrix and can be defined as

$$D = \begin{bmatrix} \frac{\partial}{\partial x} & 0 & 0 \\ 0 & \frac{\partial}{\partial y} & 0 \\ 0 & 0 & \frac{\partial}{\partial z} \\ \frac{\partial}{\partial y} & \frac{\partial}{\partial x} & 0 \\ 0 & \frac{\partial}{\partial z} & \frac{\partial}{\partial y} \\ \frac{\partial}{\partial z} & 0 & \frac{\partial}{\partial x} \end{bmatrix} \quad (3.17)$$

substituting equation 3.11 in equation 3.16 then,

$$\{\varepsilon\} = [D]^e [N]^e \{q\}^e \quad (3.18)$$

so the strain becomes ,

$$\delta\{\varepsilon\} = [D]^e \delta\{U\}^e = [D]^e [N]^e \delta\{q\}^e \quad (3.19)$$

and

$$\{\tilde{\varepsilon}\} = [D]^e [N]^e \{\ddot{q}\}^e = [B]^e \{\ddot{q}\}^e \quad (3.20)$$

where matrix $[B]^e$ is defined as

$$[B]^e = [D]^e [N]^e \quad (3.21)$$

If equation 3.14 to 3.21 are substituted in the equation 3.13, then

$$\begin{aligned} \{\ddot{q}\}^T \int_{v_e} \rho [N]^e{}^T dv + \int_{v_e} \{\{q(0)\}^{eT} [B]^e{}^T [C(t)] [B]^e dv + \int_0^t \{\dot{q}\}^{eT} [B]^e{}^T [C(t-\tau)] [B]^e d\tau\} dv \\ - \int_{S_s} \{t\}^{eT} N ds - \int_{v_e} \{f\}^T N^e dv = 0 \end{aligned} \quad (3.22)$$

The element mass and stiffness matrices and the force vector are expressed as

$$[M]^e = \int_{v_e} \rho [N]^e{}^T dv \quad (3.23)$$

$$[K(t)]^e = \int_{v_e} [B]^e{}^T [C(t)] [B]^e dv \quad (3.24)$$

$$\{F(t)\}^e = \int_{S_s} [N]^e \{t\}^e ds + \int_{v_e} \{f\}^e [N]^e dv \quad (3.25)$$

So after taking transpose, the equation 3.22 becomes

$$[M_e] \ddot{q}_e + \int_{v_e} \{\{q(0)\}^{eT} [B]^e{}^T [C(t)] [B]^e dv + \int_0^t \{\dot{q}\}^{eT} [B]^e{}^T [C(t-\tau)] [B]^e d\tau\} dv = [F(t)]^e \quad (3.26)$$

The above equation is the time domain equation of motion for a single element of a viscoelastic structure. Then the time domain equation for the whole structure is written as

$$\sum_{e=1}^n [M_e] \ddot{q}_e + \sum_{v_e} \int_{v_e} \{\{q(0)\}^{eT} [B]^e{}^T [C(t)] [B]^e + \int_0^t \{\dot{q}\}^{eT} [B]^e{}^T [C(t-\tau)] [B]^e d\tau\} dv = \sum_{e=1}^n [F(t)]^e \quad (3.27)$$

3.2.2 Laplace form of equation of motion

The equation of motion for a viscoelastic element in the Laplace domain is derived by taking the Laplace transform of the equation 3.26.

$$S^2 [M]^e \{q(s)\}^e + S [K(s)]^e \{q(s)\}^e = F(s)^e \quad (3.28)$$

where

$$S [K(s)]^e = S \int_{v_e} [B]^e{}^T [C(s)] [B]^e dv \quad (3.29)$$

By using the decomposed form of $S[C(S)]$ from equation 3.7, the equation 3.29 can be written as

$$S [K(s)]^e = \int_{v_e} [B]^e{}^T [C_0] [B]^e dv + S \int_{v_e} [B]^e{}^T [\bar{C}(s)] [B]^e dv \quad (3.30)$$

$$[K^E] = \int_{v_e} [B]^e{}^T [C_0] [B]^e dv \quad (3.31)$$

$$[K^D]^e(s) = \int_{v_e} [B]^e{}^T [\bar{C}(s)] [B]^e dv \quad (3.32)$$

$[K^D]^e(s)$ is the damping matrix. It is time-variant part of dynamic modulus in the Laplace domain. However, only one part is correspondent to the dissipation of energy [37]. The Laplace form of the equation of motion can be written as

$$S^2[M]^e\{q(s)\}^e + [K^E]^e\{q(s)\}^e + S[K^D(s)]^e\{q(s)\}^e = \{F(s)\}^e \quad (3.33)$$

The Laplace form of equation of motion for the whole structure can be written as

$$\sum_{e=1}^n S^2[M]^e\{q(s)\}^e + [K^E]^e\{q(s)\}^e + S[K^D(s)]^e\{q(s)\}^e = \sum_{e=1}^n \{F(s)\}^e \quad (3.34)$$

$$S^2[M]\{q(s)\} + [K^E]\{q(s)\} + S[K^D(s)]\{q(s)\} = \{F(s)\} \quad (3.35)$$

where $[M]$, $[K^E]$, $[K^D]$, $F(s)$ are mass, stiffness, damping matrix and force vector respectively.

3.3 Eigenvalue and eigenvector of vibration equation

The eigenvalue and eigenvector of a vibration system is a response to the free vibration of that system. To get a free vibration response of a vibration system the left hand side of equation 3.35 is equalled to zero. The equation becomes

$$S^2[M] + [K^E] + S[K^D(s)]\{q(s)\} \quad (3.36)$$

The dynamic stiffness matrix of the structure can be written as

$$D = S^2[M] + [K^E] + S[K^D(s)] \quad (3.37)$$

The determinant of the dynamic stiffness matrix is set to zero to obtain the nontrivial solution of equation 3.36. Similarly, the eigenvalue of the vibration system is obtained by setting the $\det[D]$ to 0. The eigenvalue is denoted by s_i . Correspondent to each eigenvalue there is a vector which is called eigenvector and is denoted by ϕ_i . The eigenvalue and eigenvector of a vibration system depend on mass, stiffness and damping matrix. Usually, in the analysis of a vibration system, three following scenarios happen [51].

1. **Structure is assumed to have no damping**, $K^D(s) = 0$

In this case, the determinant of equation 3.37 gives n, the total degree of freedom of the system or size of the mass and stiffness matrix. The square root of the determinant has the form of

$$S_i = \pm j\omega_i \quad (3.38)$$

Where ω_i is the natural frequency. The eigenvector also denotes the undamped mode shapes of a system and is indicated by $\{b^i\}$. This mode shapes have orthogonality properties [53].

$$[b_i]^T [M] [b_j] = m_i \delta_{ij} \quad (3.39)$$

$$[b_i]^T [K^E] [b_j] = k_i^E \delta_{ij} \quad (3.40)$$

where

$$\delta_{ij} = \begin{cases} 1, & i = j \\ 0, & i \neq j \end{cases} \quad (3.41)$$

2. **Structure with proportional type of damping**

In this case, the left and right hand side of equation 3.36 is multiplied by $\{b^i\}^T$, $\{b^j\}$. Then the equation becomes

$$m_i \delta_{ij} S^2 + S \{b^i\}^T [K^D(s)] \{b^j\} + k_i^E \delta_{ij} = 0 \quad (3.42)$$

If $[K^D(s)]$ matrix satisfies the following condition

$$[b^i]^T [K^D] [b^j] = k_i^D \delta_{ij} \quad (3.43)$$

then the equation 3.42 for $i, j = 1, 2, \dots, n$ becomes

$$m_i S_i^2 + S_i k_i^D + k_i^E = 0 \quad (3.44)$$

If the damping matrix satisfies the equation 3.43, the damping is proportional. The eigenvalue of the structure can be found by substituting the equation 3.44 in the equation 3.43 [53]. The eigenvector of a proportionally damped structure noted to be same as undamped system [51].

3. Structure with non proportional type of damping

When a structure is damaged, equation 3.43 will not be satisfied. And the damping matrix will be non proportional. In this case, identifying the eigenvalue and eigenvector of the structure is not as straight forward as an undamped and proportional damping system. The eigenvalue of the vibration system is calculated by taking the square root of the determinant of the stiffness matrix. Dependent on the type of damping matrix (a function of S), the number of eigenvalues can be $2m > 2n$. For lightly damped structure, $2m$ roots are divided by $2n$ roots, which form n conjugate pairs and $(2m - 2n)$ real values. n conjugate pairs return n pairs of conjugate mode shapes. These mode shapes are oscillatory in nature. Real eigenvalue returns $(2m - 2n)$ mode shapes. [55].

3.3.1 Eigenvalue and eigenvector of non proportional damping

There are three different approaches to determine the eigenvalue and eigenvector of the non proportional damping system. Each approach has its advantages and disadvantages [51]. The different approaches are explained below

3.3.1.1 First order perturbation method

The idea behind the first order perturbation method is that for a system with " n " degree of freedom, " n " undamped mode shapes construct eigenvector of non proportional damped system. The mode shape of the non proportional damped structure can be expressed as [51]

$$\varphi^k = \sum_{i=1}^n \alpha_i^k \{b^i\} \quad (3.45)$$

φ^k is " k^{th} " mode shapes of the non proportional damping system. Substituting equation 3.45 in equation 3.36 and multiplying the left hand side of equation 3.45 with $\{b^k\}^T$ and using the orthogonality properties of undamped mode shapes to get k_{ki} [51]

$$\alpha_k^k S_k^2 + \alpha_k^k \omega_k^2 + S_k \sum_{i=1}^n \alpha_i^k k_{ki} = 0 \quad (3.46)$$

where,

$$k_{ki} = \{b^k\}^T [K^D] \{b^i\} \quad (3.47)$$

Similarly, to get k_{mi} equation 3.45 is substituted in the equation 3.36 and the left hand side of the equation multiplies with $\{b^m\}^T$

$$\alpha_m^k S_k^2 + \alpha_m^k \omega_m^2 + S_k \sum_{i=1}^n \alpha_i^k k_{mi} = 0 \quad (3.48)$$

where

$$k_{mi} = \{b^m\}^T [K^D] \{b^i\} \quad (3.49)$$

if α_m^k and α_k^k are exclude from equation 3.48 then

$$\alpha_m^k S_k^2 + \alpha_m^k \omega_m^2 + S_k \alpha_m^k k_{mm} S_k + S_k \alpha_k^k k_{mk} + S_k \sum_{i=1, i \neq m, i \neq k}^n \alpha_i^k k_{mi} = 0 \quad (3.50)$$

If $\alpha_k^k = 1$, the components of φ^k can be obtained from $(n - 1)$ set equations such as equation 3.50, where $1 < m < n$ except $m = k$ which return 1. All the coefficient (α_i^k) of mode shape φ^k of the non proportional damped system is found from the above set of equations [55]. For a lightly damped system, the last term in equation 3.48 and 3.50 can be neglected. These assumptions lead to the first-order perturbation solution. By neglecting the last term from equation 3.48, [51]

$$S_k^2 + \omega_k^2 + S_k k_{kk} (S_k) = 0 \quad (3.51)$$

For lightly damped system, $k_{kk}(S_i) \approx k_{kk}(\pm j\omega_k)$. So this second order equation return the eigenvalue S_k as

$$S_k \approx \pm j\omega_k - \{k_{kk}(\pm j\omega_k)\}/2 \quad (3.52)$$

From the equation 3.50 by neglecting the last term, the equation becomes

$$\alpha_m^k = \frac{-S_k K_{mk}}{S_k^2 + \omega_m^2 + S_k k_{mm}} \quad (3.53)$$

3.3.1.2 Viscous analogy

The viscous damping is a special case of non proportional damping when $[K^D(S \rightarrow o)]$. The eigenvalue of the viscous damping system has the form of [55]

$$S_{k0} = -\xi_{k0}\omega_k \pm j\omega_k\sqrt{1 - \xi_k^2} \quad (3.54)$$

where,

$$\xi_{k0} = \{\varphi^{k0T}[K^D(S)]\varphi^{k0}\}/2\omega_k \quad (3.55)$$

$$S \rightarrow 0$$

The eigenvalue of the viscoelastic damped system can be expressed in a small deviated form from the viscous damping system

$$S_k = S_{k0} + \delta_k \quad (3.56)$$

Substituting equation 3.56 in equation 3.51 and expanding $k_{kk}(S_k = S_{k0} + \delta)$ with Taylor series around S_{k0} equation 3.51 becomes

$$k_{kk}(S_k) = k_{kk}(S_{0k}) + \delta_k \frac{\partial k_{kk}(S = S_{0k})}{\partial S} + \delta_k^2 \frac{\partial^2 k_{kk}(S = S_{0k})}{2i\partial S^2} + \dots \quad (3.57)$$

Keeping the first two term and substituting equation 3.57 in equation 3.51 leads to

$$(S_{k0} + \delta_k)^2 + \omega_k^2 + (S_{k0} + \delta_k)(k_{kk}(S_{0k})) + \delta_k \frac{\partial k_{kk}(S = S_{0k})}{\partial S} = 0 \quad (3.58)$$

Equation 3.58 is solved to obtain the value of δ_k [55].

$$\delta_k = \frac{-B_k - \sqrt{B_k^2 - 4A_k C_k}}{2A_k} \quad (3.59)$$

$$A_k = 1 + \frac{1}{2} \frac{\partial^2 k_{kk}(S = S_{0k})}{\partial S^2} S_{0k} + \frac{\partial k_{kk}(S = S_{0k})}{\partial S}$$

$$B_k = 2S_{0k} + S_{0k} \frac{\partial k_{kk}(S = S_{0k})}{\partial S} + k_{kk}(S = S_{0k})$$

$$C_k = S_{0k}^2 + S_{0k} k_{kk}(S = S_{0k}) + \omega_k^2$$

3.3.1.3 Damping matrix approximation

The eigen matrix of the system is defined by multiplying $[M^{-1}]$ on both side of equation 3.36

$$(S^2 I + M^{-1} K^E + S M^{-1} K^D(s)) q(s) = \quad (3.60)$$

$$U(s) = M^{-1} K^E + S M^{-1} K^D(s) \quad (3.61)$$

From matrix eigen value decomposition theory

$$U(s)\varphi^k = \lambda_k \varphi^k \quad (3.62)$$

The eigen vector of the system $q(s)$ is obtained from equation 3.60

$$S_k^2 \varphi^k + U(s)\varphi^k = 0 \quad (3.63)$$

Substituting equation 3.62 in equation 3.63 results in

$$S_k^2 = -\lambda_k \quad (3.64)$$

It means that for each "S" the eigen matrix of the system $U(s)$, return the eigenvalue and eigenvector of the system only if the equation 3.64 satisfies. An iteration approach is required to identify the exact value of "S" to satisfy both equations 3.62 and 3.64. This iteration approach is time consuming and not applicable to a large system. An approximate solution for eigenvector can be found by assuming the damping matrix to a constant value close to the eigenvalue of the system. For a lightly damped system, this approximation is quite reasonable. The eigenvalue of the system can be written as [51]

$$S_i = a_i \pm j b_i \quad (3.65)$$

The natural frequency and damping coefficient of the system can be defined as

$$\omega_k = \sqrt{a_k^2 + b_k^2} \quad (3.66)$$

$$\xi_k = \frac{-a_k}{b_k} \quad (3.67)$$

For lightly damped system, the $K^D(s)$ can be obtained by replacing "S" with $\pm j\omega_k$. The mode shapes of the system is found by solving the eigenvalue

$$(S^2[M] + K^E + S[K^D(j\omega_k)])\{q(s)\} = 0 \quad (3.68)$$

Equation 3.68 is in the form of viscous damping. The eigenvector of this system can be found by rearranging the equation 3.68 in the state space Laplace from [53].

$$(S[A] + [B])\{Q(s)\} = 0 \quad (3.69)$$

$$[A] = \begin{bmatrix} [0] & M \\ M & K^D \end{bmatrix} \quad (3.70)$$

$$[B] = \begin{bmatrix} [-M] & [0] \\ [0] & K^E \end{bmatrix} \quad (3.71)$$

$$\{Q(s)\} = \begin{Bmatrix} Sq(s) \\ q(s) \end{Bmatrix} \quad (3.72)$$

Multiplying equation 3.69 by $[A]^{-1}$

$$(S[I] + [A]^{-1}[B])\{Q(s)\} = 0 \quad (3.73)$$

This lead to eigenvalue solution of

$$[A]^{-1}[B]\{\phi^k\} = \lambda_k\{\phi^k\} \quad (3.74)$$

where,

$$\{\phi^k\} = \begin{Bmatrix} \lambda_k \varphi^k \\ \varphi^k \end{Bmatrix} \quad (3.75)$$

substituting equation 3.74 in equation 3.73 gives

$$S_k = -\lambda_k \quad (3.76)$$

More accurate eigenvector of the system is obtained when " S_k " from equation 3.52 and 3.56 is substituted in damping matrix instead of ω_k . This approach gives accurate results. However, the computational cost will be high if all the mode shapes of the system are analysed. So for damage identification based on damping, only a few first modes of vibration are considered [51].

4 Damage Modeling

In this chapter, the concept used for damage modelling is explained. Also, modelling of spar cap - shear web assembly with four different damage scenarios such as damage only in the top surface near the fixed end and midsection with 2 %, 4 % and 6 % defected area, damage in the top and core surfaces near fixed end and midsection with 2 %, 4 % and 6 % defected area are explained.

4.1 Damage modelling concept

Spar cap - shear web assembly is an important part of a blade structure. This connection provides the structural integrity to the wind turbine blade, and it carries most of the aerodynamic load. This assembly is constructed by connecting the top and bottom spar caps to the shear web using adhesive. The shear web consists of face sheets and foam, which constitute the core of the wind turbine blade. The spar cap - shear web assembly suffers from damage at the bond line, which can propagate through the structure and compromise the structural integrity [62],[22]. Usually, damage in the joint begins with the transverse cracks in the adhesive. At the same time, delamination develops in the vicinity of the transverse cracks and finally with the growth of these cracks and widening of delamination, debonding of the shear web from spar caps occurs [54].

Sharif et al., 2020 [54] conducted a fatigue test to relate the types of damages to the loss factor series of fatigue tension test on a specimen representing the adhesive-bonded connection of spar cap - shear web assembly. The purpose of this fatigue test was to produce progressive damage in the spar cap-shear web joint connection and measure the gradual change in the loss factor by experimental modal testing. The loss factor in the test specimen depends on the level of damage, frequency and strain amplitude. The results show that the loss factor of the test specimen increases with frequency and reaches the maximum value around the first natural frequency and then decreases. The maximum value also correspondent to maximum deflection or strain value [54]. The dynamic elastic properties of spar cap of the blade have been expressed in the form of (Golla-Hughes-McTavish) GHM model. In general, the dynamic modulus by GHM models is written as [19].

$$SG(S) = G_0 + \frac{a(S^2 + 2bcS)}{S^2 + 2bcS + b^2} \quad (4.1)$$

where

1. $G(S)$ is the general term for dynamic modulus.
2. a, b, c are constant parameters which are obtained from experimental tests to represent the real working condition of the wind turbine blade.
3. G_0 is the relaxed part of dynamic modulus.[51]

Equation 4.1 is used to incorporate damage into the structure. A detailed explanation is given in the chapter 4.3

4.2 Spar cap - shear web assembly

A wind turbine blade is made up of aerodynamic shell and shear web. The load-carrying aerodynamic shell of the wind turbine blade is constructed using unidirectional composite laminates such as thick GFRM (Glass Fibre Reinforced Materials). The shear web is the supporting structure of the wind turbine blade. The shear web is moulded separately using multi-axial fibre lay-ups and a core made of balsa wood or polyvinyl chloride (PVC) foam and then bonded together with the aerodynamic shell using a structural adhesive. The web body is formed by infusion of a foam core with thin skin laminates. Whereas, the webfoot is made up of multi-axial glass fibres. The web adhesive joint is assembled by bonding the webfoot onto the spar cap as shown in figure 4.1. As explained above, this web adhesive joint is a key element for the structural integrity of the wind turbine blade. If this joint suffers fatigue damage at the bond-line, the damage can propagate through the spar cap and lead to delamination and debonding of the spar cap from the shear web [54].

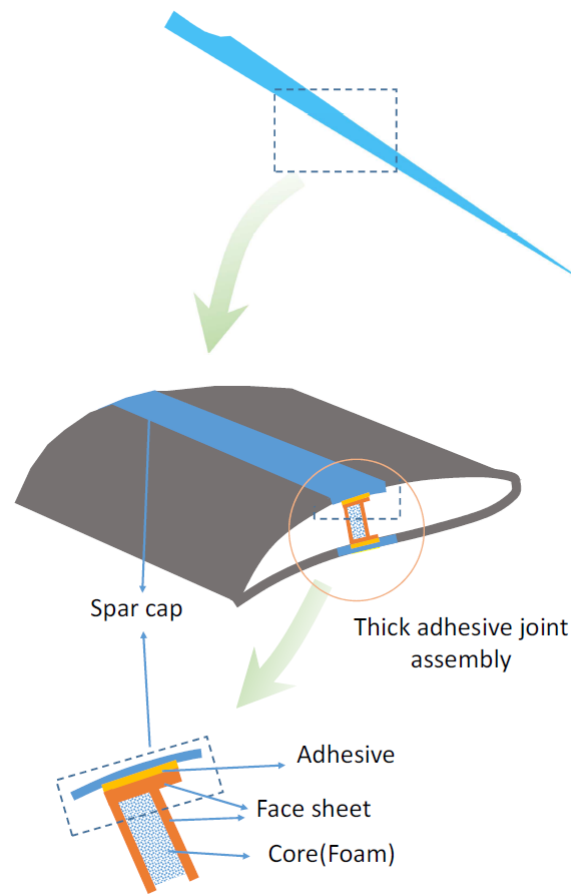


Figure 4.1: Spar cap - shear web assembly

with copyright permission from the journal [54].

4.2.1 ANSYS model

To reduce complications, the spar cap - shear web assembly is modelled as "I" beam in ANSYS 18.3 workspace. The dimensions of the blade are measured from the "NedWind 40 turbine" provided by LM Wind Power. The length of the blade was measured to be about 20 m. The width and thickness of the spar cap are measured to be about 1 m and 2 cm respectively. Similarly, the width and thickness of the Face-sheet were measured to be about 1 cm and 37.5 cm respectively. The width and thickness of adhesive were measured to be about 5 cm and 0.6 cm respectively. The materials considered for modelling the spar cap - shear web assembly in ANSYS are unidirectional Epoxy- S glass, unidirectional Epoxy- E glass, Epoxy Resin, PVC Foam for Spar cap, Face sheet, Adhesive and Foam respectively. The Epoxy Resin, PVC Foam are isotropic materials. Whereas, Epoxy- S glass and Epoxy- E glass are orthotropic materials. Since the structure has to be modelled as composite materials, all parts are designed as surfaces as shown in below figure 4.2. Figure 4.3 shows the isometric view and figure 4.4 shows the side view of the blade surfaces. For spar cap - shear web assembly, 9 different surfaces are modelled. They are top and bottom spar cap, top, bottom, left and right face sheet, top and bottom adhesive and foam.

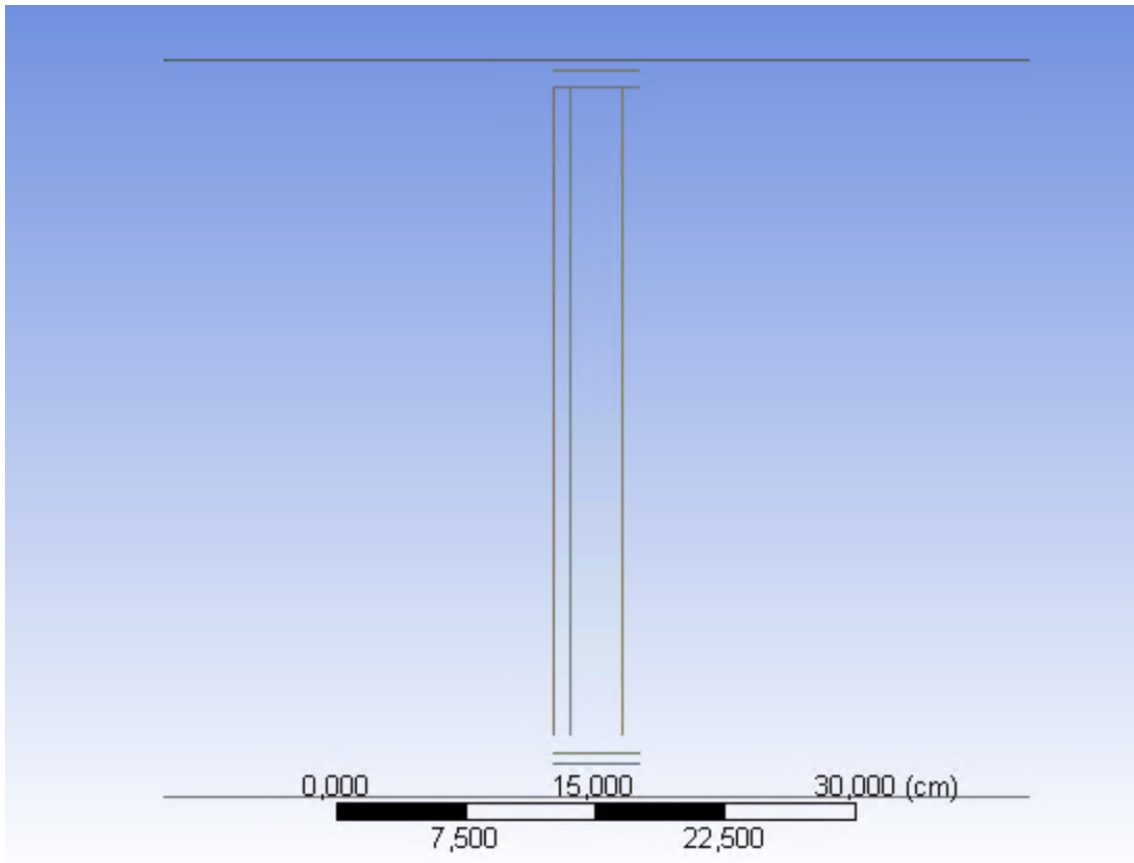


Figure 4.2: Design of spar cap - shear web assembly front view

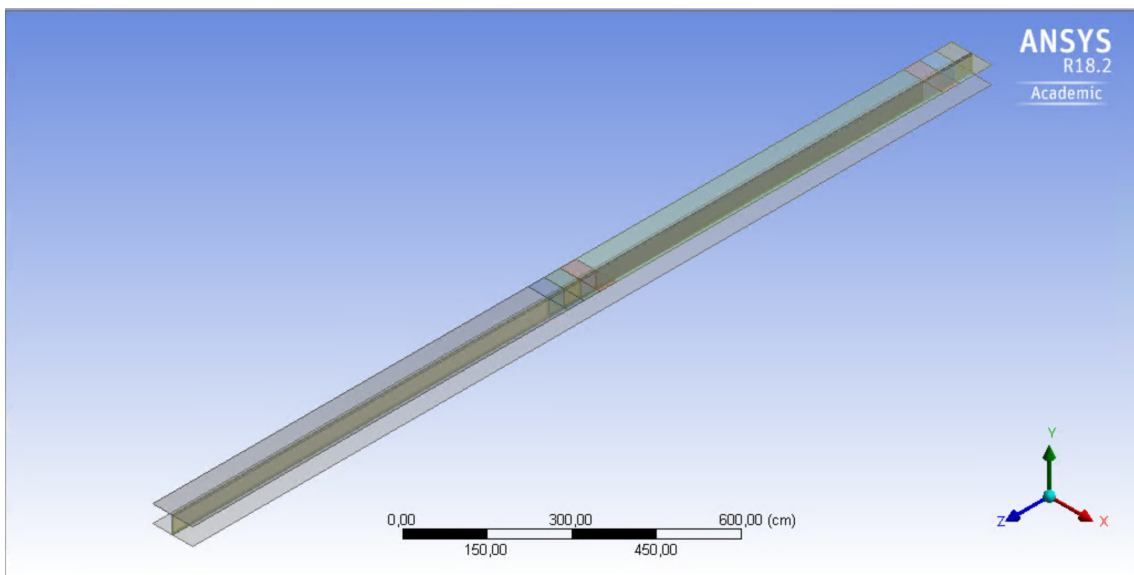


Figure 4.3: Design of spar cap - shear web assembly isometric view

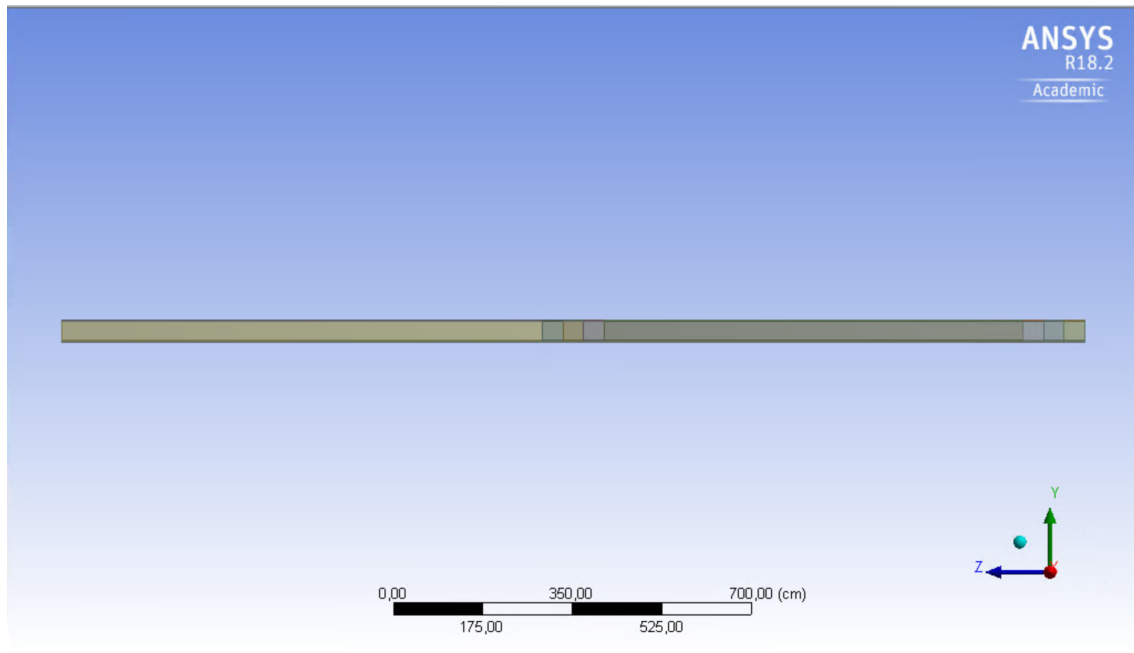


Figure 4.4: Design of spar cap - shear web assembly side view

The layers of the composites are applied in ACP setup and modal analysis setup in ANSYS workbench. The thickness of a single epoxy glass fibre is assumed to be about 1 mm and the thickness of the single foam layer is assumed to be about 3 mm. Depending on the thickness, the number of layers forming a stack varies. Spar cap has 20 layers, Face sheet and Foam has 10 layers. The Spar cap fibres are laid at 0° and fibres of face sheet are laid at $\pm 45^\circ$. Face and edge connections are used to join the parts with each other. The element size was selected to be about 25cm for meshing. Figure 4.5 shows the model after layup and meshing.

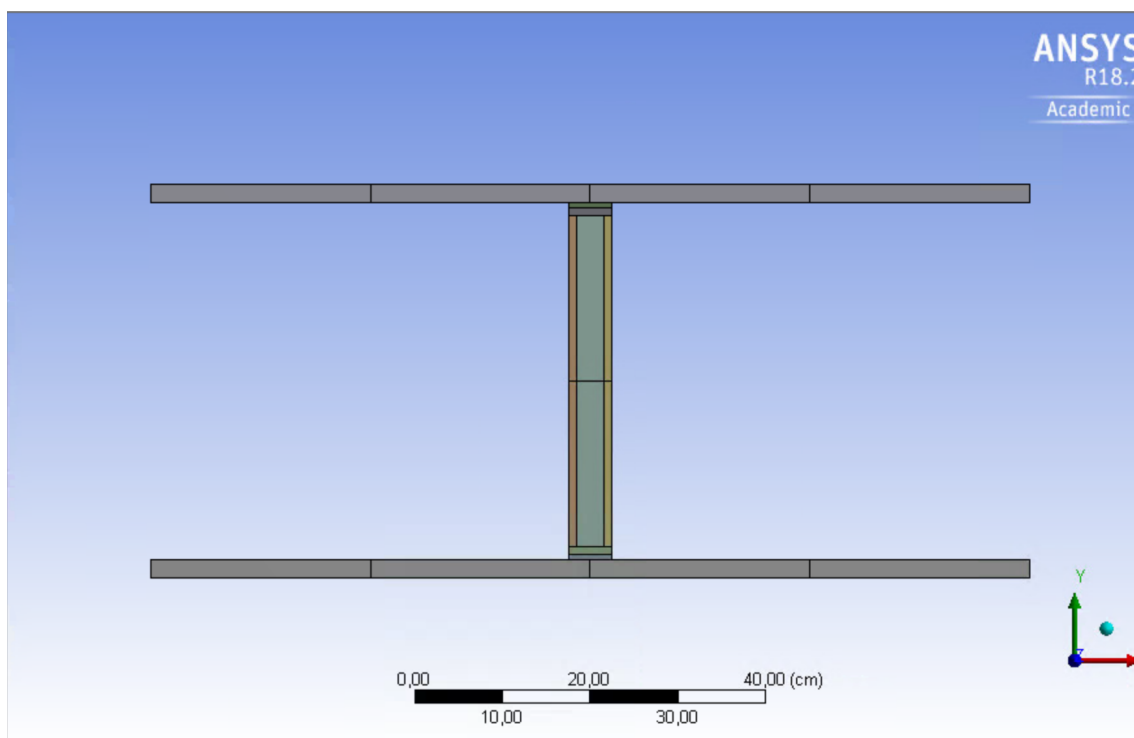


Figure 4.5: Front view spar cap - shear web assembly

Figure 4.6 shows the isometric view of the spar cap - shear web assembly.

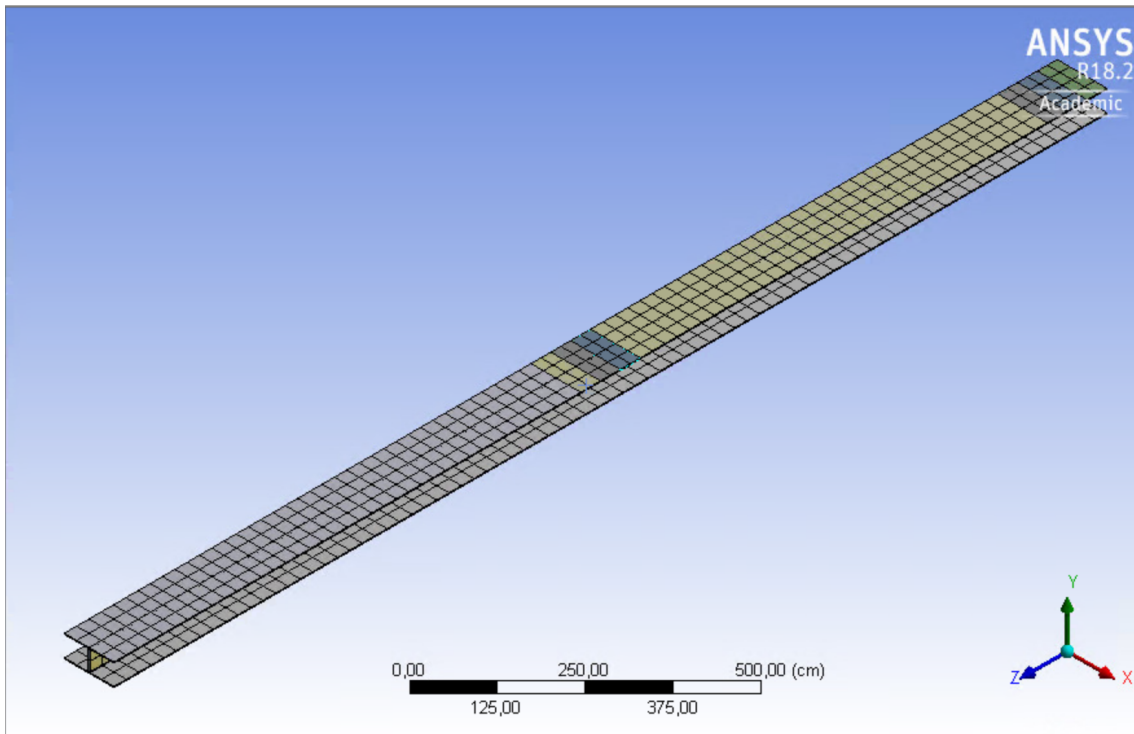


Figure 4.6: Isometric view spar cap - shear web assembly

Figure 4.7 shows the side view of the Spar cap - shear web assembly.

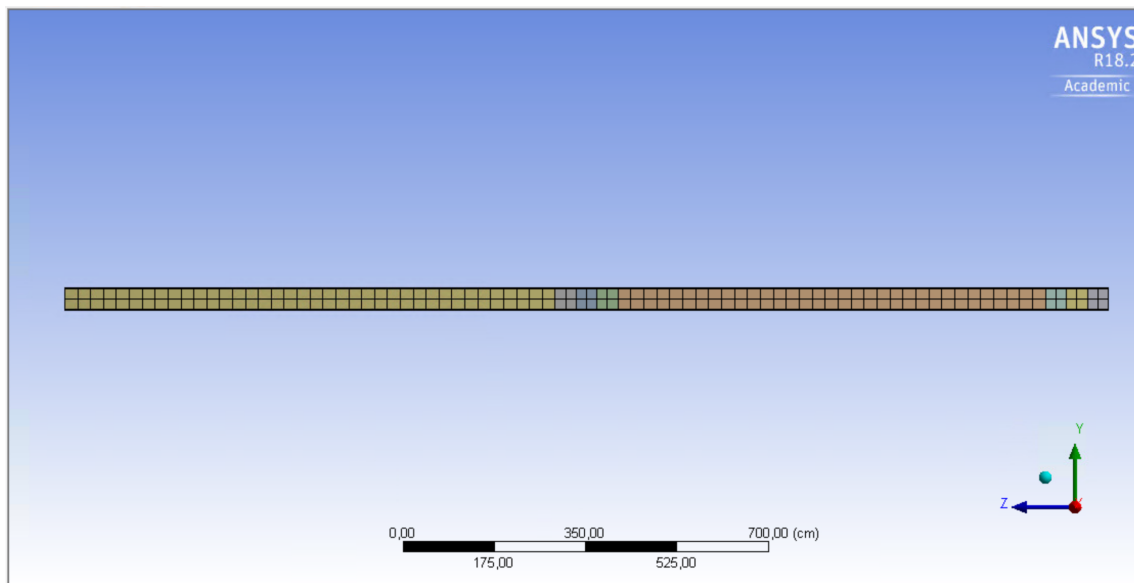


Figure 4.7: Side view spar cap - shear web assembly

4.3 Damage modelling of spar cap - shear web assembly

One end of the structure is fixed to simulate the actual working conditions. Similarly, the material property of all parts was chosen to be that of the actual wind turbine blade. The material properties of the different parts are as follows.

Table 4.1: Material properties of adhesive (Epoxy Resin)

Young's Modulus (E)	5500 MPa
Poison Ratio	0.35

Table 4.2: Material properties of PVC foam

Young's Modulus (E)	102 MPa
Poison Ratio	0.3

Table 4.3: Material properties of Epoxy- E glass (face sheet material)

Young's Modulus in X direction (E_x)	20000 MPa
Young's Modulus in Y direction (E_y)	3000 MPa
Young's Modulus in Z direction (E_z)	3000 MPa
Poison Ratio XY	0.3
Poison Ratio YZ	0.4
Poison Ratio XZ	0.3
Shear Modulus in XY direction (G_{XY})	5000 MPa
Shear Modulus in YZ direction (G_{YZ})	3000 MPa
Shear Modulus in XZ direction (G_{XZ})	5000 MPa

Table 4.4: Material properties of Epoxy- S glass (spar cap material)

Young's Modulus in X direction (E_x)	20000 MPa
Young's Modulus in Y direction (E_y)	3000 MPa
Young's Modulus in Z direction (E_z)	3000 MPa
Poison Ratio XY	0.3
Poison Ratio YZ	0.4
Poison Ratio XZ	0.3
Shear Modulus in XY direction (G_{XY})	5000 MPa
Shear Modulus in YZ direction (G_{YZ})	3000 MPa
Shear Modulus in XZ direction (G_{XZ})	5000 MPa

The element size for meshing was chosen to be about 25cm. The reasons for choosing this element size are

1. If the size of the element is below 25 cm, the size of the matrix extracted from ANSYS is big that it is difficult to use this matrix for further calculations.
2. The RAM and graphical memory of the PC was not sufficient to solve the simulation if the size of the element is below 25 cm.

The number of elements and nodes after meshing are 1476 and 2241 respectively. Using Modal Analysis, the natural frequency of the undamaged blade structure was calculated to be about

- 1st flapwise bending frequency: 0.6588 Hz ($0.6588 \times 2 \times \pi = 4.1394rad/sec$)
- 2nd flapwise bending frequency: 3.997 Hz ($3.997 \times 2 \times \pi = 25.114rad/sec$)
- 1st edgewise bending frequency: 9.261 Hz ($9.261 \times 2 \times \pi = 58.188rad/sec$)
- 2nd edgewise bending frequency: 27.66 Hz ($27.66 \times 2 \times \pi = 173.793rad/sec$)

The mass matrix M and stiffness matrix K of undamaged blade structure is extracted from ANSYS. The matrices are extracted using *DMAT [6] and *EXPORT [8] APDL command. Using extracted mass and stiffness matrices, eigenvalue and eigenvector of undamaged blade structure are calculated using *EIGEN APDL command [7]. SUBSP modal analysis [5] option is selected in ANSYS. The APDL code used is given in Appendix B. Damage is introduced into the structure in the form of microscopic damping into the material property. To incorporated damping into the structure, the loss factor obtained from experiment [51], [54] is used. The loss factor parameters (a,b and c) depends on many factors, natural frequency is once such factor. The value of a,b and c for the 1st natural frequency ($4.1394rad/sec$) is calculated for 6 different conditions. Using first order perturbation method, the value of C_1, C_2 are calculated by substituting the G_0, a, b, c and $S = j\omega$ in the equation 4.1. The material properties of the model set to C_1 , and the stiffness matrix K_1^D is extracted. The damping matrix is then given by the formula

$$K^D = K_1^D \quad (4.2)$$

The damping matrix is incorporated into the stiffness matrix using the formula

$$K_{DD} = j\omega K^D \quad (4.3)$$

$$K_{EE} = K^E + K_{DD} \quad (4.4)$$

The eigenvalue and eigenvector of the undamaged damped blade structure are calculated using *EIGEN command. DAMP [5] modal analysis option is used. K_{EE} is used in place of the stiffness matrix and zero matrix is used instead of the damping matrix. Four scenarios with three defect cases for each scenario are considered to model damage into the structure. The scenarios are

1. Damage only in top surfaces near the fixed end with 2 %, 4 %, 6 % defected area.
2. Damage only in top surfaces near mid section with 2 %, 4 %, 6 % defected area.
3. Damage in top and core surfaces near the fixed end with 2 %, 4 %, 6 % defected area.
4. Damage in top and core surfaces near mid section with 2 %, 4 %, 6 % defected area.

For each scenarios 6 damage condition is modelled, they are 50 % damage, 100 % damage, 350 % damage, 500 % damage, 650 % damage. For instance, 100 % damage means that the microscopic damping will be increased by about 0.01 compared to the damping coefficient of undamaged structure. The damping coefficient for each damage condition is given in table 4.5

Table 4.5: Loss factor and damping coefficient to represent different damaged condition

Damage Condition	Loss factor / Damping coefficient	Loss factor Parameter		
		a	b	c
Undamaged	0.01144	0.03	45	15
50 % damage	0.01523	0.04	45	15
100 % damage	0.02276	0.06	45	15
200 % damage	0.03321	0.088	45	15
350 % damage	0.04504	0.012	45	15
500 % damage	0.06325	0.017	45	15
650 % damage	0.07759	0.21	45	15

As explained earlier, the damage is incorporated into the structure in the form of microscopic damping through material property using equation 4.1. The damped material property of Undamaged structure is given in the table 4.6.

Table 4.6: Material property for loss factor 0.0114

	Foam	Adhesive	Face sheet	Spar Cap
Young's Modulus (E)	1.17 MPa	62.9 MPa		
Poison Ratio	0.35	0.3		
Young's Modulus in X direction (E_x)			229 MPa	229 MPa
Young's Modulus in Y direction (E_y)			34.3 MPa	34.3 MPa
Young's Modulus in Z direction (E_z)			34.3 MPa	34.3 MPa
Poison Ratio XY			0.3	0.3
Poison Ratio YZ			0.4	0.4
Poison Ratio XZ			0.3	0.3
Shear Modulus in XY direction (G_{XY})			57.2 MPa	57.2 MPa
Shear Modulus in YZ direction (G_{YZ})			44.0 MPa	44.0 MPa
Shear Modulus in XZ direction (G_{XZ})			57.2 MPa	57.2 MPa

The material property of 50 % damaged structure is given in the table 4.7. 50 % damage means that the damping coefficient is increased by 0.015 compared to undamaged undamped material property.

Table 4.7: Material property for loss factor 0.0152

	Foam	Adhesive	Face sheet	Spar Cap
Young's Modulus (E)	1.55 MPa	83.7 MPa		
Poison Ratio	0.35	0.3		
Young's Modulus in X direction (E_x)			305 MPa	305 MPa
Young's Modulus in Y direction (E_y)			45.7 MPa	45.7 MPa
Young's Modulus in Z direction (E_z)			45.7 MPa	45.7 MPa
Poison Ratio XY			0.3	0.3
Poison Ratio YZ			0.4	0.4
Poison Ratio XZ			0.3	0.3
Shear Modulus in XY direction (G_{XY})			76.1 MPa	76.1 MPa
Shear Modulus in YZ direction (G_{YZ})			58.6 MPa	58.6 MPa
Shear Modulus in XZ direction (G_{XZ})			76.1 MPa	76.1 MPa

The material property of 100 % damaged structure is given in the table 4.8. 100 % damage means that the damping coefficient is increased by 0.02 compared to undamaged undamped material property.

Table 4.8: Material property for loss factor 0.0227

	Foam	Adhesive	Face sheet	Spar Cap
Young's Modulus (E)	2.32 MPa	125 MPa		
Poison Ratio	0.35	0.3		
Young's Modulus in X direction (E_x)			455 MPa	455 MPa
Young's Modulus in Y direction (E_y)			68.3 MPa	68.3 MPa
Young's Modulus in Z direction (E_z)			68.3 MPa	68.3 MPa
Poison Ratio XY			0.3	0.3
Poison Ratio YZ			0.4	0.4
Poison Ratio XZ			0.3	0.3
Shear Modulus in XY direction (G_{XY})			114 MPa	114 MPa
Shear Modulus in YZ direction (G_{YZ})			87.5 MPa	87.5 MPa
Shear Modulus in XZ direction (G_{XZ})			114 MPa	114 MPa

The material property of 200 % damaged structure is given in the table 4.9. 200 % damage means that the damping coefficient is increased by 0.03 compared to undamaged undamped material property.

Table 4.9: Material property for loss factor 0.0332

	Foam	Adhesive	Face sheet	Spar Cap
Young's Modulus (E)	3.39 MPa	183 MPa		
Poison Ratio	0.35	0.3		
Young's Modulus in X direction (E_x)			664 MPa	664 MPa
Young's Modulus in Y direction (E_y)			99.6 MPa	99.6 MPa
Young's Modulus in Z direction (E_z)			99.6 MPa	99.6 MPa
Poison Ratio XY			0.3	0.3
Poison Ratio YZ			0.4	0.4
Poison Ratio XZ			0.3	0.3
Shear Modulus in XY direction (G_{XY})			166 MPa	166 MPa
Shear Modulus in YZ direction (G_{YZ})			128 MPa	128 MPa
Shear Modulus in XZ direction (G_{XZ})			166 MPa	166 MPa

The material property of 350 % damaged structure is given in the table 4.10. 350 % damage means that the damping coefficient is increased by 0.045 compared to undamaged undamped material property.

Table 4.10: Material property for loss factor 0.0450

	Foam	Adhesive	Face sheet	Spar Cap
Young's Modulus (E)	4.59 MPa	248 MPa		
Poison Ratio	0.35	0.3		
Young's Modulus in X direction (E_x)			901 MPa	901 MPa
Young's Modulus in Y direction (E_y)			135 MPa	135 MPa
Young's Modulus in Z direction (E_z)			135 MPa	135 MPa
Poison Ratio XY			0.3	0.3
Poison Ratio YZ			0.4	0.4
Poison Ratio XZ			0.3	0.3
Shear Modulus in XY direction (G_{XY})			225 MPa	225 MPa
Shear Modulus in YZ direction (G_{YZ})			173 MPa	173 MPa
Shear Modulus in XZ direction (G_{XZ})			225 MPa	225 MPa

The material property of 500 % damaged structure is given in the table 4.11. 500 % damage means that the damping coefficient is increased by 0.06 compared to undamaged undamped material property.

Table 4.11: Material property for loss factor 0.0632

	Foam	Adhesive	Face sheet	Spar Cap
Young's Modulus (E)	6.45 MPa	348 MPa		
Poison Ratio	0.35	0.3		
Young's Modulus in X direction (E_x)			1270 MPa	1270 MPa
Young's Modulus in Y direction (E_y)			190 MPa	190 MPa
Young's Modulus in Z direction (E_z)			190 MPa	190 MPa
Poison Ratio XY			0.3	0.3
Poison Ratio YZ			0.4	0.4
Poison Ratio XZ			0.3	0.3
Shear Modulus in XY direction (G_{XY})			316 MPa	316 MPa
Shear Modulus in YZ direction (G_{YZ})			243 MPa	243 MPa
Shear Modulus in XZ direction (G_{XZ})			316 MPa	316 MPa

The material property of 650 % damaged structure is given in the table 4.12. 650 % damage means that the damping coefficient is increased by 0.075 compared to undamaged undamped material property.

Table 4.12: Material property for loss factor 0.0776

	Foam	Adhesive	Face sheet	Spar Cap
Young's Modulus (E)	7.91 MPa	427 MPa		
Poison Ratio	0.35	0.3		
Young's Modulus in X direction (E_x)			1550 MPa	1550 MPa
Young's Modulus in Y direction (E_y)			233 MPa	233 MPa
Young's Modulus in Z direction (E_z)			233 MPa	233 MPa
Poison Ratio XY			0.3	0.3
Poison Ratio YZ			0.4	0.4
Poison Ratio XZ			0.3	0.3
Shear Modulus in XY direction (G_{XY})			388 MPa	388 MPa
Shear Modulus in YZ direction (G_{YZ})			298 MPa	298 MPa
Shear Modulus in XZ direction (G_{XZ})			388 MPa	388 MPa

4.3.1 Scenario 1: Damage only in top surfaces near fixed end with 2 %, 4 %, 6 % defected area

To model the damaged section, undamaged and damaged surfaces are modelled separately and joined together to form a part. Damage in top surface include defect in top spar cap, top adhesive and top face sheet.

4.3.1.1 Case 1: Top surface damage near fixed end with 2 % defected area

Figure 4.8 shows the damage in top surfaces near the fixed end with 2 % damaged area. Length of the defected area is 40 cm (2 % of 20 m i.e., length of blade). Since the element size for meshing is chosen as 25 cm there are 2 defected elements in adhesive, 2 defected elements in top face sheet and 8 defected elements in top spar cap. So totally there are 12 defected elements for this case.

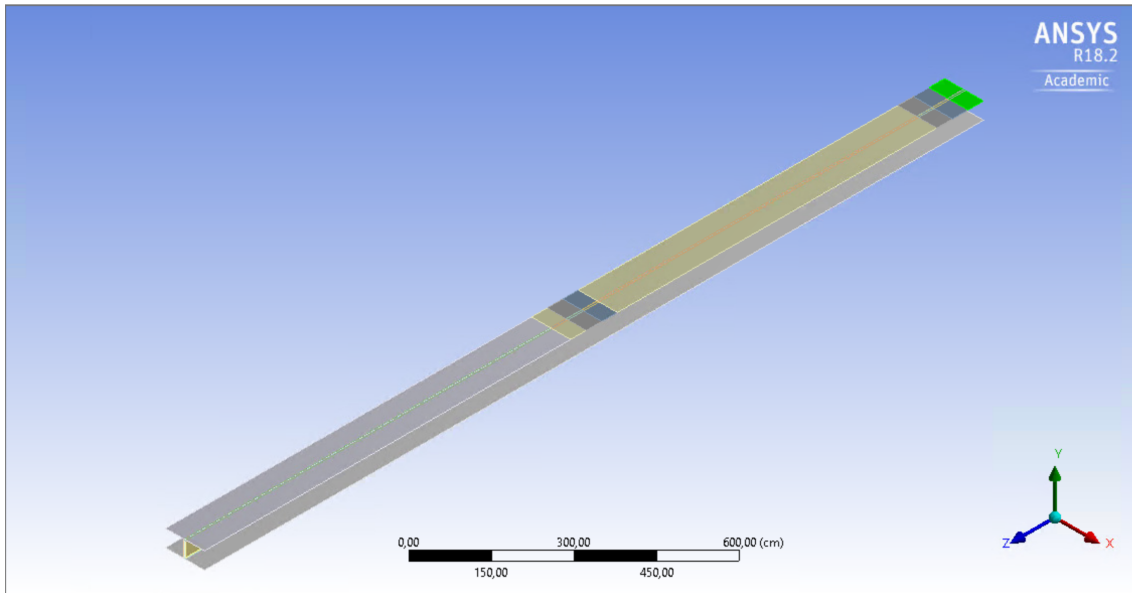


Figure 4.8: Top surface fixed end damage with 2 % defected area

4.3.1.2 Case 2: Top surface damage near the fixed end with 4 % defected area

Figure 4.9 shows the damage in top surfaces near the fixed end with 4 % damaged area. Length of the defected area is 80 cm (4 % of 20 m i.e., length of blade). There are 4 defected elements in adhesive, 4 defected elements in top face sheet and 16 defected elements in top spar cap. So totally there are 24 defected elements for this case.

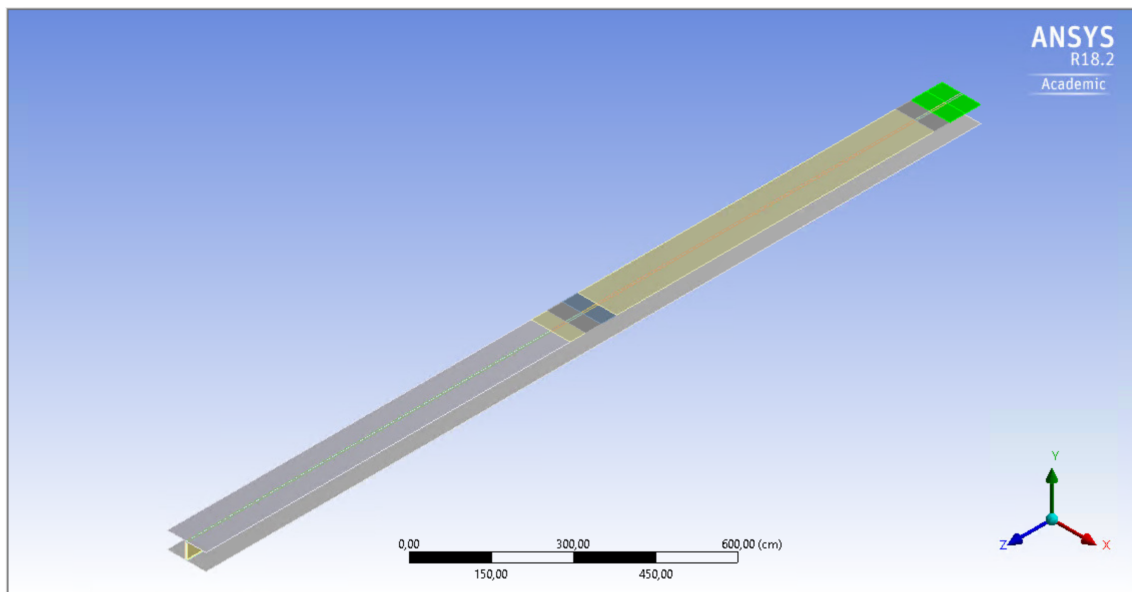


Figure 4.9: Top surface fixed end damage with 4 % defected area

4.3.1.3 Case 3: Top surface damage near the fixed end with 6 % defected area

Figure 4.10 shows the damage in top surfaces near the fixed end with 6 % damaged area. Length of the defected area is 120 cm (6 % of 20 m i.e., length of blade). There are 6 defected elements in adhesive, 6 defected elements in top face sheet and 24 defected elements in top spar cap. So totally there are 36 defected elements for this case.

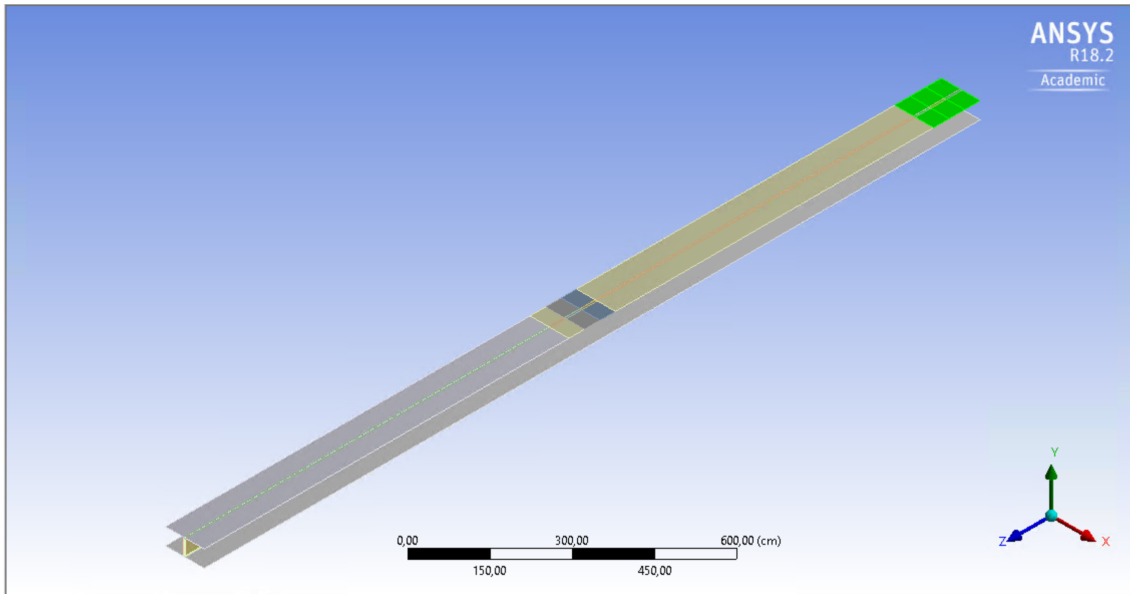


Figure 4.10: Top surface fixed end damage with 6 % defected area

4.3.2 Scenario 2: Damage only in top surfaces near mid section with 2 %, 4 %, 6 % defected area

4.3.2.1 Case 1: Top surface damage near mid section with 2 % defected area

Figure 4.11 shows the damage in top surfaces near mid section with 2 % damaged area. Length of the defected area is 40 cm (2 % of 20 m i.e., length of blade). Since the element size for meshing is chosen as 25 cm there are 2 defected elements in adhesive, 2 defected elements in top face sheet and 8 defected elements in top spar cap. So totally there are 12 defected elements for this case.

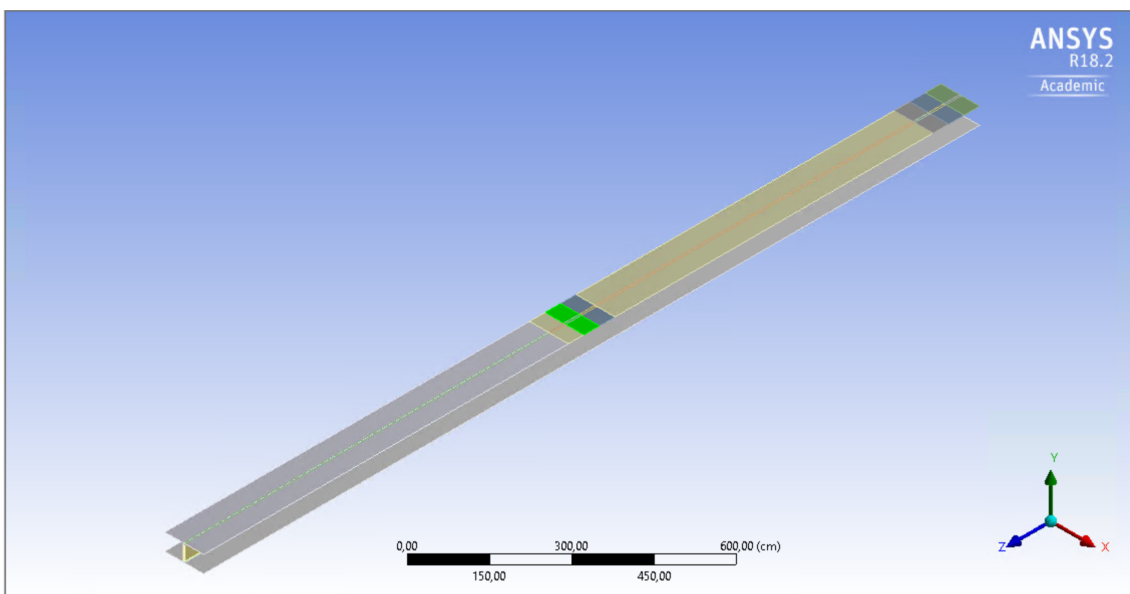


Figure 4.11: Top surface mid section damage with 2 % defected area

4.3.2.2 Case 2: Top surface damage near mid section with 4 % defected area

Figure 4.12 shows the damage in top surfaces near mid section with 4 % damaged area. Length of the defected area is 80 cm (4 % of 20 m i.e., length of blade). There are 4 defected elements in adhesive, 4 defected elements in top face sheet and 16 defected elements in top spar cap. So totally there are 24 defected elements for this case.

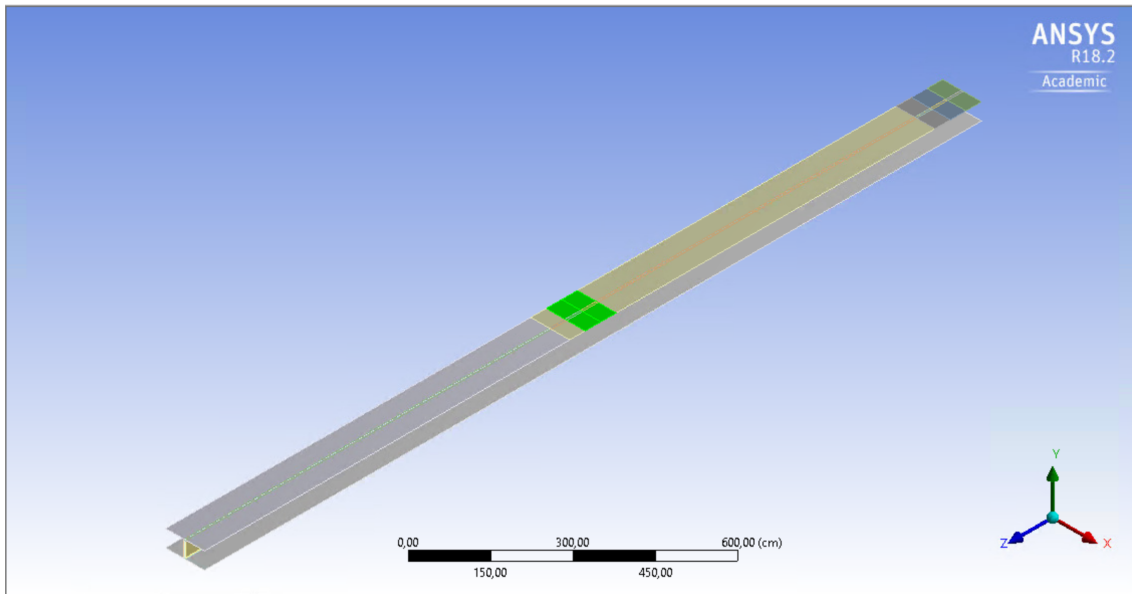


Figure 4.12: Top surface mid section damage with 4 % defected area

4.3.2.3 Case 3: Top surface damage near mid section with 6 % defected area

Figure 4.13 shows the damage in top surfaces near mid section with 6 % damaged area. Length of the defected area is 120 cm (6 % of 20 m i.e., length of blade). There are 6 defected elements in adhesive, 6 defected elements in top face sheet and 24 defected elements in top spar cap. So totally there are 36 defected elements for this case.

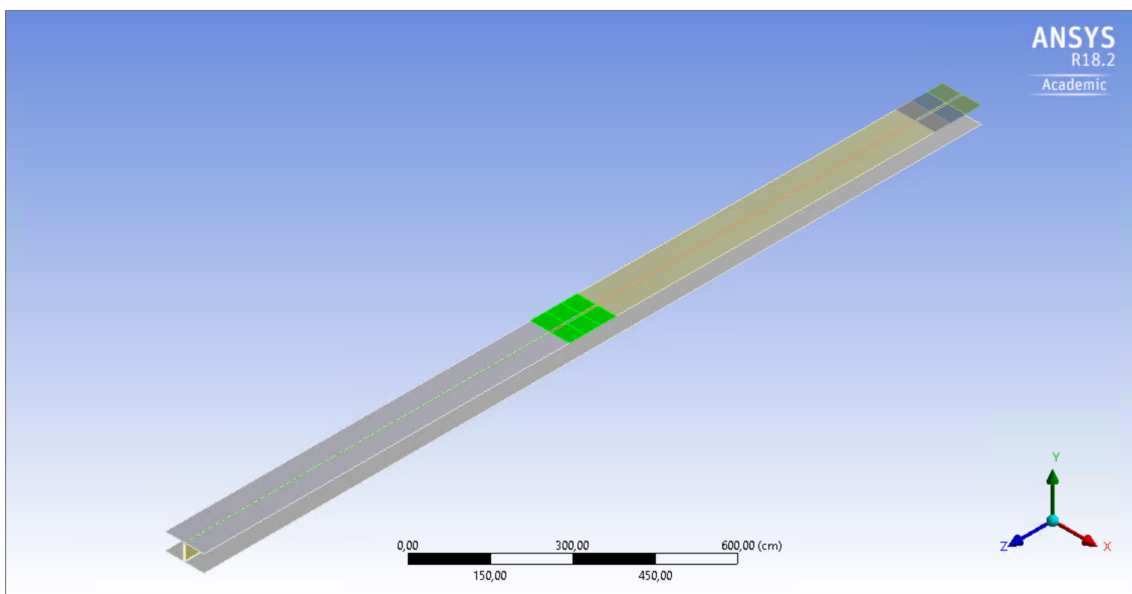


Figure 4.13: Top surface mid section damage with 6 % defected area

Damage in top and core surface includes defect in top spar cap, top adhesive, top, left and right face sheet and foam.

4.3.3 Scenario 3: Damage in top and core surfaces near fixed end with 2 %, 4 %, 6 % defected area

4.3.3.1 Case 1: Top and core surface damage near the fixed end with 2 % defected area

Figure 4.14 shows the damage in top and core surfaces near the fixed end with 2 % damaged area. Length of the defected area is 40 cm (2 % of 20 m i.e., length of blade). Since the element size for meshing is chosen as 25 cm, there are 2 defected elements in adhesive and top face sheet surface each, 8 defected elements in top spar cap and 4 defected elements in left face sheet, right face sheet and foam each. So totally there are 24 defected elements for this case.

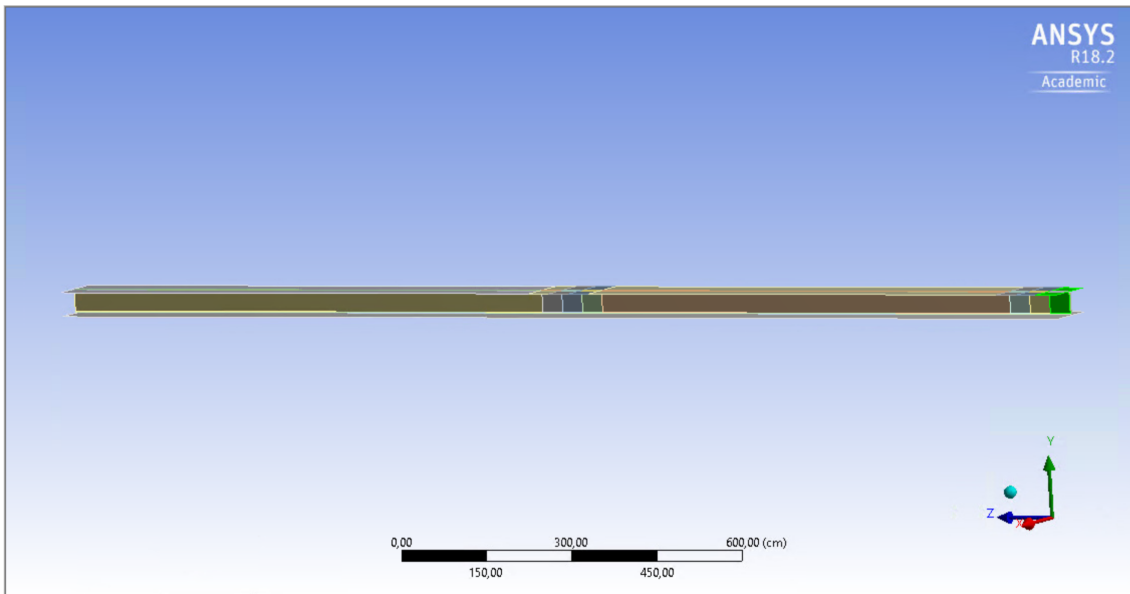


Figure 4.14: Top and core surfaces fixed end damage with 2 % defected area

4.3.3.2 Case 2: Top and core surface damage near the fixed end with 4 % defected area

Figure 4.15 shows the damage in top and core surfaces near the fixed end with 4 % damaged area. Length of the defected area is 80 cm (4 % of 20 m i.e., length of blade). There are 4 defected elements in adhesive and top face sheet surface each, 16 defected elements in top spar cap and 8 defected elements in left face sheet, right face sheet and foam each. So totally there are 48 defected elements for this case.

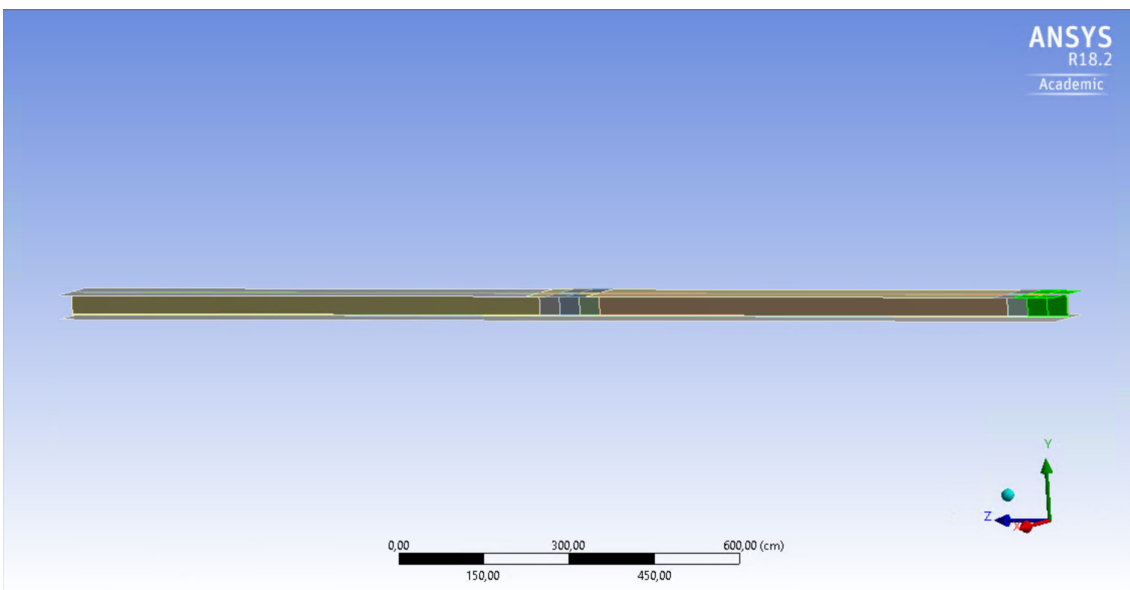


Figure 4.15: Top and core surface fixed end damage with 4 % defected area

4.3.3.3 Case 3: Top and core surface damage near the fixed end with 6 % defected area

Figure 4.16 shows the damage in top and core surfaces near the fixed end with 6 % damaged area. Length of the defected area is 120 cm (6 % of 20 m i.e., length of blade). There are 6 defected elements in adhesive and top face sheet surface each, 24 defected elements in top spar cap and 12 defected elements in left face sheet, right face sheet and foam each. So totally there are 72 defected elements for this case.

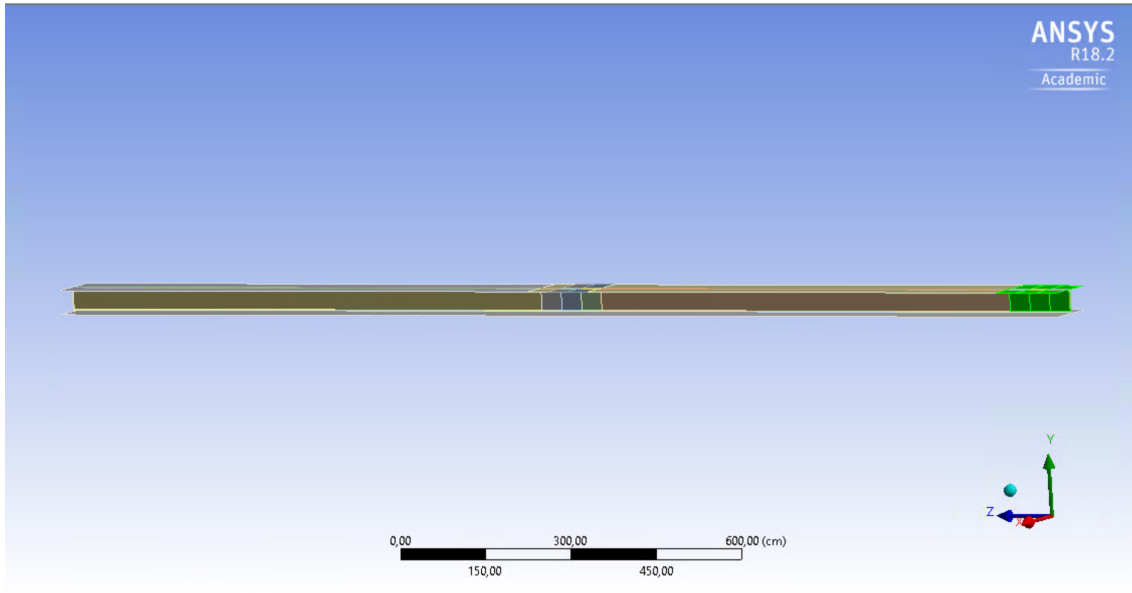


Figure 4.16: Top and core surface fixed end damage with 6 % defected area

4.3.4 Scenario 4: Damage in top and core surfaces near mid section with 2 %, 4 %, 6 % defected area

4.3.4.1 Case 1: Top and core surface damage near mid section with 2 % defected area

Figure 4.17 shows the damage in top and core surfaces near the midsection with 2 % damaged area. Length of the defected area is 40 cm (2 % of 20 m i.e., length of blade). Since the element size for meshing is chosen as 25 cm there are 2 defected elements in adhesive and top face sheet surface each, 8 defected elements in top spar cap and 4 defected elements in left face sheet, right face sheet and Foam each. So totally there are 24 defected elements for this case.



Figure 4.17: Top and core surface mid section damage with 2 % defected area

4.3.4.2 Case 2: Top and core surface damage near mid section with 4 % defected area

Figure 4.18 shows the damage in top and core surfaces near the midsection with 4 % damaged area. Length of the defected area is 80 cm (4 % of 20 m i.e., length of blade). There are 4 defected elements in adhesive and top face sheet surface each, 16 defected elements in top spar cap and 8 defected elements in left face sheet, right face sheet and Foam each. So totally there are 48 defected elements for this case.

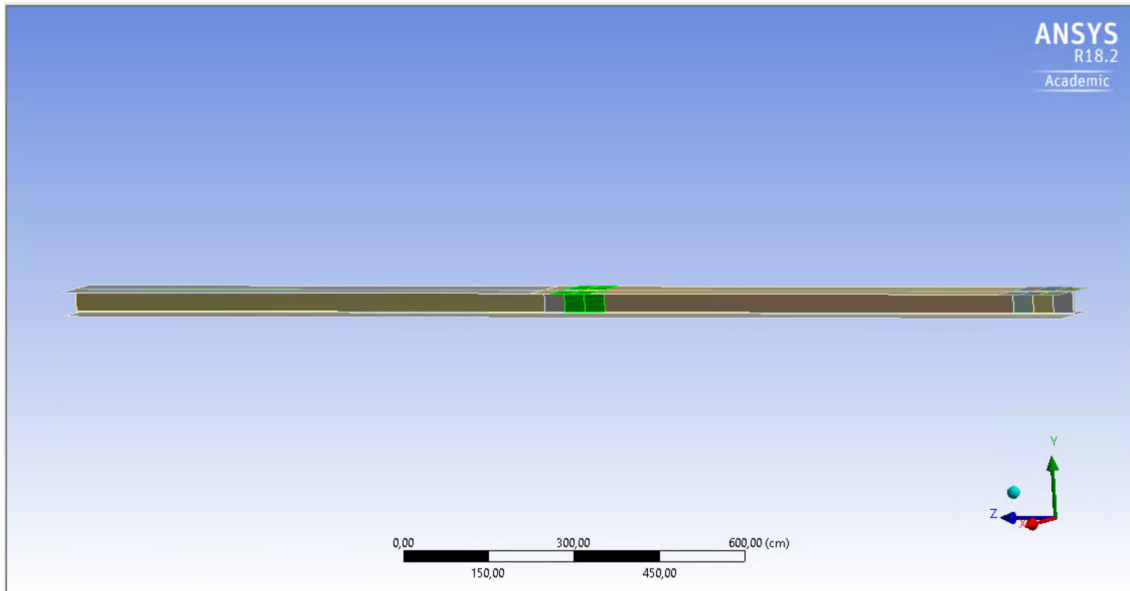


Figure 4.18: Top and core surface mid section damage with 4 % defected area

4.3.4.3 Case 3: Top and core surface damage near mid section with 6 % defected area

Figure 4.19 shows the damage in top and core surfaces near the midsection with 6 % damaged area. Length of the defected area is 120 cm (6 % of 20 m i.e., length of blade). There are 6 defected elements in adhesive and top face sheet surface each, 24 defected elements in top spar cap and 12 defected elements in left face sheet, right face sheet and Foam each. So totally there are 72 defected elements for this case.



Figure 4.19: Top and core surface mid section damage with 6 % defected area

To identify the damaged elements or node, the material property of the undamaged structure is changed to damped material properties as given in tables 4.7 - 4.12 for each scenario and the damped mass matrix and

stiffness matrix are extracted from ANSYS using *DMAT command and the eigenvalue and eigenvector is calculated using *EIGEN command and modal analysis option is chosen as DAMP.

The number of defected elements for different damage scenario is summarized in the below table for easy comparison and understanding.

Table 4.13: Number of defected elements for each scenario

		Length of Defected area	Top Spar cap	Top Adhesive	Face sheet			Foam	Total
					Top	Left	Right		
Scenario 1	Case 1	40 cm	8	2	2	-	-	-	12
	Case 2	80 cm	16	4	4	-	-	-	24
	Case 3	120 cm	24	6	6	-	-	-	36
Scenario 2	Case 1	40 cm	8	2	2	-	-	-	12
	Case 2	80 cm	16	4	4	-	-	-	24
	Case 3	120 cm	24	6	6	-	-	-	36
Scenario 3	Case 1	40 cm	8	2	2	4	4	4	24
	Case 2	80 cm	16	4	4	8	8	8	48
	Case 3	120 cm	24	6	6	12	12	12	72
Scenario 4	Case 1	40 cm	8	2	2	4	4	4	24
	Case 2	80 cm	16	4	4	8	8	8	48
	Case 3	120 cm	24	6	6	12	12	12	72

Note:

Scenario 1 : Damage only in top surfaces near the fixed end.

Scenario 2 : Damage only in top surfaces near the mid section.

Scenario 3 : Damage in top and core surfaces near the fixed end.

Scenario 4 : Damage in top and core surfaces near the mid section.

Case 1: 2 % defected area.

Case 2: 4 % defected area.

Case 3: 6 % defected area.

5 Damage Identification and Localization

The percentage increase in modal damping of the whole structure proves that the structure is damaged. To localize the damage the eigen vector that corresponds to flapwise and edgewise frequencies is noted down. From the eigen vector, phase angle is calculated. The change in node shape is compared to find the damaged elements. The node change of element which is damaged or in the vicinity of damage will be higher compared to the nodes far away from the damage. In other words, when the structure is undamaged the change in phase angle is very minimum (almost zero). However, when the structure is damaged, the change in phase angle will be higher in place of damage and the change in phase angle will keep on reducing as one move away from defected element. Since the current technology allows one to measure the node change only in top surfaces, eigen vector of the top spar cap chosen for damage identification and localization. In this chapter, the concept used to identify and localize the defect based on the change in modal damping and node shape is explained. And the defect identification and localization of Spar cap - Shear web assembly for four different damage scenarios such as damage in only in the top surface near the fixed end and midsection with 2 %, 4 % and 6 % defected area and damage in the top and core surfaces with a defect in the fixed end and midsection with 2 %, 4 % and 6 % defected area are explained.

5.1 Damage identification and localization concept

5.1.1 Damage identification

Based on the literature review, it is evident that local damage will affect the dynamic response of the wind turbine blade. Change in the dynamic response of the wind turbine blade such as modal damping and mode shapes are used to identify and localize damage. The first approach to identify damage is based on an increase in modal damping. This index shows the dissipation of energy within the whole structure. The eigenvalue of the system S_i can be written as [51]

$$S_i = -a_i \pm jb_i \quad (5.1)$$

where, a_i and b_i are real and imaginary numbers. Then the modal damping of system can be obtained by

$$I_1 = \zeta_i = \frac{-a_i}{\omega_i} \quad (5.2)$$

where, ω_i is given by

$$\omega_i = \sqrt{a_i^2 + b_i^2} \quad (5.3)$$

For the general case of damping, ω_i can be interpreted as the damped natural frequency of mode i [53]. Local damage increases the degree of non-proportionality of the system [20], [21]. The second approach to identify damage is based on an index which shows the degree of non-proportionality of the system. One of this index can be the weight of the imaginary part of the eigen mode which is defined as [19], [54]

$$I_2 = \sum_{i=1}^n \frac{\|I_m \varphi^i\|}{n \|\varphi^i\|} \quad (5.4)$$

Where I_m is the imaginary part of mode shapes, φ^i is the i^{th} mode shapes and n is the total number of oscillatory modes in the system. The index I_1 and I_2 helps identify the damage but not in localizing the damaged elements [51].

5.1.2 Damage localization

The dissipation of energy is not uniform within the structure when it is damaged. Dissipation of energy is more in the damaged area. There will be relative increases in the degree of non-proportionality at the defected area and surrounding area. This means that the phase angle change is more at the nodes close to the damaged area, and the phase angle is less prone to change far from the damaged area. This concept is used to define the third index that helps in localizing the damage. The index is given as [51]

$$I_3(\text{node}_k) = \frac{\sum_{j=1}^m \theta_{jk}^{i^D} - \sum_{j=1}^m \theta_{jk}^{i^U}}{m\pi} \quad (5.5)$$

where $\theta_{jk}^{i^D}$ is the phase of mode shape j of node k of the damaged structure, $\theta_{jk}^{i^U}$ is the phase of mode shape j of node k of the undamaged structure, m is the degree of freedom for each node and n is the total number of oscillatory modes. To calculate the damaged index first few modes are considered.

5.2 Damage identification and localization of spar cap - shear web assembly

The steps followed to identify and localize the damage in a spar cap - shear web assembly for four different damage scenarios, damage only in the top surface near the fixed end and midsection with 2 %, 4 % and 6 % defected area and damage in the top and core surfaces with a defect in the fixed end and midsection with 2 %, 4 % and 6 % defected area are as follows. To detect the damage for each scenario, the eigenvalue and eigenvector of the structure for different microscopic damping coefficient corresponding to 1st and 2nd flapwise and edgewise frequencies are compared. The concept that the damping of the structure will increase when it is damaged is used to detect the damage. The modal damping of the structure is calculated as follows. The eigenvalue of the structure with microscopic damping coefficient of 0.01 corresponding to 1st natural frequency is $-0.01560 + 0.6589i$. The modal damping of the undamaged structure is calculated using the formula 5.2

$$\begin{aligned} I_1 &= \frac{-a_i}{\sqrt{a_i^2 + b_i^2}} \\ &= \frac{0.01560}{\sqrt{0.01560^2 + 0.6589^2}} \\ &= 0.02367 \end{aligned} \quad (5.6)$$

To localize the damage, the eigenvector that corresponds to 1st and 2nd flapwise and edgewise frequencies are noted down. From the eigenvector, the phase angle is calculated using formula

$$\theta = \tan^{-1} \left(\frac{b_i}{a_i} \right) \quad (5.7)$$

To find the damaged elements, change in node shape is compared. Node change of damaged elements or elements in the vicinity of damage will be higher than the node of elements far away from the damage. In other words, when the structure is undamaged, the change in phase angle is minimum (almost zero). However, when the structure is damaged, the change in phase angle will be higher in place of damage, and the change in phase angle will keep on reducing as one move away from the defected element. The damaged node is identified by calculating the difference between the phase angle of the element and the maximum phase angle. Formula 5.8 is used to identify the damaged elements.

$$I = [\theta - \theta_m] \quad (5.8)$$

Since the current technology allows one to measure the node change only in top surfaces, eigenvector of the top spar cap chosen for damage identification and localization.

The modal damping increase for 6 different microscopic damping coefficient (damage condition) is calculated using formula 5.2 for different scenarios. The eigenvector of first natural frequency is used for modal damping calculation in each scenario. The percentage increase of damping of the structure is calculated using formula

$$\%increase = \left(\frac{I_{12} - I_1}{I_1} \right) * 100 \quad (5.9)$$

For simplicity, change in phase angle calculation, and plots for each element are done for microscopic damping coefficients 0.02, 0.045 and 0.075, among which plots corresponding to damping coefficient 0.075 is given below for each scenario. Plots of other damping coefficients are given in Appendix A. Also, in the plots corresponding to 2nd flapwise and edgewise bending frequency, there is a sudden rise in phase angle (noise) around elements 60 to 70. The reason for this sharp change in phase angle is that the real part of the eigenvector is smaller for these elements, so dividing the imaginary part with a small value for calculating the phase angle results in an unexpected rise in phase angle. Also, deflection in these nodes is very small. So, when divided by a small value results in the unusual peak in phase angle around these nodes. Since this rise happens at elements which were not modelled as defected one, this change can be neglected. [Note: Only the plots of microscopic damping coefficient 0.075 is given here. Plots of other damping coefficients are given in Appendix A]

5.2.1 Scenario 1: Damage only in top surfaces near fixed end with 2 %, 4 %, 6 % defected area

5.2.1.1 Case 1: Top surface damage near fixed end with 2 % defected area

The modal damping calculation and percent increase in damping of structure for case 1 for 6 different microscopic damping coefficient (damage condition) is given below.

Table 5.1: Modal damping and percentage increase of damping for scenario 1 case 1

Damping Coefficient	Eigen Value	Modal Damping	% Increasing in damping
0.015	-0.01580 + 0.6590i	0.02397	1.267
0.02	-0.01619 + 0.6590i	0.02456	3.76
0.03	-0.01673 + 0.6591i	0.02537	7.18
0.045	-0.01733 + 0.6592i	0.02628	11.03
0.06	-0.01820 + 0.6595i	0.02759	16.56
0.075	-0.01882 + 0.6598i	0.02851	20.45

The percentage increase in modal damping of the whole structure proves that it is damaged. For simplicity, the change in Phase angle of elements and damaged node identification plots for 1st and 2nd flapwise and edgewise frequencies are calculated and plotted for microscopic damping coefficient 0.075 and are given below.

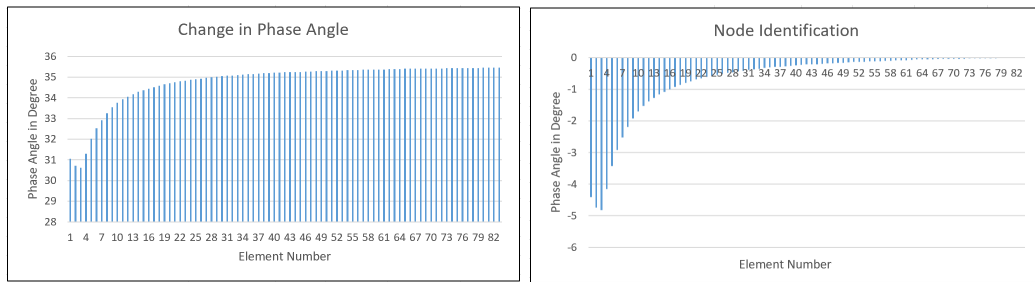


Figure 5.1: Scenario 1 case 1 650 % damage 1st flapwise bending frequency

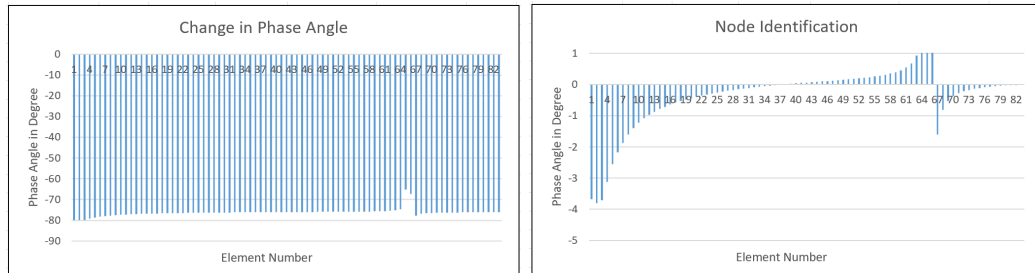


Figure 5.2: Scenario 1 case 1 650 % damage 2nd flapwise bending frequency

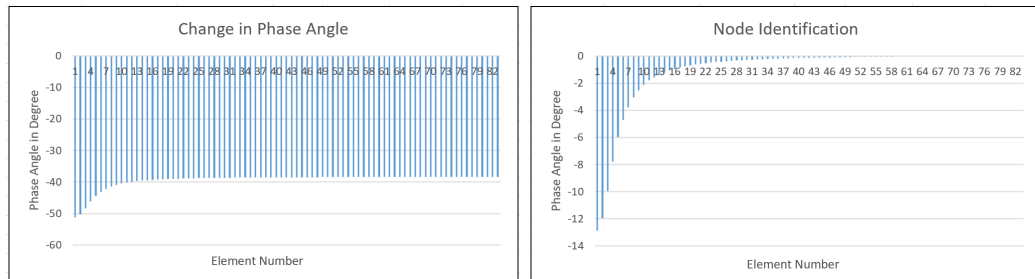


Figure 5.3: Scenario 1 case 1 650 % damage 1st edgewise bending frequency

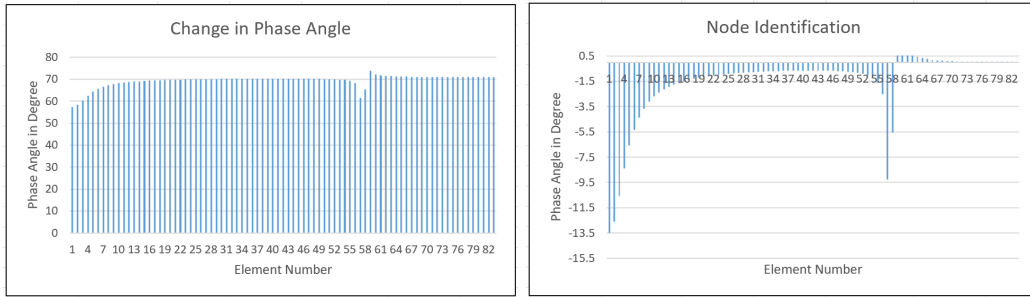


Figure 5.4: Scenario 1 case 1 650 % damage 2nd edgewise bending frequency

From the above figures, the change in phase angle is more in first 2 elements, which in turn indicates that these elements are defected.

5.2.1.2 Case 2: Top surface damage near fixed end with 4 % defected area

The modal damping calculation and percent increase in damping of structure for case 2 for 6 different microscopic damping coefficient (damage condition) is given below.

Table 5.2: Modal damping and percentage increase of damping for Scenario 1 case 2

Damping Coefficient	Eigen Value	Modal Damping	% Increasing in damping
0.015	-0.01598 + 0.6590i	0.02424	2.41
0.02	-0.01673 + 0.6590i	0.02538	7.22
0.03	-0.01776 + 0.6592i	0.02693	13.77
0.045	-0.01890 + 0.6594i	0.02865	21.04
0.06	-0.02059 + 0.6600i	0.03118	31.73
0.075	-0.02179 + 0.6605i	0.03297	39.29

The change in Phase angle of elements and damaged node identification plots for 1st and 2nd flapwise and edgewise frequencies for microscopic damping coefficient 0.075 is given below.

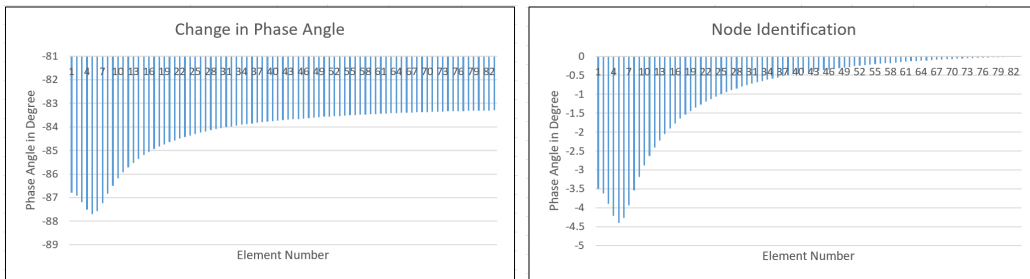


Figure 5.5: Scenario 1 case 2 650 % damage 1st flapwise bending frequency

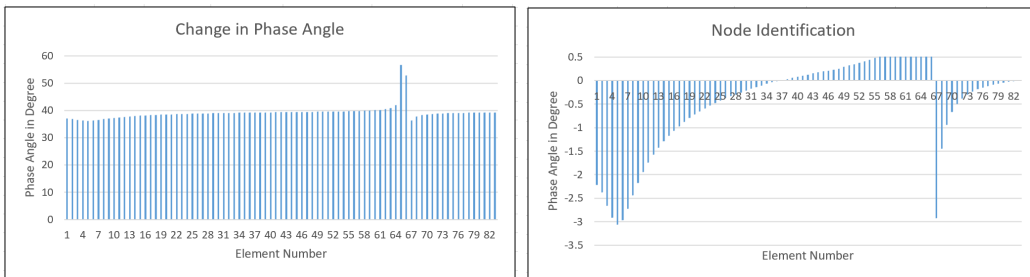


Figure 5.6: Scenario 1 case 2 650 % damage 2nd flapwise bending frequency

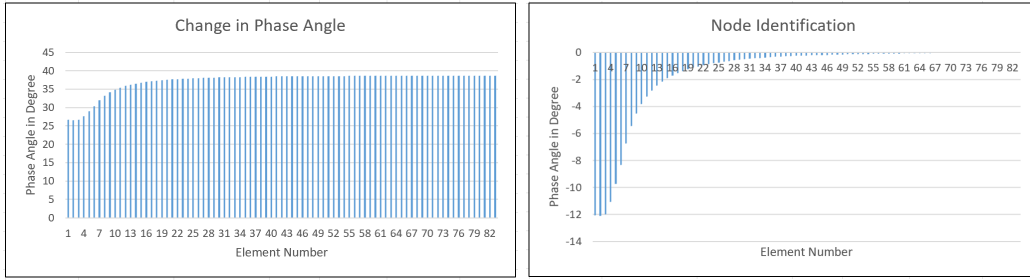


Figure 5.7: Scenario 1 case 2 650 % damage 1st edgewise bending frequency

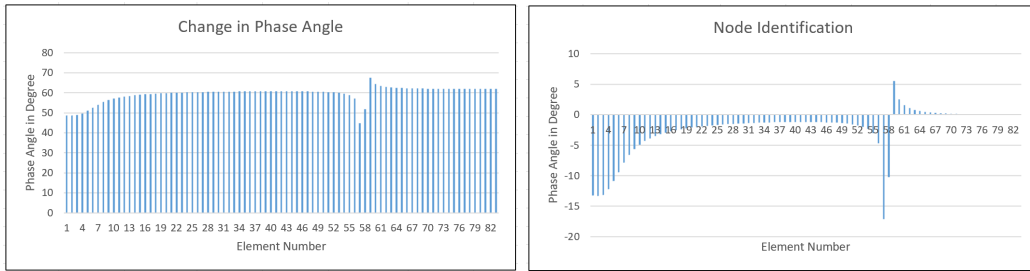


Figure 5.8: Scenario 1 case 2 650 % damage 2nd edgewise bending frequency

From the above figures, the change in phase angle is more in first 4 elements which in turn indicates that these elements are defected.

5.2.1.3 Case 3: Top surface damage near fixed end with 6 % defected area

The modal damping calculation and percent increase in damping of structure for case 3 for 6 different microscopic damping coefficient (damage condition) is given below.

Table 5.3: Modal damping and percentage increase of damping for scenario 1 case 3

Damping Coefficient	Eigen Value	Modal Damping	% Increasing in damping
0.015	-0.01615 + 0.6590i	0.02450	3.51
0.02	-0.01723 + 0.6590i	0.02614	10.44
0.03	-0.01872 + 0.6593i	0.02838	19.90
0.045	-0.02036 + 0.6596i	0.03085	30.33
0.06	-0.02280 + 0.6604i	0.03450	45.75
0.075	-0.02455 + 0.6612i	0.03710	56.74

The change in phase angle of elements and damaged node identification plots for 1st and 2nd flapwise and edgewise frequencies for microscopic damping coefficient 0.075 is given below.

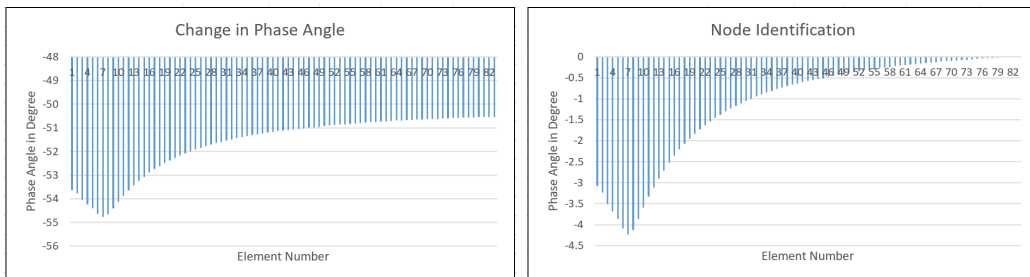


Figure 5.9: Scenario 1 case 3 650 % damage 1st flapwise bending frequency

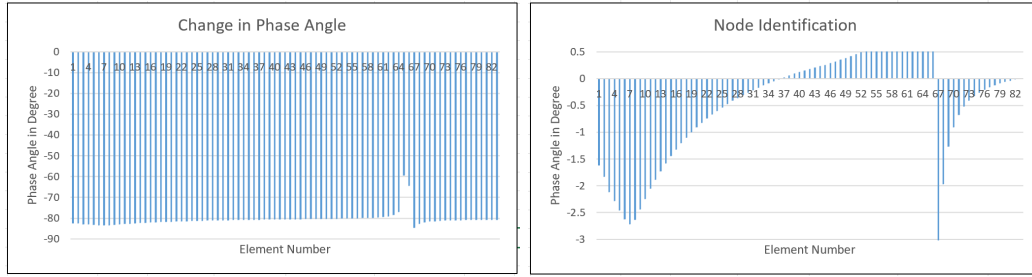


Figure 5.10: Scenario 1 case 3 650 % damage 2nd flapwise bending frequency

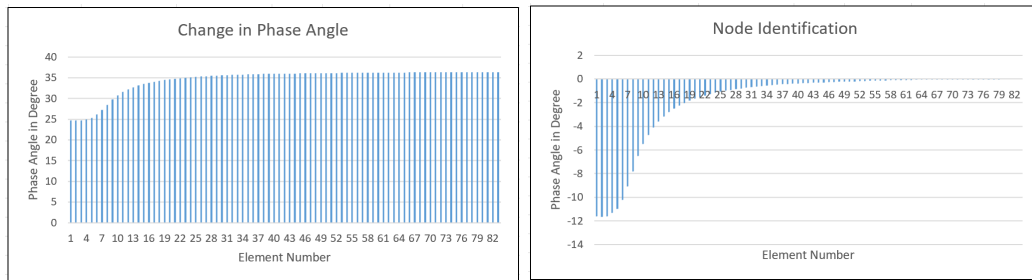


Figure 5.11: Scenario 1 case 3 650 % damage 1st edgewise bending frequency

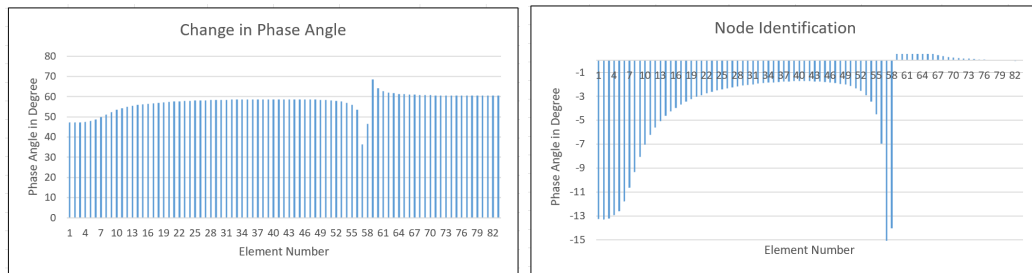


Figure 5.12: Scenario 1 case 3 650 % damage 2nd edgewise bending frequency

From the above figures, the change in phase angle is more in first 6 elements which indicates that these elements are defected.

5.2.2 Scenario 2: Damage only in top surfaces near mid section with 2 %, 4 %, 6 % defected area

5.2.2.1 Case 1: Top surface damage near mid section with 2 % defected area

The modal damping calculation and percent increase in damping of structure for case 1 for 6 different microscopic damping coefficient (damage condition) is given below.

Table 5.4: Modal damping and percentage increase of damping for Scenario 2 case 1

Damping Coefficient	Eigen Value	Modal Damping	% Increasing in damping
0.015	-0.01563 + 0.6589i	0.02371	0.17
0.02	-0.01567 + 0.6589i	0.02378	0.46
0.03	-0.01573 + 0.6590i	0.02386	0.80
0.045	-0.01580 + 0.6590i	0.02397	1.27
0.06	-0.01589 + 0.6590i	0.02411	1.86
0.075	-0.01596 + 0.6590i	0.02421	2.28

The change in Phase angle of elements and damaged node identification plots for 1st and 2nd flapwise and

edgewise frequencies for microscopic damping coefficient 0.075 is given below.

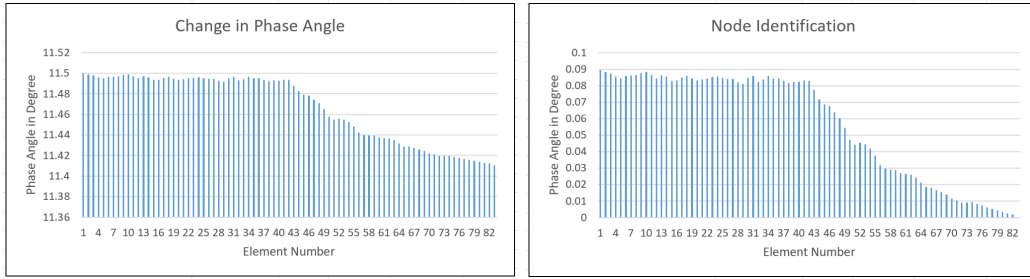


Figure 5.13: Scenario 2 case 1 650 % damage 1st flapwise bending frequency

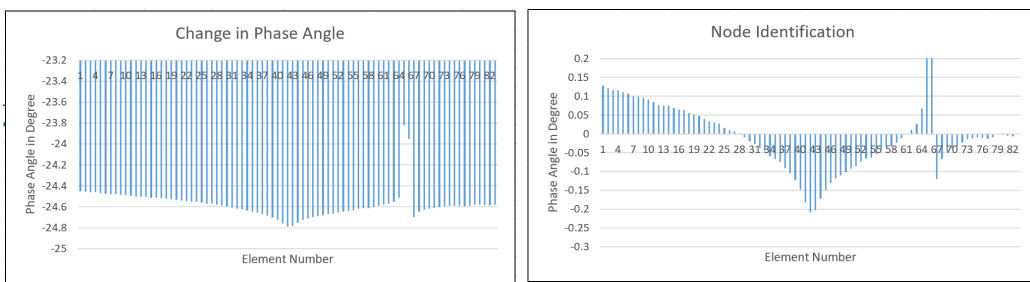


Figure 5.14: Scenario 2 case 1 650 % damage 2nd flapwise bending frequency

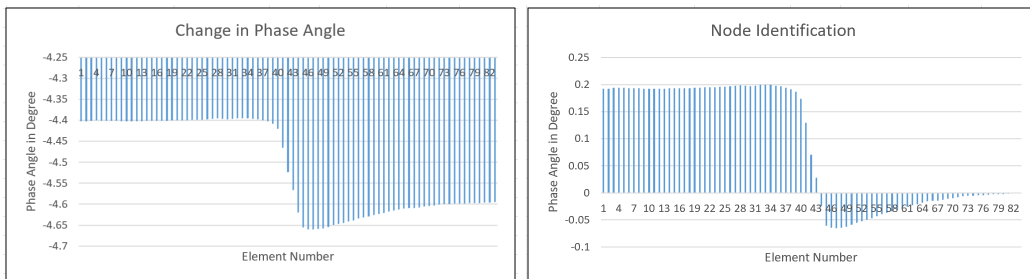


Figure 5.15: Scenario 2 case 1 650 % damage 1st edgewise bending frequency

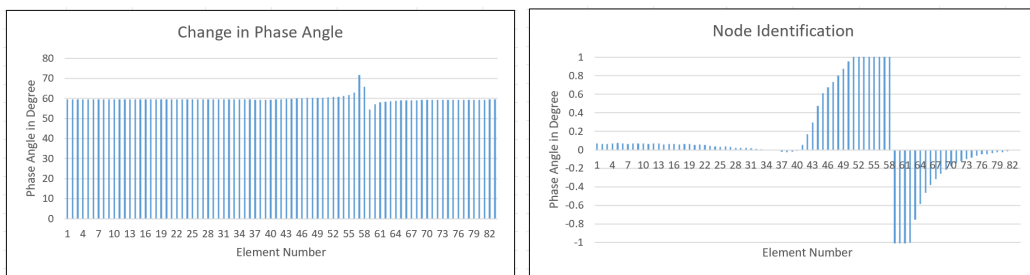


Figure 5.16: Scenario 2 case 1 650 % damage 2nd edgewise bending frequency

From the figure 5.14, the change in phase angle is more in elements 42 and 43 (2 elements) this shows that these elements are defected.

5.2.2.2 Case 2: Top surface damage near mid section with 4 % defected area

The modal damping calculation and percent increase in damping of structure for case 2 for 6 different microscopic damping coefficient (damage condition) is given below.

Table 5.5: Modal damping and percentage increase of damping for scenario 2 case 2

Damping Coefficient	Eigen Value	Modal Damping	% Increasing in damping
0.015	-0.01565 + 0.6589i	0.02375	0.34
0.02	-0.01575 + 0.6590i	0.02389	0.93
0.03	-0.01587 + 0.6590i	0.02407	1.69
0.045	-0.01602 + 0.6590i	0.02430	2.66
0.06	-0.01623 + 0.6591i	0.02462	4.01
0.075	-0.01638 + 0.6592i	0.02484	4.94

The change in phase angle of elements and damaged node identification plots for 1st and 2nd flapwise and edgewise frequencies for microscopic damping coefficient 0.075 is given below.

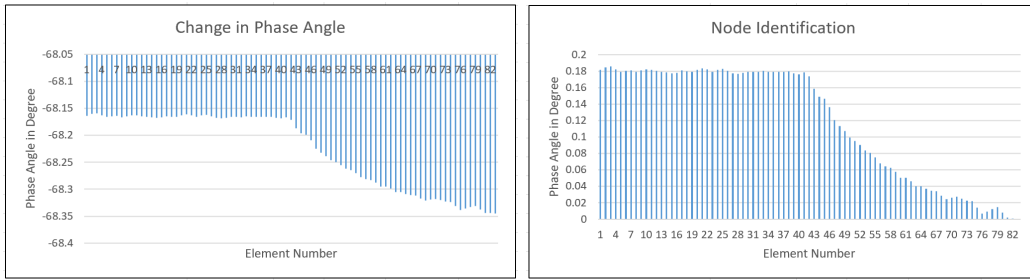


Figure 5.17: Scenario 2 case 2 650 % damage 1st flapwise bending frequency

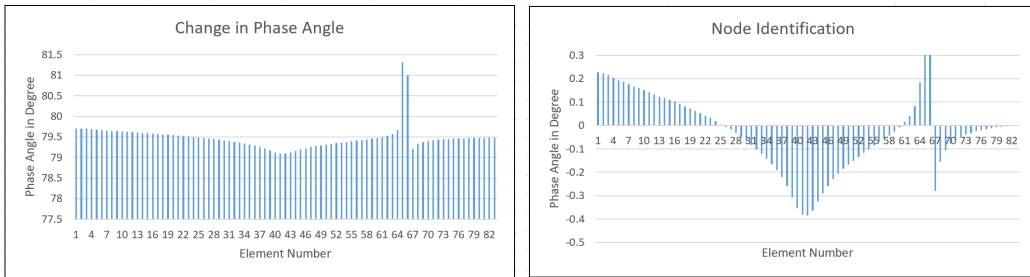


Figure 5.18: Scenario 2 case 2 650 % damage 2nd flapwise bending frequency

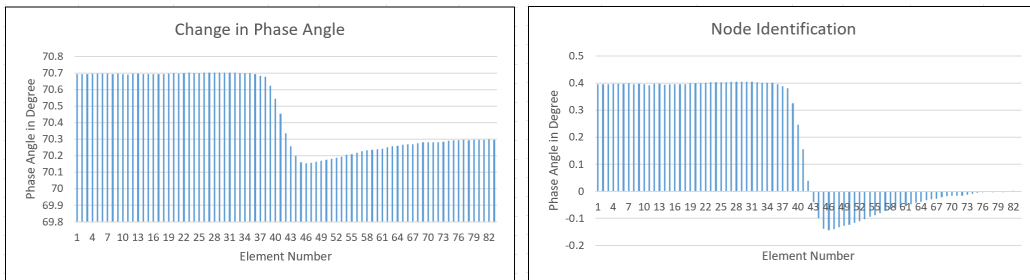


Figure 5.19: Scenario 2 case 2 650 % damage 1st edgewise bending frequency

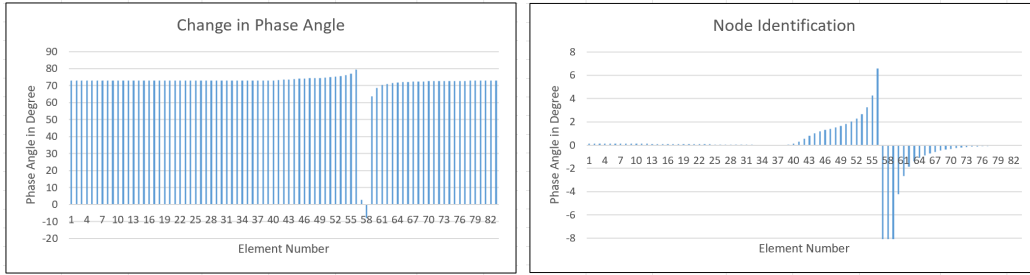


Figure 5.20: Scenario 2 case 2 650 % damage 2nd edgewise bending frequency

From figure 5.18, the change in phase angle is more in elements 40, 41, 42 and 43 (4 elements) this shows that these elements are defected.

5.2.2.3 Case 3: Top surface damage near mid section with 6 % defected area

The modal damping calculation and percent increase in damping of structure for case 3 for 6 different microscopic damping coefficient (damage condition) is given below.

Table 5.6: Modal damping and percentage increase of damping for scenario 2 case 3

Damping Coefficient	Eigen Value	Modal Damping	% Increasing in damping
0.015	-0.01567 + 0.6589i	0.02378	0.46
0.02	-0.01580 + 0.6590i	0.02397	1.27
0.03	-0.01598 + 0.6590i	0.02424	2.41
0.045	-0.01619 + 0.6590i	0.02456	3.76
0.06	-0.01648 + 0.6591i	0.02500	5.62
0.075	-0.01669 + 0.6592i	0.02531	6.93

The change in Phase angle of elements and damaged node identification plots for 1st and 2nd flapwise and edgewise frequencies for microscopic damping coefficient 0.075 is given below.

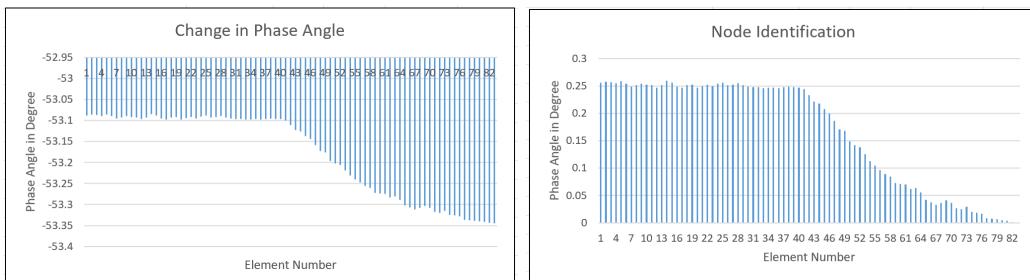


Figure 5.21: Scenario 2 case 3 650 % damage 1st flapwise bending frequency

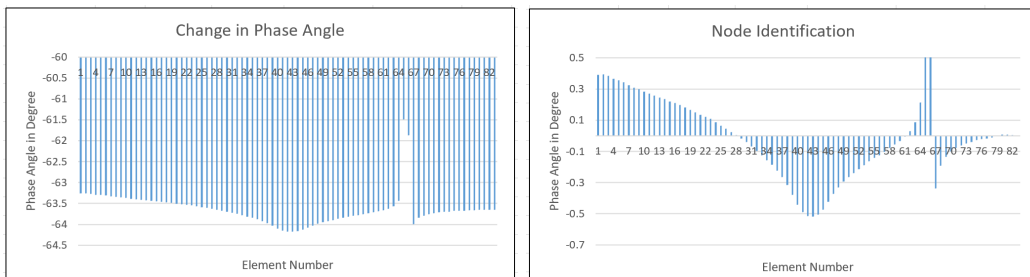


Figure 5.22: Scenario 2 case 3 650 % damage 2nd flapwise bending frequency

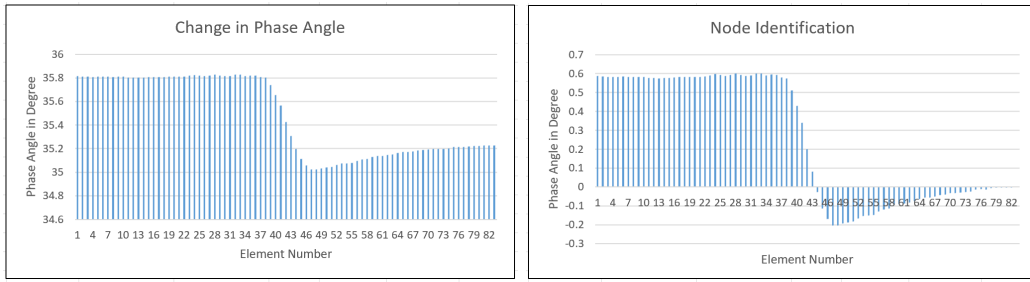


Figure 5.23: Scenario 2 case 3 650 % damage 1st edgewise bending frequency

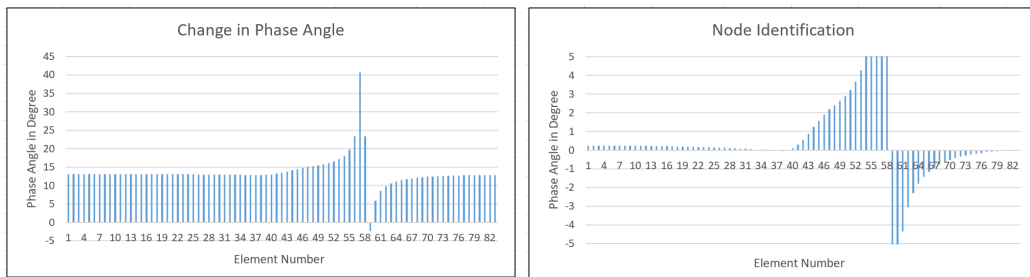


Figure 5.24: Scenario 2 case 3 650 % damage 2nd edgewise bending frequency

From figure 5.22, the change in phase angle is more in elements 40, 41, 42, 43,44 and 45 (6 elements) this shows that these elements are defected.

5.2.3 Scenario 3: Damage in top and core surfaces near fixed end with 2 %, 4 %, 6 % defected area

5.2.3.1 Case 1: Top and core surface damage near fixed end with 2 % defected area

The modal damping calculation and percent increase in damping of structure for case 1 for 6 different microscopic damping coefficient (damage condition) is given below.

Table 5.7: Modal damping and percentage increase of damping for scenario 3 case 1

Damping Coefficient	Eigen Value	Modal Damping	% Increasing in damping
0.015	-0.01586 + 0.6590i	0.02406	1.65
0.02	-0.01635 + 0.6590i	0.02480	4.77
0.03	-0.01703 + 0.6591i	0.02583	9.13
0.045	-0.01779 + 0.6592i	0.02698	13.98
0.06	-0.01892 + 0.6596i	0.02867	21.12
0.075	-0.01972 + 0.6599i	0.02987	26.19

The change in Phase angle of elements and damaged node identification plots for 1st and 2nd flapwise and edgewise frequencies for microscopic damping coefficient 0.075 is given below.

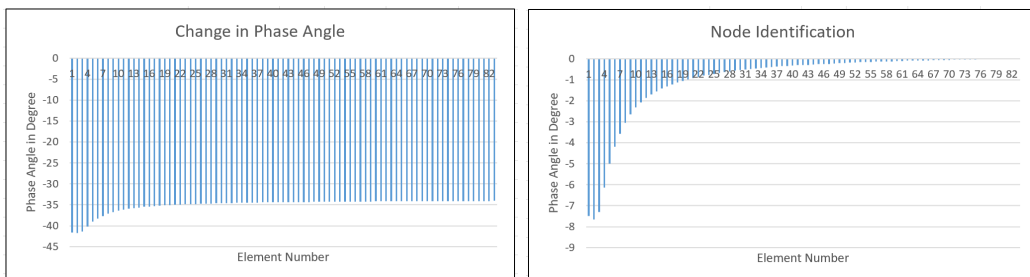


Figure 5.25: Scenario 3 case 1 650 % damage 1st flapwise bending frequency

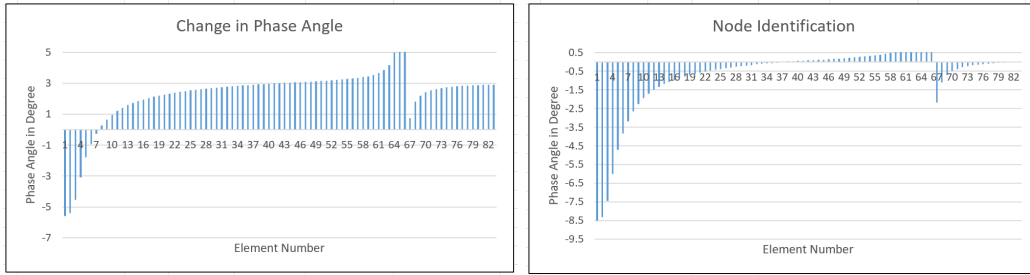


Figure 5.26: Scenario 3 case 1 650 % damage 2nd flapwise bending frequency

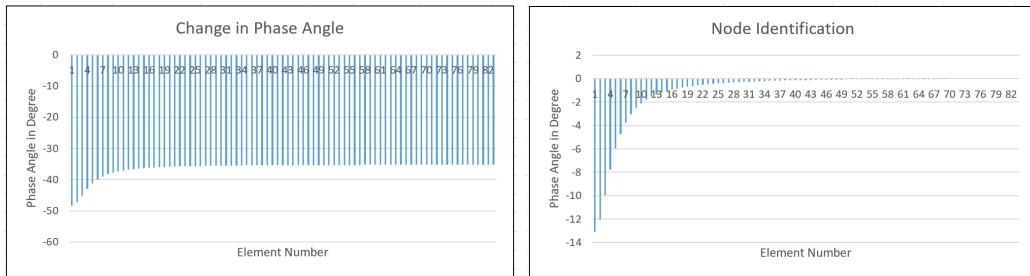


Figure 5.27: Scenario 3 case 1 650 % damage 1st edgewise bending frequency

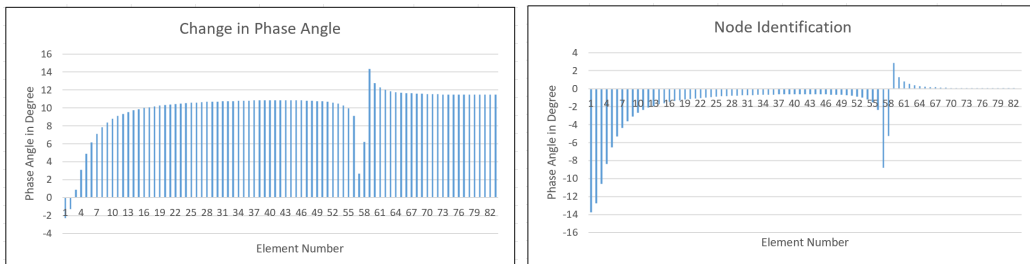


Figure 5.28: Scenario 3 case 1 650 % damage 2nd edgewise bending frequency

From the above figures, the change in phase angle is more in first 2 elements which in turn indicates that these elements are defected.

5.2.3.2 Case 2: Top and core surface damage near fixed end with 4 % defected area

The modal damping calculation and percent increase in damping of structure for case 2 for 6 different microscopic damping coefficient (damage condition) is given below.

Table 5.8: Modal damping and percentage increase of damping for scenario 3 case 2

Damping Coefficient	Eigen Value	Modal Damping	% Increasing in damping
0.015	-0.01606 + 0.6590i	0.02436	2.92
0.02	-0.01696 + 0.6590i	0.02573	8.70
0.03	-0.01820 + 0.6592i	0.02760	16.60
0.045	-0.01957 + 0.6595i	0.02966	25.31
0.06	-0.02161 + 0.6601i	0.03272	38.23
0.075	-0.02308 + 0.6607i	0.03491	47.49

The change in Phase angle of elements and damaged node identification plots for 1st and 2nd flapwise and edgewise frequencies for microscopic damping coefficient 0.075 is given below.

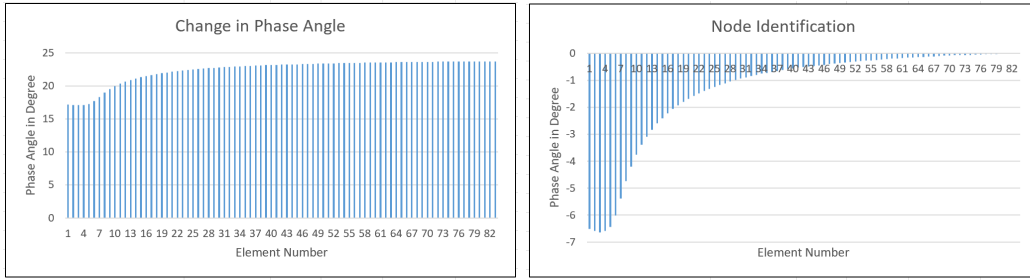


Figure 5.29: Scenario 3 case 2 650 % damage 1st flapwise bending frequency

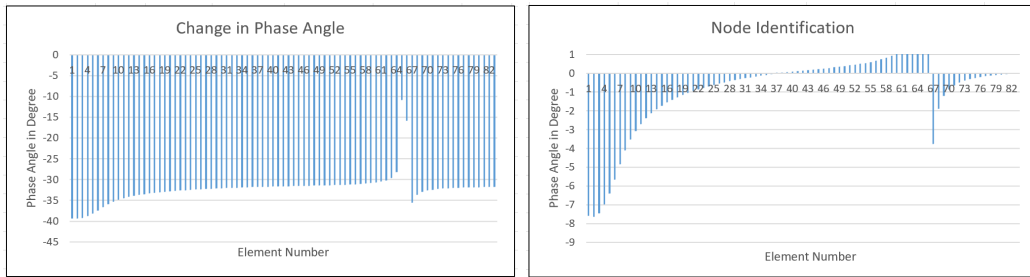


Figure 5.30: Scenario 3 case 2 650 % damage 2nd flapwise bending frequency

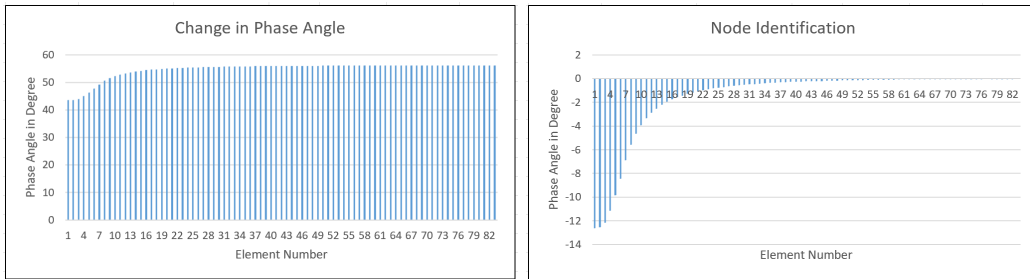


Figure 5.31: Scenario 3 case 2 650 % damage 1st edgewise bending frequency

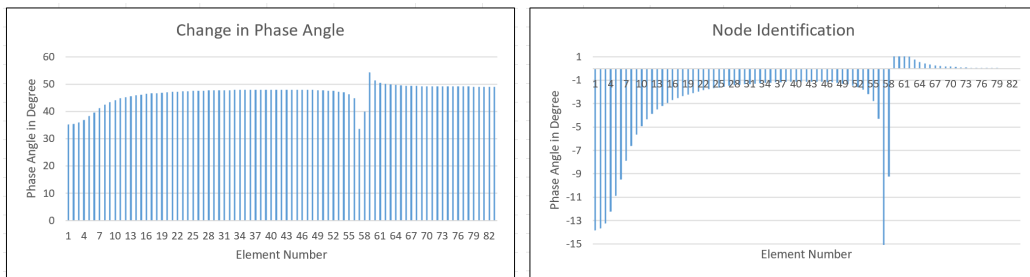


Figure 5.32: Scenario 3 case 2 650 % damage 2nd edgewise bending frequency

From the above figures, the change in phase angle is more in first 4 elements which in turn indicates that these elements are defected.

5.2.3.3 Case 3: Top and core surface damage near fixed end with 6 % defected area

The modal damping calculation and percent increase in damping of structure for case 3 for 6 different microscopic damping coefficient (damage condition) is given below.

Table 5.9: Modal damping and percentage increase of damping for scenario 3 case 3

Damping Coefficient	Eigen Value	Modal Damping	% Increasing in damping
0.015	-0.01624 + 0.6590i	0.02464	4.10
0.02	-0.01751 + 0.6591i	0.02656	12.21
0.03	-0.01924 + 0.6593i	0.02917	23.24
0.045	-0.02116 + 0.6597i	0.03206	35.45
0.06	-0.02403 + 0.6605i	0.03636	53.61
0.075	-0.02608 + 0.6614i	0.03940	66.45

The change in Phase angle of elements and damaged node identification plots for 1st and 2nd flapwise and edgewise frequencies for microscopic damping coefficient 0.075 is given below.

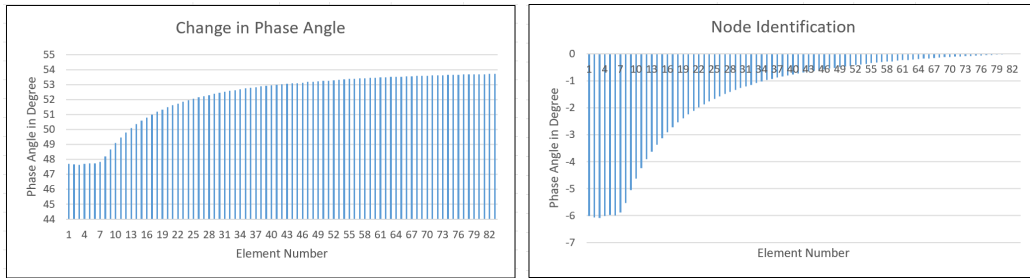


Figure 5.33: Scenario 3 case 3 650 % damage 1st flapwise bending frequency

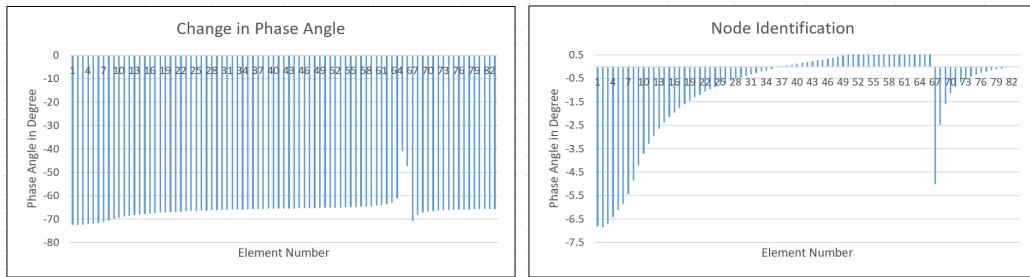


Figure 5.34: Scenario 3 case 3 650 % damage 2nd flapwise bending frequency

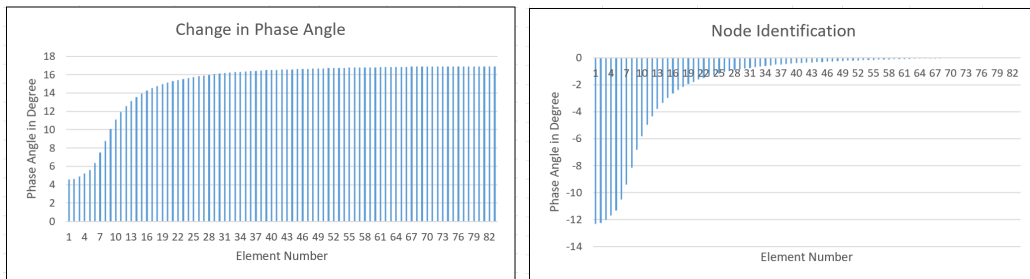


Figure 5.35: Scenario 3 case 3 650 % damage 1st edgewise bending frequency

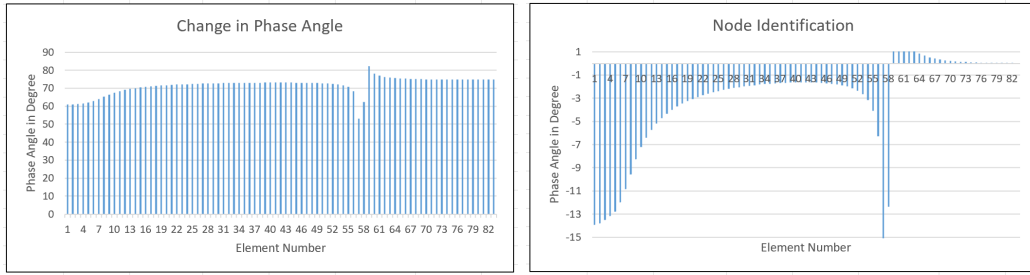


Figure 5.36: Scenario 3 case 3 650 % damage 2nd edgewise bending frequency

From the above figures, the change in phase angle is more in first 6 elements which indicates that these elements are defected.

5.2.4 Scenario 4: Damage in top and core surfaces near mid section with 2 %, 4 %, 6 % defected area

5.2.4.1 Case 1: Top and core surface damage near mid section with 2 % defected area

The modal damping calculation and percent increase in damping of structure for case 1 for 6 different microscopic damping coefficient (damage condition) is given below.

Table 5.10: Modal damping and percentage increase of damping for scenario 4 case 1

Damping Coefficient	Eigen Value	Modal Damping	% Increasing in damping
0.015	-0.01563 + 0.6589i	0.02371	0.17
0.02	-0.01568 + 0.6589i	0.02379	0.51
0.03	-0.01575 + 0.6590i	0.02389	0.93
0.045	-0.01582 + 0.6590i	0.02400	1.39
0.06	-0.01593 + 0.6590i	0.02417	2.11
0.075	-0.01601 + 0.6591i	0.02428	2.58

The change in Phase angle of elements and damaged node identification plots for 1st and 2nd flapwise and edgewise frequencies for microscopic damping coefficient 0.075 is given below.

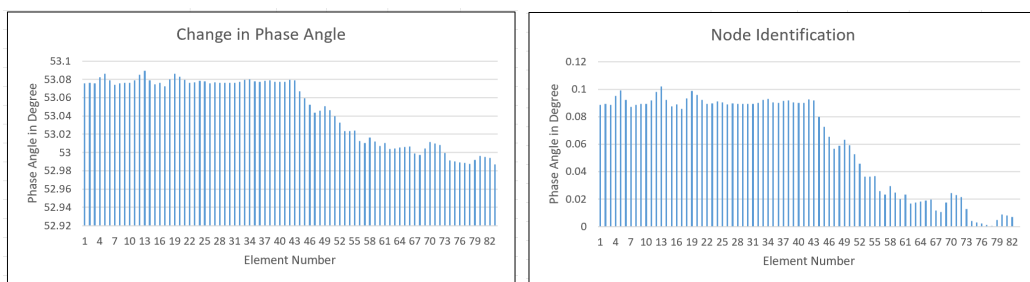


Figure 5.37: Scenario 4 case 1 650 % damage 1st flapwise bending frequency

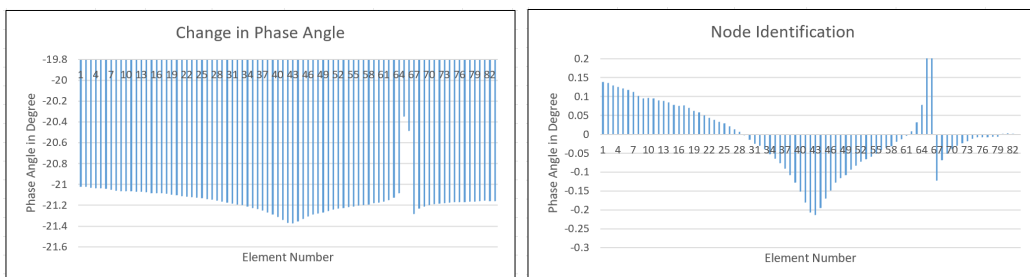


Figure 5.38: Scenario 4 case 1 650 % damage 2nd flapwise bending frequency

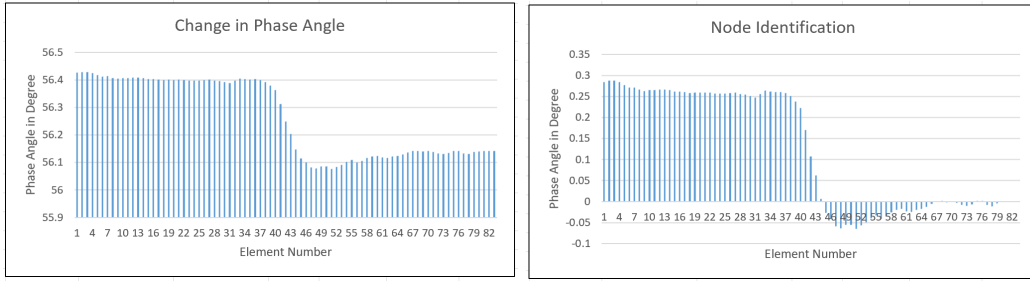


Figure 5.39: Scenario 4 case 1 650 % damage 1st edgewise bending frequency

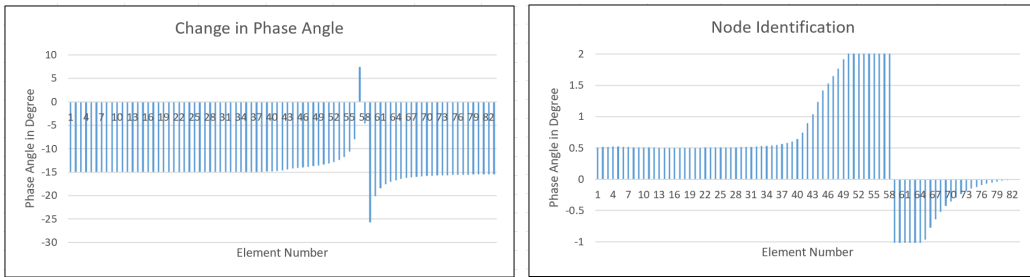


Figure 5.40: Scenario 4 case 1 650 % damage 2nd edgewise bending frequency

From figure 5.38, the change in phase angle is more in elements 42 and 43 (2 elements) this shows that these elements are defected.

5.2.4.2 Case 2: Top and core surface damage near mid section with 4 % defected area

The modal damping calculation and percent increase in damping of structure for case 2 for 6 different microscopic damping coefficient (damage condition) is given below.

Table 5.11: Modal damping and percentage increase of damping for scenario 4 case 2

Damping Coefficient	Eigen Value	Modal Damping	% Increasing in damping
0.015	-0.01566 + 0.6589i	0.02376	0.38
0.02	-0.01576 + 0.6590i	0.02391	1.01
0.03	-0.01591 + 0.6590i	0.02414	1.99
0.045	-0.01607 + 0.6590i	0.02438	3.00
0.06	-0.01631 + 0.6591i	0.02474	4.52
0.075	-0.01648 + 0.6592i	0.02499	5.58

The change in Phase angle of elements and damaged node identification plots for 1st and 2nd flapwise and edgewise frequencies for microscopic damping coefficient 0.075 is given below.

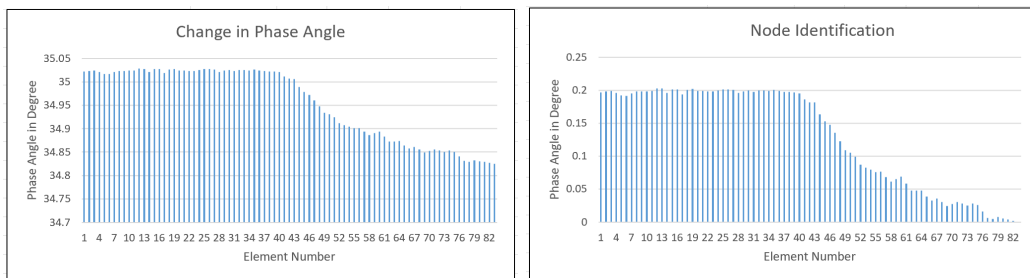


Figure 5.41: Scenario 4 case 2 650 % damage 1st flapwise bending frequency

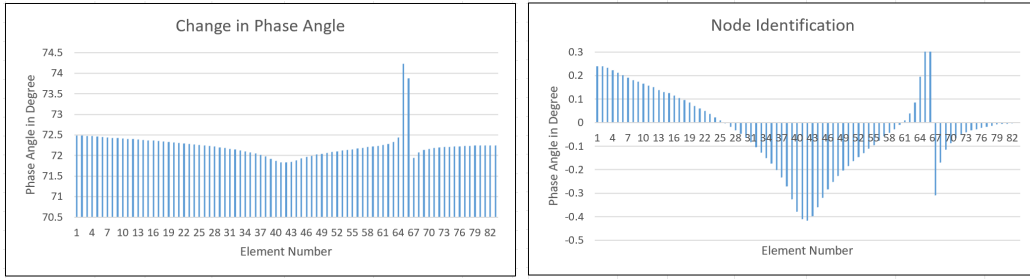


Figure 5.42: Scenario 4 case 2 650 % damage 2nd flapwise bending frequency

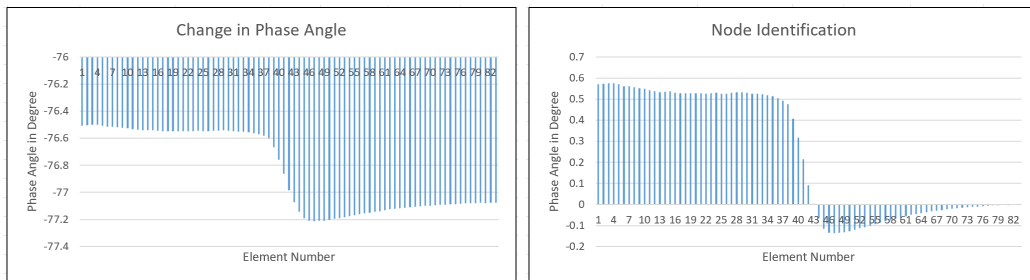


Figure 5.43: Scenario 4 case 2 650 % damage 1st edgewise bending frequency

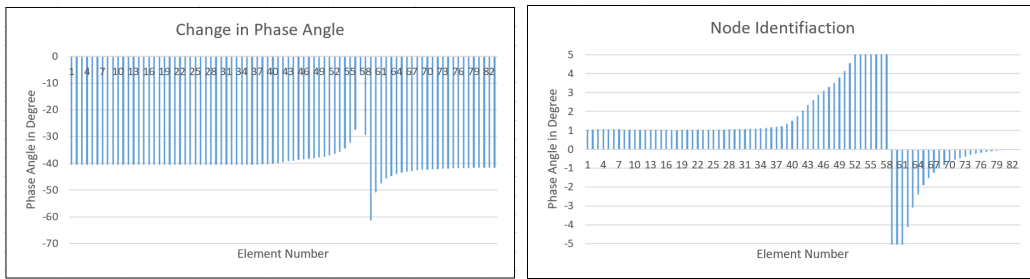


Figure 5.44: Scenario 4 case 2 650 % damage 2nd edgewise bending frequency

From figure 5.42, the change in phase angle is more in elements 40, 41, 42 and 43 (4 elements) this shows that these elements are defected.

5.2.4.3 Case 3: Top and core surface damage near mid section with 6 % defected area

The modal damping calculation and percent increase in damping of structure for case 2 for 6 different microscopic damping coefficient (damage condition) is given below.

Table 5.12: Modal damping and percentage increase of damping for scenario 4 case 3

Damping Coefficient	Eigen Value	Modal Damping	% Increasing in damping
0.015	-0.01568 + 0.6589i	0.02379	0.51
0.02	-0.01583 + 0.6590i	0.02401	1.44
0.03	-0.01604 + 0.6590i	0.02433	2.79
0.045	-0.01626 + 0.6590i	0.02467	4.22
0.06	-0.01660 + 0.6592i	0.02517	6.34
0.075	-0.01684 + 0.6593i	0.02553	7.86

The change in Phase angle of elements and damaged node identification plots for 1st and 2nd flapwise and edgewise frequencies for microscopic damping coefficient 0.075 is given below.

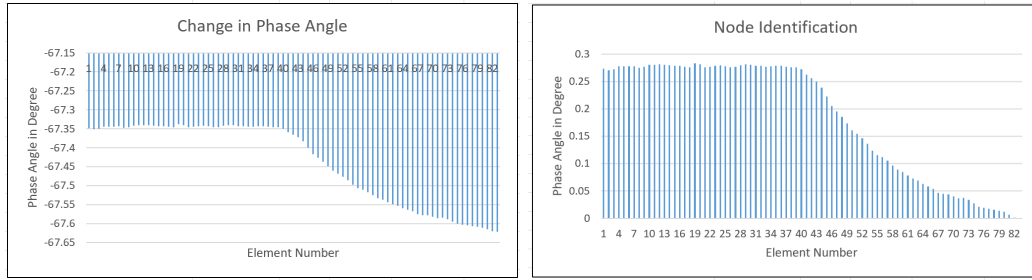


Figure 5.45: Scenario 4 case 3 650 % damage 1st flapwise bending frequency

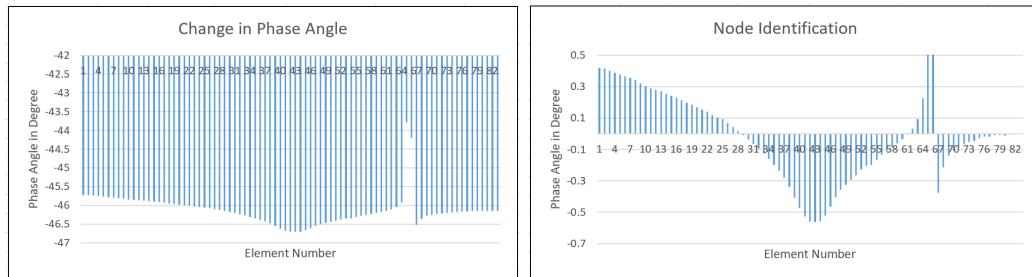


Figure 5.46: Scenario 4 case 3 650 % damage 2nd flapwise bending frequency

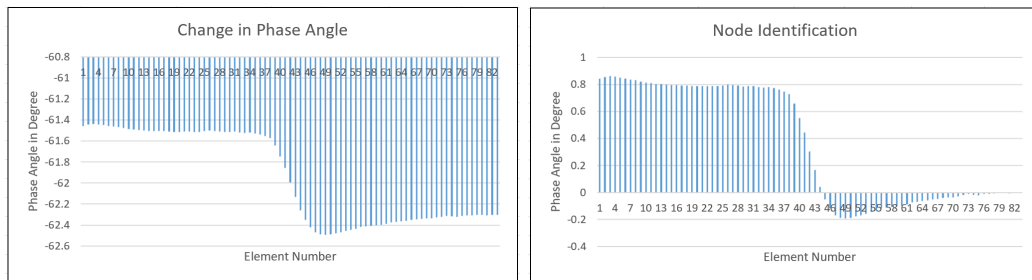


Figure 5.47: Scenario 4 case 3 650 % damage 1st edgewise bending frequency

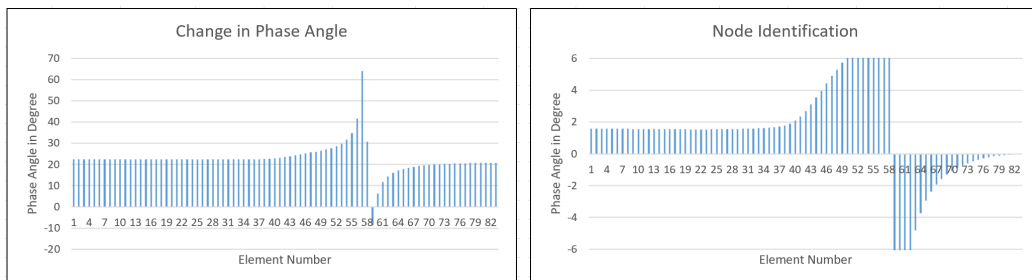


Figure 5.48: Scenario 4 case 3 650 % damage 2nd edgewise bending frequency

From the figure 5.46 the change in phase is more in elements 40, 41, 42, 43,44 and 45 (6 elements) this shows that these elements are defected.

The modal damping percent increase for different loss factor (microscopic damping coefficients) for each damaged scenario obtained from the above chapter is summarized in the below table for easy comparison and understanding

Table 5.13: Increase in overall damping of the structure for different loss factor (microscopic damping coefficients)

		Loss factor/ Microscopic Damping coefficient					
		0.015	0.02	0.03	0.045	0.06	0.075
Scenario 1	Case 1	1.27 %	3.76 %	7.18 %	11.03 %	16.56 %	20.45 %
	Case 2	2.41 %	7.22 %	13.77 %	21.04 %	31.73 %	39.29 %
	Case 3	3.51 %	10.44 %	19.90 %	30.33 %	45.75 %	56.74 %
Scenario 2	Case 1	0.17 %	0.46 %	0.80 %	1.27 %	1.86 %	2.28 %
	Case 2	0.34 %	0.93 %	1.69 %	2.66 %	4.01 %	4.94 %
	Case 3	0.46 %	1.27 %	2.41 %	3.76 %	5.62 %	6.93 %
Scenario 3	Case 1	1.65 %	4.77 %	9.13 %	13.98 %	21.12 %	26.19 %
	Case 2	2.92 %	8.70 %	16.60 %	25.31 %	38.23 %	47.49 %
	Case 3	4.10 %	12.21 %	23.24 %	35.45 %	53.61 %	66.45 %
Scenario 4	Case 1	0.17 %	0.51 %	0.93 %	1.39 %	2.11 %	2.58 %
	Case 2	0.38 %	1.01 %	1.99 %	3.00 %	4.52 %	5.58 %
	Case 3	0.51 %	1.44 %	2.79 %	4.22 %	6.34 %	7.86 %

Note:

Scenario 1 : Damage only in top surfaces near the fixed end.

Scenario 2 : Damage only in top surfaces near the mid section.

Scenario 3 : Damage in top and core surfaces near the fixed end.

Scenario 4 : Damage in top and core surfaces near the mid section.

Case 1: 2 % defected area.

Case 2: 4 % defected area.

Case 3: 6 % defected area.

6 Results and Discussions

In this chapter, results from the project are discussed and the results for each scenario are compared. The difference in the phase angle of elements for undamaged structure and 3 damaged conditions are compared to understand the effect of damage in increasing the overall damping of the structure. As explained in the previous chapter, change in phase angle vs element is plotted only for undamaged damped structure and microscopic damping coefficient of 0.02, 0.045 and 0.075. As explained before in previous chapter, in the plots corresponds to 2nd flapwise and edgewise bending frequencies there is an unexpected rise in phase angle around elements 60 to 70 because of phase angle calculation method used, so these values are not considered to avoid confusion.

6.1 Scenario 1: Damage only in top surfaces near fixed end with 2 %, 4 %, 6 % defected area

6.1.1 Case 1: Top surface damage near fixed end with 2 % defected area

The following plots show the change in phase angle for each element at different microscopic damping coefficients for a particular frequency for a top surface defect with 2 % defected area near fixed end. Figure 6.1 shows the basic layout of the damaged elements of this case. The increase in overall damping of the structure calculated using modal damping for the microscopic damping coefficients 0.02, 0.045 and 0.75 are about 3.76 %, 11.03 % and 20.45 % respectively.

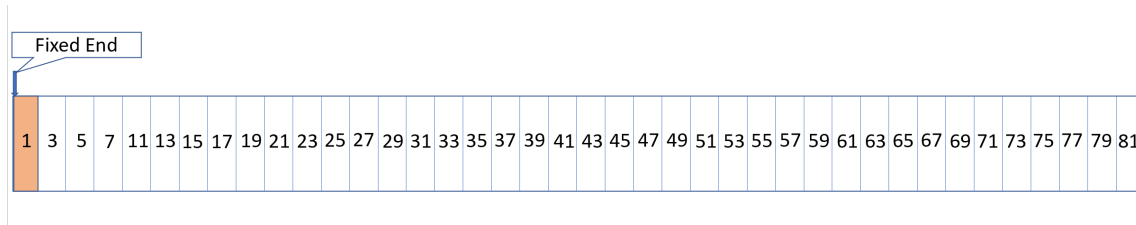


Figure 6.1: Layout of top surface damage near fixed end with 2 % defected area

Figure 6.2 shows the change in phase angle for 1st flapwise bending frequency. The maximum deflection for 1st flapwise bending frequency for the microscopic damping coefficients 0.02, 0.045 and 0.75 are about -0.85° , -2.49° and -4.73° respectively.

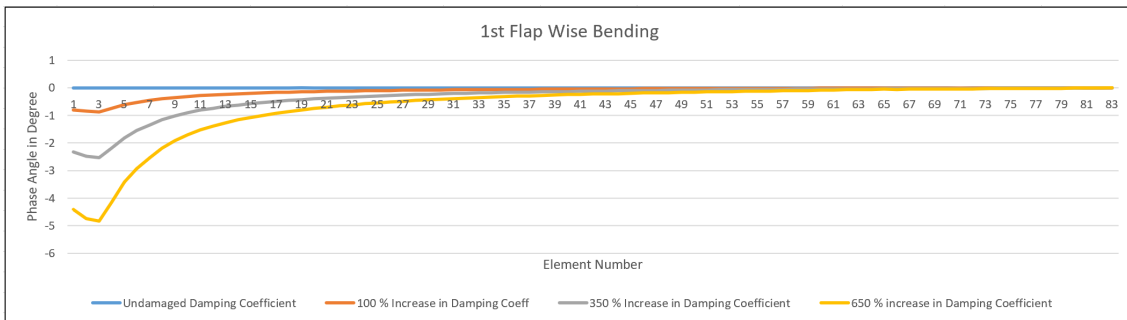


Figure 6.2: Defect identification for scenario 1 case 1 for 1st flapwise bending frequency

Figure 6.3 shows the change in phase angle for 2nd flapwise bending frequency. The maximum deflection for 2nd flapwise bending frequency for the microscopic damping coefficients 0.02, 0.045 and 0.75 are about -0.68° , -2.01° and -3.81° respectively.

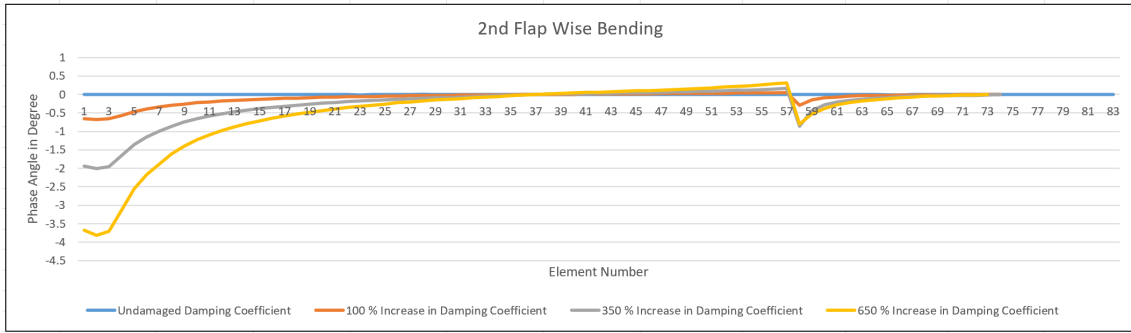


Figure 6.3: Defect identification for scenario 1 case 1 for 2nd flapwise bending frequency

Figure 6.4 shows the change in phase angle for 1st edgewise bending frequency. The maximum deflection for 1st edgewise bending frequency for the microscopic damping coefficients 0.02, 0.045 and 0.75 are about -2.29°, -6.69° and -12.87° respectively.

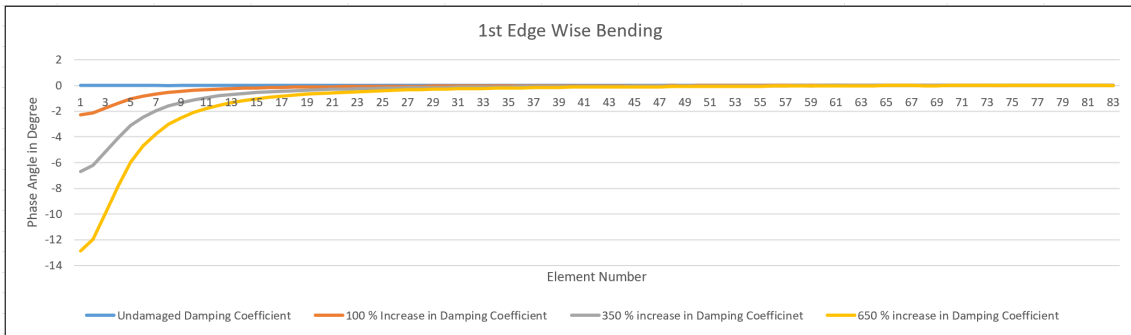


Figure 6.4: Defect identification for scenario 1 case 1 for 1st edgewise bending frequency

Figure 6.5 shows the change in phase angle for 2nd edgewise bending frequency. The maximum deflection for 2nd edgewise bending frequency for the microscopic damping coefficients 0.02, 0.045 and 0.75 are about -2.43°, -7.04° and -13.50° respectively.

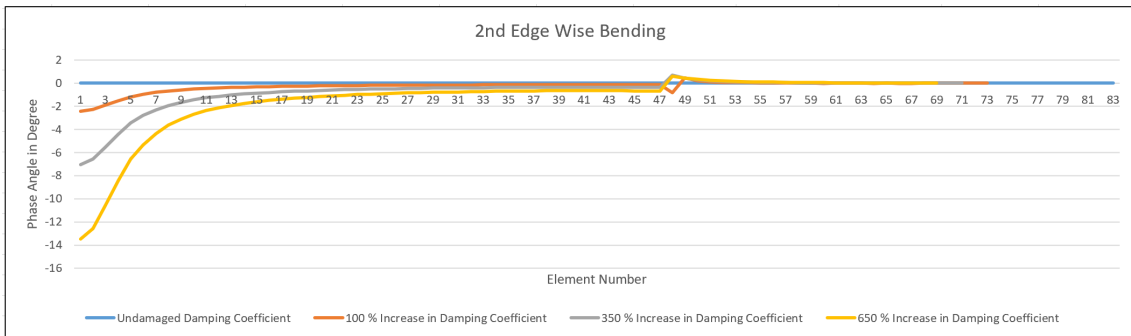


Figure 6.5: Defect identification for scenario 1 case 1 for 2nd edgewise bending frequency

Figures 6.2 and 6.4 clearly shows that the phase angle change is higher near fixed end for first 2 elements and it keep on increasing and reaches zero for the elements far away from the fixed end.

6.1.2 Case 2: Top surface damage near fixed end with 4 % defected area

The following plots show the change in phase angle for each element at different microscopic damping coefficients for a particular frequency for a top surface defect with 4 % defected area near fixed end. Figure 6.6 shows the basic layout of the damaged elements of this case. The increase in overall damping of the structure calculated using modal damping for the microscopic damping coefficient 0.02, 0.045 and 0.75 is about 7.22 %, 21.04 % and 39.29 % respectively.

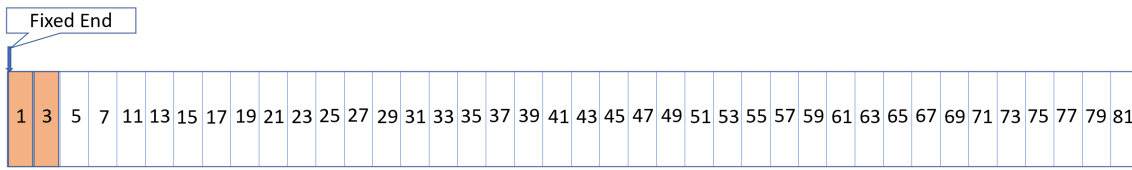


Figure 6.6: Layout of top surface damage near fixed end with 4 % defected area

Figure 6.7 shows the change in phase angle for 1st flapwise bending frequency. The maximum deflection for 1st flapwise bending frequency for the microscopic damping coefficients 0.02, 0.045 and 0.75 are about -0.75°, -2.22° and -4.21° respectively.

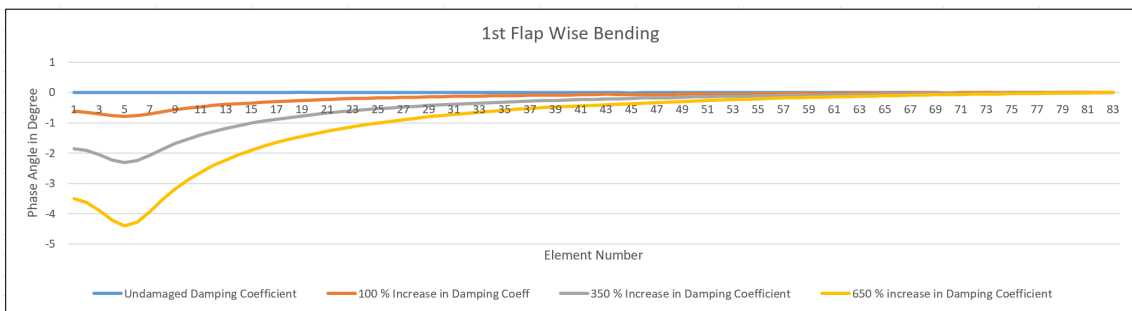


Figure 6.7: Defect identification for scenario 1 case 2 for 1st flapwise bending frequency

Figure 6.8 shows the change in phase angle for 2nd flapwise bending frequency. The maximum deflection for 2nd flapwise bending frequency for the microscopic damping coefficients 0.02, 0.045 and 0.75 are about -0.52°, -1.53° and -2.92° respectively.

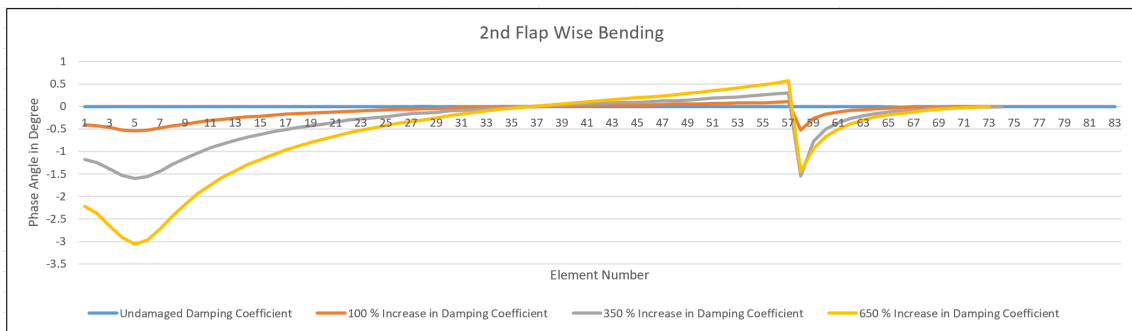


Figure 6.8: Defect identification for scenario 1 case 2 for 2nd flapwise bending frequency

Figure 6.9 shows the change in phase angle for 1st edgewise bending frequency. The maximum deflection for 1st edgewise bending frequency for the microscopic damping coefficients 0.02, 0.045 and 0.75 are about -2.15°, -6.29° and -12.11° respectively.

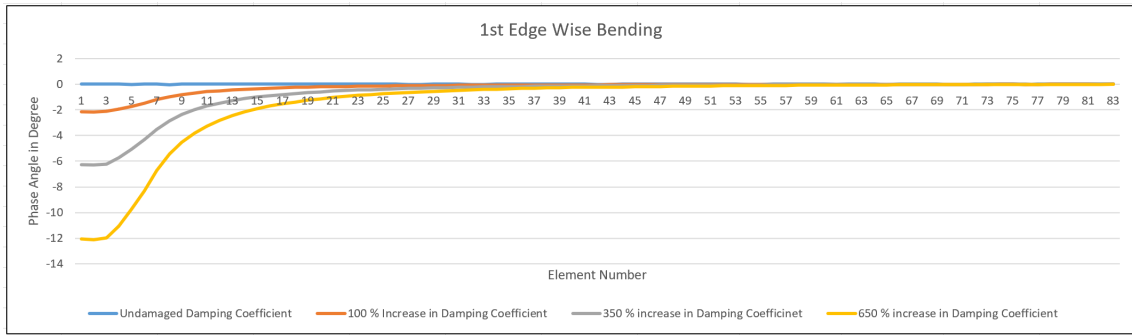


Figure 6.9: Defect identification for scenario 1 case 2 for 1st edgewise bending frequency

Figure 6.10 shows the change in phase angle for 2nd edgewise bending frequency. The maximum deflection for 2nd edgewise bending frequency for the microscopic damping coefficients 0.02, 0.045 and 0.75 are about 177.83°, -6.90° and -13.27° respectively.

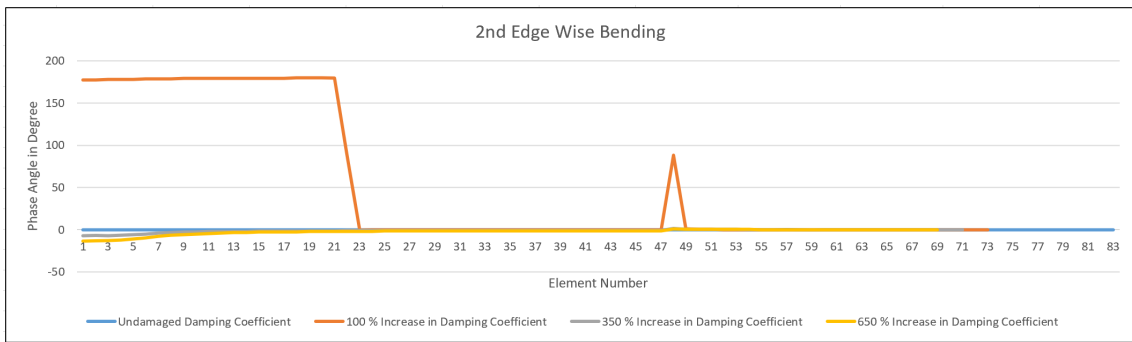


Figure 6.10: Defect identification for scenario 1 case 2 for 2nd edgewise bending frequency

In figure 6.10, even though the results for microscopic damping coefficients 0.01, 0.045 and 0.75 are as expected for 2nd edgewise bending frequency, the result corresponding to microscopic damping coefficients 0.02 is an anomaly. And the reason for this anomaly is unclear, so detailed research on this was not done. Figures 6.7 and 6.9 clearly shows that the phase angle change is higher near the fixed end for first 4 elements and it keep on increasing and reaches zero for the elements far away from the fixed end.

6.1.3 Case 3: Top surface damage near fixed end with 6 % defected area

The following plots show the change in phase angle for each element at different microscopic damping coefficients for a particular frequency for a top surface defect with 6 % defected area near fixed end. Figure 6.11 shows the basic layout of the damaged elements of this case. The increase in overall damping of the structure calculated using modal damping for the microscopic damping coefficient 0.02, 0.045 and 0.75 is about 10.44 %, 30.33 % and 56.74 % respectively.

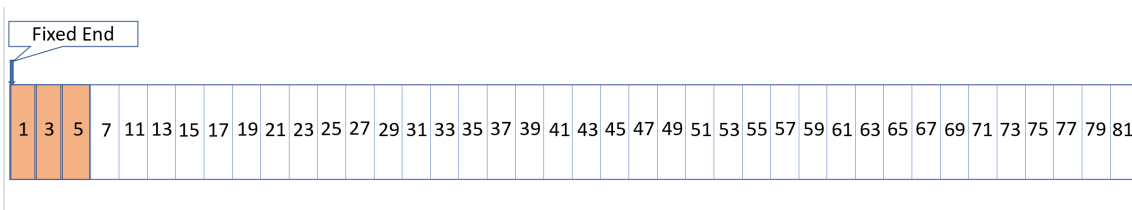


Figure 6.11: Layout of top surface damage near fixed end with 6 % defected area

Figure 6.12 shows the change in phase angle for 1st flapwise bending frequency. The maximum deflection for 1st flapwise bending frequency for the microscopic damping coefficients 0.02, 0.045 and 0.75 are about -0.73°, -2.15° and -4.09° respectively.

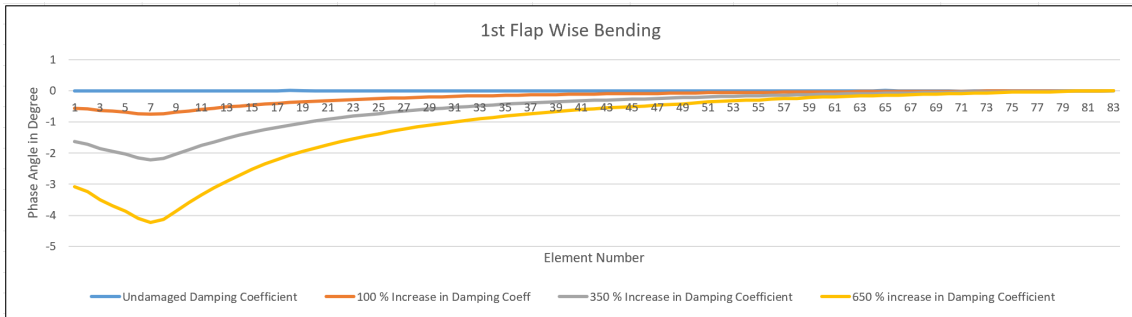


Figure 6.12: Defect identification for scenario 1 case 3 for 1st flapwise bending frequency

Figure 6.13 shows the change in phase angle for 2nd flapwise bending frequency. The maximum deflection for 2nd flapwise bending frequency for the microscopic damping coefficients 0.02, 0.045 and 0.75 are about -0.47°, -1.38° and -2.62° respectively.

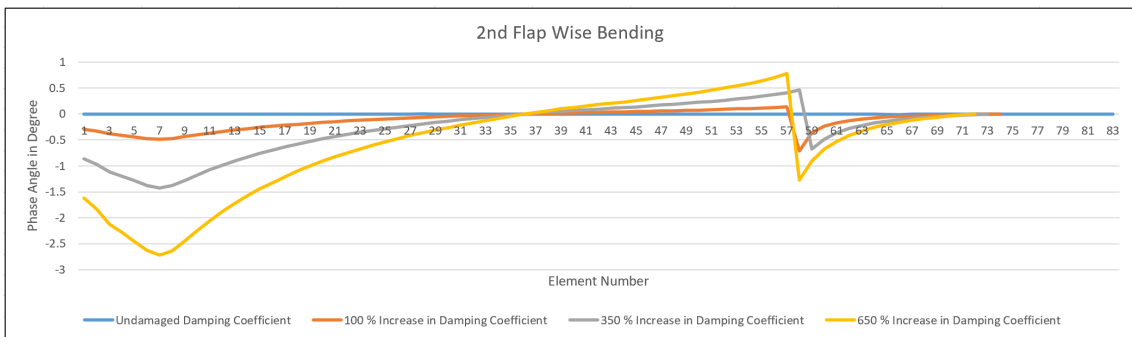


Figure 6.13: Defect identification for scenario 1 case 3 for 2nd flapwise bending frequency

Figure 6.14 shows the change in phase angle for 1st edgewise bending frequency. The maximum deflection for 1st edgewise bending frequency for the microscopic damping coefficients 0.02, 0.045 and 0.75 are about -2.07°, -6.06° and -11.66° respectively.

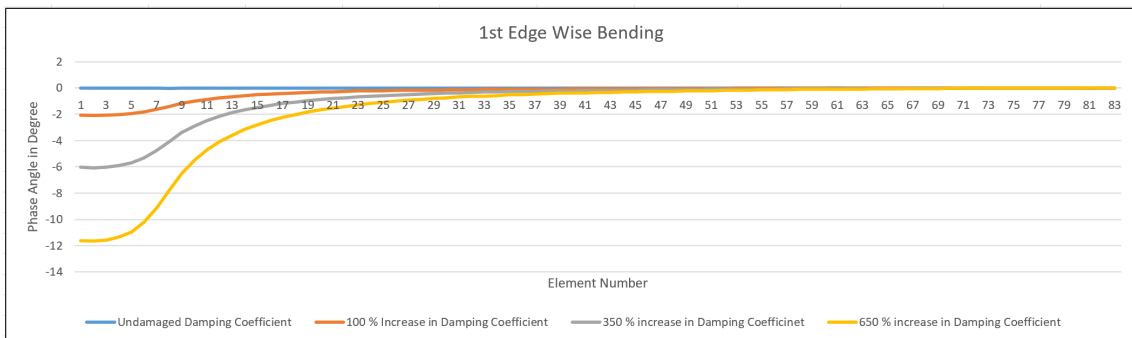


Figure 6.14: Defect identification for scenario 1 case 3 for 1st edgewise bending frequency

Figure 6.15 shows the change in phase angle for 2nd edgewise bending frequency. The maximum deflection for 2nd edgewise bending frequency for the microscopic damping coefficients 0.02, 0.045 and 0.75 are about -2.37°, -6.91° and -13.29° respectively.

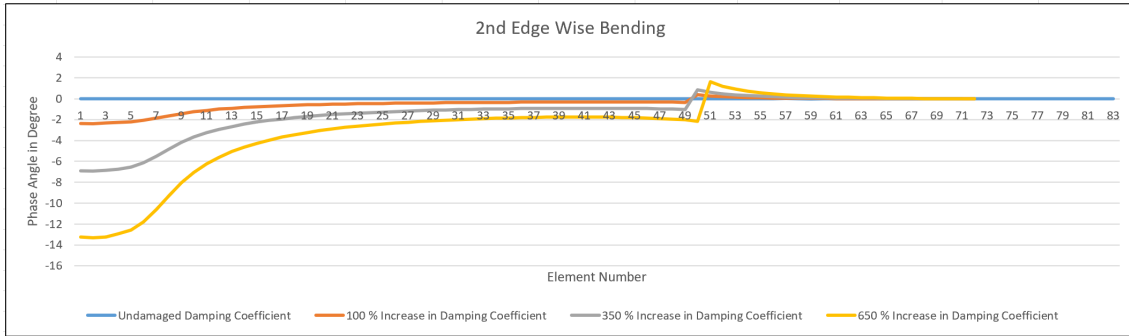


Figure 6.15: Defect identification for scenario 1 case 3 for 2nd edgewise bending frequency

Figures 6.12 and 6.14 clearly shows that the phase angle change is higher near the fixed end for first 6 elements and it keep on increasing and reaches zero for the elements far away from the fixed end.

6.2 Scenario 2: Damage only in top surfaces near mid section with 2 %, 4 %, 6 % defected area

6.2.1 Case 1: Top surface damage near mid section with 2 % defected area

The following plots show the change in phase angle for each element at different microscopic damping coefficients for a particular frequency for a top surface defect with 2 % defected area near the midsection. Figure 6.16 shows the basic layout of the damaged elements of this case. The increase in overall damping of the structure calculated using modal damping for the microscopic damping coefficient 0.02, 0.045 and 0.75 is about 0.46 %, 1.27 % and 2.28 % respectively.

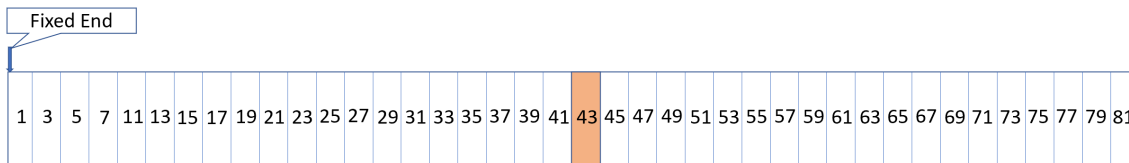


Figure 6.16: Layout of top surface damage near mid section with 2 % defected area

Figure 6.17 shows the change in phase angle for 1st flapwise bending frequency. The maximum deflection for 1st flapwise bending frequency for the microscopic damping coefficients 0.02, 0.045 and 0.75 are about 0.0047°, 0.043° and 0.083° respectively.

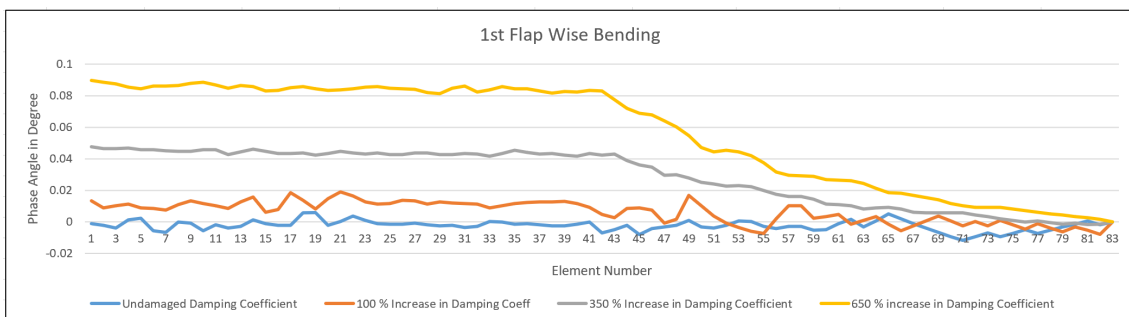


Figure 6.17: Defect identification for scenario 2 case 1 for 1st flapwise bending frequency

Figure 6.18 shows the change in phase angle for 2nd flapwise bending frequency. The maximum deflection for 2nd flapwise bending frequency for the microscopic damping coefficients 0.02, 0.045 and 0.75 are about -0.036°, -0.11° and -0.21° respectively.

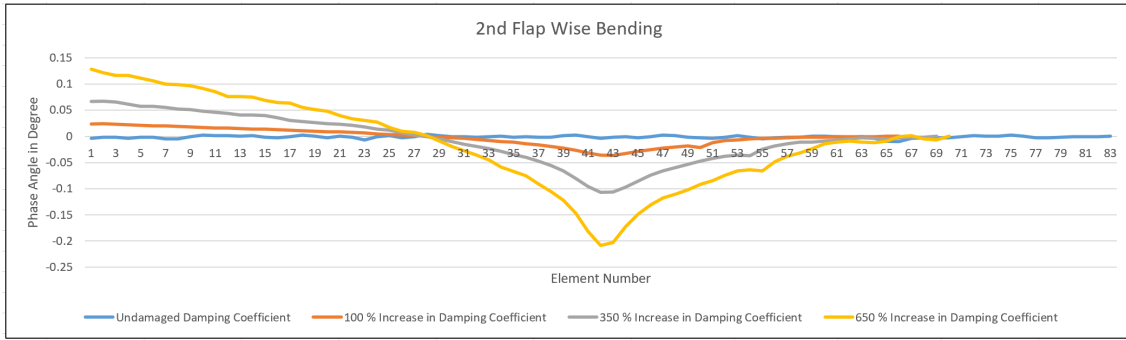


Figure 6.18: Defect identification for scenario 2 case 1 for 2nd flapwise bending frequency

Figure 6.19 shows the change in phase angle for 1st edgewise bending frequency. The maximum deflection for 1st edgewise bending frequency for the microscopic damping coefficients 0.02, 0.045 and 0.75 are about 0.015°, 0.033° and 0.071° respectively.

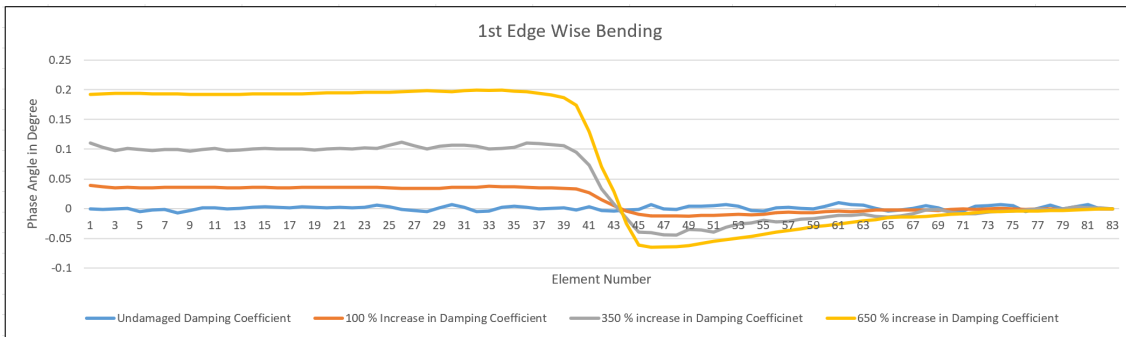


Figure 6.19: Defect identification for scenario 2 case 1 for 1st edgewise bending frequency

Figure 6.20 shows the change in phase angle for 2nd edgewise bending frequency. The maximum deflection for 2nd edgewise bending frequency for the microscopic damping coefficients 0.02, 0.045 and 0.75 are about 0.062°, 0.15° and 0.29° respectively.

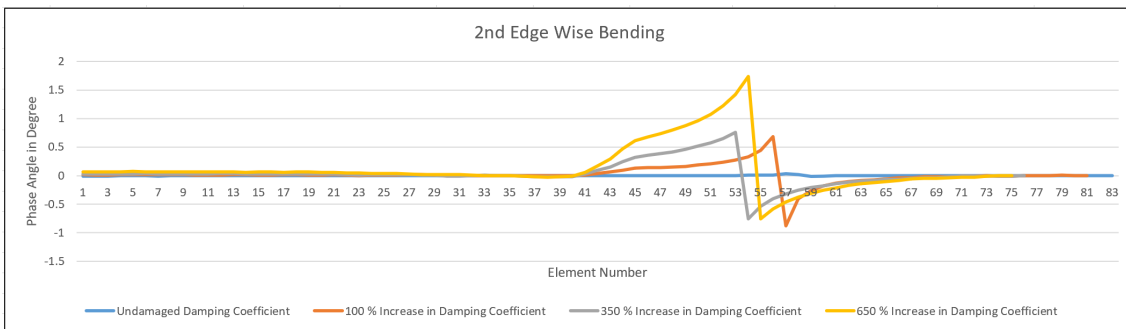


Figure 6.20: Defect identification for scenario 2 case 1 for 2nd edgewise bending frequency

Figure 6.18 clearly shows that the phase angle change is positive near the fixed end; it keeps reducing and reaches maximum change in phase angle around the elements 42, 43 (2 damaged elements) and the value keep on increasing and reaches zero for the elements far away from the damaged elements.

6.2.2 Case 2: Top surface damage near mid section with 4 % defected area

The following plots show the change in phase angle for each element at different microscopic damping coefficients for a particular frequency for a top surface defect with 4 % defected area near the midsection. Figure 6.21 shows the basic layout of the damaged elements of this case. The increase in overall damping of the structure calculated using modal damping for the microscopic damping coefficient 0.02, 0.045 and 0.75 is about 0.93 %, 2.66 % and 4.94 % respectively.

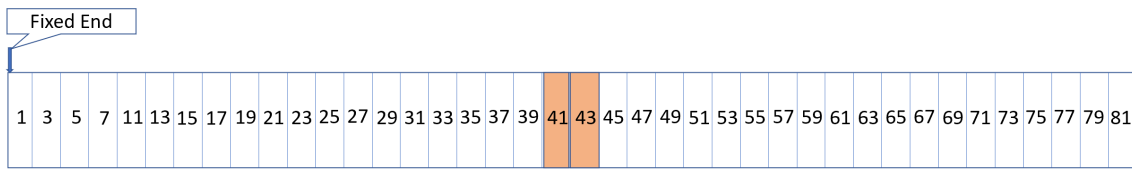


Figure 6.21: Layout of top surface damage near mid section with 4 % defected area

Figure 6.22 shows the change in phase angle for 1st flapwise bending frequency. The maximum deflection for 1st flapwise bending frequency for the microscopic damping coefficients 0.02, 0.045 and 0.75 are about 0.032°, 0.094° and 0.18° respectively.

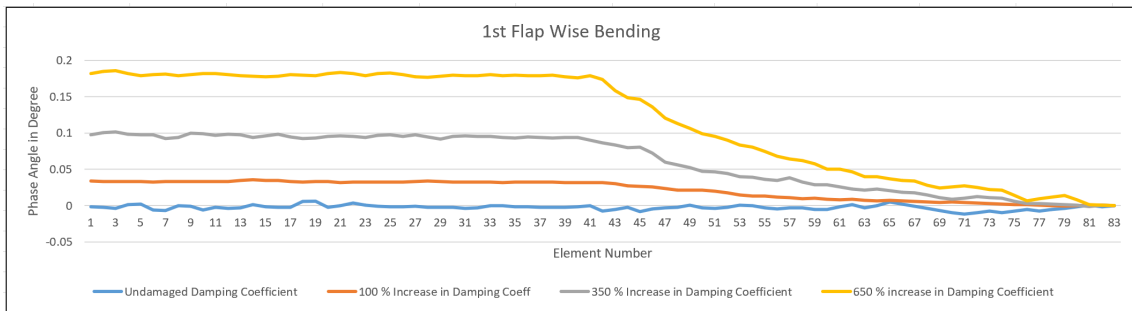


Figure 6.22: Defect identification for scenario 2 case 2 for 1st flapwise bending frequency

Figure 6.23 shows the change in phase angle for 2nd flapwise bending frequency. The maximum deflection for 2nd flapwise bending frequency for the microscopic damping coefficients 0.02, 0.045 and 0.75 are about -0.067°, -0.207° and -0.385° respectively.

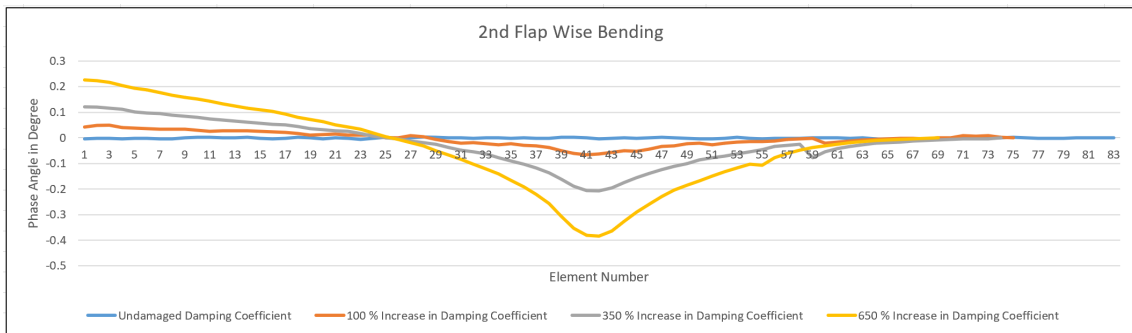


Figure 6.23: Defect identification for scenario 2 case 2 for 2nd flapwise bending frequency

Figure 6.24 shows the change in phase angle for 1st edgewise bending frequency. The maximum deflection for 1st edgewise bending frequency for the microscopic damping coefficients 0.02, 0.045 and 0.75 are about 0.047°, 0.133° and 0.246° respectively.

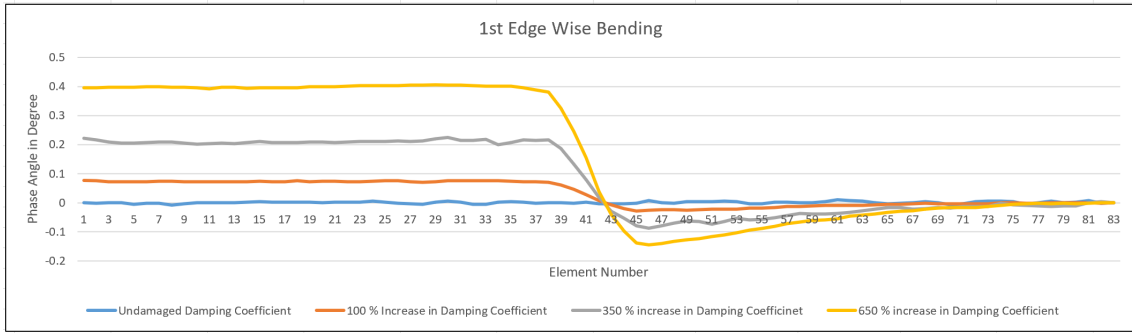


Figure 6.24: Defect identification for scenario 2 case 2 for 1st edgewise bending frequency

Figure 6.25 shows the change in phase angle for 2nd edgewise bending frequency. The maximum deflection for 2nd edgewise bending frequency for the microscopic damping coefficients 0.02, 0.045 and 0.75 are about 0.15°, 0.43° and 0.80° respectively.

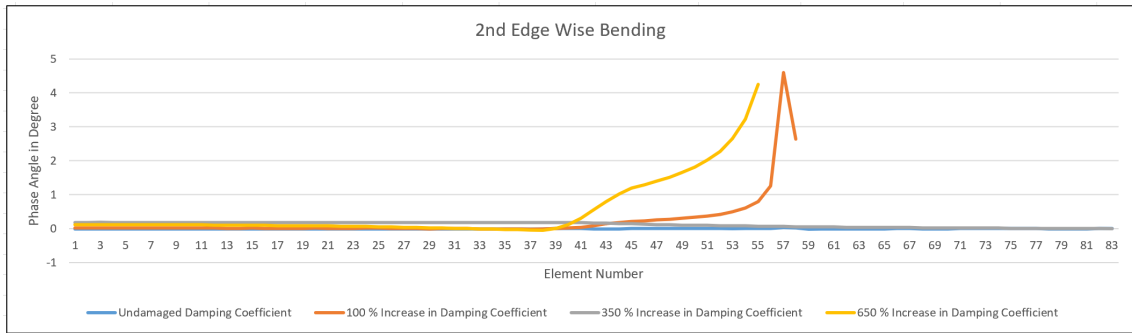


Figure 6.25: Defect identification for scenario 2 case 2 for 2nd edgewise bending frequency

Figure 6.23 clearly shows that the phase angle change is positive near the fixed end; it keeps reducing and reaches maximum change in phase angle around the elements 40, 41, 42 and 43 (4 damaged elements) and the value keeps on increasing and reaches zero for the elements far away from the damaged elements.

6.2.3 Case 3: Top surface damage near mid section with 6 % defected area

The following plots show the change in phase angle for each element at different microscopic damping coefficients for a particular frequency for a top surface defect with 6 % defected area near the midsection. Figure 6.26 shows the basic layout of the damaged elements of this case. The increase in overall damping of the structure calculated using modal damping for the microscopic damping coefficient 0.02, 0.045 and 0.75 is about 1.27 %, 3.76 % and 6.93 % respectively.

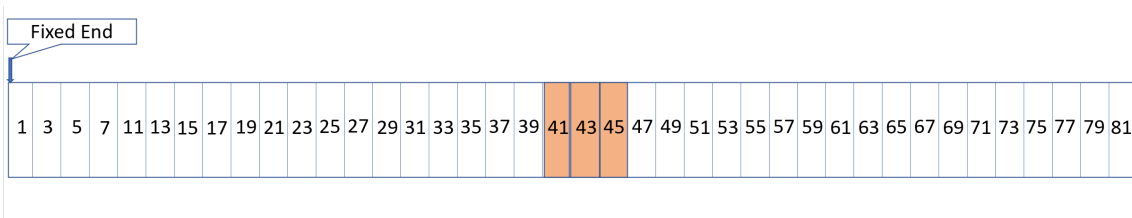


Figure 6.26: Layout of top surface damage near mid section with 6 % defected area

Figure 6.27 shows the change in phase angle for 1st flapwise bending frequency. The maximum deflection for 1st flapwise bending frequency for the microscopic damping coefficients 0.02, 0.045 and 0.75 are about 0.046°, 0.133° and 0.247° respectively.

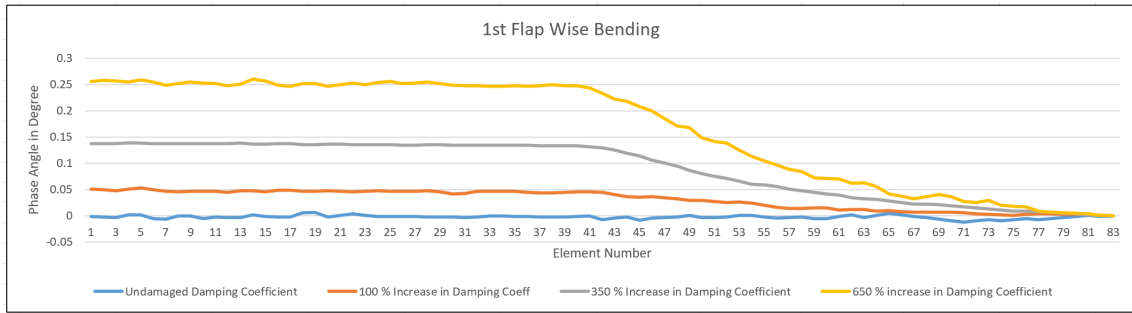


Figure 6.27: Defect identification for scenario 2 case 3 for 1st flapwise bending frequency

Figure 6.28 shows the change in phase angle for 2nd flapwise bending frequency. The maximum deflection for 2nd flapwise bending frequency for the microscopic damping coefficients 0.02, 0.045 and 0.75 are about -0.095°, -0.284° and -0.519° respectively.

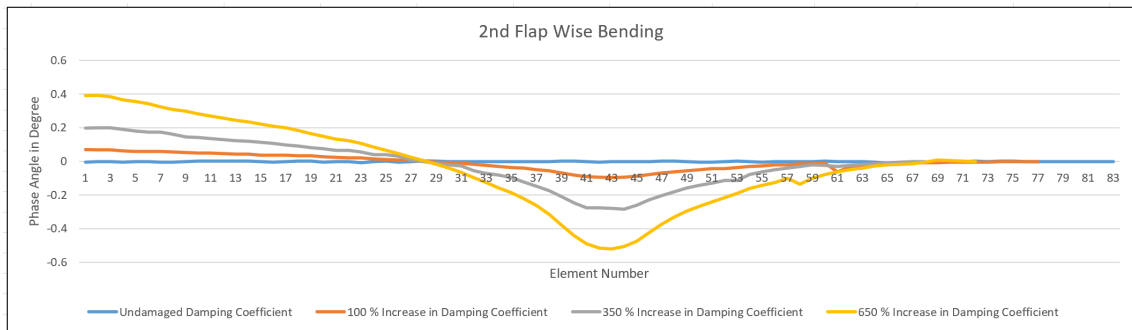


Figure 6.28: Defect identification for scenario 2 case 3 for 2nd flapwise bending frequency

Figure 6.29 shows the change in phase angle for 1st edgewise bending frequency. The maximum deflection for 1st edgewise bending frequency for the microscopic damping coefficients 0.02, 0.045 and 0.75 are about 0.086°, 0.237° and 0.428° respectively.

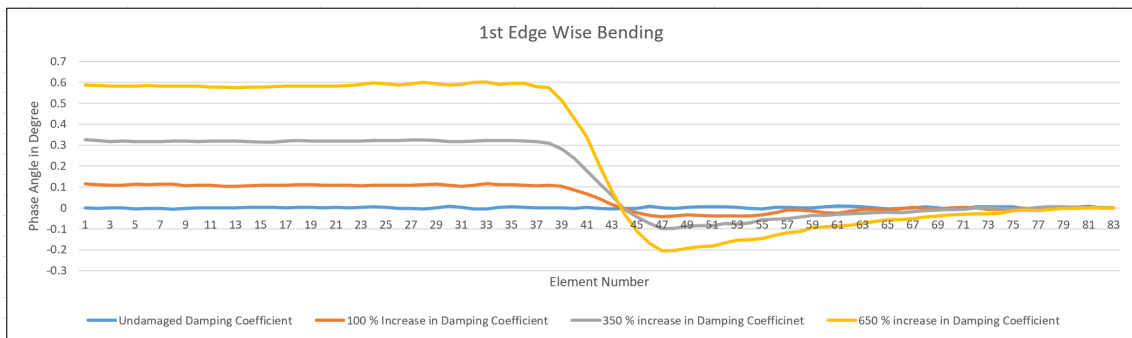


Figure 6.29: Defect identification for scenario 2 case 3 for 1st edgewise bending frequency

Figure 6.30 shows the change in phase angle for 2nd edgewise bending frequency. The maximum deflection for 2nd edgewise bending frequency for the microscopic damping coefficients 0.02, 0.045 and 0.75 are about 0.29°, 0.83° and 1.56° respectively.

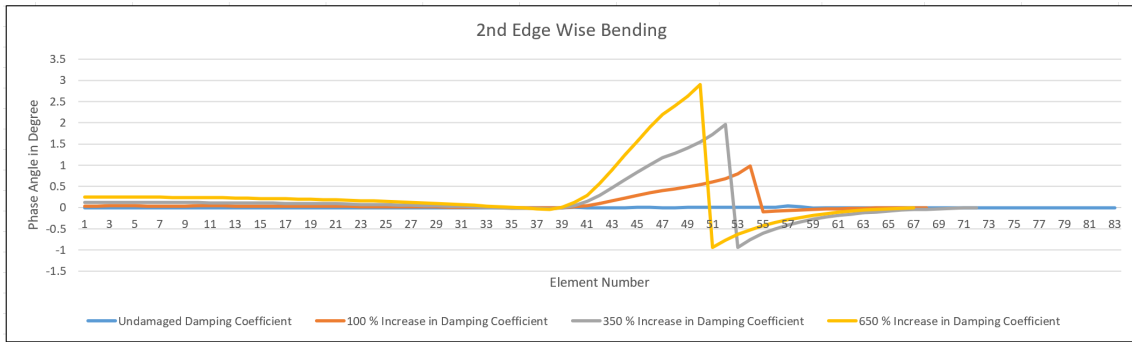


Figure 6.30: Defect identification for scenario 2 case 3 for 2nd edgewise bending frequency

Figure 6.28 clearly shows that the phase angle change is positive near the fixed end; it keeps reducing and reaches maximum change in phase angle around the elements 40, 41, 42, 43, 44 and 45 (6 damaged elements) and the value keep on increasing and reaches zero for the elements far away from the damaged elements. The plots corresponding to 1st flapwise bending frequency shows that the phase angle starts to drops gradually from the damaged element and the plots corresponding to 1st edgewise bending frequency shows that the phase angle starts to drops sharply and the goes below zero from the damaged elements. However, it is hard to identify defected elements only with a sudden change in phase angle. On the contrary, the plots corresponding to 2nd flapwise bending frequency helps in identifying the damaged elements.

6.3 Scenario 3: Damage in top and core surfaces near fixed end with 2 %, 4 %, 6 % defected area

6.3.1 Case 1: Top and core surface damage near fixed end with 2 % defected area

The following plots show the change in phase angle for each element at different microscopic damping coefficients for a particular frequency for top and core surface defect with 2 % defected area near fixed end. Figure 6.31 shows the basic layout of the damaged elements of this case. The increase in overall damping of the structure calculated using modal damping for the microscopic damping coefficients 0.02, 0.045 and 0.75 are about 4.77 %, 13.98 % and 26.19 % respectively.

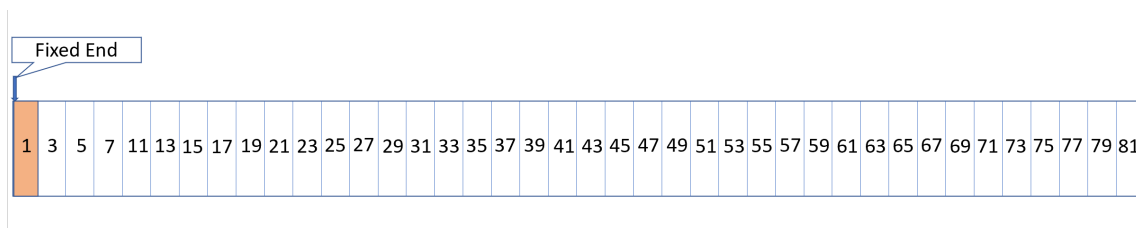


Figure 6.31: Layout of top and core surface damage near fixed end with 2 % defected area

Figure 6.32 shows the change in phase angle for 1st flapwise bending frequency. The maximum deflection for 1st flapwise bending frequency for the microscopic damping coefficients 0.02, 0.045 and 0.75 are about -1.35°, -3.98° and -7.65° respectively.

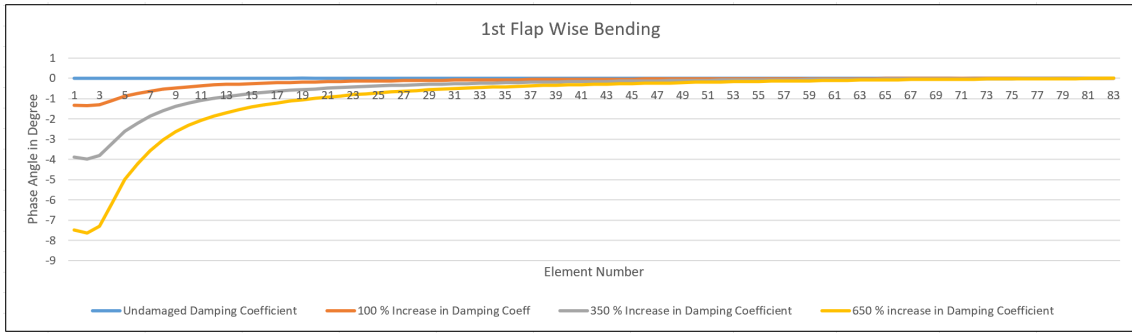


Figure 6.32: Defect identification for scenario 3 case 1 for 1st flapwise bending frequency

Figure 6.33 shows the change in phase angle for 2nd flapwise bending frequency. The maximum deflection for 2nd flapwise bending frequency for the microscopic damping coefficients 0.02, 0.045 and 0.75 are about -1.52°, -4.46° and -8.51° respectively.

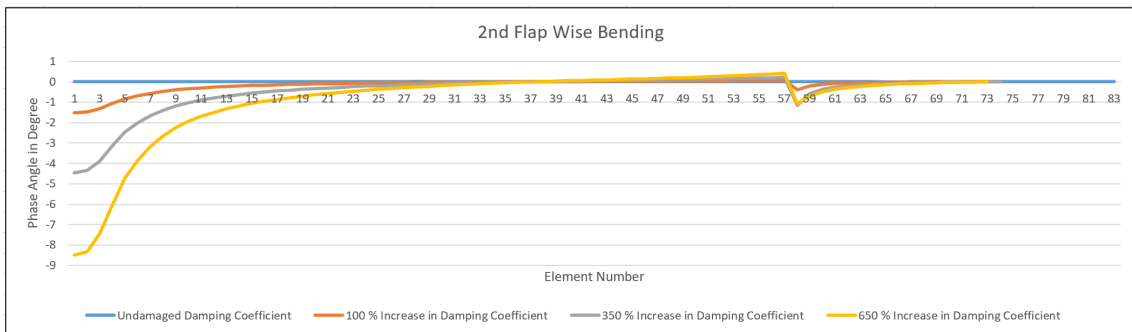


Figure 6.33: Defect identification for scenario 3 case 1 for 2nd flapwise bending frequency

Figure 6.34 shows the change in phase angle for 1st edgewise bending frequency. The maximum deflection for 1st edgewise bending frequency for the microscopic damping coefficients 0.02, 0.045 and 0.75 are about -2.33°, -6.81° and -13.08° respectively.

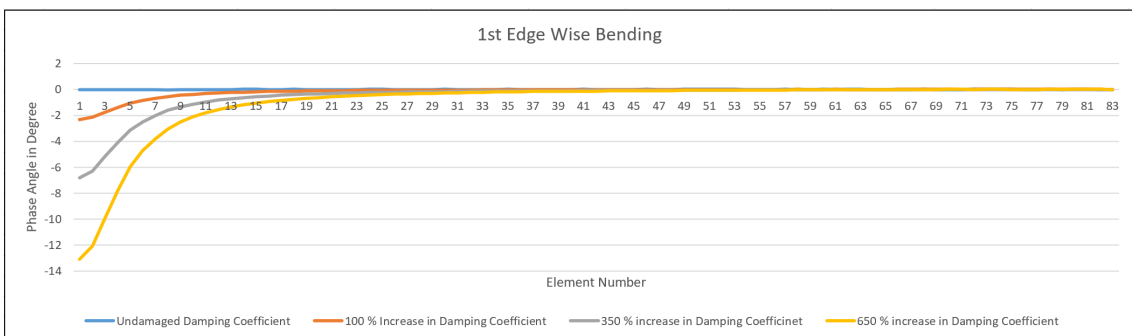


Figure 6.34: Defect identification for scenario 3 case 1 for 1st edgewise bending frequency

Figure 6.35 shows the change in phase angle for 2nd edgewise bending frequency. The maximum deflection for 2nd edgewise bending frequency for phase for the microscopic damping coefficients 0.02, 0.045 and 0.75 are about -2.47°, -7.17° and -13.77° respectively.

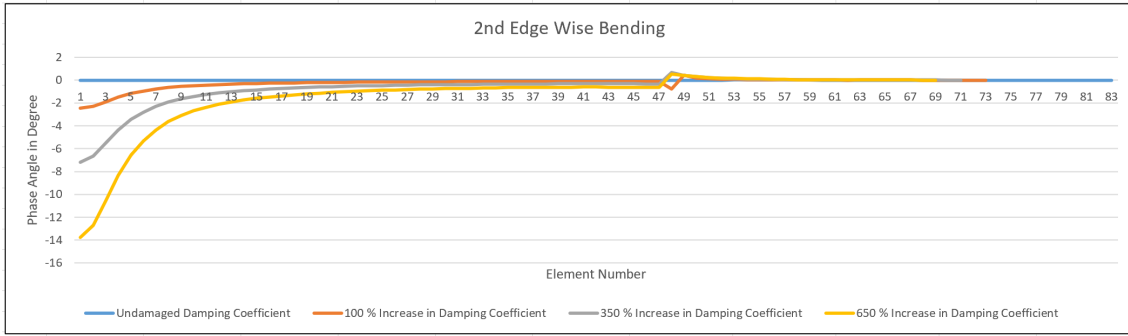


Figure 6.35: Defect identification for scenario 3 case 1 for 2nd edgewise bending frequency

Figures 6.32 and 6.34 clearly shows that the phase angle change is higher near the fixed end for first 2 elements and it keep on increasing and reaches zero for the elements far away from the fixed end.

6.3.2 Case 2: Top and core surface damage near fixed end with 4 % defected area

The following plots show the change in phase angle for each element at different microscopic damping coefficients for a particular frequency for top and core surface defect with 4 % defected area near fixed end. Figure 6.36 shows the basic layout of the damaged elements of this case. The increase in overall damping of the structure calculated using modal damping for the microscopic damping coefficient 0.02, 0.045 and 0.75 is about 8.70 %, 25.31 % and 47.49 %

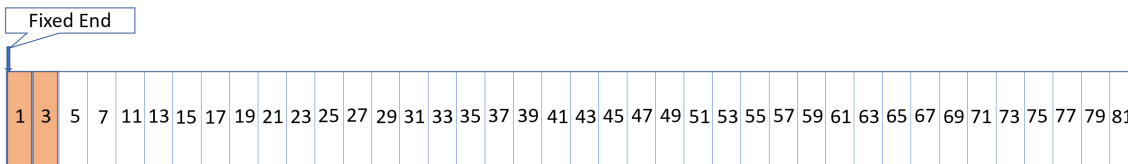


Figure 6.36: Layout of top and core surface damage near fixed end with 4 % defected area

Figure 6.37 shows the change in phase angle for 1st flapwise bending frequency. The maximum deflection for 1st flapwise bending frequency for the microscopic damping coefficients 0.02, 0.045 and 0.75 are about -1.18°, -3.47° and -6.63° respectively.

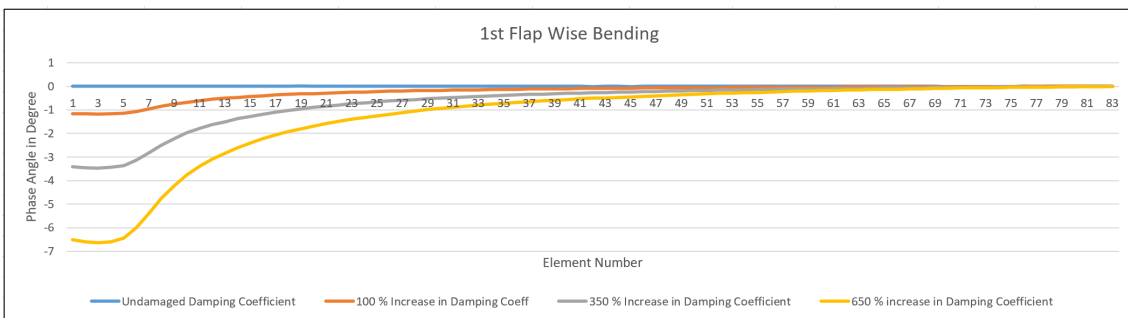


Figure 6.37: Defect identification for scenario 3 case 2 for 1st flapwise bending frequency

Figure 6.38 shows the change in phase angle for 2nd flapwise bending frequency. The maximum deflection for 2nd flapwise bending frequency for the microscopic damping coefficients 0.02, 0.045 and 0.75 are about -1.36°, -3.99° and -7.63° respectively.

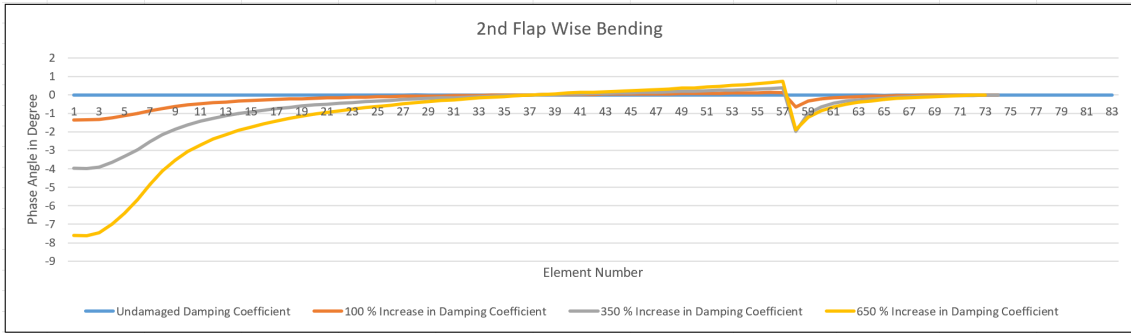


Figure 6.38: Defect identification for scenario 3 case 2 for 2nd flapwise bending frequency

Figure 6.39 shows the change in phase angle for 1st edgewise bending frequency. The maximum deflection for 1st edgewise bending frequency for the microscopic damping coefficients 0.02, 0.045 and 0.75 are about -2.25°, -6.57° and -12.64° respectively.

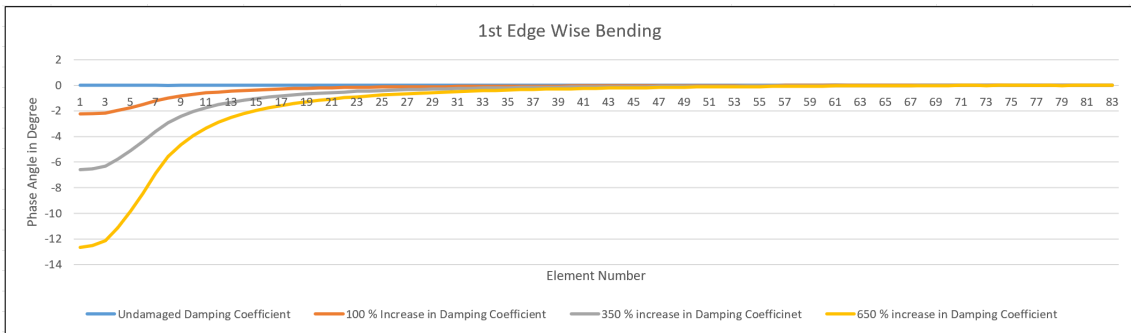


Figure 6.39: Defect identification for scenario 3 case 2 for 1st edgewise bending frequency

Figure 6.40 shows the change in phase angle for 2nd edgewise bending frequency. The maximum deflection for 2nd edgewise bending frequency for the microscopic damping coefficients 0.02, 0.045 and 0.75 are about -2.46°, -7.21° and -13.83° respectively.

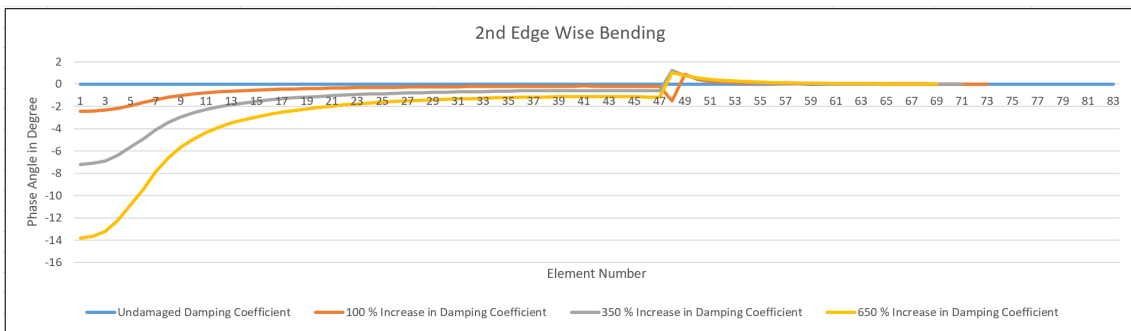


Figure 6.40: Defect identification for scenario 3 case 2 for 2nd edgewise bending frequency

Figures 6.37 and 6.39 clearly shows that the phase angle change is higher near the fixed end for first 4 elements and it keep on increasing and reaches zero for the elements far away from the fixed end.

6.3.3 Case 3: Top and core surface damage near fixed end with 6 % defected area

The following plots show the change in phase angle for each element at different microscopic damping coefficients for a particular frequency for top and core surface defect with 6 % defected area near fixed end. Figure 6.41 shows the basic layout of the damaged elements of this case. The increase in overall damping of the structure calculated using modal damping for the microscopic damping coefficient 0.02, 0.045 and 0.75 is about 12.21 %, 35.45 % and 66.45 %

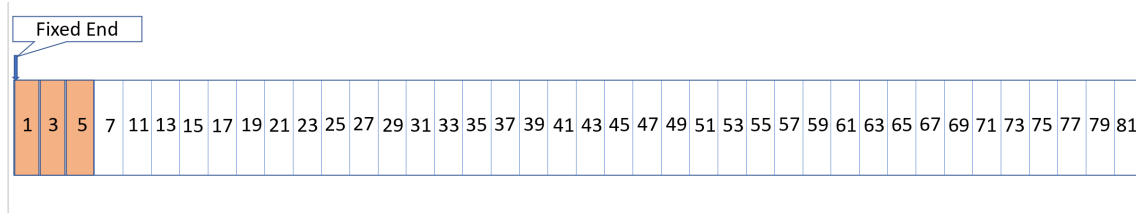


Figure 6.41: Layout of top and core surface damage near fixed end with 6 % defected area

Figure 6.42 shows the change in phase angle for 1st flapwise bending frequency. The maximum deflection for 1st flapwise bending frequency for the microscopic damping coefficients 0.02, 0.045 and 0.75 are about -1.08°, -3.17° and -6.08° respectively.

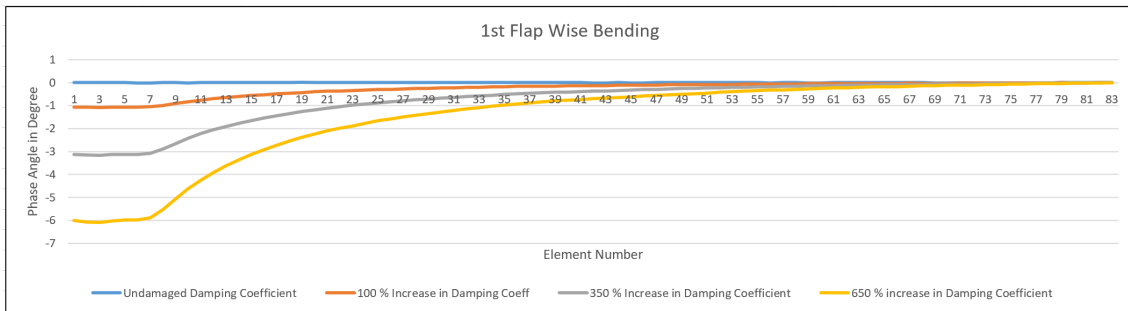


Figure 6.42: Defect identification for scenario 3 case 3 for 1st flapwise bending frequency

Figure 6.43 shows the change in phase angle for 2nd flapwise bending frequency. The maximum deflection for 2nd flapwise bending frequency for the microscopic damping coefficients 0.02, 0.045 and 0.75 are about -1.21°, -3.58° and -6.85° respectively.

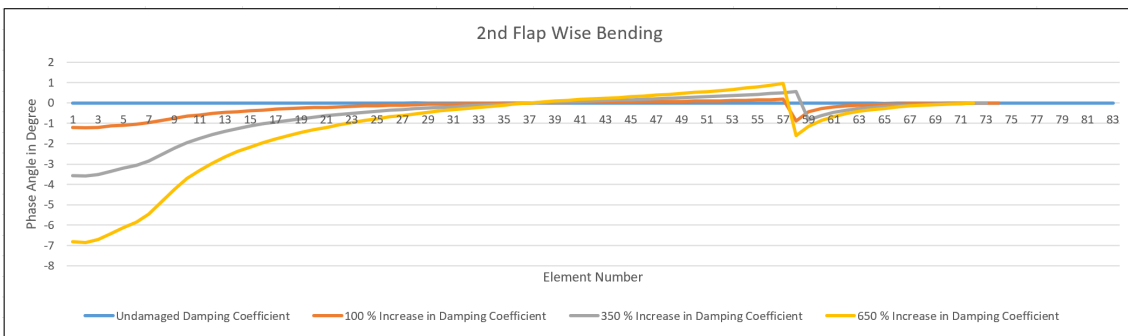


Figure 6.43: Defect identification for scenario 3 case 3 for 2nd flapwise bending frequency

Figure 6.44 shows the change in phase angle for 1st edgewise bending frequency. The maximum deflection for 1st edgewise bending frequency for the microscopic damping coefficients 0.02, 0.045 and 0.75 are about -2.19°, -6.40° and -12.33° respectively.

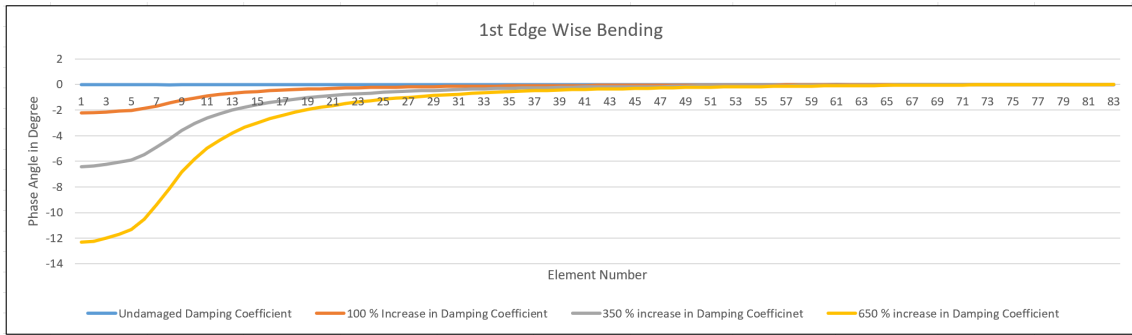


Figure 6.44: Defect identification for scenario 3 case 3 for 1st edgewise bending frequency

Figure 6.45 shows the change in phase angle for 2nd edgewise bending frequency. The maximum deflection for 2nd edgewise bending frequency for the microscopic damping coefficients 0.02, 0.045 and 0.75 are about -2.48°, -7.23° and -13.90° respectively.

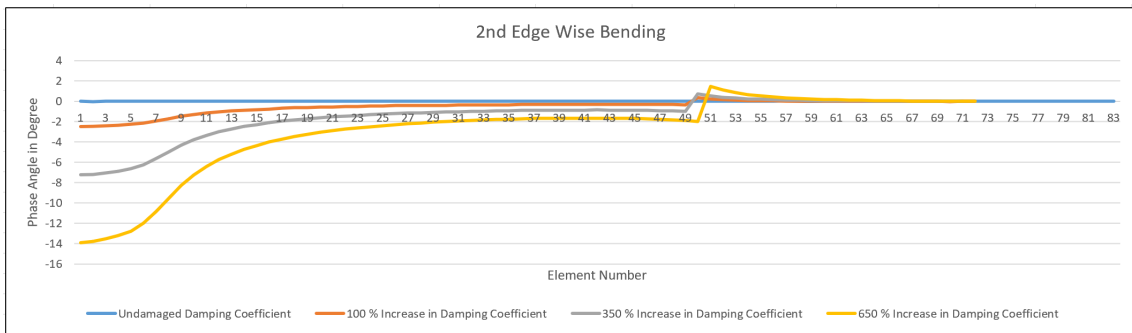


Figure 6.45: Defect identification for scenario 3 case 3 for 2nd edgewise bending frequency

Figures 6.42 and 6.44 clearly shows that the phase angle change is higher near the fixed end for first 6 elements and it keep on increasing and reaches zero for the elements far away from the fixed end.

6.4 Scenario 4: Damage in top and core surfaces near mid section with 2 %, 4 %, 6 % defected area

6.4.1 Case 1: Top and core surface damage near mid section with 2 % defected area

The following plots show the change in phase angle for each element at different microscopic damping coefficients for a particular frequency for top and core surface defect with 2 % defected area near the midsection. Figure 6.46 shows the basic layout of the damaged elements of this case. The increase in overall damping of the structure calculated using modal damping for the microscopic damping coefficient 0.02, 0.045 and 0.75 is about 0.51 %, 1.39 % and 2.58 %.

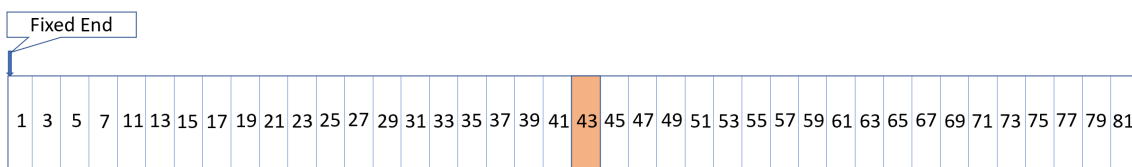


Figure 6.46: Layout of top and core surface damage near mid section with 2 % defected area

Figure 6.47 shows the change in phase angle for 1st flapwise bending frequency. The maximum deflection for 1st flapwise bending frequency for the microscopic damping coefficients 0.02, 0.045 and 0.75 are about 0.014°, 0.055° and 0.093° respectively.

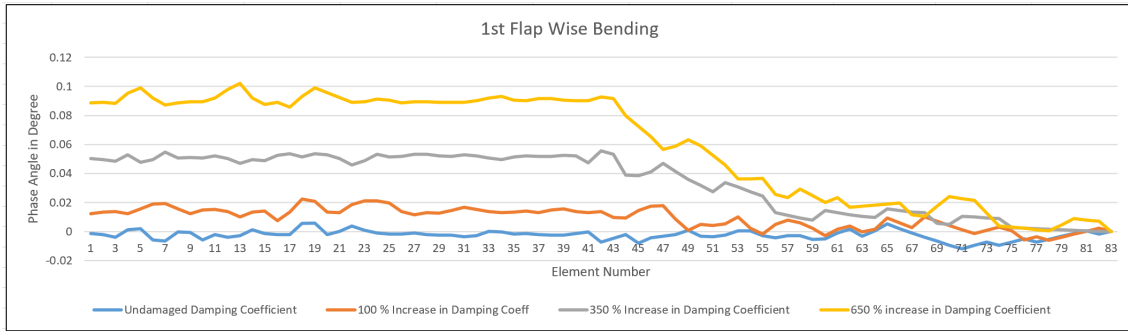


Figure 6.47: Defect identification for scenario 4 case 1 for 1st flapwise bending frequency

Figure 6.48 shows the change in phase angle for 2nd flapwise bending frequency. The maximum deflection for 2nd flapwise bending frequency for the microscopic damping coefficients 0.02, 0.045 and 0.75 are about -0.039°, -0.119° and -0.213° respectively.

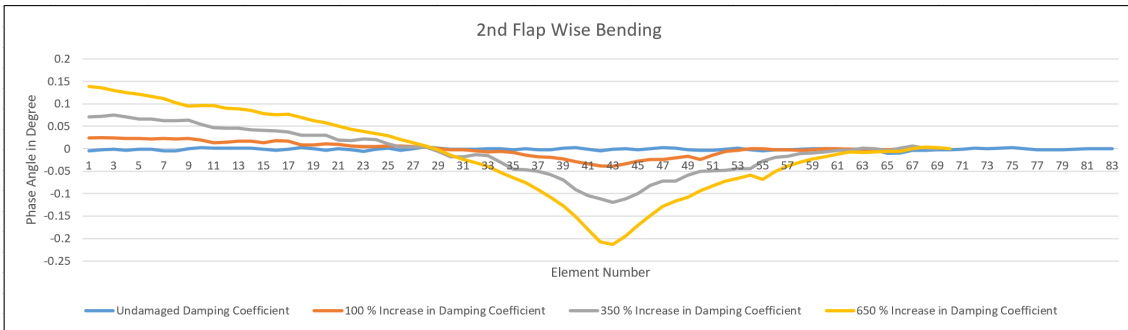


Figure 6.48: Defect identification for scenario 4 case 1 for 2nd flapwise bending frequency

Figure 6.49 shows the change in phase angle for 1st edgewise bending frequency. The maximum deflection for 1st edgewise bending frequency for the microscopic damping coefficients 0.02, 0.045 and 0.75 are about 0.019°, 0.057° and 0.107° respectively.

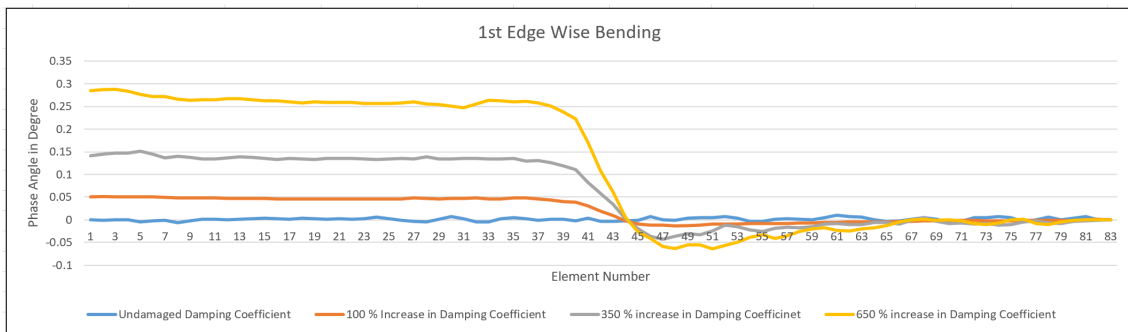


Figure 6.49: Defect identification for scenario 4 case 1 for 1st edgewise bending frequency

Figure 6.50 shows the change in phase angle for 2nd edgewise bending frequency. The maximum deflection for 2nd edgewise bending frequency for the microscopic damping coefficients 0.02, 0.045 and 0.75 are about 0.166°, 0.540° and 1.036° respectively.

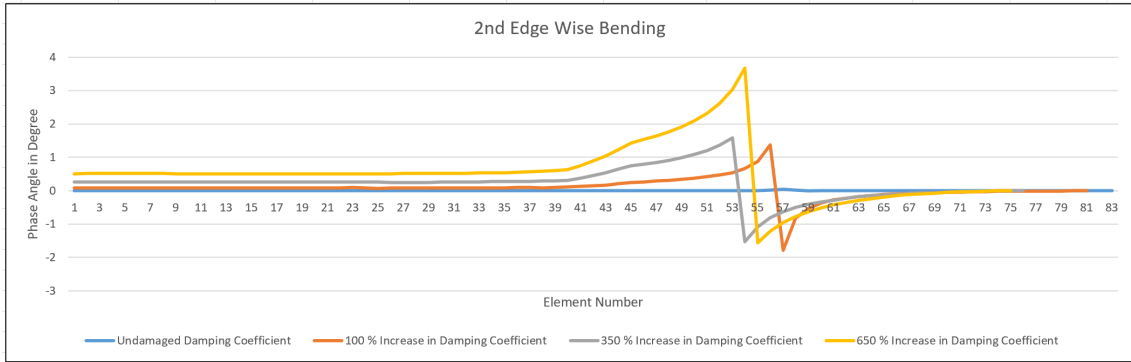


Figure 6.50: Defect identification for scenario 4 case 1 for 2nd edgewise bending frequency

Figure 6.48 clearly shows that the phase angle change is positive near the fixed end and it keeps reducing and reaches maximum change in phase angle around the elements 42, 43 (2 damaged elements) and the value keep on increasing and reaches zero for the elements far away from the damaged elements.

6.4.2 Case 2: Top and core surface damage near mid section with 4 % defected area

The following plots show the change in phase angle for each element at different microscopic damping coefficients for a particular frequency for top and core surface defect with 4 % defected area near the midsection. Figure 6.51 shows the basic layout of the damaged elements of this case. The increase in overall damping of the structure calculated using modal damping for the microscopic damping coefficient 0.02, 0.045 and 0.75 is about 1.01 %, 3.00 % and 5.58 %.

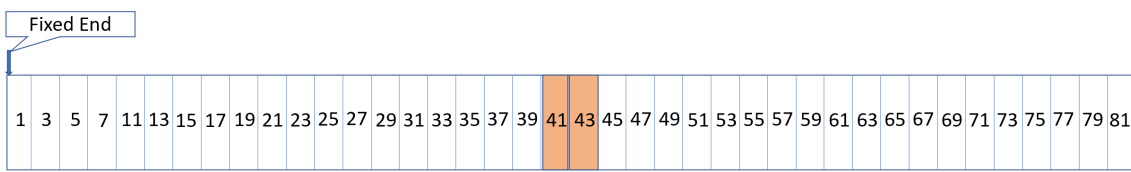


Figure 6.51: Layout of top and core surface damage near mid section with 4 % defected area

Figure 6.52 shows the change in phase angle for 1st flapwise bending frequency. The maximum deflection for 1st flapwise bending frequency for the microscopic damping coefficients 0.02, 0.045 and 0.75 are about 0.046°, 0.101° and 0.195° respectively.

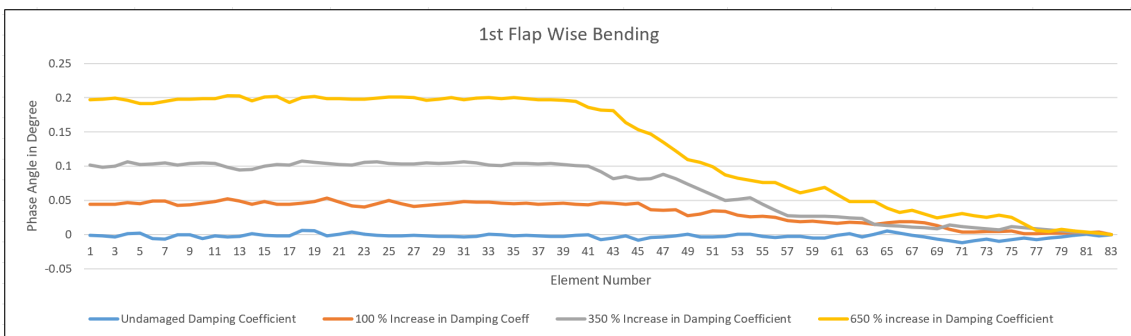


Figure 6.52: Defect identification for scenario 4 case 2 for 1st flapwise bending frequency

Figure 6.53 shows the change in phase angle for 2nd flapwise bending frequency. The maximum deflection for 2nd flapwise bending frequency for the microscopic damping coefficients 0.02, 0.045 and 0.75 are about -0.0765°, -0.224° and -0.416° respectively.

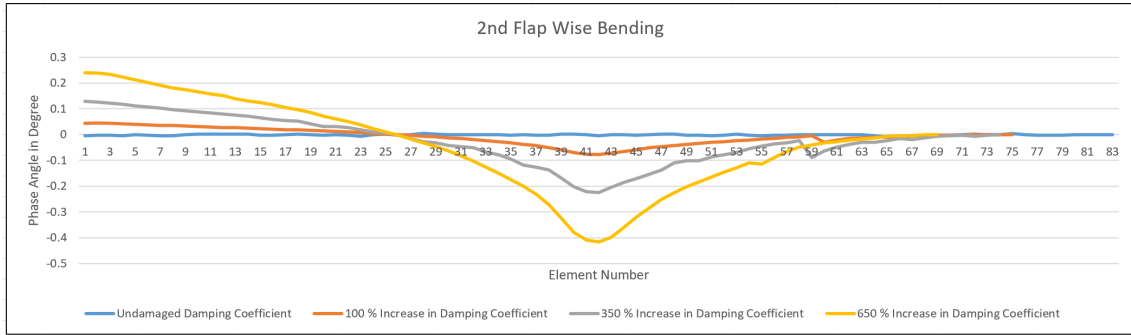


Figure 6.53: Defect identification for scenario 4 case 2 for 2nd flapwise bending frequency

Figure 6.54 shows the change in phase angle for 1st edgewise bending frequency. The maximum deflection for 1st edgewise bending frequency for the microscopic damping coefficients 0.02, 0.045 and 0.75 are about 0.058°, 0.168° and 0.317° respectively.

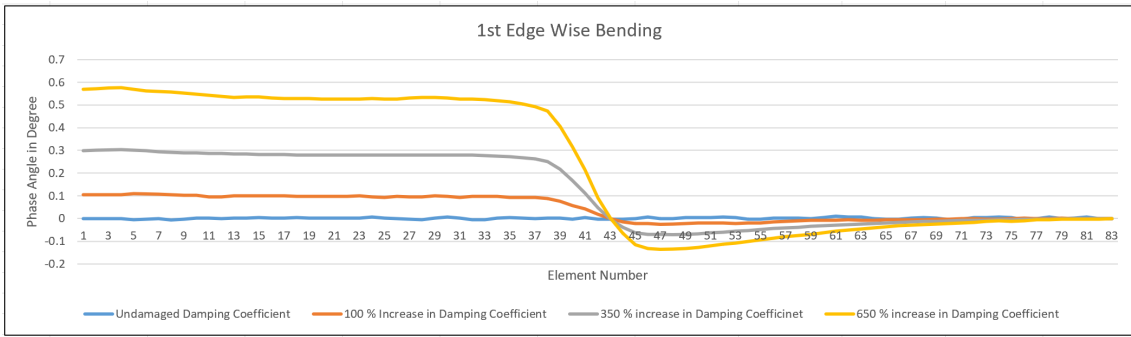


Figure 6.54: Defect identification for scenario 4 case 2 for 1st edgewise bending frequency

Figure 6.55 shows the change in phase angle for 2nd edgewise bending frequency. The maximum deflection for 2nd edgewise bending frequency for the microscopic damping coefficients 0.02, 0.045 and 0.75 are about 0.416°, 1.22° and 2.35° respectively.

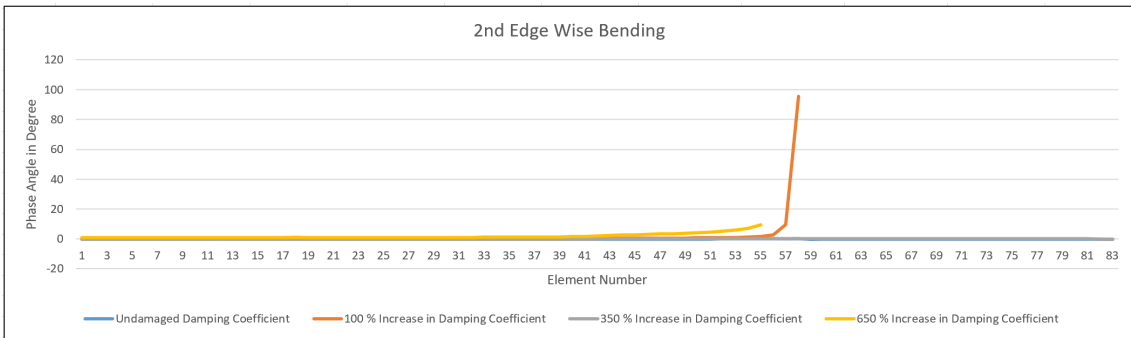


Figure 6.55: Defect identification for scenario 4 case 2 for 2nd edgewise bending frequency

Figure 6.53 clearly shows that the phase angle change is positive near the fixed end; it keeps reducing and reaches maximum change in phase angle around the elements 40, 41, 42 and 43 (4 damaged elements) and the value keep on increasing and reaches zero for the elements far away from the damaged elements.

6.4.3 Case 3: Top and core surface damage near mid section with 6 % defected area

The following plots show the change in phase angle for each element at different microscopic damping coefficients for a particular frequency for top and core surface defect with 6 % defected area near the midsection. Figure 6.56 shows the basic layout of the damaged elements of this case. The increase in overall damping of the structure

calculated using modal damping for the microscopic damping coefficient 0.02, 0.045 and 0.75 is about 1.44 %, 4.22 % and 7.86 %.

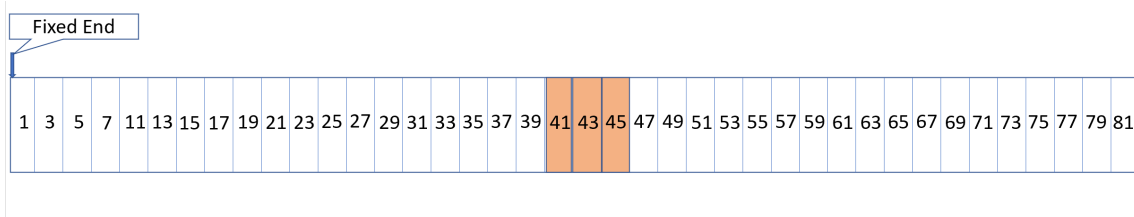


Figure 6.56: Layout of top and core surface damage near mid section with 6 % defected area

Figure 6.57 shows the change in phase angle for 1st flapwise bending frequency. The maximum deflection for 1st flapwise bending frequency for the microscopic damping coefficients 0.02, 0.045 and 0.75 are about 0.0518°, 0.147° and 0.272° respectively.

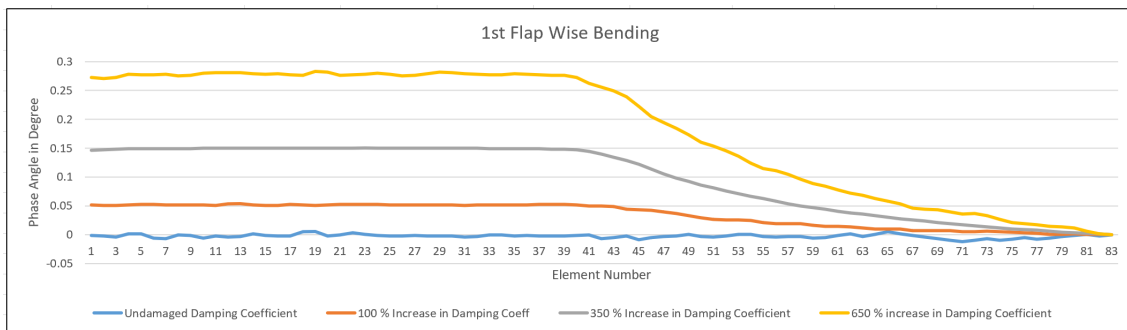


Figure 6.57: Defect identification for scenario 4 case 3 for 1st flapwise bending frequency

Figure 6.58 shows the change in phase angle for 2nd flapwise bending frequency. The maximum deflection for 2nd flapwise bending frequency for the microscopic damping coefficients 0.02, 0.045 and 0.75 are about -0.105°, -0.304° and -0.563° respectively.

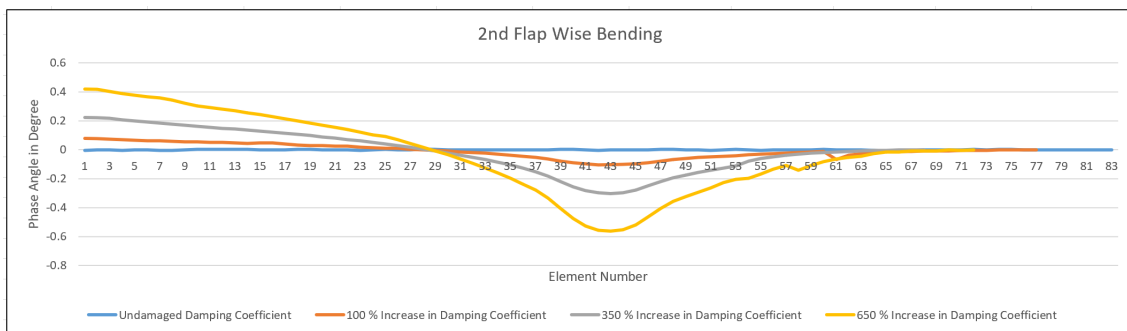


Figure 6.58: Defect identification for scenario 4 case 3 for 2nd flapwise bending frequency

Figure 6.59 shows the change in phase angle for 1st edgewise bending frequency. The maximum deflection for 1st edgewise bending frequency for the microscopic damping coefficients 0.02, 0.045 and 0.75 are about 0.100°, 0.299° and 0.553° respectively.

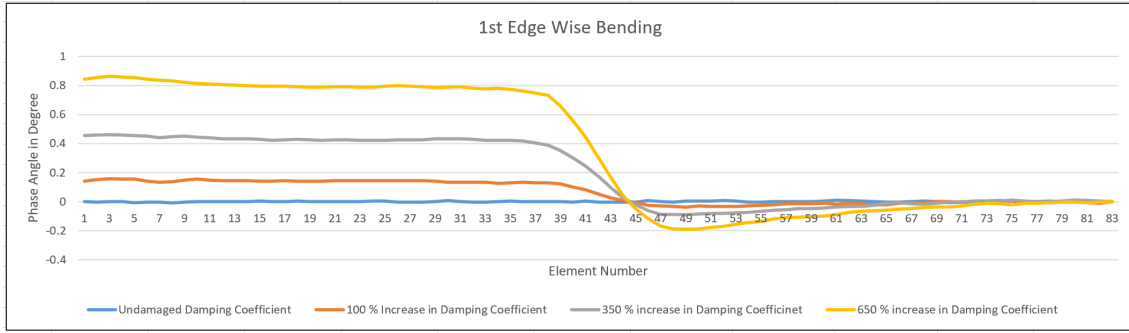


Figure 6.59: Defect identification for scenario 4 case 3 for 1st edgewise bending frequency

Figure 6.60 shows the change in phase angle for 2nd edgewise bending frequency. The maximum defection for 2nd edgewise bending frequency for the microscopic damping coefficients 0.02, 0.045 and 0.75 are about 0.71°, 2.07° and 3.97° respectively.

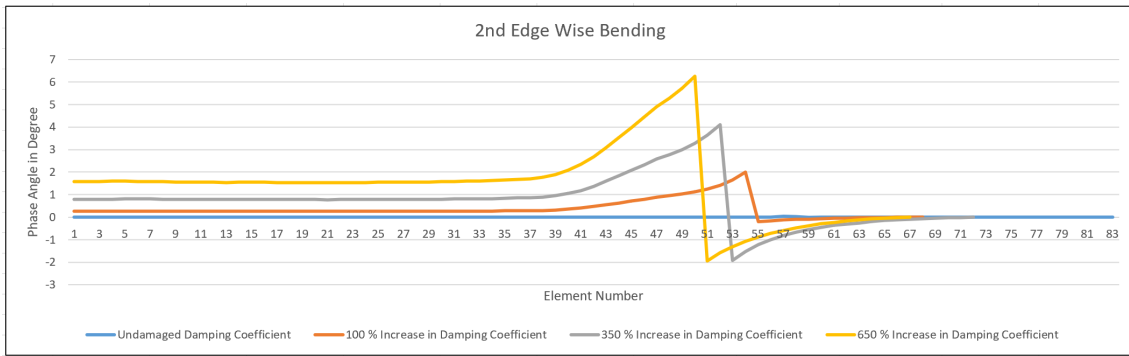


Figure 6.60: Defect identification for scenario 4 case 3 for 2nd edgewise bending frequency

Figure 6.58 clearly shows that the phase angle change is positive near the fixed end; it keeps reducing and reaches maximum change in phase angle around the elements 40, 41, 42, 43, 44 and 45 (6 damaged elements) and the value keep on increasing and reaches zero for the elements far away from the damaged elements. As the microscopic damping is increased, the modal damping of the structure also increases. This means that as the damage increases the damping of the structure also increases. From the above plots, following results are observed.

1. 1st flap and edgewise bending frequencies are suitable for identifying the defects near the fixed end.
2. 2nd flapwise bending frequency is suitable for identifying the defect near the mid area. However, 2nd edgewise bending frequency is not suitable for identifying the defect near the mid area.
3. The phase angle change of defected elements and the modal damping percent increase is more for scenarios 3 and 4 compared to scenarios 1 and 2. It shows that the defect in the top and core areas affects the modal parameters more compared to defect only in the top surface.

The results discussed in the above chapter is compiled in table 6.1 for easy comparison and understanding. The values given in this table is the maximum difference between the phase angle of defected elements and the maximum phase angle θ_m . The maximum phase angle θ_m not necessarily be at the defected nodes (or) elements. A threshold value of 2° is chosen from an experimental study to highlight the given values in red. These values would be useful to identify the microscopic damping conditions which are suitable to localize the defect. Also, the phase angle corresponding to 2nd flapwise bending frequency of scenarios 2 and 4 is highlighted in orange to show that this 2nd flapwise frequency is suitable to identify defects at the midsection. From the table 6.1, it can be observed that

- The 2nd flapwise bending frequency can be potentially used to detect the damage in the midsection for a higher level of damage i.e., higher microscopic damping with a loss factor greater than 0.075.

- Even though the change in phase angle of defected elements corresponding to 2nd edgewise bending frequency is more than that of 2nd flapwise bending frequency in scenarios 2 and 4, 2nd edgewise bending frequency is not suitable for identifying defects near the midsection because the defected elements are closer to the nodes with zero displacement. As explained in chapter 5.2, these nodes (or) elements have higher phase angle change compared to other elements.

Table 6.1: Change in phase angle of the structure for different loss factor (microscopic damping coefficients)

			Loss factor		
			0.02	0.045	0.075
Scenario 1 (Top surface defect near fixed end)	Case 1 (2 % defected area)	1 st flapwise bending frequency	-0.85°	-2.49°	-4.73°
		2 nd flapwise bending frequency	-0.68°	-2.01°	-3.81°
		1 st edgewise bending frequency	-2.29°	-6.69°	-12.87°
		2 nd edgewise bending frequency	-2.43°	-7.04°	-13.50°
	Case 2 (4 % defected area)	1 st flapwise bending frequency	-0.75°	-2.22°	-4.21°
		2 nd flapwise bending frequency	-0.52°	-1.53°	-2.92°
		1 st edgewise bending frequency	-2.15°	-6.29°	-12.11°
		2 nd edgewise bending frequency	177.83°	-6.90°	-13.27°
	Case 3 (6 % defected area)	1 st flapwise bending frequency	-0.73°	-2.15°	-4.09°
		2 nd flapwise bending frequency	-0.47°	-1.38°	-2.62°
		1 st edgewise bending frequency	-2.07°	-6.06°	-11.66°
		2 nd edgewise bending frequency	-2.37°	-6.91°	-13.29°
Scenario 2 (Top surface defect near mid section)	Case 1 (2 % defected area)	1 st flapwise bending frequency	0.0047°	0.043°	0.083°
		2 nd flapwise bending frequency	-0.036°	-0.11°	-0.211°
		1 st edgewise bending frequency	0.015°	0.033°	0.071°
		2 nd edgewise bending frequency	0.062°	0.15°	0.29°
	Case 2 (4 % defected area)	1 st flapwise bending frequency	0.032°	0.094°	0.18°
		2 nd flapwise bending frequency	-0.067°	-0.207°	-0.385°
		1 st edgewise bending frequency	0.047°	0.133°	0.246°
		2 nd edgewise bending frequency	0.15°	0.43°	0.80°
	Case 3 (6 % defected area)	1 st flapwise bending frequency	0.046°	0.133°	0.247°
		2 nd flapwise bending frequency	-0.095°	-0.284°	-0.519°
		1 st edgewise bending frequency	0.086°	0.237°	0.428°
		2 nd edgewise bending frequency	0.29°	0.83°	1.56°
Scenario 3 (Top and core defect near fixed end)	Case 1 (2 % defected area)	1 st flapwise bending frequency	-1.35°	-3.98°	-7.65°
		2 nd flapwise bending frequency	-1.52°	-4.46°	-8.51°
		1 st edgewise bending frequency	-2.33°	-6.81°	-13.08°
		2 nd edgewise bending frequency	-2.47°	-7.17°	-13.77°
	Case 2 (4 % defected area)	1 st flapwise bending frequency	-1.18°	-3.47°	-6.63°
		2 nd flapwise bending frequency	-1.36°	-3.99°	-7.63°
		1 st edgewise bending frequency	-2.25°	-6.57°	-12.64°
		2 nd edgewise bending frequency	-2.46°	-7.21°	-13.83°
	Case 3 (6 % defected area)	1 st flapwise bending frequency	-1.08°	-3.17°	-6.08°
		2 nd flapwise bending frequency	-1.21°	-3.58°	-6.85°
		1 st edgewise bending frequency	-2.19°	-6.40°	-12.33°
		2 nd edgewise bending frequency	-2.48°	-7.23°	-13.90°
Scenario 4 (Top and core defect near mid section)	Case 1 (2 % defected area)	1 st flapwise bending frequency	0.014°	0.055°	0.093°
		2 nd flapwise bending frequency	-0.039°	-0.119°	-0.213°
		1 st edgewise bending frequency	0.019°	0.057°	0.107°
		2 nd edgewise bending frequency	0.166°	0.540°	1.036°
	Case 2 (4 % defected area)	1 st flapwise bending frequency	0.046°	0.101°	0.195°
		2 nd flapwise bending frequency	-0.0765°	-0.224°	-0.416°
		1 st edgewise bending frequency	0.058°	0.168°	0.317°
		2 nd edgewise bending frequency	0.416°	1.22°	2.35°
	Case 3 (6 % defected area)	1 st flapwise bending frequency	0.0518°	0.147°	0.272°
		2 nd flapwise bending frequency	-0.105°	-0.304°	-0.563°
		1 st edgewise bending frequency	0.100°	0.299°	0.553°
		2 nd edgewise bending frequency	0.71°	2.07°	3.97°

7 Sensitivity Analysis

A sensitive analysis is done to check how the results vary for different element sizes. For this analysis, the element size for meshing was changed from 25cm to 40 cm and 20 cm. The number of elements and nodes are 658 and 1136 for element size of 40 cm and 2822 and 3928 for element size of 20 cm. As explained earlier in chapter 4.3 the RAM was not sufficient to extract matrix from ANSYS for element size 20cm. So, damage identification and localization calculation are not performed for this element size.

The damage modelling is done for structure with an element size of 40 cm. For simplicity, only two scenarios,

1. Damage at the fixed end with 2 % defected area
2. Damage at the midsection with 2 % defected area

are considered to modal damage into the structure. Also, microscopic damping coefficient of 0.075 is considered for this analysis. Since the element size is 40 cm, there are 8 defected elements in each case. The modal damping is calculated using the formula 5.2. The results obtained are as follows.

Table 7.1: Sensitivity analysis results: Modal damping calculation

Case	Eigen Value	Modal Damping	% Increasing in damping
Undamaged	$-1.573 + 6.885i$	0.2227	-
Damage at fixed end	$-1.631 + 6.956i$	0.2283	2.51
Damage at mid section	$-1.6315 + 6.933i$	0.2295	3.05

The phase angle is calculated using formula 5.7 and formula 5.8 is used to identify the damaged elements. The change in phase angle corresponding to 1st and 2nd flapwise and edgewise bending frequency is given in below table.

Table 7.2: Sensitivity analysis results: Change in phase angle

Case	frequency	Change in phase angle in degree
Damage at fixed end	1 st flapwise bending frequency	-32.11°
	2 nd flapwise bending frequency	-33.054°
	1 st edgewise bending frequency	-29.23°
	2 nd edgewise bending frequency	-29.03°
Damage at mid section	1 st flapwise bending frequency	0.152°
	2 nd flapwise bending frequency	-1.44°
	1 st edgewise bending frequency	0.392°
	2 nd edgewise bending frequency	-0.805°

The change in phase angle and node identification plots for defect at the fixed end case for microscopic damping coefficient of 0.075 is as follows.

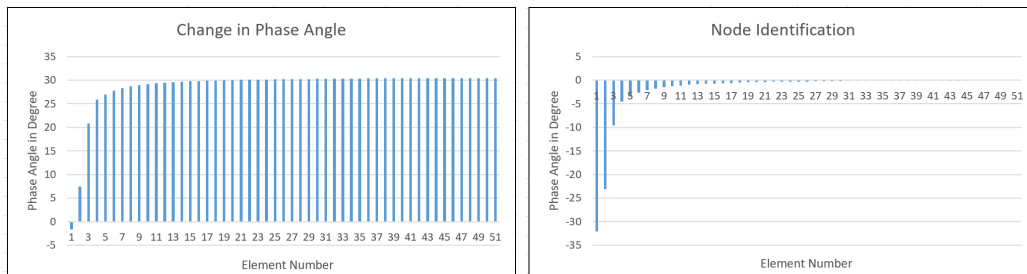


Figure 7.1: Fixed end defect: 1st flapwise bending frequency

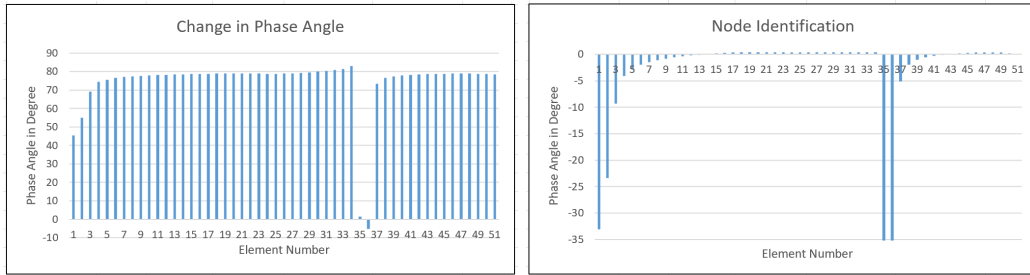


Figure 7.2: Fixed end defect: 2nd flapwise bending frequency

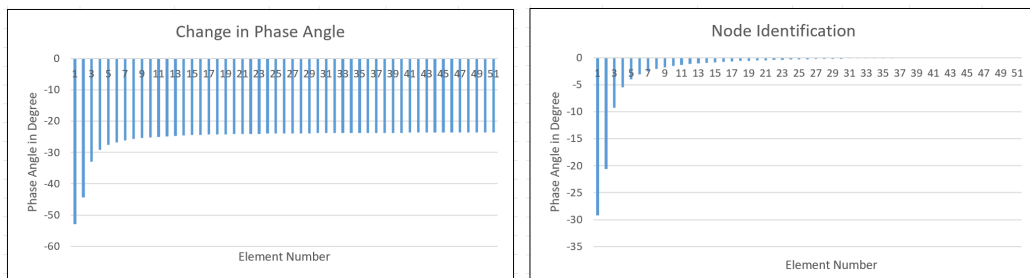


Figure 7.3: Fixed end defect: 1st edgewise bending frequency

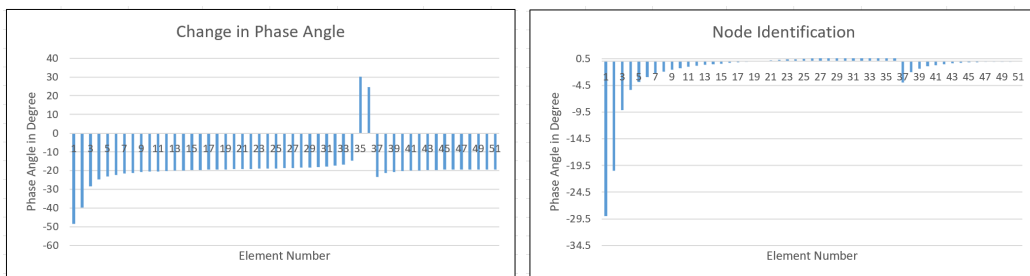


Figure 7.4: Fixed end defect: 2nd edgewise bending frequency

Following are the change in phase angle and node identification plots for defect at midsection case for microscopic damping coefficient of 0.075.

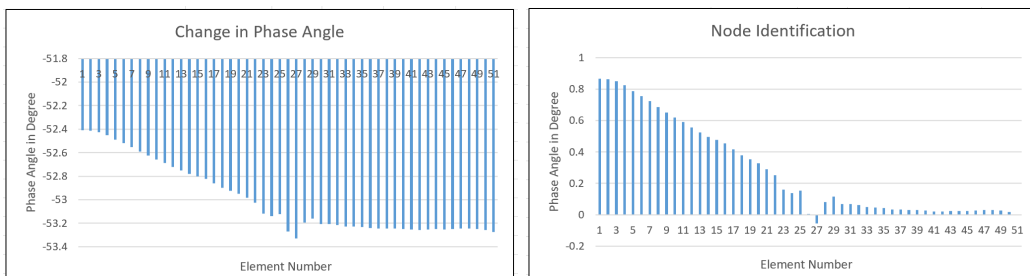
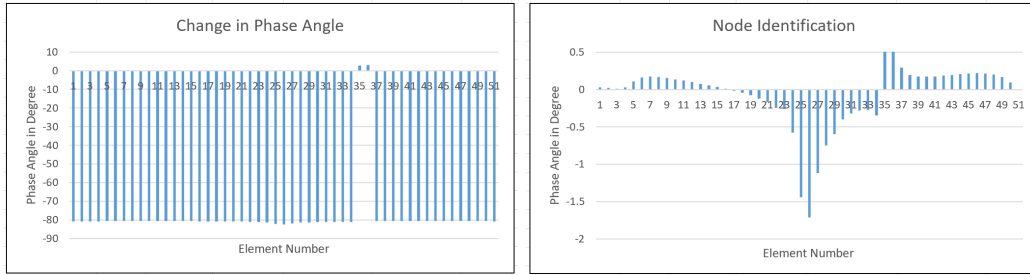
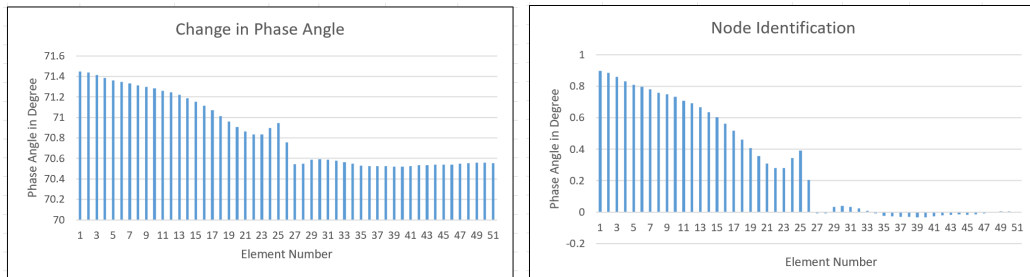
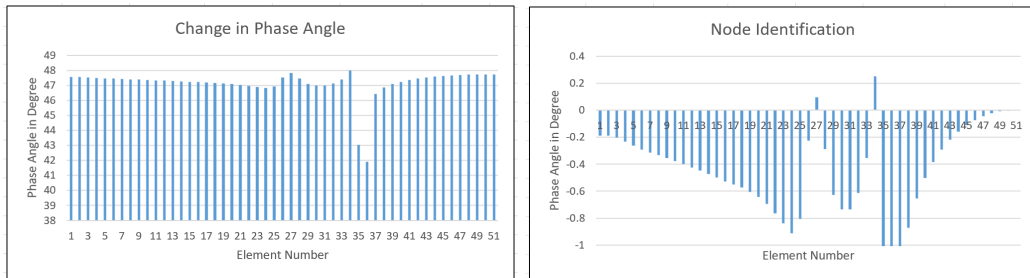


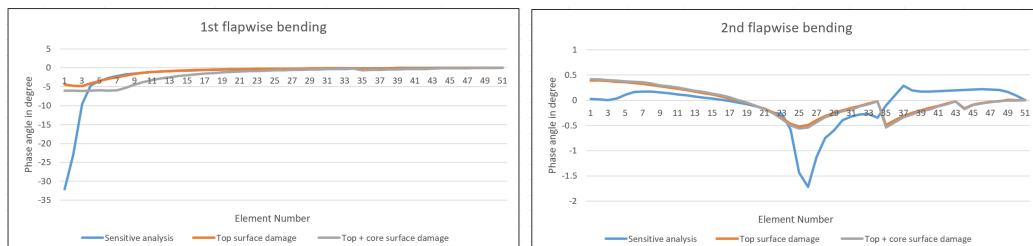
Figure 7.5: Midsection defect: 1st flapwise bending frequency

Figure 7.6: Midsection defect: 2^{nd} flapwise bending frequencyFigure 7.7: Midsection defect: 1^{st} edgewise bending frequencyFigure 7.8: Midsection defect: 2^{nd} edgewise bending frequency

From the above plots, it is evident that 1^{st} flapwise and edgewise bending frequency is suitable for identifying defects at the fixed end and 2^{nd} flapwise bending frequency is suitable for identifying defects near the midsection. Also, these plots follow a similar pattern as the plots given in chapter 5.2, which proves that this model provides similar results for different element size. To show this the change in phase angle for each element obtained from sensitive analysis results is compared with the results of following cases

- Top surface damage near fixed end with 6 % defected area and top and core surface damage near fixed end with 6 % defected area.
- Top surface damage near midsection with 6 % defected area and top and core surface damage near midsection with 6 % defected area.

for the loss factor 0.075 in figure 7.9.

Figure 7.9: Comparison of results for 1^{st} and 2^{nd} flapwise bending frequency

8 Conclusion and Recommendation

In this chapter, the important results and findings of the thesis are explained. Later, some recommendations for future work are given. The main objective of this thesis is to use smeared crack modelling and integrating it with FEM tools to identify the damage in the wind turbine blade. After reviewing the literature, two research questions were formulated

1. Can increase in material damping due to defect initiation be used effectively to identify the defect location and size effectively?
 - Can the modal damping be used to identify defect in spar cap and shear web assembly?
2. Is it possible to model the vibration analysis based on the viscoelastic damping?

8.1 Using increase in modal damping percent to identify damage location and size

The first objective of the thesis is to formulate a finite element model to identify damage location and size using increase in modal damping percent. A wind turbine blade is made up of aerodynamic shell (spar cap) and shear web. To reduce complications, the spar cap - shear web assembly is modelled as "I" beam in ANSYS. The dimension of the blade is measured from the "NedWind 40 turbine" provided by LM Wind Power. The structure has been modelled using composite materials. The spar cap fibres are laid at 0° , and the fibres of face sheet are laid at $\pm 45^\circ$. One end of the structure is fixed to simulate the actual working conditions. Similarly, the material property of all parts was chosen to represent an actual wind turbine blade. The element size was selected to be about 25 cm for meshing. The number of elements and nodes after meshing are 1476 and 2241 respectively. Using Modal Analysis in ANSYS, the natural frequency of the undamaged blade structure was calculated. Damage is introduced into the structure in the form of microscopic damping into the material property using formula 4.1. To incorporate damping into the structure, the loss factor equation derived from experiment [54] is used. The loss factor parameters (a,b and c) depends on natural frequency. The value of a,b and c for the 1st natural frequency is used to calculate six different microscopic damping coefficients. Mass matrix and stiffness matrix of the structure is extracted from ANSYS for six microscopic damping coefficients. Using the extracted mass and stiffness matrices, eigenvalue and eigenvector of the structure is calculated. Four scenarios with three defect cases are considered to model the damage into the structure. The scenarios are

1. Damage only in top surfaces near fixed end with 2 %, 4 %, 6 % defected area.
2. Damage only in top surfaces near mid section with 2 %, 4 %, 6 % defected area.
3. Damage in top and core surfaces near fixed end with 2 %, 4 %, 6 % defected area.
4. Damage in top and core surfaces near mid section with 2 %, 4 %, 6 % defected area.

Eigenvalue was used to calculate the modal damping using the formula 5.2.

From chapter 5.2, it is noticeable that the modal damping of the damaged structure is higher than that of the undamaged structure. Also, the modal damping percent increases significantly when the microscopic damping increases. This means that the damping of the structure increase when the severity of the damage increases.

The displacement is given by the eigenvector, which is used to calculate the phase angle for each element. The change in phase angle is used to localize the damaged elements. There will be a lag in the phase angle of a damaged element compared to the phase angle of the undamaged element. Chapter 6 shows plots of change in phase of each element for different microscopic damping coefficients. The observations from these plots are as follows

1. 1st flap and edgewise bending frequencies are suitable for identifying the defects near the fixed end.
2. 2nd flap wise bending frequency is suitable for identifying the defect near the mid area. However, 2nd edgewise bending frequency is not suitable for identifying the defect near the mid area.
3. The phase angle change of defected elements and increase modal damping percent is more for scenarios 3 and 4 compared to scenarios 1 and 2. It means that the defect in the top and core areas affects the modal parameters more compared to defect only in the top surface.

To answer the first research question, the increase in damping of the structure shows that the structure is damaged. 1st flapwise and edgewise bending frequencies are suitable for localizing the defects near the fixed end and 2nd flapwise bending frequency is suitable for localizing the defect near the mid area. Also, modal damping

increase percent and change in phase angle is higher for top and core defects compared to defects only at top surfaces.

This method is more suitable for identifying defects in the fixed end and midsection because, the kinetic energy transfer through the elements will be higher at the fixed end and it will gradually decrease and reaches to almost zero for the elements away from the fixed end. This is the reason why the increase in modal damping percent is less for the defects around the midsection (scenarios 2 and 4). Since the kinetic energy of the elements near the tail end is very low, the change in phase angle is very less to identify the defected elements in these areas.

8.2 Modelling the vibration analysis based on the viscoelastic damping

The second objective of the thesis is to model the vibration analysis based on viscoelastic damping. From chapter 2.4 it is understandable that the viscoelastic damping depends on frequency. To answer this research question, as explained in the previous section 8.1 the damage is introduced into the structure in the form of microscopic damping. The loss factor parameters obtained from experiment [54] is used to incorporate damping into the material property. The value of a,b and c depends on natural frequency. For this thesis, the frequency corresponding to 1st flap wise bending is considered for all scenarios and damaged conditions.

8.3 Future work

In future, the thesis can be developed further in the following ways.

1. The length of the current ANSYS model is 20m. Compared to the present wind turbine blade lengths, the length of the blade modelled is small. So in future, the longer blades can be modelled and analysed.
2. Current mesh size of the model is 25 cm, in future more complex meshing can be done to get more accurate results.
3. As explained in the chapter 8.2, only 1st flap wise bending frequency is considered now for modelling viscoelastic damping. Continuing this thesis in future more detailed analysis can be done by considering other frequencies to model viscoelastic damping.

References

1. Abdulraheem, K. F., & Al-Kindi, G. (2017). A simplified wind turbine blade crack identification using experimental modal analysis (ema). *International Journal of Renewable Energy Research*, Vol.7, No.2. Retrieved from <https://www.ijrer.org/ijrer/index.php/ijrer/article/view/5617/pdf>
2. Agarwalla, D., & Parhi, D. (2013). Effect of crack on modal parameters of a cantilever beam subjected to vibration. *Procedia Engineering: Chemical, Civil and Mechanical Engineering Tracks of the 3rd Nirma University International Conference*. Retrieved from [sciencedirect.com/science/article/pii/S1877705813000957](https://www.sciencedirect.com/science/article/pii/S1877705813000957)
3. A. K, B., & P. Sankar, T. K. P. (2008). Crack detection in cantilever beam using vibration response. *Vibration Problems*. Retrieved from https://link.springer.com/chapter/10.1007/978-1-4020-9100-1_4#citeas doi: https://doi.org/10.1007/978-1-4020-9100-1_4
4. Andrew, H. (1998). Dynamic analysis of both on and offshore wind turbines in the frequency domain. *University of London*. Retrieved from <https://discovery.ucl.ac.uk/id/eprint/1317858/1/287980.pdf>
5. ANSYS. (2020a, 08). *Damp command reference*. Retrieved from https://www.mm.bme.hu/~gyebro/files/ans_help_v182/ans_cmd/Hlp_C_MODALOPT.html
6. ANSYS. (2020b, 02). *Dmat command reference*. Retrieved from https://www.mm.bme.hu/~gyebro/files/ans_help_v182/ans_cmd/Hlp_C_DMAT.html
7. ANSYS. (2020c, 07). *Eigen command reference*. Retrieved from https://www.mm.bme.hu/~gyebro/files/ans_help_v182/ans_cmd/Hlp_C_EIGEN.html
8. ANSYS. (2020d, 07). *Export command reference*. Retrieved from https://www.mm.bme.hu/~gyebro/files/ans_help_v182/ans_cmd/Hlp_C_EXPORT.html
9. Ashwani, K., Arpit, D., Vipul, P., & Pravin, P. (2014). Free vibration analysis of a 2024 wind turbine blade designed for uttarakhand region based on fea. *Procedia Technology*. Retrieved from <https://www.sciencedirect.com/science/article/pii/S2212017314000802> doi: <https://doi.org/10.1016/j.protcy.2014.08.044>
10. Association, W. W. E. (2019). *World wind capacity at 650,8 gw, corona crisis will slow down markets in 2020, renewables to be core of economic stimulus programmes*. Retrieved from <https://wwindea.org/blog/2020/04/16/world-wind-capacity-at-650-gw/>
11. Barbero, E. (2008). Finite element analysis of composite materials. *Finite Element Analysis of Composite Materials using Abaqus*. Retrieved from https://www.researchgate.net/publication/275581960_Finite_Element_Analysis_of_Composite_Materials doi: 10.1201/b16295
12. Cai, C., Zheng, H., Khan, M., & Hung, C. K. (2002, 01). Modeling of material damping properties in ansys. *Users Conference and Exhibition - Pittsburgh ANSYS*. Retrieved from https://www.researchgate.net/publication/239533996_Modeling_of_Material_Damping_Properties_in_ANSYS
13. Chady, T., SIKORA, R., Lopato, P., Psuj, G., Szymanik, B., Balasubramaniam, K., & Rajagopal, P. (2016). Wind turbine blades inspection techniques. *PRZEGLĄD ELEKTROTECHNICZNY*. Retrieved from https://www.researchgate.net/publication/301906885_Wind_Turbine_Blades_Inspection_Techniques doi: 10.15199/48.2016.05.01
14. Chandgude, N., Gadhawe, N., Taware, G., & Patil, N. (2019, 05). Investigation of stiffness of small wind turbine blade based on vibration analysis technique. *Wind Engineering*, 44. Retrieved from https://www.researchgate.net/publication/333322190_Investigation_of_stiffness_of_small_wind_turbine_blade_based_on_vibration_analysis_technique doi: 10.1177/0309524X19849824
15. Chen, C., Zhang, Y., Zhou, B., & Zhang, S. (2012). The finite element simulation of crack growth of a wind turbine blade. *Advanced Materials Research*. Retrieved from https://www.researchgate.net/publication/272055175_The_Finite_Element_Simulation_of_Crack_Growth_of_a_Wind_Turbine_Blade doi: 10.4028/www.scientific.net/AMR.591-593.2028

16. Chia, C. C., & Bang, H.-J. (2008). Structural health monitoring for a wind turbine system: A review of damage detection method. *Measurement Science and Technology*. Retrieved from https://www.researchgate.net/publication/230937312_Structural_health_monitoring_for_a_wind_turbine_system_A_review_of_damage_detection_method doi: 10.1088/0957-0233/19/12/122001
17. Di Lorenzo, E., Petrone, G., Manzato, S., Peeters, B., Desmet, W., & Marulo, F. (2016). Damage detection in wind turbine blades by using operational modal analysis. *Structural Health Monitoring*, 15. Retrieved from https://www.researchgate.net/publication/303289122_Damage_detection_in_wind_turbine_blades_by_using_operational_modal_analysis doi: 10.1177/1475921716642748
18. Dinesh, S., Prasad, B., Pritesh, G., Mayur, C., & Tejas, A. (2017). Crack detection in cantilever shaft beam using natural frequency. *Materials Today Proceedings: 5th International Conference of Materials Processing and Characterization*. Retrieved from <https://www.sciencedirect.com/science/article/pii/S221478531730158X> doi: <https://doi.org/10.1016/j.matpr.2017.01.158>
19. D. J. McTavish, P. C. H. (1993). Modeling of linear viscoelastic space structures. *Journal of Vibration and Acoustics*, Jan 1993, 115(1): 103-110 (8 pages). Retrieved from <https://asmedigitalcollection.asme.org/vibrationacoustics/article-abstract/115/1/103/441153/Modeling-of-Linear-Viscoelastic-Space-Structures?redirectedFrom=fulltext> doi: <https://doi.org/10.1115/1.2930302>
20. E. Lofrano, G. R. A. T., A. Paolone. (2017). Perturbation damage indicators based on complex modes. *Procedia Engineering*, Volume 199, Pages 1949-1954. Retrieved from <https://www.sciencedirect.com/science/article/pii/S1877705817337797> doi: <https://doi.org/10.1016/j.proeng.2017.09.297>
21. Fabrizio Iezzi, C. V. (2017). Modal density influence on modal complexity quantification in dynamic systems. *Procedia Engineering*, Volume 199, Pages 942-947. Retrieved from <https://www.sciencedirect.com/science/article/pii/S1877705817336974> doi: <https://doi.org/10.1016/j.proeng.2017.09.245>
22. Florian Sayer, A. v. W., Alexandros Antoniou. (2012). Investigation of structural bond lines in wind turbine blades by sub-component tests. *International Journal of Adhesion and Adhesives*, Volume 37, Pages 129-135. Retrieved from <https://www.sciencedirect.com/science/article/pii/S014374961200022X> doi: <https://doi.org/10.1016/j.ijadhadh.2012.01.021>
23. F. Marulo, V. D. E. D. L., G. Petrone. (2014). Operational modal analysis on a wind turbine blade. Retrieved from http://past.isma-isaac.be/downloads/isma2014/papers/isma2014_0684.pdf
24. Ganeriwala, S., Yang, J., & Richardson, M. (2011). Using modal analysis for detecting cracks in wind turbine blades. *Sound and Vibration*. Retrieved from https://www.researchgate.net/publication/287844049_Using_Modal_Analysis_for_Detecting_Cracks_in_Wind_Turbine_Blades
25. Gaurd, W. (2020). *Wind turbine cost: How much? are they worth it in 2020?* Retrieved from <https://weatherguardwind.com/how-much-does-wind-turbine-cost-worth-it/>
26. Inspectioneering. (2020). *Overview of vibration analysis*. Retrieved from <https://inspectioneering.com/tag/vibration+analysis>
27. Jin Zeng, W. Z. B. W., Hui Ma. (2017). Dynamic characteristic analysis of cracked cantilever beams under different crack types. *Engineering Failure Analysis*, Volume 74, Pages 80-94. Retrieved from <https://www.sciencedirect.com/science/article/pii/S1350630716309554> doi: <https://doi.org/10.1016/j.engfailanal.2017.01.005>
28. Jitendra, G., Vijaykumar, B., & Jayant V, K. (2014). Experimental investigation of crack detection in cantilever beam using vibration analysis. *2014 International Conference on Networks Soft Computing (ICNSC)*. Retrieved from https://www.researchgate.net/publication/286733870_Experimental_investigation_of_crack_detection_in_cantilever_beam_using_vibration_analysis doi: 10.1109/ICNSC.2014.6906685
29. Jonathan, T. (2020). *Vibration analysis explained*. Retrieved from <https://www.reliableplant.com/vibration-analysis-31569>

30. Kaushar, H., D.S, S., & Vyas, V. (2013). Crack detection in cantilever beam by frequency based method. *Procedia Engineering: Chemical, Civil and Mechanical Engineering Tracks of the 3rd Nirma University International Conference*. Retrieved from <https://www.sciencedirect.com/science/article/pii/S1877705813001112>
31. Khalid Fatihi Abdullaheem, G. A.-K. (2018). Wind turbine blade fault detection using wavelet power spectrum and experimental modal analysis. *International Journal of Renewable Energy Research, Vol.8, No.4*. Retrieved from <https://www.ijrer.org/ijrer/index.php/ijrer/article/view/8471/pdf>
32. Khiem, N., & Lien, T. (2004, 05). Multi-crack detection for beam by the natural frequencies. *Journal of Sound and Vibration, Volume 273, Issues 1–2, Pages 175-184*. Retrieved from <https://www.sciencedirect.com/science/article/pii/S0022460X03004243> doi: [https://doi.org/10.1016/S0022-460X\(03\)00424-3](https://doi.org/10.1016/S0022-460X(03)00424-3)
33. Kim, S., Adams, D. E., & Sohn, H. (2013). Crack detection on wind turbine blades in an operating environment using vibro-acoustic modulation technique. *American Institute of Physics Conference Series, 1511, 286-293*. Retrieved from <https://ui.adsabs.harvard.edu/abs/2013AIPC.1511..286K/> doi: 10.1063/1.4789060
34. Lagouge Tartibu, J. v. d. M., Maria Kilfoil. (2015). Vibration analysis of a variable length blade wind turbine. *International Journal of advances in Engineering and Technology, Volume 4, 630-639*. Retrieved from https://www.researchgate.net/publication/267825087_Vibration_Analysis_of_a_Variable_Length_Blade_Wind_Turbine
35. Larsen, G., Hansen, M., Baumgart, A., & Carlen, I. (2002). *Modal analysis of wind turbine blades* (No. 1181(EN)). Retrieved from <https://orbit.dtu.dk/en/publications/modal-analysis-of-wind-turbine-blades-2>
36. Lukasz, D., & Marek, K. (2020). Analysis of modal parameters using a statistical approach for condition monitoring of the wind turbine blade. *Department of Mechatronics and High Voltage Engineering, Faculty of Electrical and Control Engineering, Gdansk University of Technology*. Retrieved from <https://www.mdpi.com/2076-3417/10/17/5878/htm> doi: <https://doi.org/10.3390/app10175878>
37. McTavish, D., & Hughes, P. (2012). Finite element modeling of linear viscoelastic structures - the ghm method. *Aerospace Research Central*. Retrieved from <https://arc.aiaa.org/doi/pdf/10.2514/6.1992-2380> doi: <https://doi.org/10.2514/6.1992-2380>
38. Mohammad, T. (2014a). *Classic model damping*. Retrieved from <https://www.slideshare.net/mohammadtawfik/visco-damping01-maxwellandkelvin-30718731>
39. Mohammad, T. (2014b). *Viscoelastic damping*. Retrieved from <https://www.slideshare.net/mohammadtawfik/viscoelastic-damping140202>
40. Mohammad, T. (2014c). *Zener model damping*. Retrieved from <https://www.slideshare.net/mohammadtawfik/visco-damping02-zener>
41. Munteanu, M., Stanciu, M., Nastac, S., & Savin, A. (2018, 11). Modal analysis of small turbine blade made from glass fibres composites. *IOP Conference Series: Materials Science and Engineering, 444*. Retrieved from https://www.researchgate.net/publication/329288609_Modal_analysis_of_small_turbine_blade_made_from_glass_fibres_composites doi: 10.1088/1757-899X/444/6/062004
42. Nandwana, B., & Maiti, S. (1996). Detection of the location and size of a crack in stepped cantilever beams based on measurements of natural frequencies. *Journal of Sound and Vibration, Volume 203, Issue 3, Pages 435-446*. Retrieved from <https://www.sciencedirect.com/science/article/pii/S0022460X96908561> doi: <https://doi.org/10.1006/jsvi.1996.0856>
43. Nigam, P., Tenguria, N., & Pradhan, D. M. (2019, 01). Modal analysis of large e-glass / carbon fibre hawt blade. Retrieved from https://www.researchgate.net/publication/338555488_Modal_Analysis_of_Large_E-Glass_Carbon_Fibre_HAWT_Blade
44. Nikishkov, G. (2012). Introduction to the finite element method. , *Lecture Notes, UCLA*. Retrieved from <http://nliebeaux.free.fr/ressources/introfem.pdf>

45. Parhi, D., & Choudhury, S. (2011). Smart crack detection of a cracked cantilever beam using fuzzy logic technology with hybrid membership functions. *J. Eng. Technol. Res.* Retrieved from https://www.researchgate.net/publication/267949387_Smart_crack_detection_of_a_cracked_cantilever_beam_using_fuzzy_logic_technology_with_hybrid_membership_functions
46. Raisutis, R., Jasiuniene, E., Sliteris, R., & Vladisauskas, A. (2008). The review of non-destructive testing techniques suitable for inspection of the wind turbine blades. *ISSN 1392-2114 ULTRAGARSAS*. Retrieved from <http://www.ultragarsas.ktu.lt/index.php/USnd/article/view/17066>
47. Rane Harshal, S., Barjibhe, R. B., & Patil, A. V. (2014, 07). Numerical solution to the crack detection in cracked beam using fuzzy logic. *International Journal of Engineering Research Technology (IJERT)*, Vol. 3 Issue 7. Retrieved from <https://www.ijert.org/research/numerical-solution-to-the-crack-detection-in-cracked-beam-using-fuzzy-logic-IJERTV3IS070875.pdf>
48. Ranjan, K., Anish, P., & Dayal, R. (2014). Numerical and experimental verification of a method for prognosis of inclined edge crack in cantilever beam based on synthesis of mode shapes. *Procedia Technology: 2nd International Conference on Innovations in Automation and Mechatronics Engineering, ICIAME*. Retrieved from <https://www.sciencedirect.com/science/article/pii/S2212017314000462> doi: <https://doi.org/10.1016/j.procs.2017.09.038>
49. Ravi Prakash Babu, K., Raghu Kumar, B., Narayana, K., & Mallikarjuna Rao, K. (2015, 03). Multiple crack detection in beams from the differences in curvature mode shapes. *ARPJN Journal of Engineering and Applied Sciences*, VOL. 10, NO. 4. Retrieved from http://www.arpnjournals.com/jeas/research_papers/rp_2015/jeas_0315_1653.pdf
50. Report, G. (2019). *Extreme measures: At 107 meters, the world's largest wind turbine blade is longer than a football field. here's what it looks like*. Retrieved from <https://www.ge.com/reports/extreme-measures-107-meters-worlds-largest-wind-turbine-blade-longer-football-field-heres-looks-like/#:~:text=Top%20and%20above%3A%20At%20107,Images%20credit%3A%20GE%20Renewable%20Energy>.
51. Roderic, L. (2009). *Viscoelastic materials*. Cambridge University Press. Retrieved from www.cambridge.org/9780521885683
52. Ruijgrok, E., van Druten, E., & Bulder, B. (2019). *Cost evaluation of north sea offshore wind post 2030*. Retrieved from <https://northseawindpowerhub.eu/wp-content/uploads/2019/02/112522-19-001.830-rapd-report-Cost-Evaluation-of-North-Sea-Offshore-Wind...pdf>
53. Rune, B., & Ventura, C. (2015). *Introduction to operational modal analysis*. John Wiley and Sons, Ltd. Retrieved from <https://onlinelibrary.wiley.com/doi/abs/10.1002/9781118535141> doi: 10.1002/9781118535141
54. Sharif, K., Simon J, W., & Dimitrios, Z. (2020). Characterisation of fatigue damage in a thick adhesive joint based on changes in material damping. *Journal of Physics: Conference Series*. Retrieved from <https://iopscience.iop.org/article/10.1088/1742-6596/1618/2/022058/pdf> doi: 10.1088/1742-6596/1618/2/022058
55. Sondipon, A. (2014). *Structural dynamic analysis with generalized damping models*. John Wiley and Sons, Ltd. Retrieved from <https://onlinelibrary.wiley.com/doi/abs/10.1002/9781118572023> doi: 10.1002/9781118572023
56. Tai-Hong, C., Ming, R., Zhen-Zhe, L., & Yun-De, S. (2015). Vibration and damping analysis of composite fiber reinforced wind blade with viscoelastic damping control. *Advances in Materials Science and Engineering*. Retrieved from <https://www.hindawi.com/journals/amse/2015/146949/> doi: <https://doi.org/10.1155/2015/146949>
57. Taware, G., Mankar, S., B., G., P., B., & Kale, S. (2016, 10). Vibration analysis of a small wind turbine blade. *International Journal of Engineering and Technology*, 8. Retrieved from https://www.researchgate.net/publication/309626057_Vibration_Analysis_of_a_Small_Wind_Turbine_Blade doi: 10.21817/ijet/2016/v8i5/160805431
58. Weiwei, Z., Zhihua, W., & Hongwei, M. (2009, 08). Identification of crack location in beam structures using wavelet transform and fractal dimension. *Acta Mechanica Solida Sinica*, Vol. 22, No. 4. Retrieved from <https://www.sciencedirect.com/science/article/pii/S0894916609602858> doi: [https://doi.org/10.1016/S0894-9166\(09\)60285-8](https://doi.org/10.1016/S0894-9166(09)60285-8)

-
59. Yanbin, C., Lei, S., & Feng, Z. (2010, 01). Modal analysis of wind turbine blade made of composite laminated plates. Retrieved from https://www.researchgate.net/publication/251925041_Modal_Analysis_of_Wind_Turbine_Blade_Made_of_Composite_laminated_plates doi: 10.1109/APPEEC.2010.5448923
60. Yanfeng, W., Ming, L., & Jiawei, X. (2014). Damage detection method for wind turbine blades based on dynamics analysis and mode shape difference curvature information. *Mechanical Systems and Signal Processing*. Retrieved from <https://www.sciencedirect.com/science/article/abs/pii/S0888327014000818> doi: <https://doi.org/10.1016/j.ymsp.2014.03.006>
61. Yong-Ying, J., Bing, L., Zhou-Suo, Z., & Xue-Feng, C. (2015). Identification of crack location in beam structures using wavelet transform and fractal dimension. *Journal in Shock and Vibration*. Retrieved from https://www.researchgate.net/publication/283192009_Identification_of_Crack_Location_in_Beam_Structures_Using_Wavelet_Transform_and_Fractal_Dimension doi: 10.1155/2015/832763
62. Zarouchas, D. S. V. H. V. W., Makris, A. (2012). Investigations on the mechanical behavior of a wind rotor blade subcomponent. *Composites Part B: Engineering, Volume 43, Issue 2, Pages 647-654*. Retrieved from <https://www.sciencedirect.com/science/article/pii/S1359836811004562> doi: <https://doi.org/10.1016/j.compositesb.2011.10.009>
63. ZHENZHEN, X. (2011). *An inverse finite element analysis and a parametric study of small punch tests*. Retrieved from <https://pdfs.semanticscholar.org/9944/c9656287f8be82046b64b6ea4c4c28dd27f85.pdf>

Appendix A: Damage identification and localization support plots

Scenario 1: Damage only in top surfaces near the fixed end with 2 %, 4 %, 6 % defected area

Case 1: Top surface damage near fixed end with 2 % defected area (Damping Coefficient 0.02)

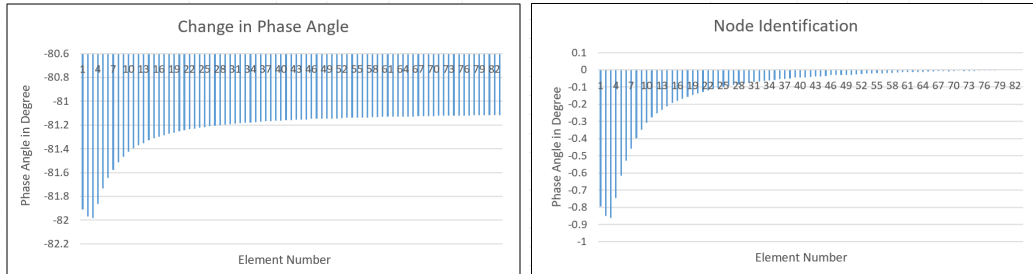


Figure 8.1: Scenario 1 case 1 100 % damage 1st flap wise bending

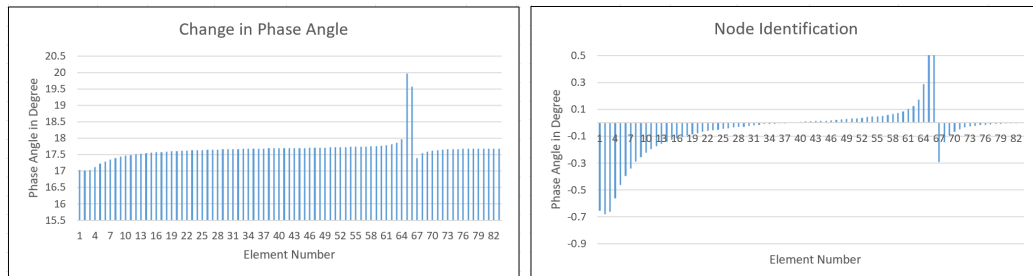


Figure 8.2: Scenario 1 case 1 100 % damage 2nd flap wise bending

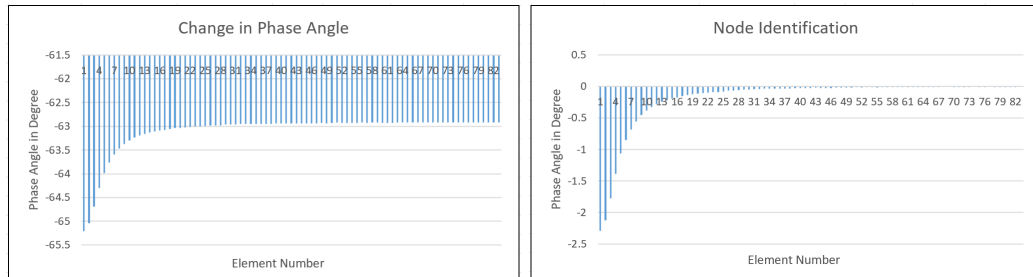


Figure 8.3: Scenario 1 case 1 100 % damage 1st edge wise bending

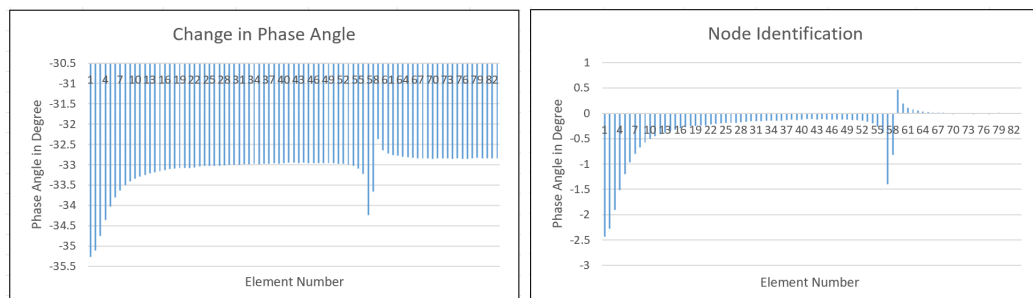


Figure 8.4: Scenario 1 case 1 100 % damage 2nd edge wise bending

Case 1: Top surface damage near fixed end with 2 % defected area (Damping Coefficient 0.045)

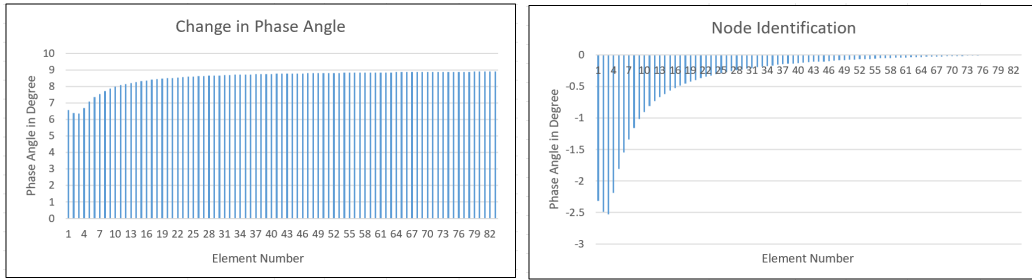


Figure 8.5: Scenario 1 case 1 350 % damage 1st flap wise bending

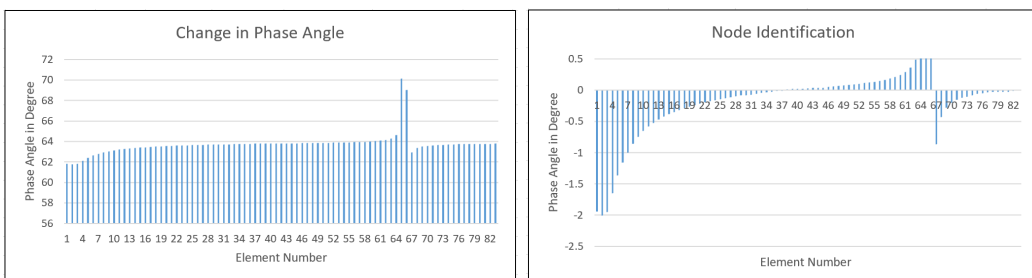


Figure 8.6: Scenario 1 case 1 350 % damage 2nd flap wise bending

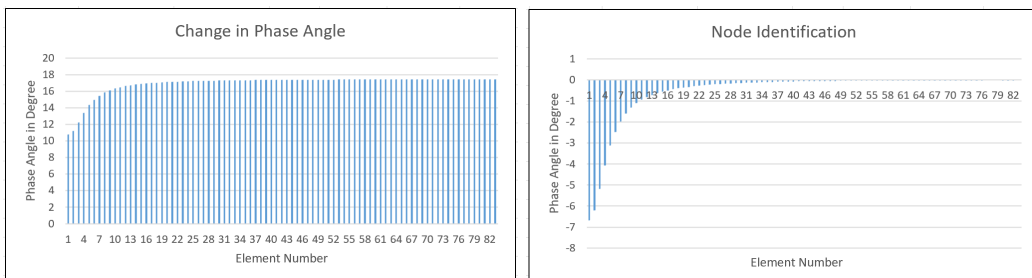


Figure 8.7: Scenario 1 case 1 350 % damage 1st edge wise bending

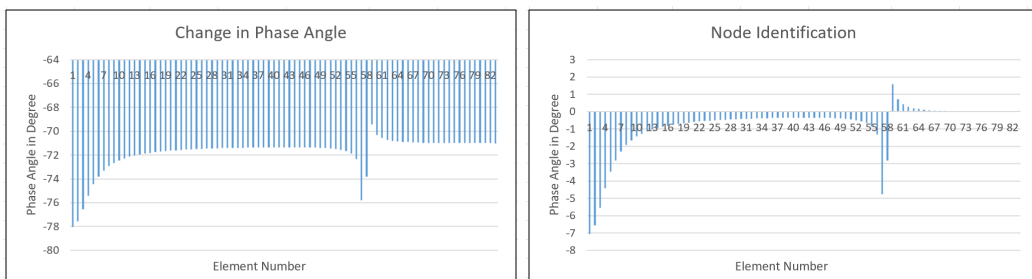


Figure 8.8: Scenario 1 case 1 350 % damage 2nd edge wise bending

Case 2: Top surface damage near fixed end with 4 % defected area (Damping Coefficient 0.02)

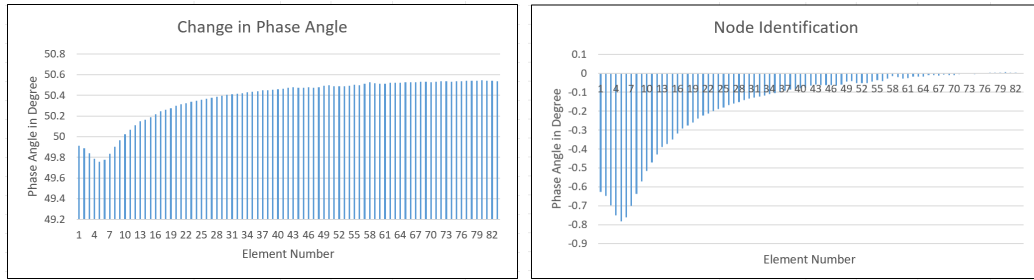


Figure 8.9: Scenario 1 case 2 100 % damage 1st flap wise bending

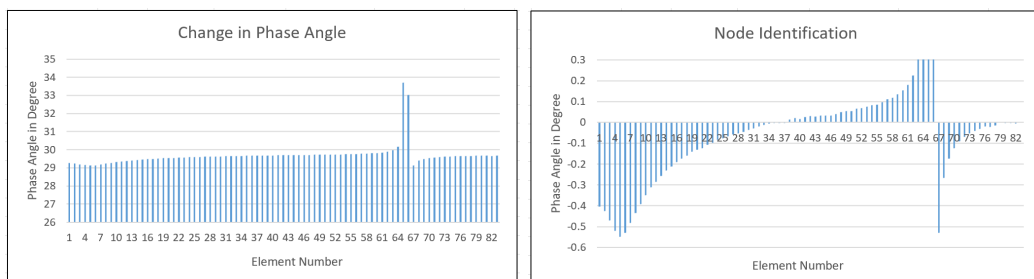


Figure 8.10: Scenario 1 case 2 100 % damage 2nd flap wise bending

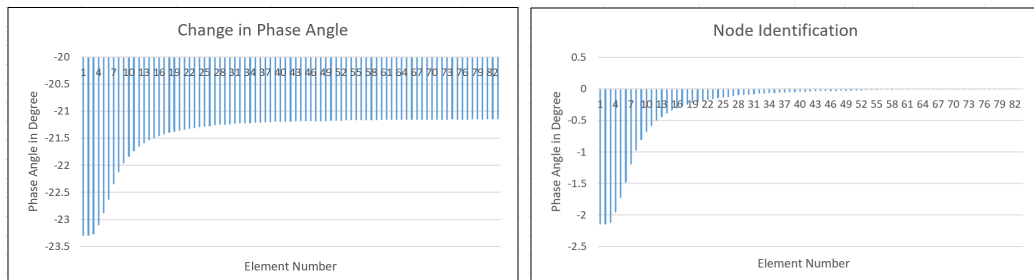


Figure 8.11: Scenario 1 case 2 100 % damage 1st edge wise bending

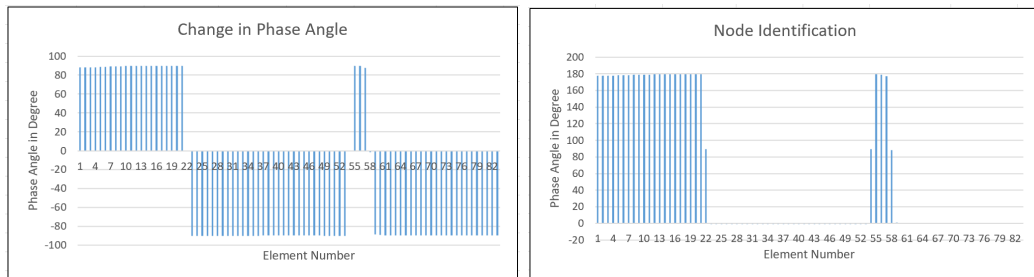


Figure 8.12: Scenario 1 case 2 100 % damage 2nd edge wise bending

Case 2: Top surface damage near fixed end with 4 % defected area (Damping Coefficient 0.045)

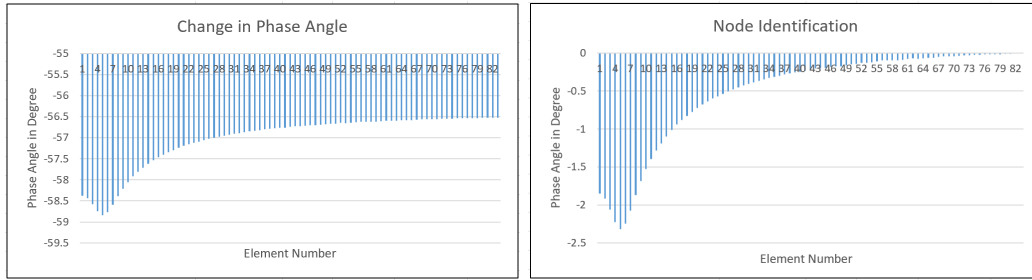


Figure 8.13: Scenario 1 case 2 350 % damage 1st flap wise bending

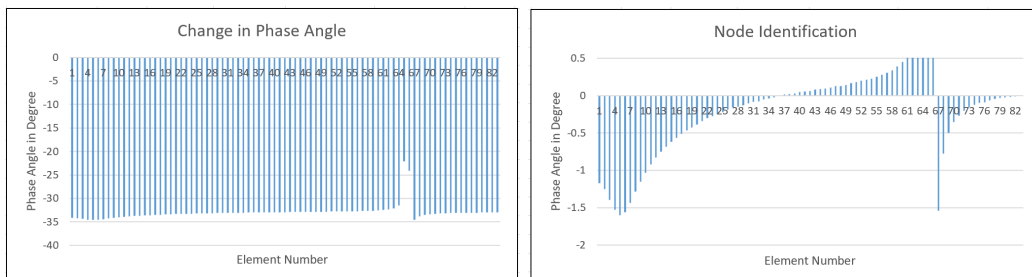


Figure 8.14: Scenario 1 case 2 350 % damage 2nd flap wise bending

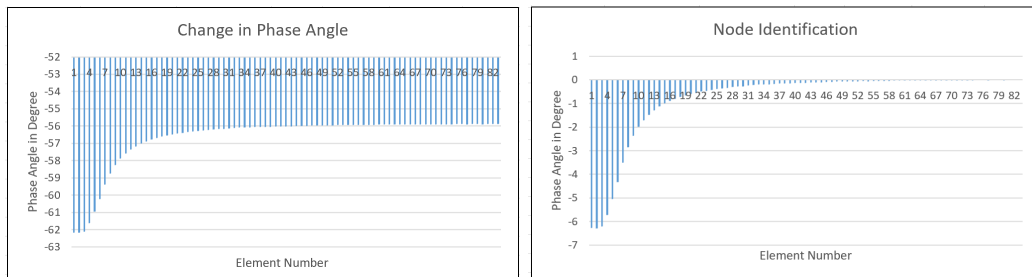


Figure 8.15: Scenario 1 case 2 350 % damage 1st edge wise bending

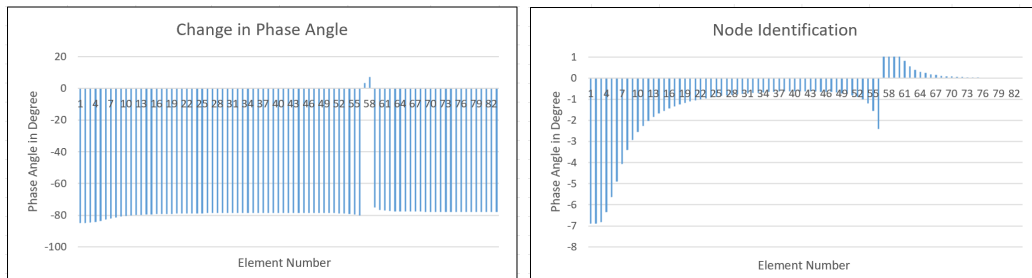


Figure 8.16: Scenario 1 case 2 350 % damage 2nd edge wise bending

Case 3: Top surface damage near fixed end with 6 % defected area (Damping Coefficient 0.02)

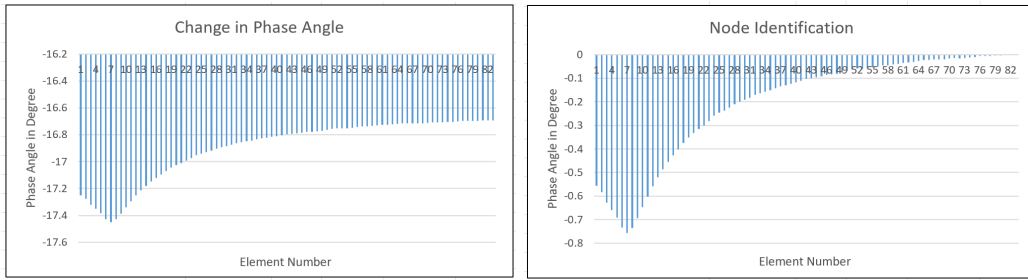


Figure 8.17: Scenario 1 case 3 100 % damage 1st flap wise bending

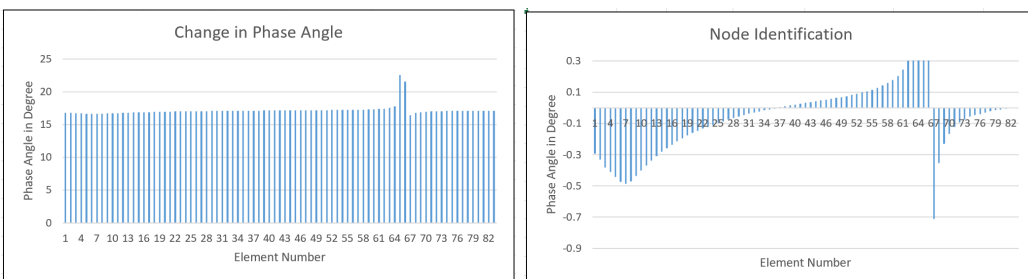


Figure 8.18: Scenario 1 case 3 100 % damage 2nd flap wise bending

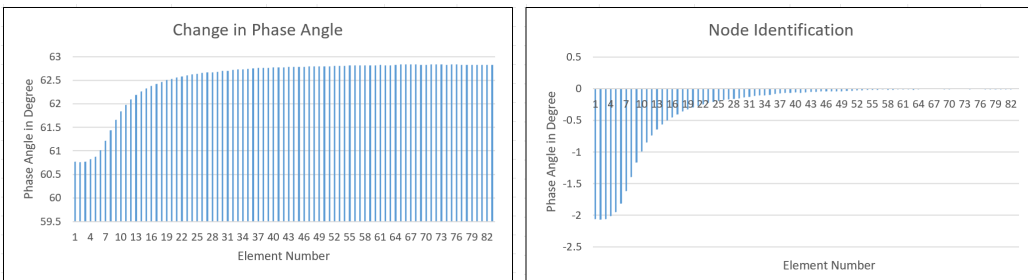


Figure 8.19: Scenario 1 case 3 100 % damage 1st edge wise bending

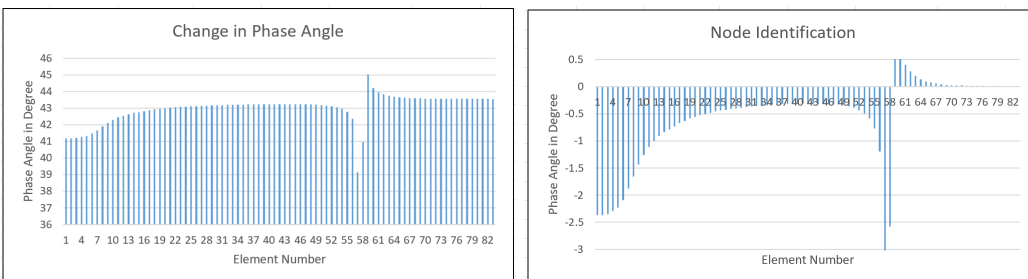


Figure 8.20: Scenario 1 case 3 100 % damage 2nd edge wise bending

Case 3: Top surface damage near fixed end with 6 % defected area (Damping Coefficient 0.045)

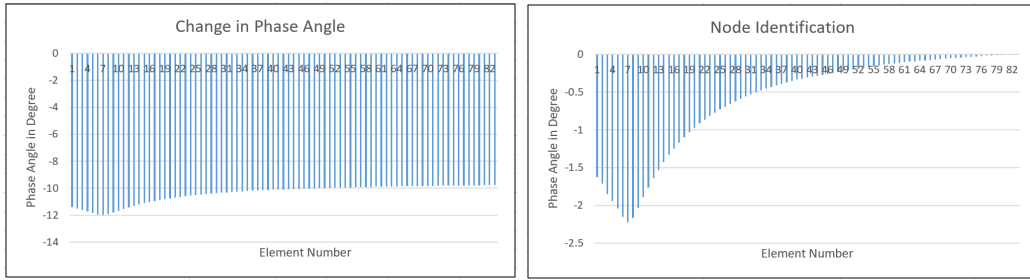


Figure 8.21: Scenario 1 case 3 350 % damage 1st flap wise bending

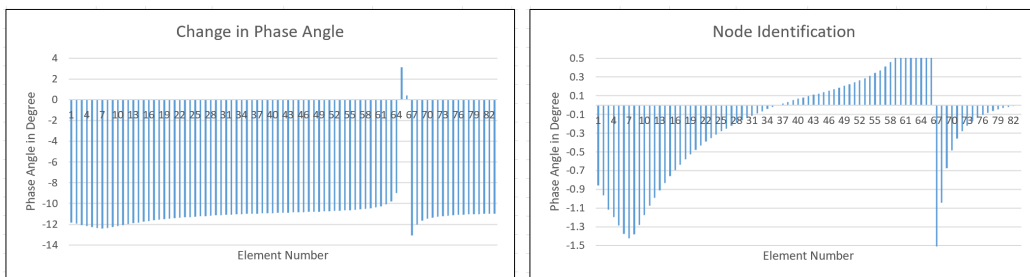


Figure 8.22: Scenario 1 case 3 350 % damage 2nd flap wise bending

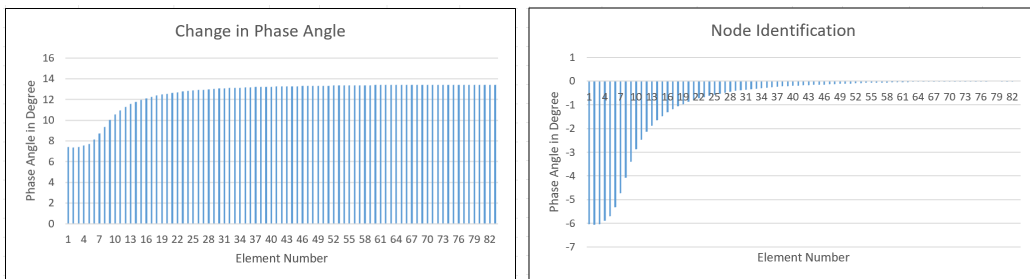


Figure 8.23: Scenario 1 case 3 350 % damage 1st edge wise bending

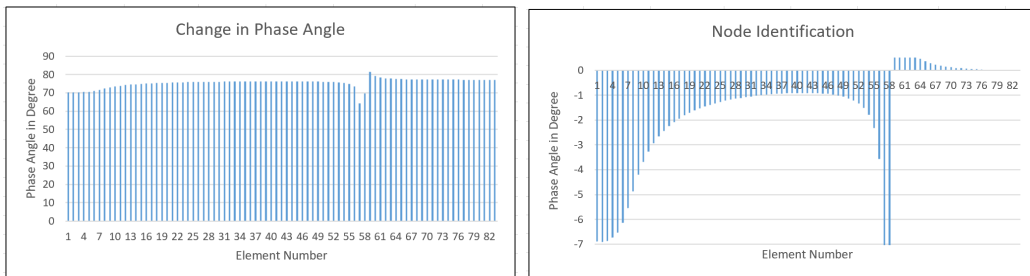


Figure 8.24: Scenario 1 case 3 350 % damage 2nd edge wise bending

Scenario 2: Damage only in top surfaces near the mid section with 2 %, 4 %, 6 % defected area

Case 1: Top surface damage near mid section with 2 % defected area (Damping Coefficient 0.02)

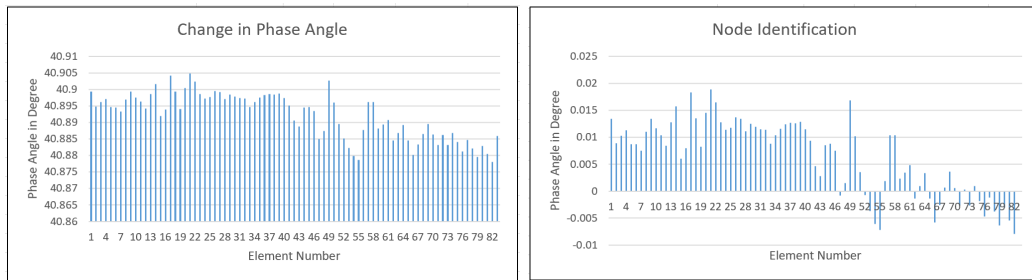


Figure 8.25: Scenario 2 case 1 100 % damage 1st flap wise bending

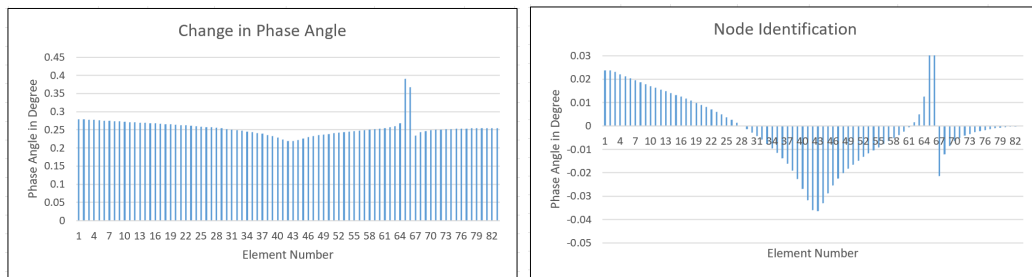


Figure 8.26: Scenario 2 case 1 100 % damage 2nd flap wise bending

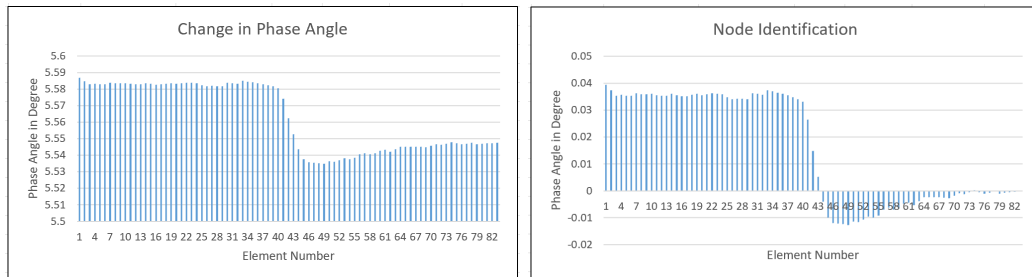


Figure 8.27: Scenario 2 case 1 100 % damage 1st edge wise bending

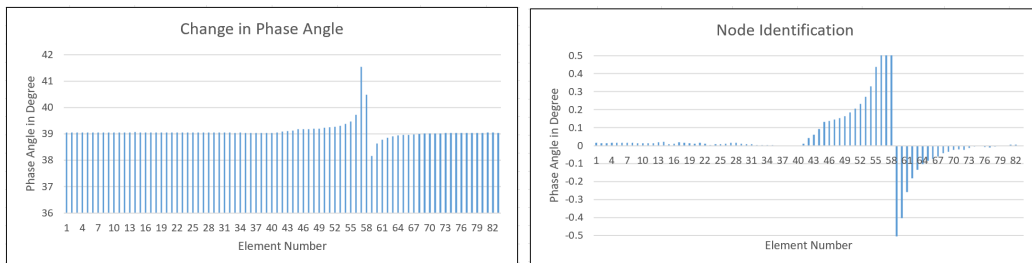


Figure 8.28: Scenario 2 case 1 100 % damage 2nd edge wise bending

Case 1: Top surface damage near mid section with 2 % defected area (Damping Coefficient 0.045)

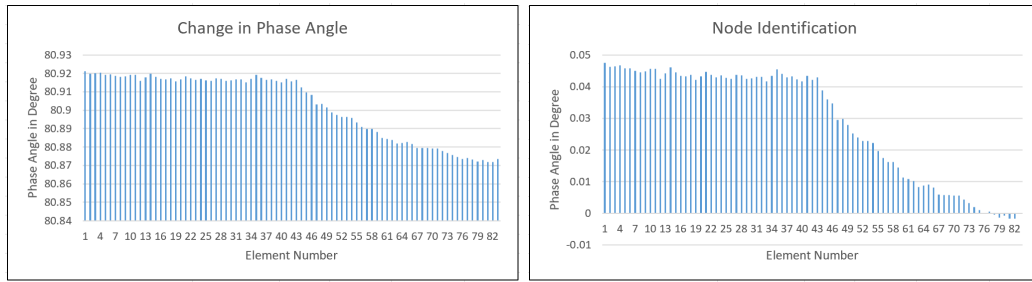


Figure 8.29: Scenario 2 case 1 350 % damage 1st flap wise bending

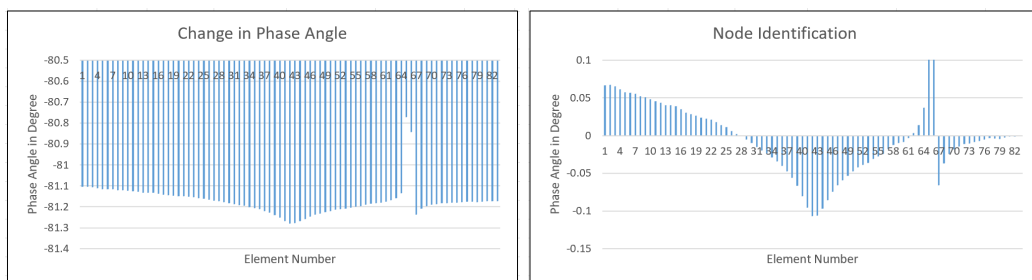


Figure 8.30: Scenario 2 case 1 350 % damage 2nd flap wise bending

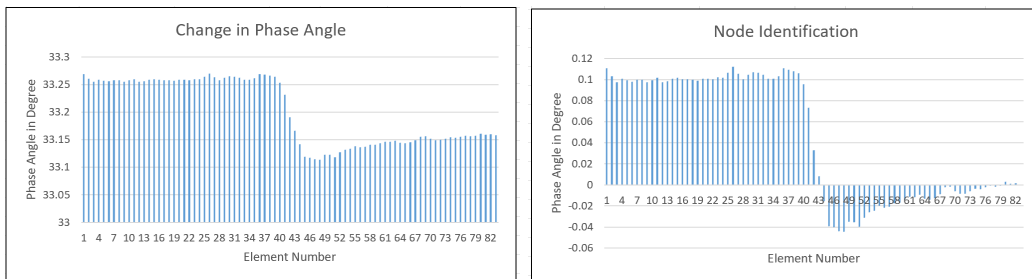


Figure 8.31: Scenario 2 case 1 350 % damage 1st edge wise bending

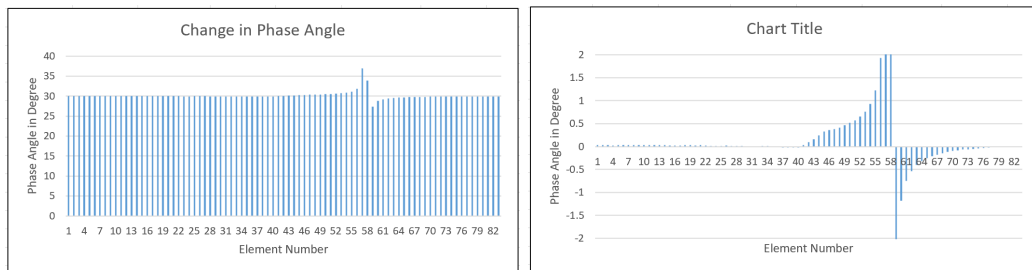


Figure 8.32: Scenario 2 case 1 350 % damage 2nd edge wise bending

Case 2: Top surface damage near mid section with 4 % defected area (Damping Coefficient 0.02)

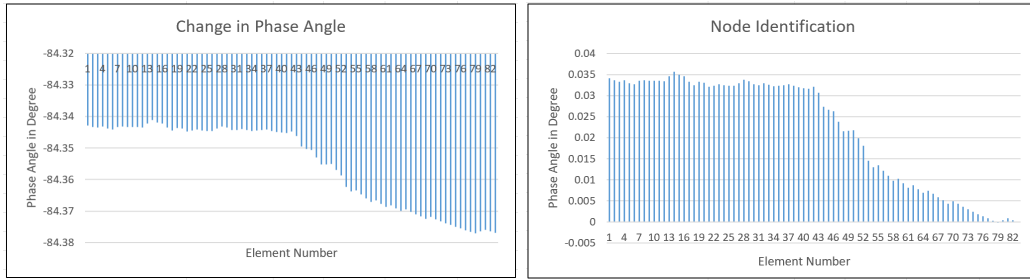


Figure 8.33: Scenario 2 case 2 100 % damage 1st flap wise bending

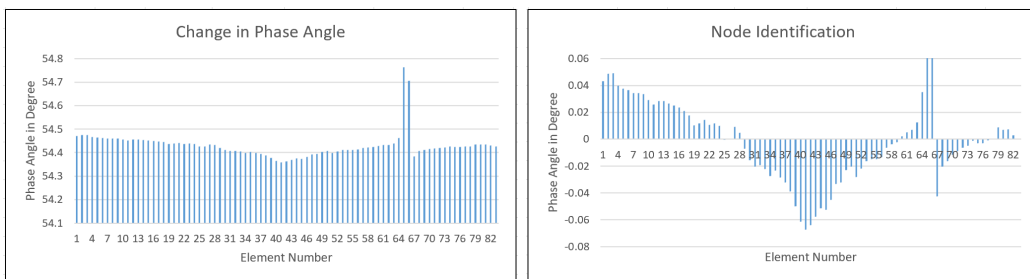


Figure 8.34: Scenario 2 case 2 100 % damage 2nd flap wise bending

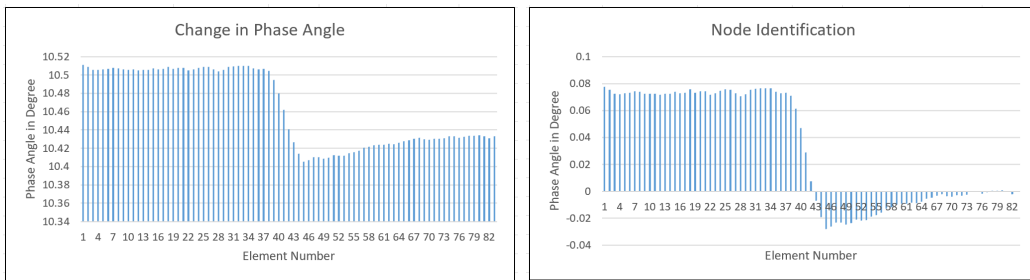


Figure 8.35: Scenario 2 case 2 100 % damage 1st edge wise bending

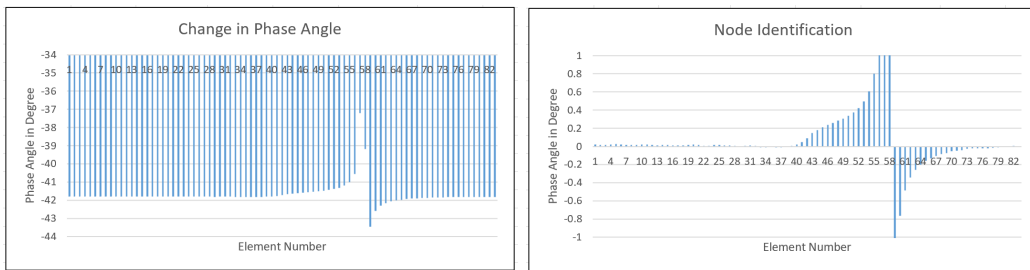


Figure 8.36: Scenario 2 case 2 100 % damage 2nd edge wise bending

Case 2: Top surface damage near mid section with 4 % defected area (Damping Coefficient 0.045)

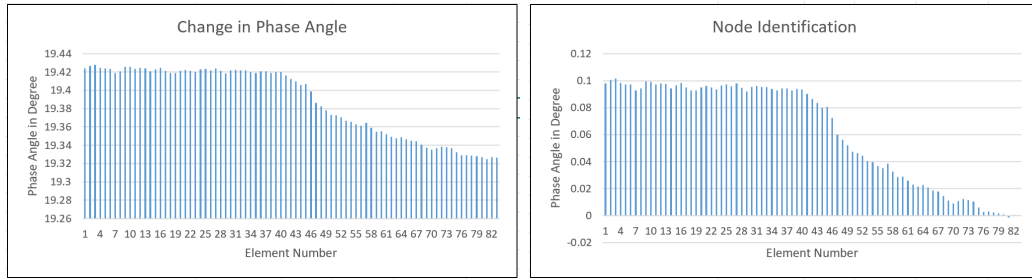


Figure 8.37: Scenario 2 case 2 350 % damage 1st flap wise bending

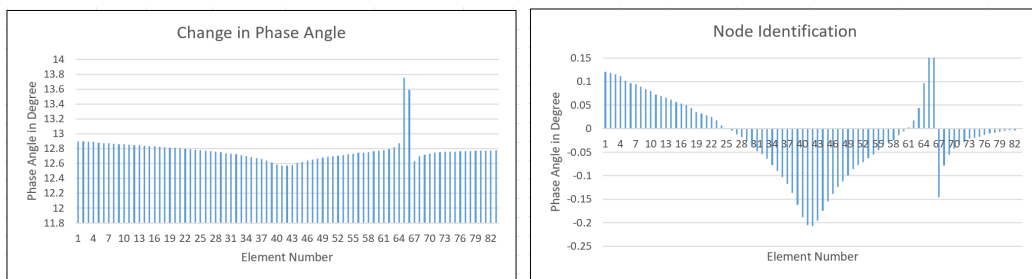


Figure 8.38: Scenario 2 case 2 350 % damage 2nd flap wise bending

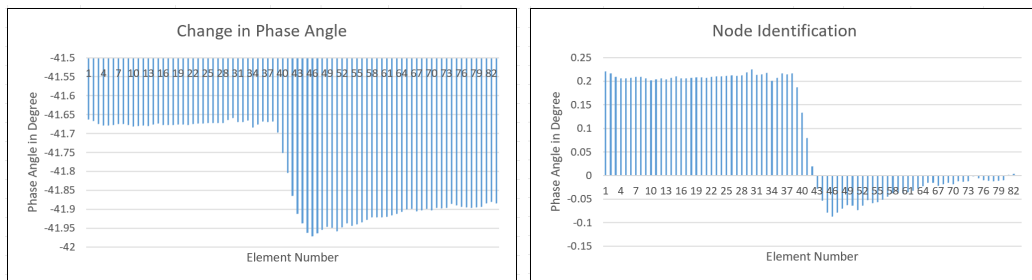


Figure 8.39: Scenario 2 case 2 350 % damage 1st edge wise bending

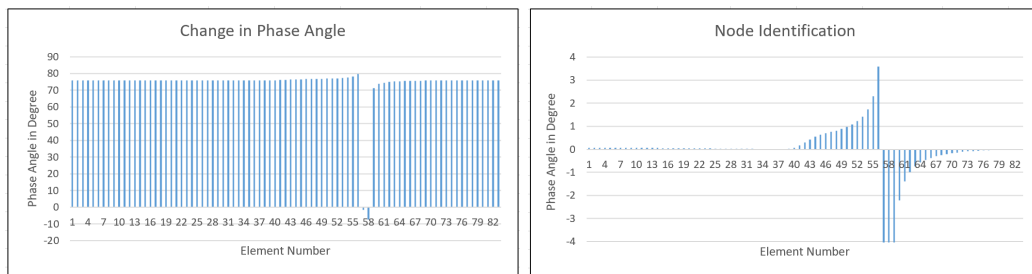


Figure 8.40: Scenario 2 case 2 350 % damage 2nd edge wise bending

Case 3: Top surface damage near fixed end with 6 % defected area (Damping Coefficient 0.02)

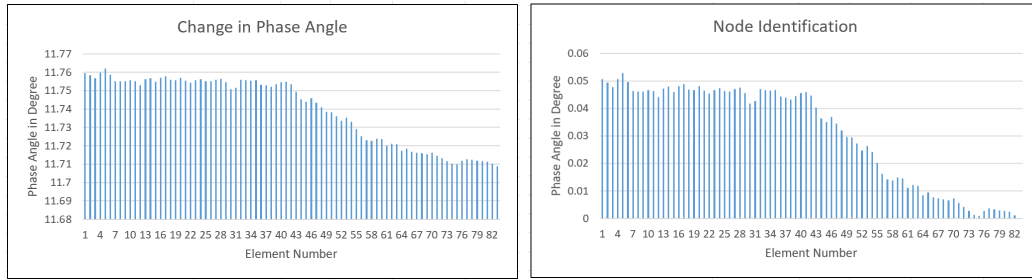


Figure 8.41: Scenario 2 case 3 100 % damage 1st flap wise bending

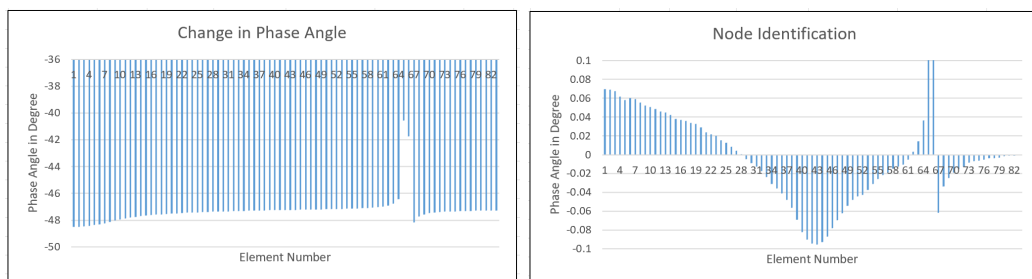


Figure 8.42: Scenario 2 case 3 100 % damage 2nd flap wise bending

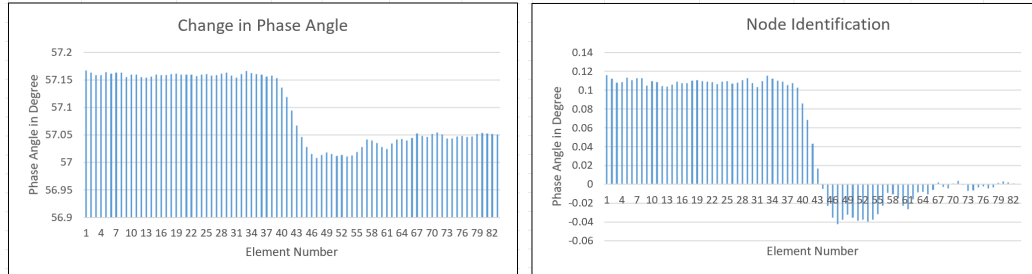


Figure 8.43: Scenario 2 case 3 100 % damage 1st edge wise bending

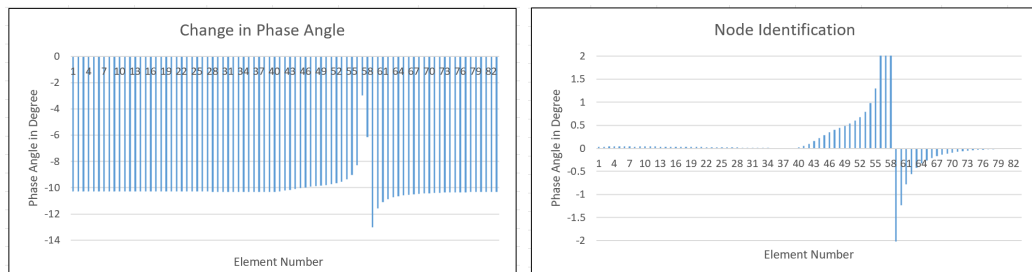


Figure 8.44: Scenario 2 case 3 100 % damage 2nd edge wise bending

Case 3: Top surface damage near fixed end with 6 % defected area (Damping Coefficient 0.045)

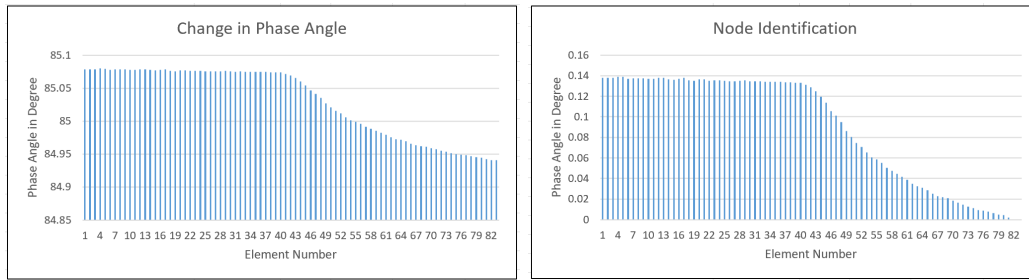


Figure 8.45: Scenario 2 case 3 350 % damage 1st flap wise bending

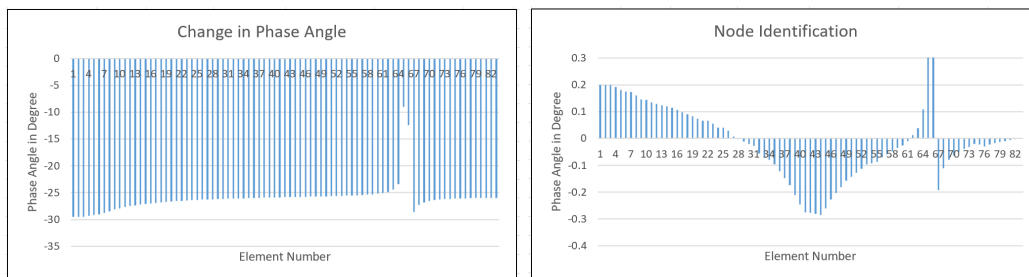


Figure 8.46: Scenario 2 case 3 350 % damage 2nd flap wise bending

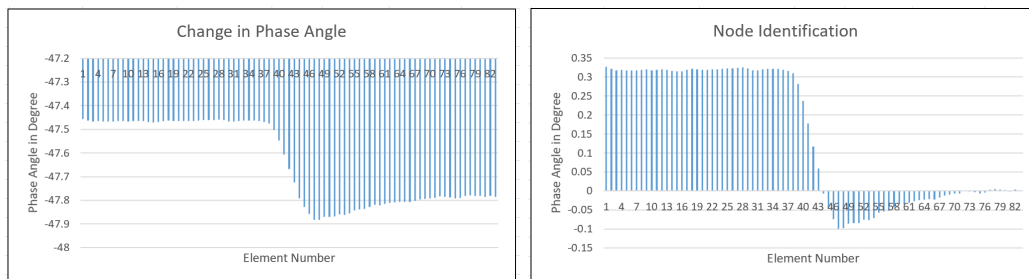


Figure 8.47: Scenario 2 case 3 350 % damage 1st edge wise bending

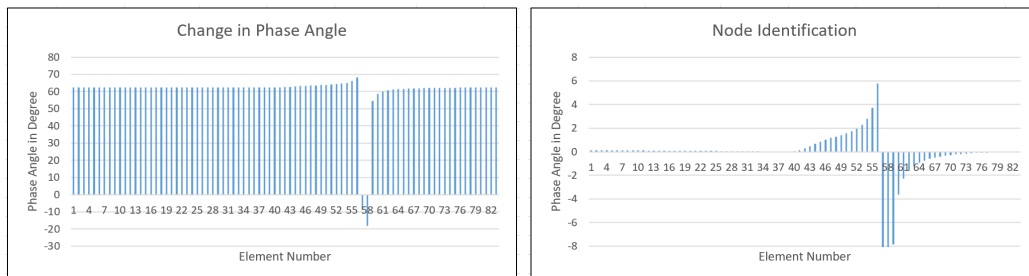


Figure 8.48: Scenario 2 case 3 350 % damage 2nd edge wise bending

Scenario 3: Damage in top and core surfaces near the fixed end with 2 %, 4 %, 6 % defected area
Case 1: Top and core surface damage near fixed end with 2 % defected area (Damping Coefficient 0.02)

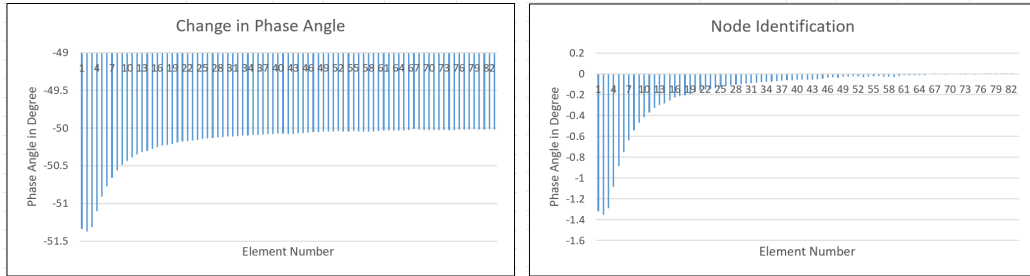


Figure 8.49: Scenario 3 case 1 100 % damage 1st flap wise bending

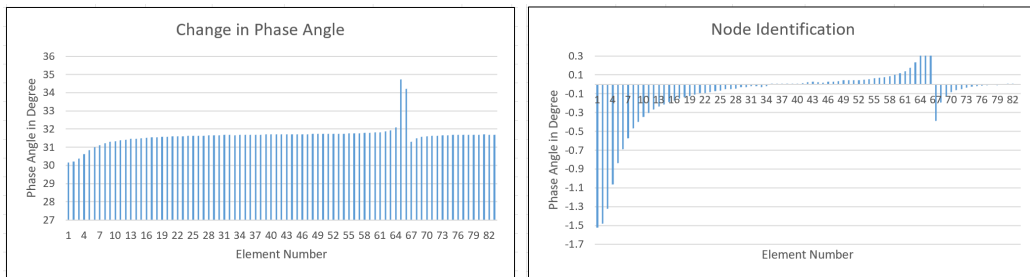


Figure 8.50: Scenario 3 case 1 100 % damage 2nd flap wise bending

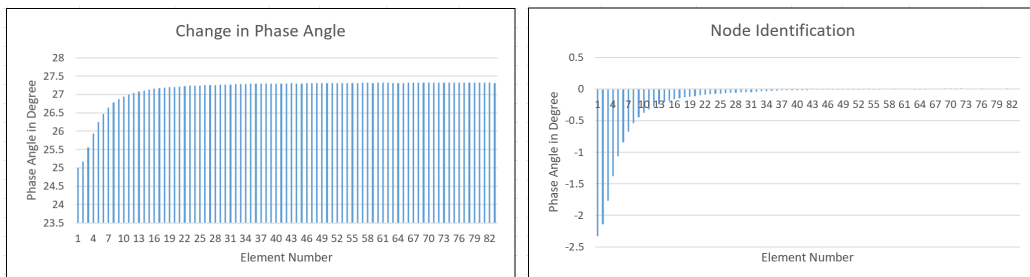


Figure 8.51: Scenario 3 case 1 100 % damage 1st edge wise bending

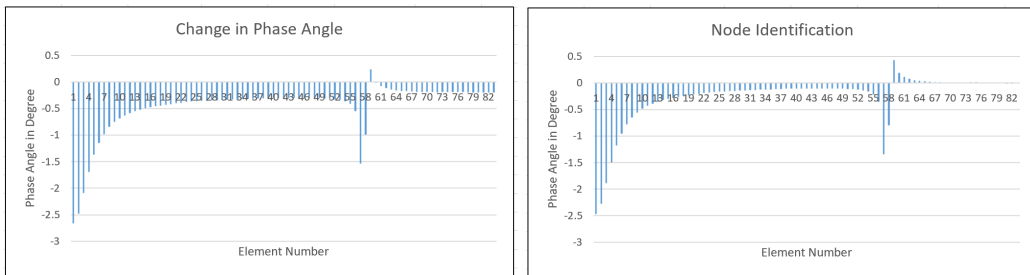


Figure 8.52: Scenario 3 case 1 100 % damage 2nd edge wise bending

Case 1: Top and core surface damage near fixed end with 2 % defected area (Damping Coefficient 0.045)

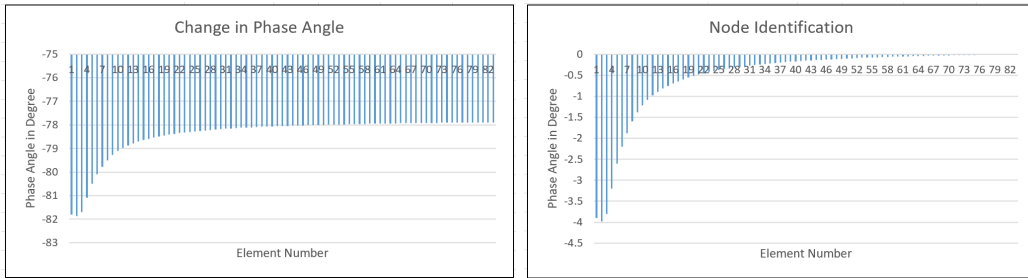


Figure 8.53: Scenario 3 case 1 350 % damage 1st flap wise bending

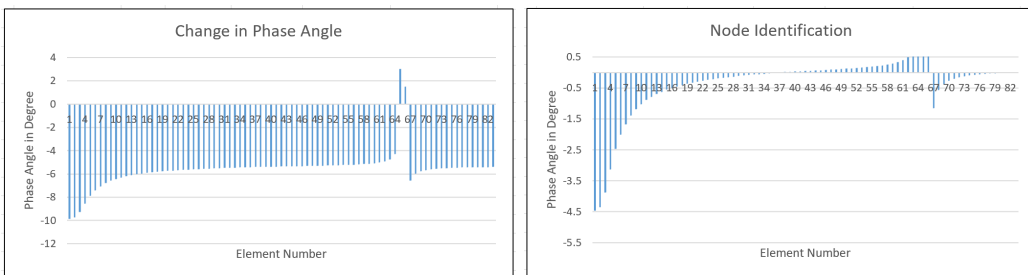


Figure 8.54: Scenario 3 case 1 350 % damage 2nd flap wise bending

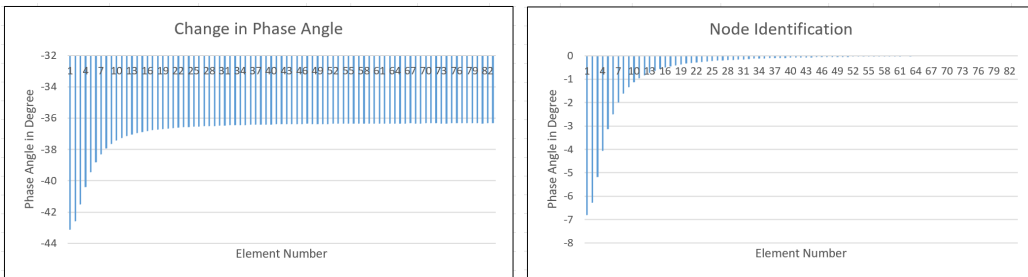


Figure 8.55: Scenario 3 case 1 350 % damage 1st edge wise bending

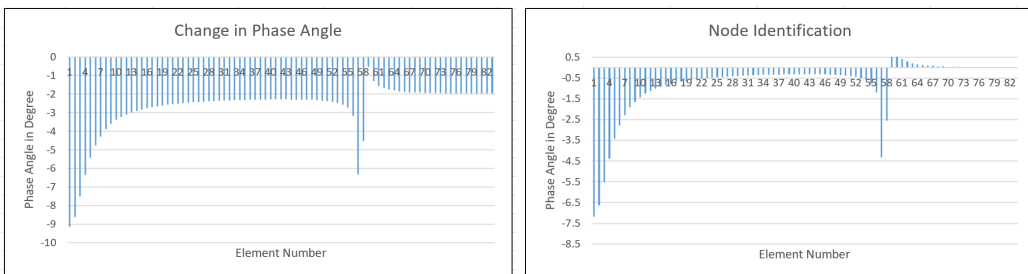


Figure 8.56: Scenario 3 case 1 350 % damage 2nd edge wise bending

Case 2: Top and core surface damage near fixed end with 4 % defected area (Damping Coefficient 0.02)

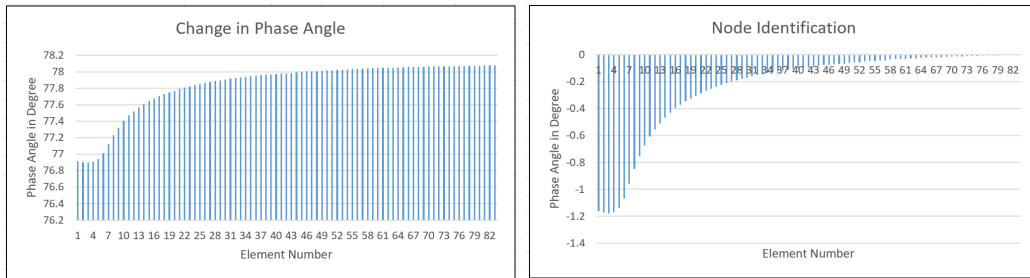


Figure 8.57: Scenario 3 case 2 100 % damage 1st flap wise bending

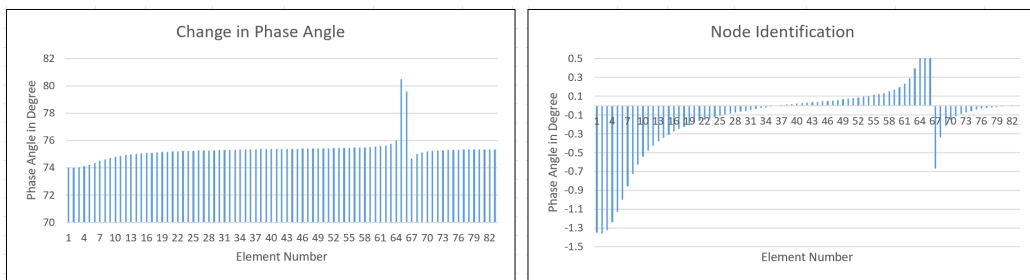


Figure 8.58: Scenario 3 case 2 100 % damage 2nd flap wise bending

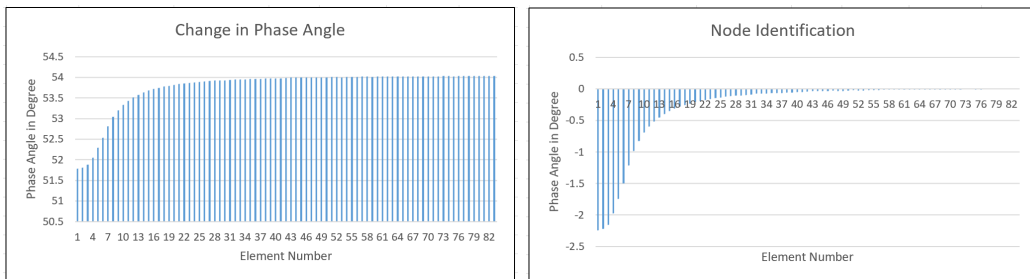


Figure 8.59: Scenario 3 case 2 100 % damage 1st edge wise bending

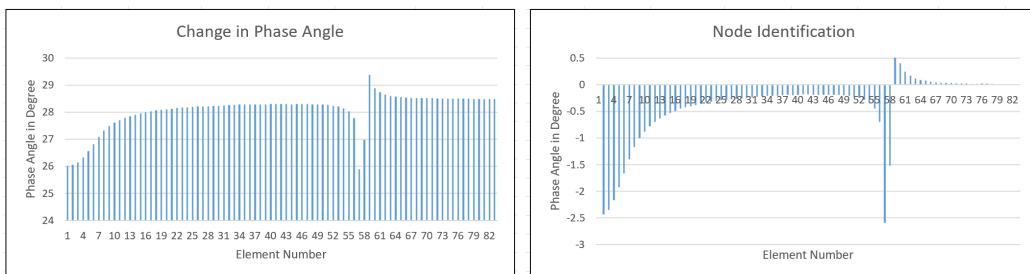


Figure 8.60: Scenario 3 case 2 100 % damage 2nd edge wise bending

Case 2: Top and core surface damage near fixed end with 4 % defected area (Damping Coefficient 0.045)

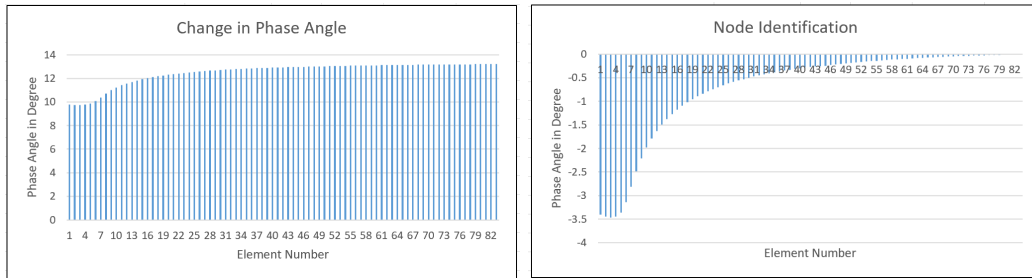


Figure 8.61: Scenario 3 case 2 350 % damage 1st flap wise bending

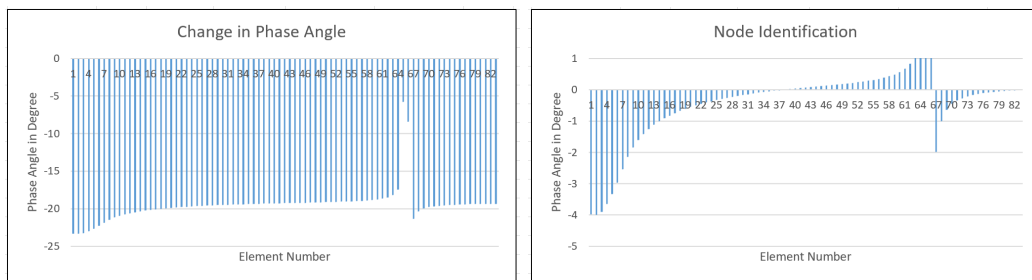


Figure 8.62: Scenario 3 case 2 350 % damage 2nd flap wise bending

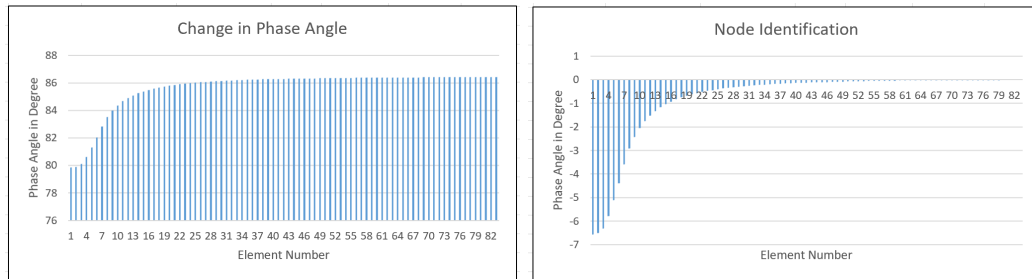


Figure 8.63: Scenario 3 case 2 350 % damage 1st edge wise bending

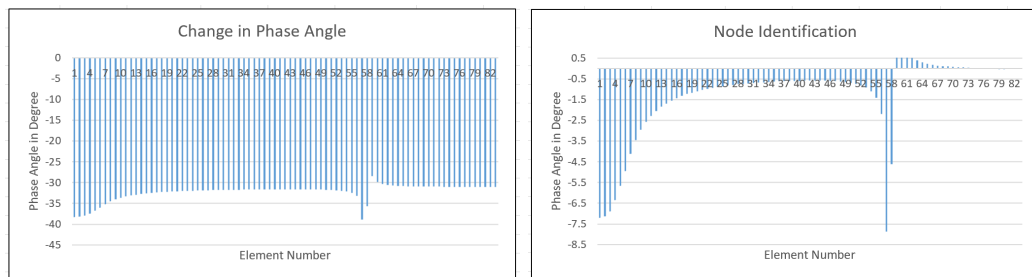


Figure 8.64: Scenario 3 case 2 350 % damage 2nd edge wise bending

Case 3: Top and core surface damage near fixed end with 6 % defected area (Damping Coefficient 0.02)

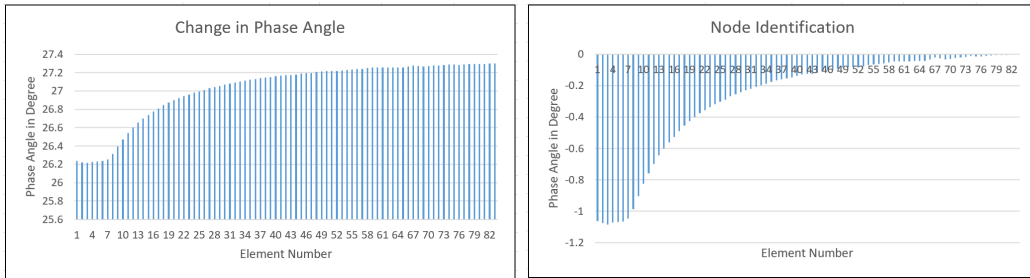


Figure 8.65: Scenario 3 case 3 100 % damage 1st flap wise bending

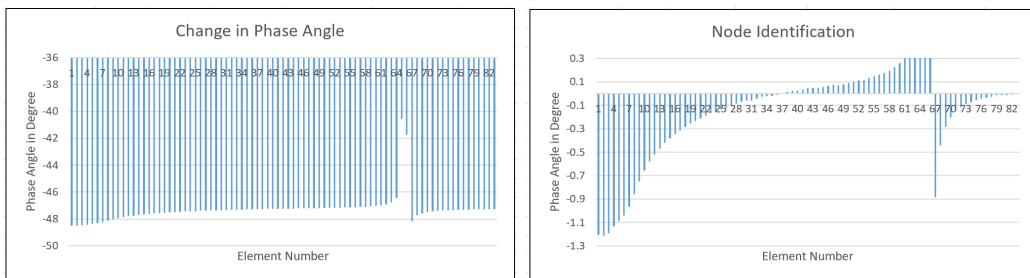


Figure 8.66: Scenario 3 case 3 100 % damage 2nd flap wise bending

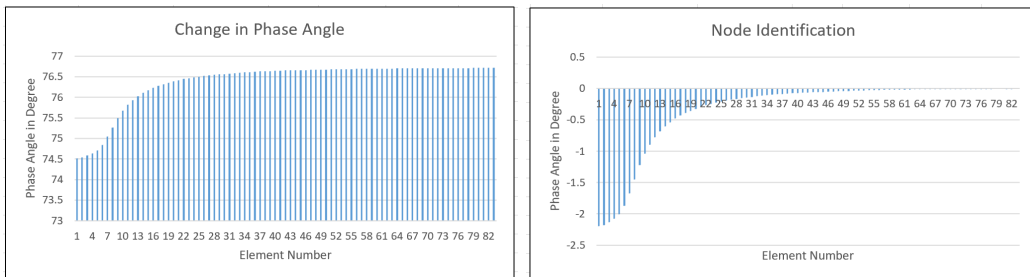


Figure 8.67: Scenario 3 case 3 100 % damage 1st edge wise bending

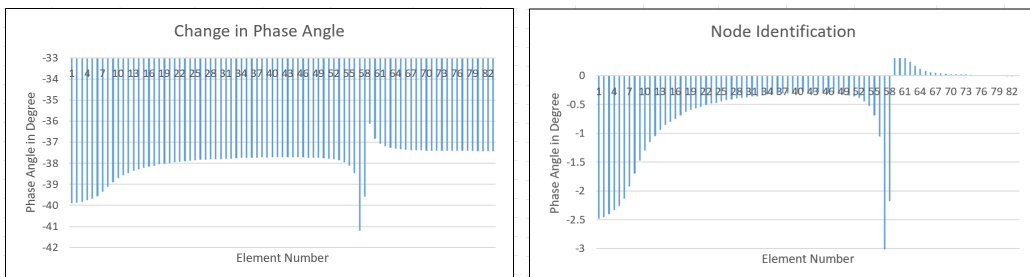


Figure 8.68: Scenario 3 case 3 100 % damage 2nd edge wise bending

Case 3: Top and core surface damage near fixed end with 6 % defected area (Damping Coefficient 0.045)

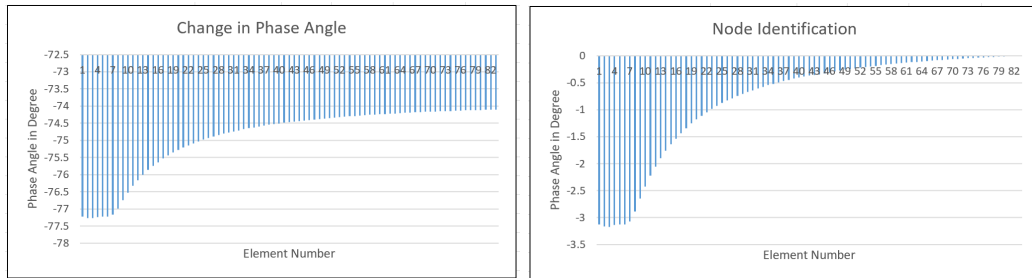


Figure 8.69: Scenario 3 case 3 350 % damage 1st flap wise bending

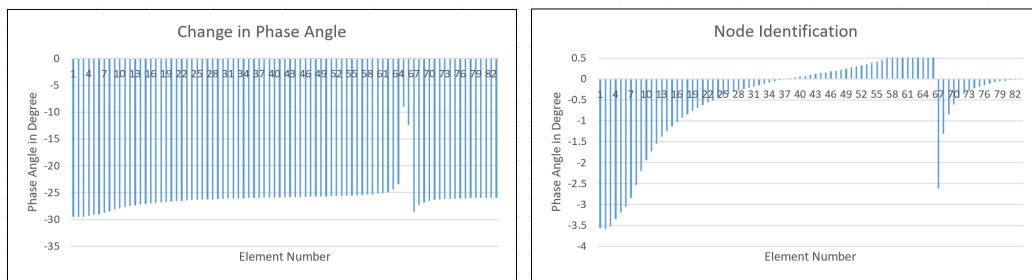


Figure 8.70: Scenario 3 case 3 350 % damage 2nd flap wise bending

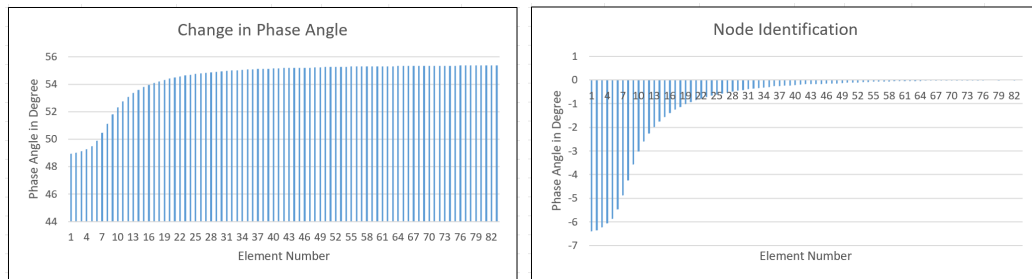


Figure 8.71: Scenario 3 case 3 350 % damage 1st edge wise bending

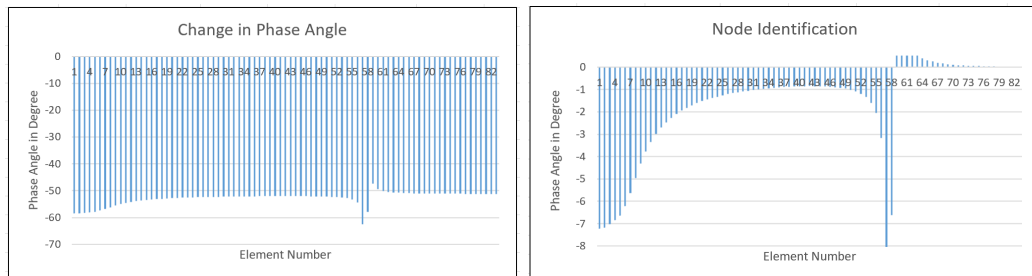


Figure 8.72: Scenario 3 case 3 350 % damage 2nd edge wise bending

Scenario 4: Damage in top and core surfaces near the mid section with 2 %, 4 %, 6 % defected area

Case 1: Top and core surface damage near Mid section with 2 % defected area (Damping Coefficient 0.02)

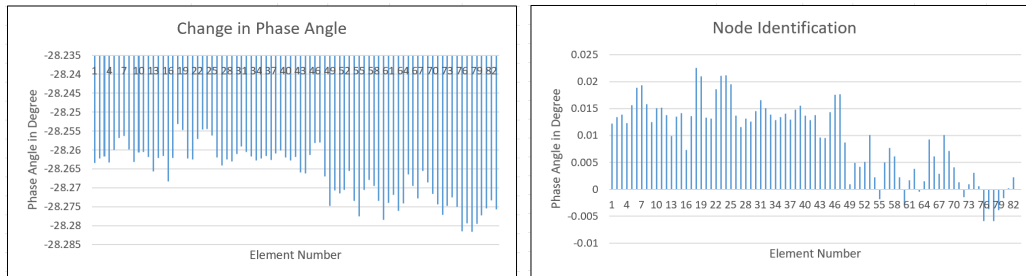


Figure 8.73: Scenario 4 case 1 100 % damage 1st flap wise bending

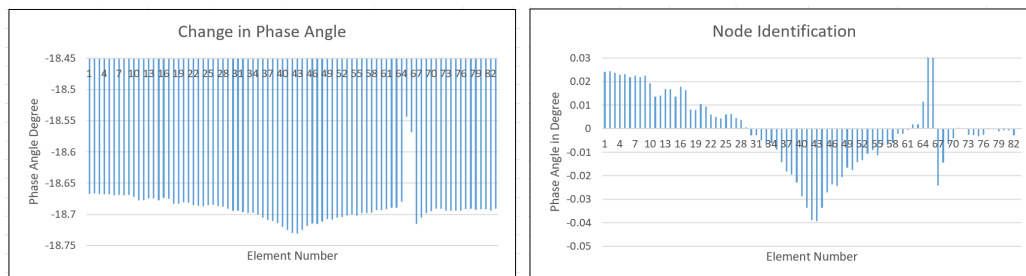


Figure 8.74: Scenario 4 case 1 100 % damage 2nd flap wise bending

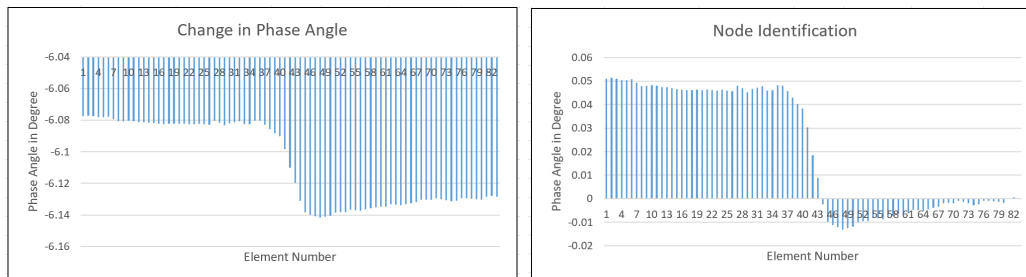


Figure 8.75: Scenario 4 case 1 100 % damage 1st edge wise bending

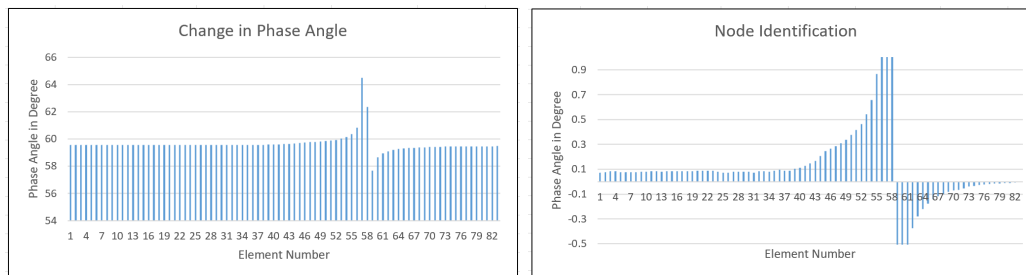


Figure 8.76: Scenario 4 case 1 100 % damage 2nd edge wise bending

Case 1: Top and core surface damage near Mid section with 2 % defected area (Damping Coefficient 0.045)

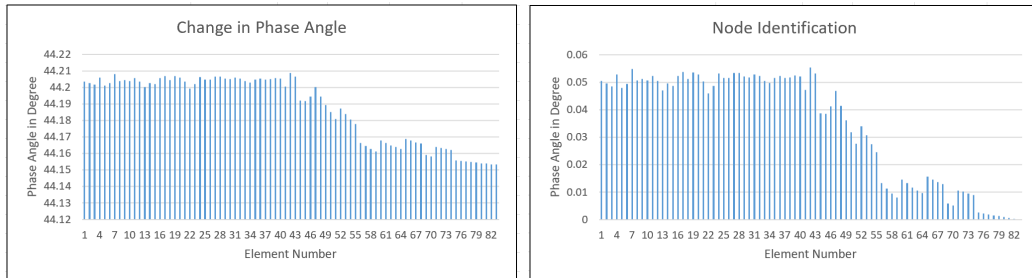


Figure 8.77: Scenario 4 case 1 350 % damage 1st flap wise bending

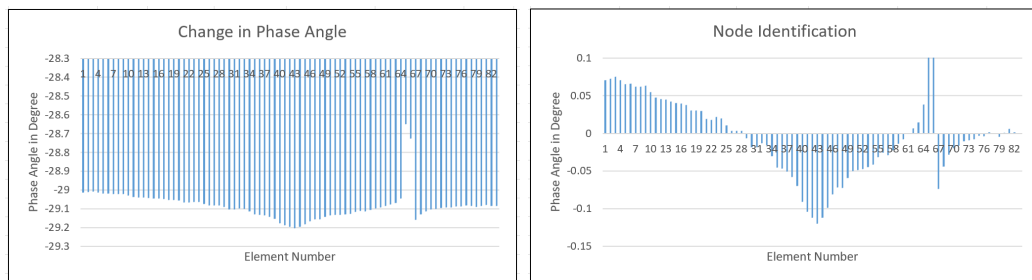


Figure 8.78: Scenario 4 case 1 350 % damage 2nd flap wise bending

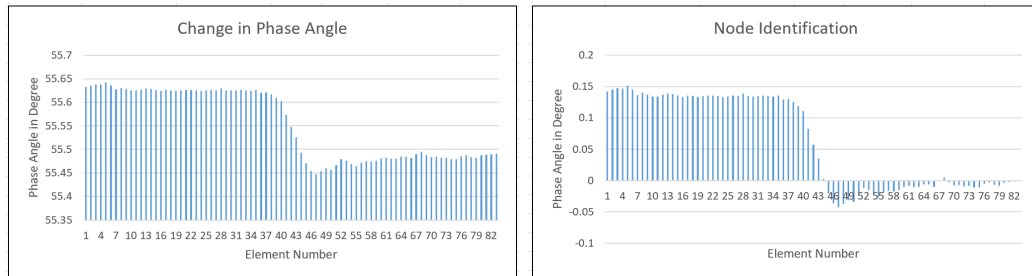


Figure 8.79: Scenario 4 case 1 350 % damage 1st edge wise bending

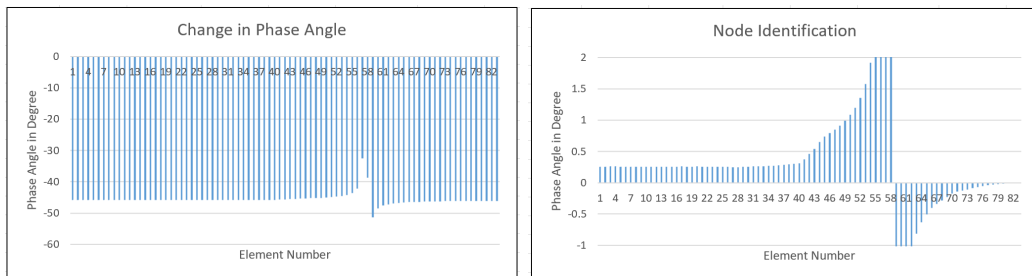


Figure 8.80: Scenario 4 case 1 350 % damage 2nd edge wise bending

Case 2: Top and core surface damage near Mid section with 4 % defected area (Damping Coefficient 0.02)

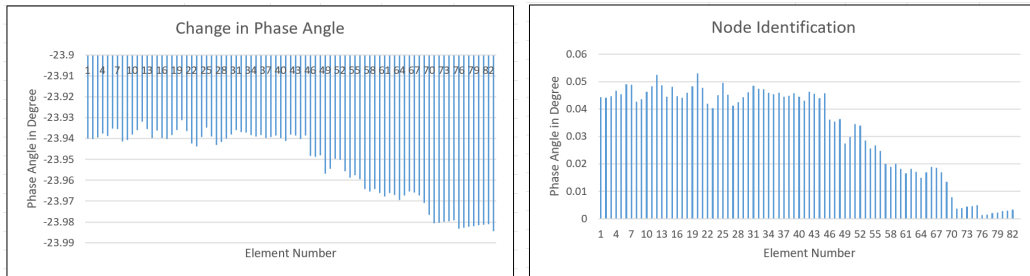


Figure 8.81: Scenario 4 case 2 100 % damage 1st flap wise bending

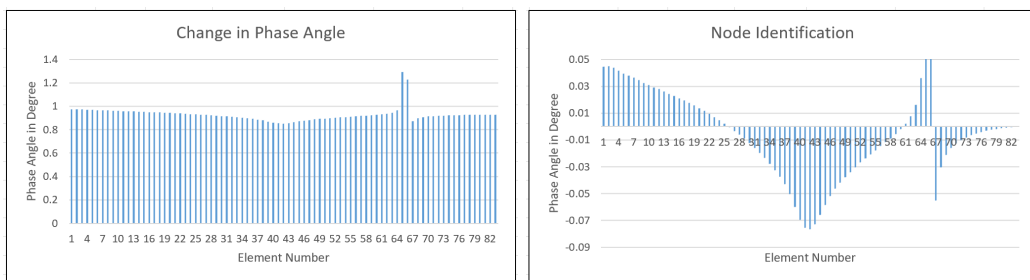


Figure 8.82: Scenario 4 case 2 100 % damage 2nd flap wise bending

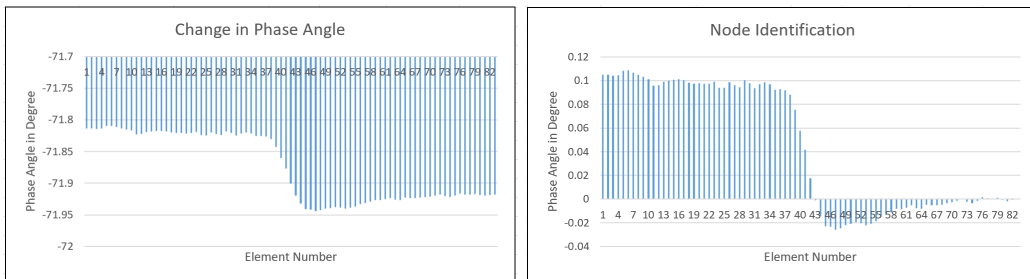


Figure 8.83: Scenario 4 case 2 100 % damage 1st edge wise bending

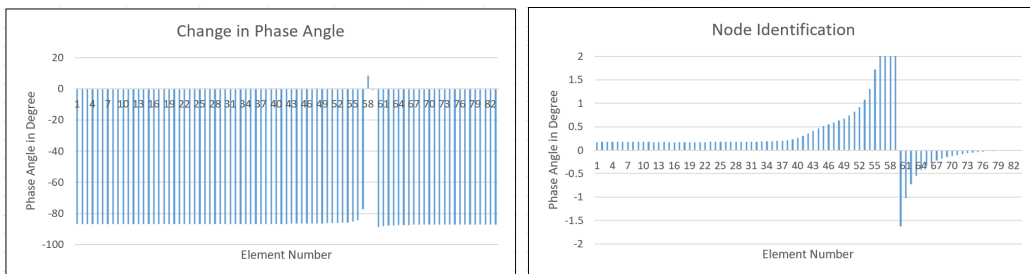


Figure 8.84: Scenario 4 case 2 100 % damage 2nd edge wise bending

Case 2: Top and core surface damage near Mid section with 4 % defected area (Damping Coefficient 0.045)

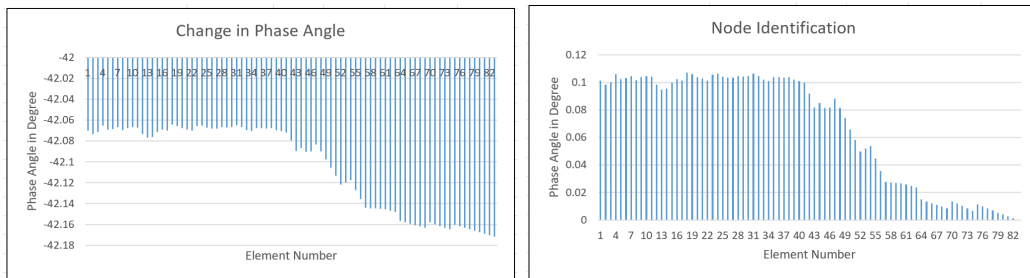


Figure 8.85: Scenario 4 case 2 350 % damage 1st flap wise bending

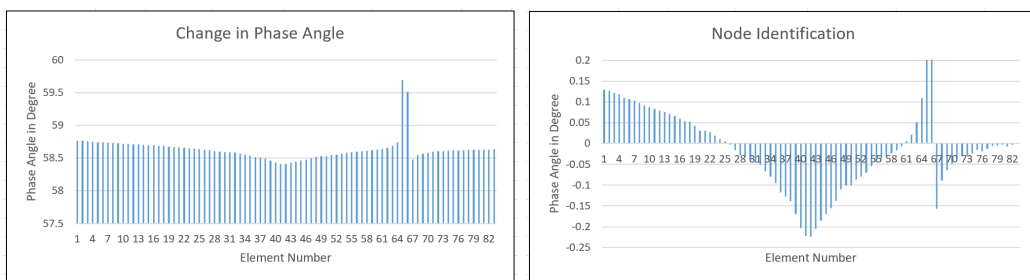


Figure 8.86: Scenario 4 case 2 350 % damage 2nd flap wise bending

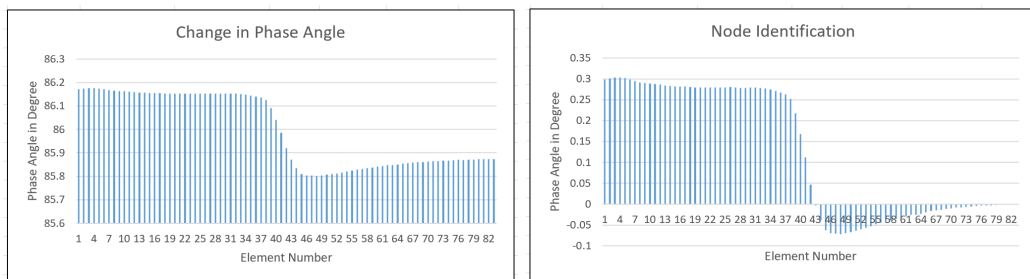


Figure 8.87: Scenario 4 case 2 350 % damage 1st edge wise bending

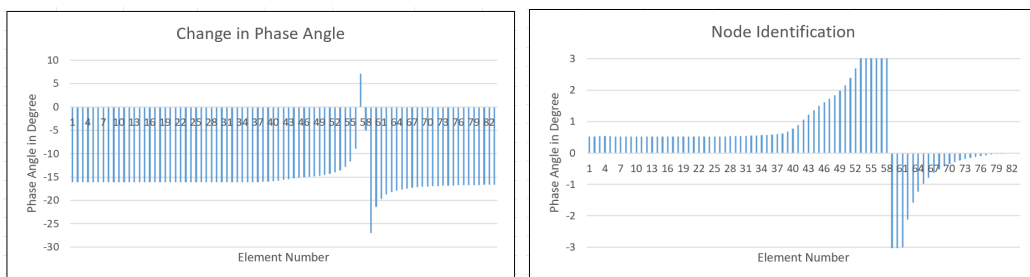


Figure 8.88: Scenario 4 case 2 350 % damage 2nd edge wise bending

Case 3: Top and core surface damage near Mid section with 6 % defected area (Damping Coefficient 0.02)

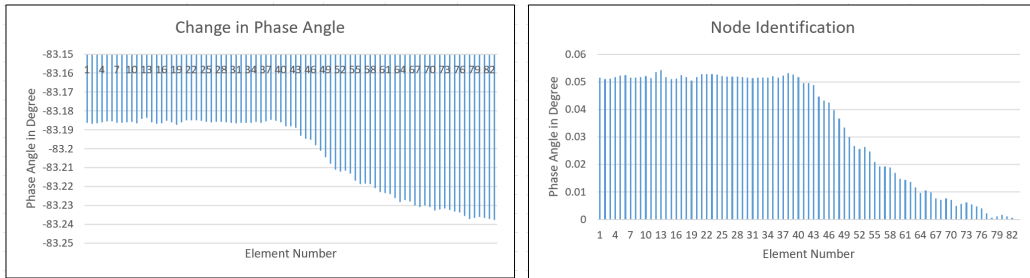


Figure 8.89: Scenario 4 case 3 100 % damage 1st flap wise bending

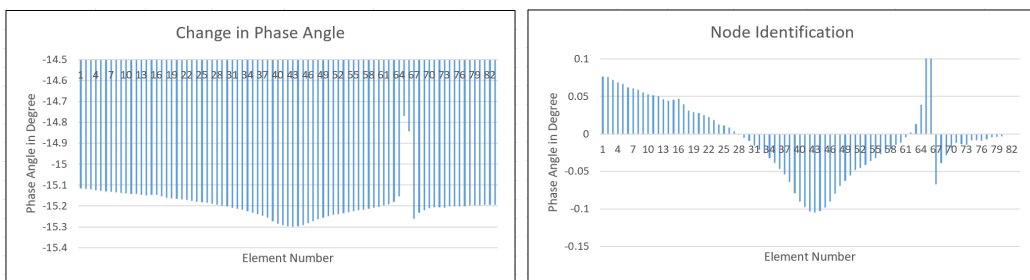


Figure 8.90: Scenario 4 case 3 100 % damage 2nd flap wise bending

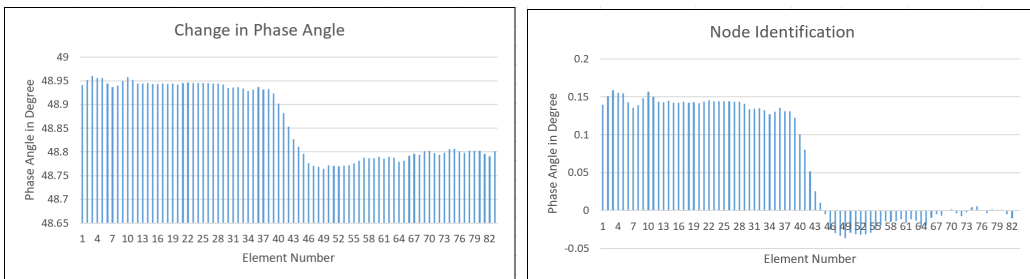


Figure 8.91: Scenario 4 case 3 100 % damage 1st edge wise bending

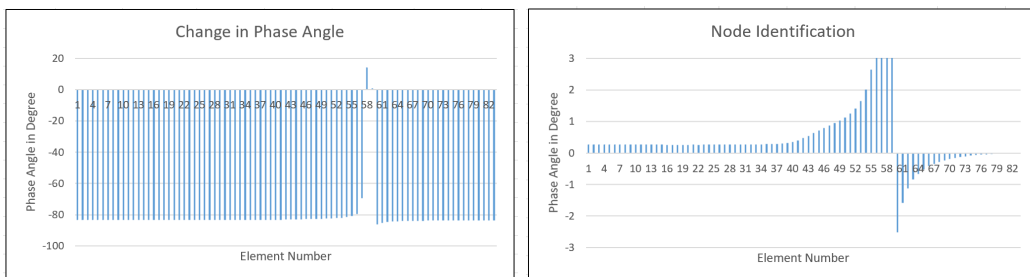


Figure 8.92: Scenario 4 case 3 100 % damage 2nd edge wise bending

Case 3: Top and core surface damage near Mid section with 6 % defected area (Damping Coefficient 0.045)

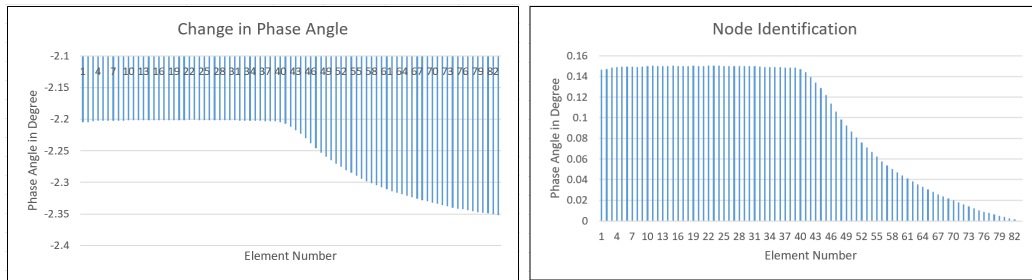


Figure 8.93: Scenario 4 case 3 350 % damage 1st flap wise bending

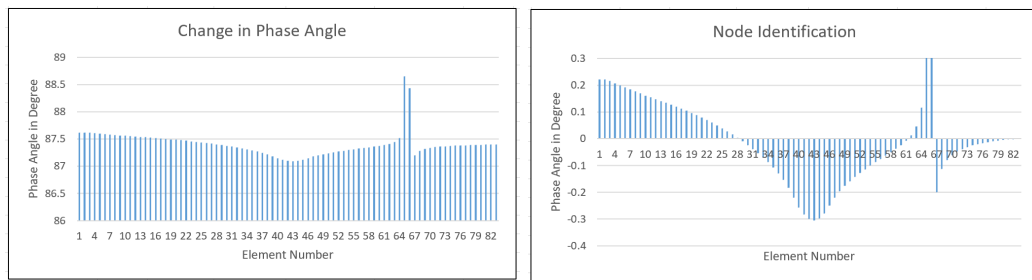


Figure 8.94: Scenario 4 case 3 350 % damage 2nd flap wise bending

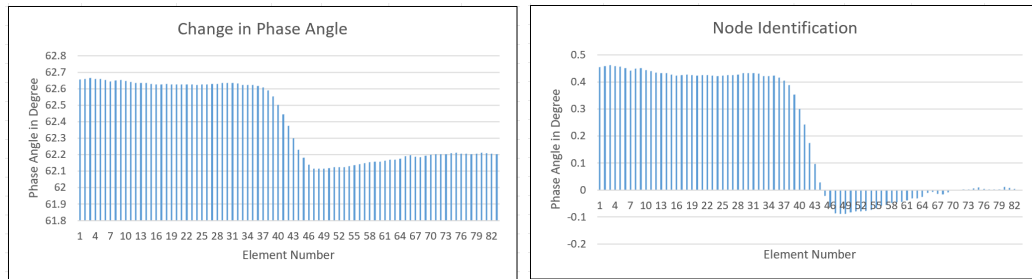


Figure 8.95: Scenario 4 case 3 350 % damage 1st edge wise bending

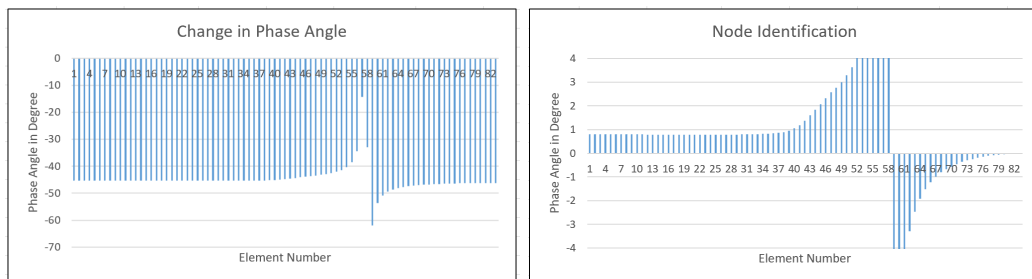


Figure 8.96: Scenario 4 case 3 350 % damage 2nd edge wise bending

Appendix B:APDL Code

```
!UNDAMAGED Structure
!stiffness
*DMAT,K,Z, IMPORT,FULL, file.full ,STIFF
*EXPORT, K, MAT, KDense,,,
!*DMAT,MatK,Z, IMPORT,MAT,KDense
!*PRINT,MatK,Kdense.txt

!Mass
*DMAT,M,D, IMPORT,FULL, file.full ,MASS
*EXPORT, M, MAT, MDense,,,
!*DMAT,MatM,D,IMPORT,MAT,MDense
!*PRINT,MatM,Mdense.txt

!Kd1
!*DMAT,Kd1,Z, IMPORT,FULL, file.full ,STIFF
!*EXPORT, Kd1, MAT, KD1,,,
!*DMAT,MatKd1,Z, IMPORT,MAT,KD1
!*PRINT,MatKd1,Kd1.txt

!Kd2
!*DMAT,Kd2,Z, IMPORT,FULL, file.full ,STIFF
!*EXPORT, Kd2, MAT, KD2,,,
!*DMAT,MatKd2,Z, IMPORT,MAT,KD2
!*PRINT,MatKd2,Kd2.txt
*DMAT,M,D, IMPORT,FULL, file.full ,MASS
*EXPORT, M, MAT, MDense,,,

!Damping Matrix
!*DMAT,MatKd1,Z,IMPORT,MAT,KD1
!*DMAT,MatKd2,Z,IMPORT,MAT,KD2
!*AXPY,1,,MatKd1,-1,MatKd2
!*EXPORT, MatKd2, MAT, KD,,,
!*DMAT,MatKd,Z, IMPORT,MAT,KD
!*PRINT,MatKd,Kd.txt

!KDD
*DMAT,MatKd,Z, IMPORT,MAT,KD1
*SCAL, MatKd,0,10

!KEE
*DMAT,MatK,Z, IMPORT,MAT,KDense
*AXPY,1,,MatK,1,,MatKd

!DAMAGED Structure
!Damaged Kd1
!*DMAT,DKd1,Z, IMPORT,FULL, file.full ,STIFF
!*EXPORT, DKd1, MAT, DamagedKD1,,,
!*DMAT,MatDamagedKd1,Z, IMPORT,MAT,DamagedKD1
!*PRINT,MatDamagedKd1,DKd1.txt

!Damaged Kd2
!*DMAT,DKd2,Z, IMPORT,FULL, file.full ,STIFF
!*EXPORT, DKd2, MAT, DamagedKD2,,,
!*DMAT,MatDamagedKd2,Z, IMPORT,MAT,DamagedKD2
!*PRINT,MatDamagedKd2,DKd2.txt
```

```

!Damaged Damping Matrix
!*DMAT,MatDKd1,Z,IMPORT,MAT,DamagedKD1
!*DMAT,MatDKd2,Z,IMPORT,MAT,DamagedKD2
!*AXPY,1,,MatDKd1,-1,MatDKd2
!*EXPORT,MatDKd2,MAT,DamagedKD,,
!*DMAT,MatDKd,Z,IMPORT,MAT,DamagedKD
!*PRINT,MatDKd,DamagedKd.txt

!Damaged KDD
!*DMAT,MatDKd,Z,IMPORT,MAT,DamagedKD
!*SCAL,MatDKd,,10

!Damaged KEE
!*DMAT,MatK,Z,IMPORT,MAT,KDense
!*AXPY,1,,MatK,1,,MatDKd

!*DMAT,MatK,Z,IMPORT,MAT,KDense
!*DMAT,MatM,D,IMPORT,MAT,MDense
!*DMAT,MatC,Z,IMPORT,MAT,KD
!/solu
!antype,modal
!MODOPT,SUBSP,2
!*EIGEN,MatDKd,MatM,,eigvalue,eigvector
!*print,eigvalue,UDeigvalue.txt
!*print,eigvector,UDeigvector.txt

!Zero matrix
*DMAT,MatK,Z,IMPORT,MAT,KDense
*DMAT,MatM,Z,IMPORT,MAT,MDense
*AXPY,,MatK,,MatM
*EXPORT,MatM,MAT,MatZ

*DMAT,K,Z,IMPORT,MAT,Kdense
*DMAT,M,D,IMPORT,MAT,Mdense
/solu
antype,modal
MODOPT,SUBSP,20
*EIGEN,K,M,,eigvalue,eigvector
*print,eigvalue,UDeigvalue.txt
*print,eigvector,UDeigvector.txt
!Damped eigen value
!KDD
*DMAT,MatKd,Z,IMPORT,MAT,KD1
*SCAL,MatKd,0,177.03

!KEE
*DMAT,MatK,Z,IMPORT,MAT,KDense
*AXPY,1,,MatK,1,,MatKd

*DMAT,MatC,Z,IMPORT,MAT,MatZ
*DMAT,MatM,D,IMPORT,MAT,MDense
/solu
antype,modal
MODOPT,DAMP,6
*EIGEN,MatKd,MatM,MatC,eigvalue,eigvector
*print,eigvalue,Dampedeigvalue.txt
*print,eigvector,Dampedeigvector.txt

```

```
Damaged1
!KDD
*DMAT,MatKd1,Z,IMPORT,MAT,DamagedKD1
*SCAL,MatKd1,0,177.03

!KEE
*DMAT,MatK,Z,IMPORT,MAT,KDense
*XPY,1,,MatK,1,,MatKd1

*DMAT,MatC,Z,IMPORT,MAT,MatZ
*DMAT,MatM,D,IMPORT,MAT,Mdense
/solu
antype,modal
MODOPT,DAMP,6
*EIGEN,MatKd1,MatM,MatC,eigvalue,eigvector
*print,eigvalue,Damagedeigvalue.txt
*print,eigvector,Damagedeigvector.txt

! Mapping
fini
/filename,I ele Mid Defect ! name of the super element
/solu
antype,MODAL ! analysis type: substructure
seopt,I ele Mid Defect,2 ! saves mass and stiffness matrix
m,all,all ! creates master nodes
solve
fini

/AUX2
FILE,I ele Mid Defect ,full
HBMAT,aux2_stiffmatrix ,txt , ,ASCII,STIFF,YES,YES
FINISH

/AUX2
FILE,I ele Mid Defect ,full
HBMAT,aux2_massmatrix ,txt , ,ASCII,MASS,YES,YES
FINISH
```